Sources térahertz produites par des impulsions laser ultra-intenses

Jérémy Déchard Déchard

NNT : 2019SACLS358

Thèse de doctorat

Sources térahertz produites par des impulsions laser ultra-intenses

Thèse de doctorat de l'Université Paris-Saclay
préparée à l'Université Paris-Sud
au sein du Commissariat à l'Énergie Atomique et aux Énergies Alternatives

École doctorale n°572 Ondes et Matière (EDOM)
Specialité de doctorat: Physique des Plasmas

Thèse présentée et soutenue à Saclay, le Lundi 14 Octobre 2019, par

M. Jérémy Déchard

Composition du jury :

Guy Bonnaud Professeur, Université Paris-Saclay	Président du jury
Howard Milchberg Professeur, Université du Maryland	Rapporteur
Emmanuel d'Humières Professeur, Université de Bordeaux	Rapporteur
Caterina Riconda Professeur, Sorbonne Université	Examinateur
Jérôme Faure Directeur de recherche, École Polytechnique	Examinateur
Olle Lundh Maître de conférence, Université de Lund	Examinateur
Luc Bergé CEA/DAM Bruyères-le-Châtel	Directeur de thèse
Laurent Gremillet CEA/DAM Bruyères-le-Châtel	Co-directeur de thèse
Xavier Davoine CEA/DAM Bruyères-le-Châtel	Invité

Remerciements

Je tiens tout d'abord à remercier le jury, composé de Caterina Riconda, Jérôme Faure et Olle Lundh, d'avoir lu mon manuscrit et d'avoir assister à la soutenance. Un merci particulier à Emmanuel d'Humières pour avoir rapporté la thèse, ainsi qu'à Howard Milchberg : thank you for crossing the Atlantic Ocean to come to the defense ! Enfin, un grand merci à Guy Bonnaud pour avoir présider le jury pendant cette journée si spéciale.

La thèse présentée dans ce manuscrit a été effectuée au Commissariat à l'Énergie Atomique et aux énergies alternatives, sur le centre de Bruyères-le-Châtel. Je souhaite ainsi remercier les différentes personnes rencontrées durant ces trois années.

Merci donc à Catherine Cherfils pour m'avoir accueilli au sein du département ainsi qu'à Brigitte pour ta gentillesse, pour nos discussions et pour ta maitrise des questions administratives. Merci Florian pour ta gestion du service et du temps que tu as pu me consacrer.

La réussite de cette thèse tient en grande partie à la solidité de l'équipe dont j'ai pu faire partie. Merci Luc d'avoir été un directeur de thèse rigoureux et disponible. Je salue aussi ton engagement constant dans nos travaux qui ont forcé, et force toujours, mon admiration.

Les rencontres qui marquent sont rares et précieuses, celle avec toi, Laurent, fut l'une d'entre elle. Un immense merci pour l'ensemble de ton travail honnête et rigoureux. Mais surtout merci pour les débriefs de tes escapades, de tes comptes rendus culinaires (aaah ces ris de veaux au Cornichon), de tes explications sur la politique étrangère, de tes décryptages de l'actualité et de tes jeux de mots moins bon que ton sens physique !

Bravo et merci à Xavier D. pour avoir supporté mes incessantes questions sur CALDER ainsi que mes questions tout court. Tu as été un formidable Maître Jedi : calme, pragmatique, disponible, en un mot : cool.

Enfin, merci à Arnaud pour ta participation active dans le projet mais surtout merci de m'avoir envoyé à Nusa Penida (Indonésie) nager avec des raies mantas. Prochaine destination : Fakarava.

Cela fut un plaisir de venir travailler au laboratoire, notamment grâce aux personnes que j'ai pu côtoyer. Je citerai Christophe et Philipe pour la partie la plus éloignée du couloir, merci pour les discussions toujours sympathiques que nous avons eu. Un grand merci à Jean-Etienne et Didier pour avoir animé les débats lors de nos repas.

Bien sûre je n'oublie pas ce vieux bouc de Serge dont j'ai subi les farces tout au long de la thèse : merci pour ces bonnes parties de rigolades, j'ai hâte de revenir t'embêter de temps en temps.

J'ai une pensée toute particulière pour Sylvie, merci d'avoir rendu la vie au labo plus facile et

plus chaleureuse. Merci surtout pour tes rires, ton amitié et ta complicité.

Entre mon arrivée et mon départ j'ai eu la chance de croiser la route de nombreux jeunes chercheurs à commencer par Pedro et Alisée qui ont su me prendre sous leur aile et m'initier aux arcanes du térahertz. Un peu en vrac merci à Simon, Antoine, Vivien, Manu, Marine, Xavier V., Witold, Arno et Pierre-Louis pour le partage de notre quotidien de "thésitifs", comme dirons certains, entre la cantine, le trajet en bus et les sorties sur Paris. Un merci spécial à Gaëtan pour le SAV de la physique des plasmas.

Pendant deux et demi il aura partagé mon bureau 8 heures par jour sans broncher, même lors de mes envolées lyriques, j'ai nommé le patient et infaillible Bertrand : merci infiniment à toi pour ces moments ! C'est non sans crainte que j'ai attendu ton digne successeur... Ce fut David, qui a su relever le défi avec panache et brio. C'est ainsi que, si proche du but, j'ai bien failli trébucher à force de discussions enflammées. Merci surtout d'avoir enduré la phase de rédaction et de soutenance, projets BULLDOZER et INSOUTENABLE, respectivement.

Le soutien de mes proches a aussi été infaillible hors du laboratoire, à commencer par Anthonin, Chloé et Marc : merci d'avoir été là pour la soutenance ! Merci à Romain et Anne d'avoir, trois années durant, tentés de comprendre mon sujet de thèse sans y parvenir vraiment : voilà j'ai terminé de jouer avec mes lasers ! Je souhaite aussi remercier chaleureusement le meilleur des professeurs, merci Pierre pour ce que tu m'as enseigné, je ne l'oublierai pas.

Evidemment le soutien sans faille de ma famille m'a permis d'avancer avec confiance dans ce projet de recherche. Merci à toi papa, merci à toi maman. Merci à mes frères Nico et Florent (and to my first sister-in-law Dru !). Merci à ma soeur Aurore, merci à Mat et aux enfants : Noam, Simon et Joséphine.

Merci à Nathalie d'avoir veiller sur moi et à Stéphane pour être venu jusqu'à B3 pour me nourrir à coups de pizzas.

Enfin, et ce n'est un secret pour personne, je ne serais que bien peu de chose sans elle tant elle me complète. Merci à toi Alexia d'avoir été d'un soutien sans faille au point de m'aider à écrire, en ce moment même, ces remerciements !

Merci à tous,

Mots clés : Sources térahertz intenses, Interaction laser-plasma, Plasmas relativistes
Résumé : Les impulsions laser femtosecondes produisent des phénomènes non linéaires extrêmes dans la matière, conduisant à une forte émission de rayonnement secondaire qui couvre un domaine en fréquence allant du terahertz (THz) aux rayons X et gamma. De nombreuses applications utilisent la bande de fréquences térahertz (0.1-100 THz) afin de sonder la matière (spectroscopie, médecine, science des matériaux). Ce travail est dédié à l'étude théorique et numérique du rayonnement THz généré par interaction laser-plasma. Comparé aux techniques conventionnelles, ces impulsions laser permettent de créer des sources THz particulièrement énergétiques et à large bande. Notre objectif a donc été d'étudier ces régimes d'interaction relativiste, encore peu explorés, afin d'optimiser l'efficacité de conversion du laser vers les fréquences THz. L'étude de l'interaction laser-gaz en régime classique nous permet, d'abord, de valider un modèle de propagation unidirectionnelle prenant en compte la génération d'impulsion THz et de le comparer à la solution exacte des équations de Maxwell. Ensuite, en augmentant l'intensité laser au-delà du seuil relativiste, nous simulons à l'aide d'un code PIC une onde plasma non linéaire dans le sillage du laser, accélérant ainsi des électrons à plusieurs centaines de MeV. Nous montrons que le mécanisme standard des photocourrants est dominé par le rayonnement de transition cohérent induit par les électrons accélérés dans l'onde de sillage. La robustesse de ce rayonnement est ensuite observée grâce à une étude paramétrique faisant varier la densité du plasma sur plusieurs ordres de grandeur. Nous démontrons également la pertinence des grandes longueurs d'ondes laser qui sont à même de déclencher une forte pression d'ionisation augmentant la force pondéromotrice du laser. Enfin, les rayonnements THz émis à partir d'interactions laser-solide sont examinés dans le contexte de cibles ultra fines, mettant en lumière les différents processus impliqués.

Keywords: Intense terahertz sources, Laser-plasma interaction, Relativistic plasmas
Abstract: Femtosecond laser pulses trigger extreme nonlinear events in matter, leading to intense secondary radiations spanning the frequency ranges from terahertz (THz) to X and gamma-rays. This work is dedicated to the theoretical and numerical study of THz radiation generated by laser-driven plasmas. Despite the inherent difficulty in accessing the THz spectral window (0.1-100 THz), many coming applications use the ability of THz frequencies to probe matter (spectroscopy, medicine, material science). Laser-driven THz sources appear well-suited to provide simultaneously an energetic and broadband signal compared to other conventional devices. Our goal is to investigate previously little explored interaction regimes in order to optimize the laser-to-THz conversion efficiency. Starting from classical interactions in gases, we validate a unidirectional propagation model accounting for THz pulse generation, which we compare to the exact solution of Maxwell's equations. We next increase the laser intensity above the relativistic threshold in order to trigger a nonlinear plasma wave in the laser wake, accelerating electrons to a few hundreds of MeV. We show that the standard photocurrent mechanism is overtaken by coherent transition radiation induced by wakefield-accelerated electron bunch. Next, successive studies reveal the robustness of this latter process over a wide range of plasma parameters. We also demonstrate the relevance of long laser wavelengths in augmenting THz pulse generation through the ionization-induced pressure that increases the laser ponderomotive force. Finally, THz emission from laser-solid interaction is examined in the context of ultra-thin targets, shedding light on the different processes involved.

Contents

Chapter 1

Introduction

Contents

1.1 The science of laser plasma interaction

1.1.1 Ultra high-intensity lasers

Since its proof of concept brought by Maiman in 1960 [Maiman 1960], the LASER (Light Amplification by Stimulated Emission of Radiation) has become an ubiquitous tool in every day life as well as in research. Basically, a laser relies on the stimulated radiation occurring in a gain medium put in an excited state by an external source of energy, e.g., flash lamps. Photons of energy $\hbar\omega$ ($\hbar$ being the reduced Planck's constant and ω the radiation frequency) are emitted coherently along the same polarization direction, forming a laser beam. The gain medium, Ti:sapphire or Nd:YAG, imposes the laser wavelength to be 800 nm and 1064 nm, respectively. The operation mode can be continuous or pulsed, the latter being characterized by a certain duration delivered at a given repetition rate. Laser applications are numerous: To name just a few they span from medicine, manufacturing, metrology to communication and even energy production. Laser systems are becoming irreplaceable in research as they deliver unique sources of coherent light on small spatial and time scales reaching high local powers.

This search of power has required several technological breakthroughs. Shortly after the demonstration by Maiman, McClung & Hellwarth [1962] introduced a Kerr cell[1] in the optical cavity to stop the lasing effect. The quality factor Q of the cavity, which increases with the energy stored in the gain medium, becomes quickly degraded and the accumulated photons are rapidly released, resulting in a short pulse of light. The Kerr cell offers an externally-controlled variable attenuator for this function. Once it is turned off, the energy goes out in a short pulse. This so-called "Q-switch" method allowed to reach short pulse durations covering a few

[1] A Kerr cell is an optical device using the birefringence of a liquid (nitrobenzene) under an applied DC voltage to act as a shutter for an incoming light.

nanoseconds. Hence few Joules laser systems were able, at that time, to produce high peak powers of about $P = \mathrm{J}/\ \mathrm{ns} \sim 1$ GW.

A few years after the invention of the Q-switch technique, longitudinal modes oscillating in the optical cavity were put in phase to add-up coherently, resulting in an amplitude increase and pulse shortening. This "mode-locking" technique [Fork *et al.* 1981, 1984] can be active, by means of an electro-optic modulator, or passive when using saturable absorbers. With this method, pulse durations in the picosecond (10^{-12} s), even femtosecond (10^{-15} s) ranges were achieved, with still small pump energy engaged. Such short durations allowed to probe fast molecule dynamics with pump-probe experiments and provided the first optical scalpels for eye-surgery. Laser systems close to the TW level became affordable and widespread in many laboratories. Once focused, intensities of $\sim 10^{15}$ W/cm^2 were reached, opening the research fields to laser-driven plasmas and subsequent nonlinear effects such as harmonic generation, four-wave mixing, self-focusing or Raman/Brillouin instabilities.

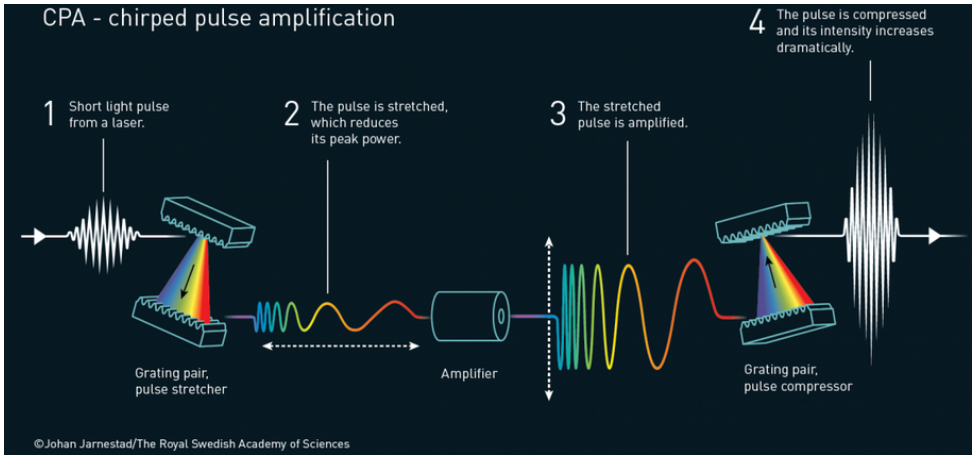

Figure 1.1: Illustration of the chirped pulse amplification technique (CPA) proposed by Strickland & Mourou [1985] and awarded by the 2018 Nobel Prize in Physics. From Johan Jarnestad for The Royal Swedish Academy of Sciences.

However, higher laser energy excites the nonlinear response of the gain media, in particular the Kerr effect leads to local amplification of the light pulse and can generate thermal growths that is able to damage the amplification material. This is why further attention was paid on the duration of the laser pulse and not on its energy in order to increase the instantaneous power. The original technique discovered by Strickland & Mourou [1985] was to temporally stretch a laser pulse generated by a mode-locked cavity with a grating according to its frequency components and to produce a chirped pulse. Then, each frequency is amplified by the gain medium below the damage threshold. After this amplification stage, the frequencies are all recombined by another (identical) grating adding up to form an ultrashort pulse (see Fig. 1.1), which can then convey a few hundreds of TW power. Once tightly focused, such laser pulses attain intensities increasing from 10^{15} to 10^{20-21} W/cm^2, hence undergoing an impressive growth by five to six orders of magnitude. The laser field amplitudes are thus sufficiently high to fully ionize common materials, which opened the route to study laser-plasma interactions on ultrashort time scales. More importantly, charged particles (electrons, protons) can be accelerated to the high velocities, reproducing high energy processes observed in astrophysics (collisionless shocks, lepton jets from pulsars, magnetic reconnection). Also, the multitude of nonlinear effects triggered at these high intensity levels (nonlinear plasma waves, inverse Compton scattering, Bremsstrahlung) can be exploited to realize new radiation sources (THz, betatron X-rays and γ-rays) showing remarkable

features (see next Section).

Nowadays intensive researches in laser technology are carried out to reach peak powers even above the PW level (see Fig. 1.2). This new generation of lasers will be able to accelerate heavy ions, produce various high energy radiations (X-rays, γ-rays) and trigger quantum electrodynamic effects (electron-positron pairs for instance). All these phenomena requiring extreme intensities lie at the intersection between plasma physics and high energy physics. Large facilities around the world are currently under construction to reach this goal. Different approaches are tested: the ELI project in East Europe aims at combining two 10 PW laser beams[2] into a 20 PW pulse while the project APOLLON in France plans to reach 10 PW with 150 J delivered in 15 fs. Other facilities bet on laser upgrades like VULCAN (UK) concentrating 400 J in 20 fs light pulses and thereby leading to a single 20 PW beam.

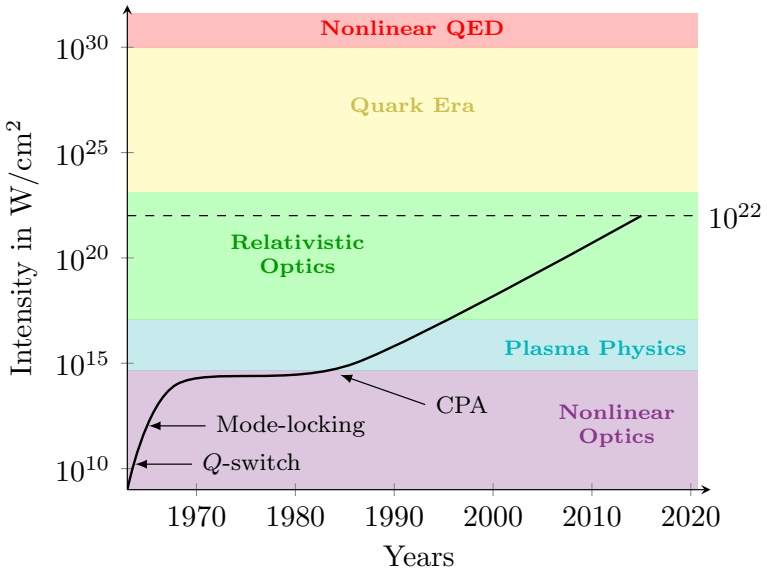

Figure 1.2: Evolution of the laser intensity since 1960. *Adapted from* Mourou *et al.* [2006].

1.1.2 Source of particles and radiation

As evidenced in Fig. (1.2), current laser intensities are high enough to extract electrons from atoms creating a plasma. This fourth state of matter is composed of ions and electrons driven by electromagnetic interactions. Once formed, charged particles are subject to intense plasma and electromagnetic fields capable to drag them to relativistic velocities and to be even more accelerated through appropriate plasma dynamics. The resulting so-called "laser-plasma accelerators" then appear to provide compact, affordable and performant sources of electrons (in gases) or protons (in solids).

Since the work by Tajima & Dawson [1979], we know that laser pulses propagating in an underdense gas can resonantly excite a plasma wave in the laser wake. Photoionized electrons are pushed by the laser ponderomotive force - following alternatively the rising and falling laser intensity profile - which can coincide with the restoring force exerted by ions if the laser duration (τ_0) matches the plasma period ($2\pi/\omega_{pe}$). This resonance induces a nonlinear plasma wave when ultra high-intensity (UHI) lasers are employed. Then, a small population of electrons can be accelerated, like a surfer on a wave which acquires larger velocity and more kinetic energy, which

[2]The ELI-NP facility reached the 10 PW level recently (March 2019), making it the most powerful laser in the world.

constitutes the key idea behind the concept of laser wakefield accelerator (LWFA). Recently, electron beams at 8 GeV (record value) have been demonstrated by Gonsalves *et al.* [2019] using 0.85 PW laser focused into a capillary tube filled with an underdense hydrogen gas. In order to reach the TeV level and compete with standard accelerators, one has to stage multiples GeV acceleration sections to form a complete accelerator [Steinke *et al.* 2016]. The main challenge is then to couple each stage with a minimal energy loss. Compared to conventional facilities (linear SLAC[3], or circular LHC[4]) the dimensions of laser-based accelerator setups are greatly reduced, together with its cost.

The interaction with solid targets leads to ion acceleration (mainly protons) through various mechanisms such as the Target Normal Sheath Acceleration (TNSA) or the Radiation Pressure Acceleration (RPA), which will be detailed further in the present manuscript. Such proton beams are particularly useful as diagnostics to probe matter under extreme temperature and pressure conditions as met in experiments dedicated to inertial confinement fusion [Mariscal *et al.* 2018]. This is the reason why laser driven fusion facilities are often equipped with additional UHI lasers able to produce proton beams with tens of MeV energy (PETAL for Laser Mega Joule in Le Barp, France and ARC for the National Ignition Facility in Livermore, USA). In addition, such particle sources can be used for the production of warm dense matter by, e.g., isochoric heating, in the fast ignition concept for inertial fusion, to trigger nuclear reactions by interaction with a secondary target or in medicine to treat cancer by proton therapy [Macchi *et al.* 2013]. The record for current maximum energy reached by accelerated protons is about 94 MeV and has been obtained recently by Higginson *et al.* [2018] on the VULCAN laser facility with $\sim$ 210 J energy during $\sim$ 1 ps leading, once focused, to $\sim 3 \times 10^{20}$ W/cm^2 intensity. Now, progress remains to be done to obtain a high frequency repetition laser system able to produce such energetic proton beams routinely.

In addition to particle acceleration, ultra-intense laser-plasma interaction results in the production of secondary electromagnetic sources. Indeed, as it is well known, accelerated particles radiate [Jackson 1999]. Due to the intrinsic femtosecond interaction feature, very short ($\sim$ fs), small ($\sim \mu$m) and bright high energy secondary electromagnetic sources can then be produced.

In relativistic plasmas created from gases, a bunch of wakefield-accelerated electrons oscillates transversally and, simultaneously, moves close to the speed of light along the laser propagation axis, producing thereby a synchrotron-like spectrum [Esarey *et al.* 2002; Fourmaux *et al.* 2011]. These oscillations of betatron-type lead to keV X-ray radiation with low divergence ($\sim$ mmrad). The same electron beam can also interact with a counter-propagating laser to generate X-rays through inverse Compton/Thomson scattering [Esarey *et al.* 1993; Schwoerer *et al.* 2006]. Another important research field is the production of high harmonics of the laser frequency during the ionization-recombination process of electrons [Corkum 1993; Brabec & Krausz 2000] for laser intensities $\sim 10^{15}$ W/cm^{-2}. Accelerated electrons also constitute a relevant source of X-rays [Seres *et al.* 2005], and eventually produce attosecond (10^{-18} s) pulses after collision with their parent ion down to 80 as duration [Sansone *et al.* 2006; Goulielmakis *et al.* 2008], opening the way to follow electron or molecular transitions over fractions of the laser period. Nevertheless, the generation of high harmonics breaks down beyond a few $\sim 10^{15}$ W/cm^{-2} due to multiple ionization. These limitations can be circumvented by using UHI lasers focused on initially-solid targets. The laser pulse interacts with a sharp overdense plasma (plasma mirror) emitting high harmonics, and thus attosecond pulses, following two dominant mechanisms namely the coherent wake emission or the relativistic oscillating mirror depending on the laser intensity value [Thaury

[3]Stanford Linear Accelerator Center
[4]Large Hadron Collider

& Quéré 2010].

To continue with solid targets, the population of hot electrons generated by the interaction can be deflected by the atomic Coulomb field and emit γ-ray bursts through Bremsstrahlung [Galy *et al.* 2007], particularly when using high atomic number (Z) material. This new source of photons now opens the possibility to study photonuclear reactions (activation, fission, fusion and transmutation) without the need of large scale facilities such as conventional particle accelerators or nuclear reactors [Ledingham *et al.* 2000]. Finally for intensities exceeding 10^{22} W/cm^2, quantum radiation of accelerated particles can nowadays be explored for instance the creation of electron-positron pairs by the nonlinear Breit-Wheeler process [Lobet *et al.* 2017] or γ-ray generation by synchrotron radiation [Grismayer *et al.* 2016].

1.2 Terahertz waves

1.2.1 Definition and applications

As underlined above, laser-matter interaction leads to secondary radiation sources for either classical or relativistic intensities using gaseous or solid interaction targets. These sources are rather energetic as they produce X or γ photons. In contrast, during this PhD work we shall focus on the production of electromagnetic waves with much lower energies, and characterized by smaller frequencies, namely, the terahertz frequencies (1 THz = 10^{12} Hz). Traditionally defined between 0.1 and 30 THz, this band of the electromagnetic spectrum is usually denominated "THz gap" due to the difficulty to produce and detect such frequencies. Indeed, the latter are, at the same time, too fast for electronic chips and too slow for purely optical devices. Nevertheless, their interest has been steadily growing since the past two decades, due to their numerous potential applications in medical imaging, spectroscopy or even telecommunication.

Due to their small frequencies compared to the optical spectrum, THz waves carry weak energy, between 1 up to a few hundreds of meV, rendering the radiation non-ionizing, unlike X-rays for instance. This feature is particularly interesting since THz pulses can penetrate a few millimeters of synthetic or organic materials whereas metals are opaque to such radiation. One direct future application is homeland security with THz imaging in order to detect dangerous items (knifes, guns, explosives) [Liu & Zhang 2014]. Also, the ability to penetrate into the first skin layers made THz imaging suitable for cancer diagnostics without damaging the DNA [Woodward *et al.* 2003]. In addition, the difference in cell composition influences the wave reflexion and can provide valuable information on the water content (for instance) to discriminate between healthy and ill (tumoral) cells over millimetric depths. Similarly, manufacturing defects in industrial products can be detected by THz imaging, e.g., for food inspection [Chan *et al.* 2007].

The main advantage of THz waves, the characteristic period of which is close to the picosecond, is their typical variation time scale adapted to slow molecular motions, whereas optical photons are rather adapted tools to track electronic transitions in atoms. THz photons are suited for detecting lower energy and picosecond timescale motions such as rotations or slow vibrations of molecules. Also, hydrogen bonds in molecular structures can be excited by THz waves, revealing informations about a material or even during some internal transitions. Hence, THz spectroscopy may have the capability of characterizing complex chemical components of a given sample as well as its close environment and, thus, to establish a unique map of its characteristic fingerprints (see Fig. 1.3). This technique known as THz-time domain spectroscopy (THz-TDS) is, moreover, easy to establish since the emitting and the detection sources are usu-

ally identical. This has been used to recognize the nature of different narcotics [Tonouchi 2007] or energetic materials to mention a few [Bergé *et al.* 2019]. Let us here recall that the main drawback of THz-TDS is the absorption of such frequencies by water vapor in ambient air over less than 1 meter distances. To overcome this limitation in long-range detection setups, two workarounds can be considered. First, one can imagine to produce remotely the THz pulse, the closer possible to the sample. Second, we can alternatively produce the highest possible THz energy yield expected to be propagated as far as possible. In this regards, laser-plasma based sources are particularly well suited compared to other existing techniques.

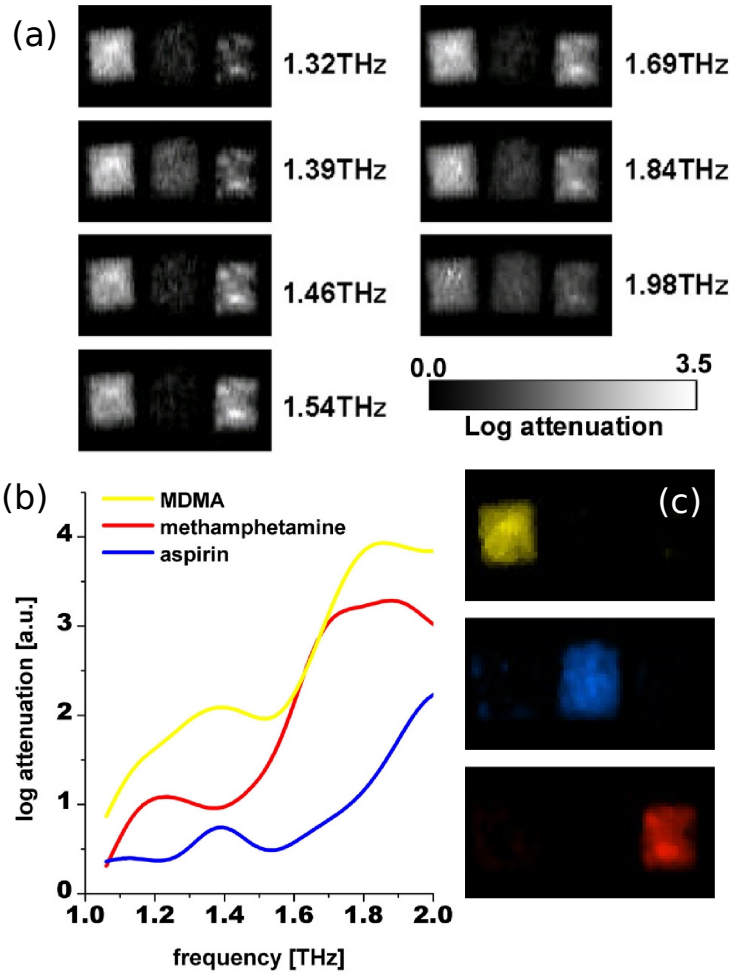

Figure 1.3: (a) Multispectral images of three samples (MDMA, methamphetamine and aspirin) in the THz domain. (b) Absorption spectra and (c) extracted spatial patterns. *Extracted from* Kawase *et al.* [2003].

1.2.2 Existing techniques for THz pulse generation

We here give a rapid overview of the existing current devices for the generation of THz waves and then mention the advantages of laser-plasma solutions. Generally speaking, THz waves are produced by downconversion of higher frequencies coming from the optical spectrum. This downconversion is handled by nonlinear processes.

Used since thirty years, photoconductive antenna are made of two electrodes etched on a semi-conductor chip where a biased electric field is applied. A femtosecond laser beam focused on the semiconductor triggers a free-carrier charge, forming a transient photocurrent that emits

THz frequencies in the far-field [Burford & El-Shenawee 2017]. This technique is directly limited by the damage threshold of the semiconductor and, therefore, is limited to the production of maximum THz amplitude of about 0.1 GV/m only. In addition, the generated spectral band is relatively narrow ($\sim$ 5 THz) and depends strongly on the carrier lifetime. Lasers emitting directly in the THz band have been proposed. In particular, quantum cascade lasers deliver mW continuous powers below 10 THz relying on electron intersubband transitions [Williams 2007]. The last widely used method based on solid materials is the optical rectification of femtosecond light pulses in nonlinear crystals. The asymmetric structure of crystals promote strong quadratic susceptibilities $\chi^{(2)}$ in the polarization vector of bounded electrons $P \propto \chi^{(2)}E^2$, where E is the laser electric field. As a result, a low frequency component $2\omega - \omega - \omega \to 0$ is created, corresponding to THz frequencies. Recently, impressive progresses have been achieved by fulfilling optimum phase-matching conditions using the "tilted-front-pulse" technique [Ravi *et al.* 2015] or by exploiting large surface organic crystals. State-of-the-art setups are today able to deliver mJ THz energy with percent order conversion efficiency [Fülöp *et al.* 2014]. Nevertheless, the spectral bandwidth reached by these two latter techniques stays limited to a few THz only and the constraint on their own damage threshold remains strong.

Alternatively, ultrashort laser pulses focused on gaseous or solid targets can also be used to produce THz frequencies [Hamster *et al.* 1993]. Historically, the laser-gas setup attracted a lot of interest due to its simplicity and efficiency. Depending on the involved laser intensity, different generation processes have to be considered. For non-ionizing pulses ($\sim 10^{12}$ W/cm^2), the nonlinear Kerr effect induces spatially a self-focusing of the beam and third harmonic generation in the pulse spectrum. When employing a laser pulse composed of a fundamental and its second harmonic, four-wave-mixing leads to low-frequency emission as it was initially proposed by Cook & Hochstrasser [2000]. At higher intensities ($> 10^{13}$ W/cm^2), plasma effects can readily overcome nonlinear optical converters. In this respect, to explain the generation of intense THz pulses in atmospheric gases reported in the latter reference, Kim *et al.* [2007] were the first to propose the photocurrent model relying on time-asymmetric laser pulses to produce an efficient quasi-DC current. When the beam intensity is high enough, a plasma spot is created and acts as a nonlinear frequency converter. Photoionized electrons are accelerated by the laser field and build up a macroscopic current containing low-frequencies. The advantages of this technique are manifold. First, the laser-induced plasma is not subject to any damage threshold such that high laser energy can be engaged to increase the THz output. The THz energy yield indeed linearly increases with the pump energy up to saturation beyond a few tens of mJ energy pump [Oh *et al.* 2013]. Second, the filamentation dynamics, resulting from the interplay between Kerr self-focusing and plasma defocusing [Bergé *et al.* 2007] is able to produce an emitting point source remotely, close to the sample, and thereby overcome water absorption in ambient air. Finally, the emitted spectrum is particularly broad, up to 100 THz, with field amplitude reaching routinely 0.1 GV/m. The sum of these unique features make laser-plasma sources an attractive solution for generating intense THz pulses to be used in futur spectroscopy experiments.

However, so far, THz generation by relativistic laser pulses focused in gases has been little studied. Leemans *et al.* [2003] proposed to exploit electrons accelerated in the laser wake to generate low-frequency coherent transition radiation from the plasma-vacuum interface. However, THz energy per pulse remained weak (3-5 nJ in 30 mrad collection angle) and limited by the acceleration process as well as by the plasma configuration. In the present work, we shall examine the already well-known mechanisms exhibited in the classical regime and investigate their predominance in the relativistic regime where transition radiation moreover occurs as a

key player. In addition, this latter radiation process will be carefully studied in order to find an optimum in term of radiated energy.

1.3 Outline of the manuscript

This PhD work is devoted to THz field emissions by laser-plasma interactions. Its originality lies in the broad range of interaction scenarios addressed. Indeed, dedicated investigations will be carried out in classical and relativistic regimes in the context of laser-gas setups. Then, the transition between rarefied and dense plasmas will be studied, along with the influence of the laser wavelength in the high intensity regime. Finally, dense relativistic plasmas created from solid targets will be explored in order to clear up the underlying physics of THz emission.

Throughout this work, attention will be paid to (i) understand the different processes and their interplay leading to THz emission and (ii) optimizing these mechanisms in terms of THz pulse amplitude, energy, spectral width for future applications. This prospective point of view will lead us to explore a wide range of laser-plasma parameters and to tackle numerous physical processes. Therefore, this doctoral dissertation is composed of four main chapters.

Chapter 2 introduces the fundamentals of laser-plasma interaction in underdense plasmas, either in the classical or relativistic regime. The generation of THz pulses in classical regime is fairly well-understood and constitutes the basis to understand THz emissions by ionized gases. The driving process relies on the so-called photocurrent scenario proposed by Kim *et al.* [2007, 2008] and exploited by means of two-color laser pulses. Two theoretical and numerical approaches used to describe THz emissions are compared to each other, constituting the first result of this PhD dissertation. This study sheds light on the influence of backscattered light on THz generation at a plasma-vacuum interface created by an ionizing laser pulse and clears up some limitations of current unidirectional propagation models. Then, we shall consider higher laser intensities and emphasize new phenomena arising in the relativistic regime. Due to the complex physics involved (wave-particle interaction) and its numerous nonlinearities, we shall rely on massively parallel multidimensional particle-in-cell (PIC) simulations, the algorithm of which will be explained. Finally, the transition radiation emitted by charged particle going from one medium to another one having different optical properties and arising in relativistic laser-plasma interaction will be exposed.

Chapter 3 presents two correlated studies. The first one extends a semi-analytical model used in classical laser-gas interactions to the relativistic regime. A quasi-3D PIC simulation validates this model and, furthemore, proves the relevance of the coherent transition radiation (CTR) at the plasma-vacuum interface. The second study deals with transition radiation only and provides a parametric scan from rarefied to dense plasmas. We demonstrate the robustness of the CTR, which may deliver mJ THz energy over a wide range of plasma density, with an optimum for highly charged and rather low energetic electron beams. Also, an analytical model based on the generalized Biot-Savart law is presented to evaluate in PIC simulations the radiated field of a relativistic electron beam and the true amount of energy being propagated far from the emitting source. We find that at most 25 % of the THz energy yield emitted by wakefield-accelerated electrons can be associated with CTR.

Chapter 4 discusses the interest of using long laser wavelengths in the relativistic regime, particularly for THz pulse generation. By means of PIC simulations we demonstrate the existence of a strong redshift in the optical spectrum induced by the feedback of the nonlinear plasma waves. We also prove the nontrivial role of the field ionization in this regime, which amplifies the standard laser ponderomotive force at long laser wavelengths. This impacts the

longitudinal and transverse phase space as displayed qualitatively by a 1D, quasi-static fluid model. At the same time, efficient electron acceleration leads to transition radiation with good conversion efficiency close to the percent level.

To end with, Chapter 5 investigates the still unclear physical processes involved in THz emission in the case of laser-solid relativistic interactions. We first present a summary of the electron heating mechanisms and ion acceleration regimes occurring with our laser parameters using ultra-thin targets. Next, a detailed state-of-the-art of THz emission in such targets recalls the lack of clearly identified THz emitters in this domain. 2D PIC simulations are conducted and they display evidence that THz emissions are the results of several combined processes. The ejection of a large amount of charge (electrons and ions) induces transition radiation and also surface currents traveling towards the target edges. There, antenna-like emission is reported periodically as long as electron recirculation takes place over the target surface. Meanwhile, target deformations and quasi-static field structures deflect a part of the surface current, which contribute to low-frequency emissions. Finally the expansion of ions in vacuum is also reported and shown to be a possible source of THz emission.

Chapter 2

Physics of laser-gas interaction: from the classical to the relativistic regime

Contents

The physical background and related numerical tools used in our work are addressed in the present chapter. Two distinct regimes of laser-gas interaction are described in the context of THz emission. Section 2.1 deals with the standard nonrelativistic regime. The main nonlinear phenomena, namely the Kerr and photocurrent effects, responsible for low-frequency emission during the propagation of a short and intense laser pulse in a gas, are discussed. A widely used model for THz emission, based on a unidirectional pulse description, is compared to the exact solution of Maxwell equations, which constitutes the first result of this thesis. Section 2.2 then focuses on laser-plasma interactions in the relativistic regime. We first present the Vlasov-Maxwell coupled equations as well as the kinetic code CALDER employed to solve them. Next, the principle of the Laser Wakefield Accelerator (LWFA) is discussed. This acceleration scheme is exploited to produce THz waves through coherent transition radiation. Finally, Sec. 2.3 reviews various theoretical descriptions of the latter mechanism, which are illustrated by a number of academic problems.

2.1 THz emitters in the classical regime

This section deals with the terahertz conversion mechanisms triggered by femtosecond (< 100 fs) duration, TW peak power laser pulses propagating in a transparent medium such as ambient air. Due to the strong electromagnetic fields at play, a plasma is formed along the laser propagation, thereby exciting nonlinear processes. Two different physical systems are coupled: the propagation of the intense light pulse, described by Maxwell's equations, and the plasma dynamics governed by the kinetic (Vlasov) plasma equations. To begin with, we derive the propagation equation of an electromagnetic wave in a partially ionized medium from Maxwell's equations (Sec. 2.1.1). To alleviate the computational cost, it turns out that only modeling the forward-propagating component of the laser wave supplies a reasonably good description over long interaction distances. This corresponds to the widely used unidirectional pulse propagation equation (UPPE) which will be here studied. Nonlinear effects come from either the bound or free electrons through the Kerr effect (Sec. 2.1.2) or the excitation of photocurrents (Sec. 2.1.3) and linear electron plasma waves (Sec. 2.1.4), respectively. We also detail how such nonlinearities can specifically produce THz pulses. The last part of this section (Sec. 2.1.5) is dedicated to the analytical and numerical resolutions of the wave equation (WE) and of the UPPE. Our study will pinpoint differences between the two models of pulse propagation.

2.1.1 Maxwell's Equations and Propagation Equation in a Plasma

Maxwell's equations

Electromagnetic waves are classically described by Maxwell's equations. The electric and magnetic inductions are $\mathbf{D}$ and $\mathbf{B}$ (also often called magnetic field), the electric and magnetic fields are $\mathbf{E}$ and $\mathbf{H}$. The charge and current densities are represented by ρ and $\mathbf{J}$. Maxwell's equations read [Jackson 1999]:

$$\nabla \cdot \mathbf{B} = 0, \tag{2.1}$$

$$\nabla \cdot \mathbf{D} = \rho, \tag{2.2}$$

$$\nabla \times \mathbf{E} = -\partial_t \mathbf{B}, \tag{2.3}$$

$$\nabla \times \mathbf{H} = \partial_t \mathbf{D} + \mathbf{J}. \tag{2.4}$$

This set of equations is completed by the following relations between the electric and magnetic inductions ($\mathbf{D}$, $\mathbf{B}$) and the electromagnetic field ($\mathbf{E}$, $\mathbf{H}$)

$$\mathbf{D} = \epsilon_0 \mathbf{E} + \mathbf{P}, \tag{2.5}$$

$$\mathbf{B} = \mu_0 \mathbf{H} + \mathbf{M}, \tag{2.6}$$

where ϵ_0 and μ_0 are the electric permittivity and magnetic permeability in vacuum, respectively. In the absence of material magnetization we set $\mathbf{M} = \mathbf{0}$, while the polarization vector, $\mathbf{P}$ describes the response of the bound electrons. We can combine these equations to derive the propagation equation of an electromagnetic pulse in a transparent nonlinear medium.

Wave equation (WE) in a transparent nonlinear medium

Combining Maxwell's equations (2.3), (2.4) and Eq. (2.6) gives:

$$\nabla \times \nabla \times \mathbf{E} = \nabla \times (-\partial_t \mathbf{B}) = -\partial_t (\nabla \times \mathbf{B}) \tag{2.7}$$

$$= -\mu_0 \left(\partial_t \mathbf{J} + \partial_t^2 \mathbf{D}\right). \tag{2.8}$$

Using Eq. (2.5) and the vectorial identity $\nabla \times \nabla \times = \nabla(\nabla \cdot) - \nabla^2$ we get an equation function of $\mathbf{E}$ only:

$$\nabla^2 \mathbf{E} - \nabla(\nabla \cdot \mathbf{E}) - c^{-2}\partial_t^2 \mathbf{E} = \mu_0 \left(\partial_t \mathbf{J} + \partial_t^2 \mathbf{P}\right). \tag{2.9}$$

The polarization vector $\mathbf{P}$ can be decomposed into a linear ($\mathbf{P}_\mathrm{L}$) and a nonlinear ($\mathbf{P}_\mathrm{NL}$) contribution, both describing the response of bound electrons. The linear contribution describes the chromatic dispersion of a light wave with frequency ω through the refractive index $n(\omega)$ of the medium. In the real domain, $\mathbf{P}_\mathrm{L}$ can be expressed as a convolution product between the linear susceptibility $\chi^{(1)}$ and the electric field:

$$\mathbf{P}_\mathrm{L}(\mathbf{r}, t) = \epsilon_0 \chi^{(1)} * \mathbf{E} = \epsilon_0 \int_{-\infty}^{t} \chi^{(1)}(\mathbf{r}, t - t')\mathbf{E}(\mathbf{r}, t')\, dt', \tag{2.10}$$

where $\chi^{(1)}$ is linked to the refractive index and to the permittivity ϵ of the medium by the relationship:

$$\epsilon = n^2 = 1 + \chi^{(1)}. \tag{2.11}$$

Hence, by expanding $\mathbf{P}$ and using Eqs. (2.10), (2.11), we can take into account dispersion effects in the propagator operator. As a result, we obtain the vectorial wave equation:

$$\nabla^2 \mathbf{E} - \nabla(\nabla \cdot \mathbf{E}) - c^{-2}\partial_t^2 \int_{-\infty}^{t} n^2(\mathbf{r}, t - t')\mathbf{E}(\mathbf{r}, t')\, dt' = \mu_0 \left(\partial_t \mathbf{J} + \partial_t^2 \mathbf{P}_\mathrm{NL}\right). \tag{2.12}$$

Equation (2.12) then describes the propagation of a laser pulse in a dispersive medium subject to Kerr effect (see Section 2.1.2), represented by the $\partial_t^2 \mathbf{P}_\mathrm{NL}$ term, and to plasma generation, represented by $\partial_t \mathbf{J}$. We can decompose the total plasma current density as $\mathbf{J} \equiv \mathbf{J}_p + \mathbf{J}_\mathrm{loss}$, where $\mathbf{J}_p$ is the free charge current density (see Section 2.1.3), and $\mathbf{J}_\mathrm{loss}$ the loss current density modeling the laser energy depleted in the ionization process by virtue of the Poynting theorem. The coupling of the incident field and these phenomena leads to a spectral broadening of the pulse down to the THz ranges as detailed in Secs. 2.1.2 and 2.1.3. Note that the term $\nabla(\nabla \cdot \mathbf{E})$ gathers vectorial effects when the electric field does not remain transverse ($\nabla \cdot \mathbf{E} \neq 0$). It should *a priori* be retained in order to take account of charge separation ($\rho \neq 0$).

Due to the time-convolution product between the refractive index and the electric field it is more convenient to work in Fourier domain. After performing a Fourier transform in time on Eq. (2.12) we have:

$$\nabla^2 \widehat{\mathbf{E}} - \nabla(\nabla \cdot \widehat{\mathbf{E}}) - \frac{\omega^2 n^2(\omega)}{c^2}\widehat{\mathbf{E}} = \mu_0 \left(-i\omega \widehat{\mathbf{J}} - \omega^2 \widehat{\mathbf{P}}_\mathrm{NL}\right), \tag{2.13}$$

where the symbol $\widehat{\cdot}$ denotes temporal Fourier transform. This equation can be recast by defining the wave vector $k(\omega) = \omega n(\omega)/c$ and splitting the Laplacian operator into a longitudinal part[1] (∂_x^2) and a transverse part ($\nabla_\perp^2 = \partial_y^2 + \partial_z^2$) accounting for diffraction. One can also express the

[1] The propagation of the laser pulse axis is set along the x-axis.

$\nabla(\nabla \cdot \widehat{\mathbf{E}})$ term by combining Eq. (2.2) and Eq. (2.5) to find:

$$\nabla(\nabla \cdot \widehat{\mathbf{E}}) = \frac{1}{\epsilon_0 n^2(\omega)} \nabla \left(\widehat{\rho} - \nabla \cdot \widehat{\mathbf{P}}_{\mathrm{NL}} \right), \tag{2.14}$$

thus leading to

$$\left[\partial_x^2 + \nabla_\perp^2 + k^2(\omega)\right] \widehat{\mathbf{E}} = -\mu_0 \omega^2 \left(\widehat{\mathbf{P}}_{\mathrm{NL}} + \frac{i\widehat{\mathbf{J}}}{\omega} \right) + \frac{1}{\epsilon_0 n^2(\omega)} \nabla \left(\widehat{\rho} - \nabla \cdot \widehat{\mathbf{P}}_{\mathrm{NL}} \right). \tag{2.15}$$

The continuity equation for the charge density, derived from the zeroth order moment of Vlasov's equation (see Section 2.2.1), allows us to eliminate $\widehat{\rho}$ since $\partial_t \rho + \nabla \cdot \mathbf{J} = 0 \rightarrow \widehat{\rho} = -i\nabla \cdot \widehat{\mathbf{J}}/\omega$ and to gather all nonlinear terms under the general expression,

$$\widehat{\boldsymbol{\mathcal{F}}}_{\mathrm{NL}} \equiv \widehat{\mathbf{P}}_{\mathrm{NL}} + \frac{i\widehat{\mathbf{J}}}{\omega}, \tag{2.16}$$

This yields the nonlinear, vectorial Helmholtz equation satisfied by $\widehat{\mathbf{E}}$:

$$\left[\partial_x^2 + \nabla_\perp^2 + k^2(\omega)\right] \widehat{\mathbf{E}} = -\mu_0 \omega^2 \left[\widehat{\boldsymbol{\mathcal{F}}}_{\mathrm{NL}} + \frac{\nabla(\nabla \cdot \widehat{\boldsymbol{\mathcal{F}}}_{\mathrm{NL}})}{k^2(\omega)} \right]. \tag{2.17}$$

Fourier transforming in space the RHS of Eq. (2.17) leads to

$$-\mu_0 \omega^2 \left[\widehat{\boldsymbol{\mathcal{F}}}_{\mathrm{NL}} + \frac{\nabla(\nabla \cdot \widehat{\boldsymbol{\mathcal{F}}}_{\mathrm{NL}})}{k^2(\omega)} \right] = -\mu_0 \omega^2 \left[\begin{pmatrix} \widehat{\mathcal{F}}_{\mathrm{NL},x} \\ \widehat{\mathcal{F}}_{\mathrm{NL},y} \\ \widehat{\mathcal{F}}_{\mathrm{NL},z} \end{pmatrix} - \frac{1}{k^2} \begin{pmatrix} \widehat{\mathcal{F}}_{\mathrm{NL},x} k_x^2 + \widehat{\mathcal{F}}_{\mathrm{NL},y} k_x k_y + \widehat{\mathcal{F}}_{\mathrm{NL},z} k_x k_z \\ \widehat{\mathcal{F}}_{\mathrm{NL},x} k_x k_y + \widehat{\mathcal{F}}_{\mathrm{NL},y} k_y^2 + \widehat{\mathcal{F}}_{\mathrm{NL},z} k_y k_z \\ \widehat{\mathcal{F}}_{\mathrm{NL},x} k_x k_z + \widehat{\mathcal{F}}_{\mathrm{NL},y} k_y k_z + \widehat{\mathcal{F}}_{\mathrm{NL},z} k_z^2 \end{pmatrix} \right]. \tag{2.18}$$

The $\nabla(\nabla \cdot \widehat{\boldsymbol{\mathcal{F}}}_{\mathrm{NL}})$ term can be neglected if the beam is not too tightly focused, e.g., if the transverse spectral extent of the simulated waveform ($\sim 2\pi k_\perp$) is large enough relative to the inverse of the pulse wavelength (λ_0). In the spectral domain, this paraxial condition expresses as:

$$\sqrt{k_y^2 + k_z^2} = k_\perp^2 \ll k^2. \tag{2.19}$$

Neglecting terms scaling as $O(k_\perp^2/k^2)$, Eq. (2.18) simplifies as

$$-\mu_0 \omega^2 \left[\widehat{\boldsymbol{\mathcal{F}}}_{\mathrm{NL}} + \frac{\nabla(\nabla \cdot \widehat{\boldsymbol{\mathcal{F}}}_{\mathrm{NL}})}{k^2(\omega)} \right] \approx -\mu_0 \omega^2 \begin{pmatrix} -\widehat{\mathcal{F}}_{\mathrm{NL},y} k_x k_y / k^2 - \widehat{\mathcal{F}}_{\mathrm{NL},z} k_x k_z / k^2 \\ \widehat{\mathcal{F}}_{\mathrm{NL},y} - \widehat{\mathcal{F}}_{\mathrm{NL},x} k_x k_y / k^2 \\ \widehat{\mathcal{F}}_{\mathrm{NL},z} - \widehat{\mathcal{F}}_{\mathrm{NL},x} k_x k_z / k^2 \end{pmatrix}. \tag{2.20}$$

Second, we make use of Eq. (2.14), re-expressed as

$$\nabla \cdot \widehat{\mathbf{E}} = -\frac{\nabla \cdot \widehat{\boldsymbol{\mathcal{F}}}_{\mathrm{NL}}}{\epsilon_0 n^2(\omega)}, \tag{2.21}$$

to find that $\partial_x E_x + \nabla_\perp E_\perp = O(1)$, and hence that $\widehat{E}_x \sim \widehat{\mathcal{F}}_{\mathrm{NL},x}$ scales as $O(k_\perp/k)$. Vectorial coupling is thus negligible on the propagation axis: the nonlinearities are smooth enough to preserve the transverse polarization of the electromagnetic field. We can then define $\mathbf{E} \equiv E\mathbf{e}_s^\perp$,

where **E** obeys the scalar form of the propagation equation (2.17):

$$\left[\partial_x^2 + \nabla_\perp^2 + k^2(\omega)\right] \widehat{E} = -\mu_0 \omega^2 \widehat{\mathcal{F}}_{\mathrm{NL}}. \tag{2.22}$$

This equation has been implemented in the MAXFLU1D code (see Appendix A.1). This code considers a 1D geometry ($\nabla_\perp^2 = 0$) and two types of source terms: the Kerr effect (associated with the nonlinear polarization) and the electron plasma current density (modeled in the cold-fluid limit).

The Unidirectional Pulse Propagation Equation (UPPE)

Due to the bi-directional character of its solution, the wave equation (2.22) is computationally demanding when integrated over long propagation distances. To reduce its cost, approximate wave equations have been proposed, such as, e.g. the Nonlinear Envelope Equation [Brabec & Krausz 1997], based on a three dimensions envelope description which was found to hold down to the pulse carrier period. Interesting reviews of the history of such reduced methods are given by Bergé *et al.* [2007] and Couairon & Mysyrowicz [2007]. An example of prime interest for modeling laser-driven THz sources is the UPPE, first proposed by Kolesik & Moloney [2004]. This model takes into account dispersion effects and allows one to recover all models previously proposed. Note that other theories exist: for instance Kinsler *et al.* [2005] proposed to use energy flows in the forward ($\mathbf{G}^+$) and backward ($\mathbf{G}^-$) directions built from combined electric and magnetic field variables. The advantage of this approach is to easily include electro-optic medium properties and nonlinearities. Also, its underlying assumption of a weak backward contribution can be straightforwardly tested by comparing both energy fluxes.

Let us now derive the UPPE, from the wave equation (2.22). A set of approximations will be made to extract a system of coupled scalar equations that describes both the forward and backward propagations of the electric field. From this system, the standard scalar UPPE for forward-propagating waves will be obtained assuming weak backscattering.

To derive the usual form of the UPPE, one can rewrite Eq. (2.22) using a direct decomposition into a forward and a backward operator [Bergé *et al.* 2007]. Note that alternative methods exist based on projection operators [Kolesik & Moloney 2004] or transformation of a partial differential equation (PDE) into an inhomogeneous ordinary differential equation (ODE) [Andreasen & Kolesik 2012].

We first pass into the Fourier domain for transverse components hence, $\nabla_\perp^2 \to -k_\perp^2 = -(k_y^2 + k_z^2)$, and define the forward/backward propagation operators

$$\widehat{D}_\pm = \partial_x \mp i\sqrt{k^2(\omega) - k_\perp^2} = \partial_x \mp i k_x(\omega), \tag{2.23}$$

such that

$$\widehat{D}_+ \widehat{D}_- \widehat{E} = -\mu_0 \omega^2 \widehat{\mathcal{F}}_{\mathrm{NL}}. \tag{2.24}$$

The use of the $\widehat{D}_\pm$ operators leads to a decomposition of the electric field into its forward and backward-propagating components:

$$\widehat{E} = \widehat{E}_+ e^{ik_x x} + \widehat{E}_- e^{-ik_x x}. \tag{2.25}$$

Applying $\widehat{D}_-$ to the forward component (thus $\widehat{E} = \widehat{E}_+ e^{ik_x x}$) gives

$$\widehat{D}_- \widehat{E} = (\partial_x + ik_x)\left(\widehat{E}_+ e^{ik_x x}\right) = \left(\cancel{\partial_x \widehat{E}_+} + 2ik_x \widehat{E_+}\right) e^{ik_x x} \simeq 2ik_x \widehat{E}, \tag{2.26}$$

assuming paraxial propagation of the forward envelope, i.e., its amplitude does not vary significantly upon distances of a few λ_0 when applying $\widehat{D}_-$. The forward operator is next applied to obtain

$$\widehat{D}_+\widehat{D}_-\widehat{E} = (\partial_x - ik_x)\left(2ik_x\widehat{E}\right) = 2ik_x\left(\partial_x\widehat{E} - ik_x\widehat{E}\right). \tag{2.27}$$

Using the above equation into Eq. (2.24) leads to the equation of forward propagation. The same treatment can be done on the backward electric field in order to finally obtain the following set of coupled equations:

$$\partial_x\widehat{E}_F = ik_x\widehat{E}_F + \frac{i\omega^2}{2\epsilon_0 c^2 k_x}\left[\widehat{P}_{\mathrm{NL}} + \frac{i\widehat{J}}{\omega}\right], \tag{2.28}$$

$$\partial_x\widehat{E}_B = -ik_x\widehat{E}_B - \frac{i\omega^2}{2\epsilon_0 c^2 k_x}\left[\widehat{P}_{\mathrm{NL}} + \frac{i\widehat{J}}{\omega}\right], \tag{2.29}$$

where the index F (B) refers to the forward (resp. backward) projected component of the total electric field [$\widehat{E}_{F/B} \equiv \widehat{E}_\pm \exp(\pm ik_x x)$].

Unfortunately, the formulation (2.28, 2.29) is barely tractable numerically, because the knowledge of the backward wave is needed to calculate the evolution of the forward wave. This coupling occurs through the nonlinear terms that depend on the total electric field [Kolesik & Moloney 2004]. To simplify the problem, we thus consider that backscattering is weak, hence that the nonlinear responses are mainly conveyed by the forward-propagating field:

$$\widehat{P}_{\mathrm{NL}}(\widehat{E}),\ \widehat{J}(\widehat{E}) \to \widehat{P}_{\mathrm{NL}}(\widehat{E}_F),\ \widehat{J}(\widehat{E}_F). \tag{2.30}$$

Alternatively, following Fibich *et al.* [2002], we can inject the electric field decomposition (2.25) into equation (2.24) and expand the action of the propagation operators. After integration over the interval $x - \pi/2k \leq x \leq x + \pi/2k$, corresponding to one carrier period, the resulting equation is:

$$2ik_x\partial_x\widehat{E}_- \sim -\frac{e^{2ik_x x}}{2ik_x}\partial_x(\nabla_\perp^2 + \mu_0\omega^2\widehat{\mathcal{F}}_{\mathrm{NL}})\widehat{E}_+. \tag{2.31}$$

In Fourier domain $\nabla_\perp^2 \sim -k_\perp^2$, such that the backward part of the electric field remains weak when we assume $k_\perp^2 \ll k^2(\omega)$ and small nonlinearities. At least 90% of the pulse energy is expected to be carried by the forward-propagating field [Bergé *et al.* 2007]. This is the reason why the UPPE is not an exact propagation equation, but it appears to be as close as possible to a complete description of the real electric field. To summarize, the canonical UPPE is finally given by:

$$\partial_x\widehat{E} = ik_x\widehat{E} + \frac{i\omega^2}{2\epsilon_0 c^2 k_x}\left[\widehat{P}_{\mathrm{NL}} + \frac{i\widehat{J}}{\omega}\right], \tag{2.32}$$

where, for notational convenience, we henceforth omit the index F. This is the $x-$propagated approach of the UPPE equation. Let us recall that a $t-$propagated solution also exists, which might be best suited for tight focusing scenarios when non-paraxial effects have to be taken into account [Kolesik & Moloney 2004].

2.1.2 Kerr nonlinearity

Intense laser pulses can trigger in gases (e.g. the air) nonlinearities such as optical Kerr self-focusing (or four-wave mixing) and plasma generation as the pulse propagates. The Kerr effect

comes from the third-order susceptibility tensor characterizing the material response and, when it is positive-definite, is responsible for the local increase in the refractive index, and ultimately, to self-focusing.

Indeed, in Kerr-sensitive materials the refractive index is linearly dependent on the intensity, $n(I) = n_0 + n_2 I$, so that the pulse wavefront converges on the axis (n_0 and $n_2 > 0$ are the linear and nonlinear index of the medium, respectively) during its propagation. This dynamics is accompanied by a spatial self-compression of the beam, leading to an additional increase in its intensity I. In turn, the medium acts as a lens causing "wave self-focusing" or "wave collapse". This singular dynamics occurs when the peak power of the pulse $P = \int |E|^2 dydz$ is higher than a critical value [Bergé *et al.* 2007]:

$$P_{cr} \approx \frac{3.72\,\lambda_0^2}{8\pi n_0 n_2}, \tag{2.33}$$

where the coordinates (y, z) refer to the transverse plane. In the absence of dissipative or saturation effects, the beam collapses, i.e., it forms a singularity at a finite propagation distance located on the x axis. In real gases, such a singularity never occurs, because it is stopped by plasma generation (see Section 2.1.3). The balance between Kerr self-focusing and plasma generation gives rise to a "string of light" alternating focusing-defocusing cycles. At high enough power, due to sequences of focusing and defocusing events, the pulse is able to propagate over much longer distances than the typical Rayleigh (diffraction) length while keeping a narrow beam width. Figure 2.1(a) shows the balance between Kerr effect (focusing) and diffraction (defocusing) while plasma induced defocusing, which acts in conjunction with standard diffraction, is not modeled here.

The nonlinear response is carried by a fraction of the bound electrons oscillating at different frequencies, which is accounted for in the nonlinear part of the polarization vector. Assuming small [compared to the atomic field ($E_{\text{au}} = m^2 q^5/(\hbar^{4/3} 4\pi\epsilon_0)^3 \approx 5.14 \times 10^{11}$ V/m] and instantaneous nonlinearities, the medium response can be expanded into power series of the electric field $\mathbf{E}$ [Agrawal 2012]:

$$\widehat{\mathbf{P}} = \widehat{\mathbf{P}}_{\text{L}} + \widehat{\mathbf{P}}_{\text{NL}} \tag{2.34}$$

$$= \epsilon_0 \left(\chi^{(1)} \widehat{\mathbf{E}} + \chi^{(2)} \widehat{\mathbf{E}}^2 + \chi^{(3)} \widehat{\mathbf{E}}^3 + ... \right). \tag{2.35}$$

Formally, $\chi^{(j)}$ denotes the j-th order susceptibility tensor. This expression can be simplified by considering an isotropic and homogeneous propagation material far from local resonances. In the case of propagation through air or gas cells, the interaction material is indeed centrosymmetric. For symmetry reasons, even orders in the susceptibility tensor are null. At the lowest perturbation order, when moreover assuming a stationnary $\chi^{(j)}$, the Kerr response is described by a third-order nonlinear term in power of $\mathbf{E}$ reading as

$$\widehat{\mathbf{P}}_{\text{NL}} = \epsilon_0 \chi^{(3)} \widehat{\mathbf{E}}^3. \tag{2.36}$$

Now, if we consider a laser pulse propagating along the x-axis, we can express its electric field in the form

$$E = \frac{1}{2} \left[\mathcal{E} \exp\left(ik_0 x - i\omega_0 t\right) + \mathcal{E}^* \exp\left(-ik_0 x + i\omega_0 t\right) \right], \tag{2.37}$$

leading to

$$E^3 = \frac{1}{8} [\mathcal{E} \exp\left(i3k_0 x - i3\omega_0 t\right) + 3|\mathcal{E}|^2 \mathcal{E} \exp\left(ik_0 x - i\omega_0 t\right) + c.c.]. \tag{2.38}$$

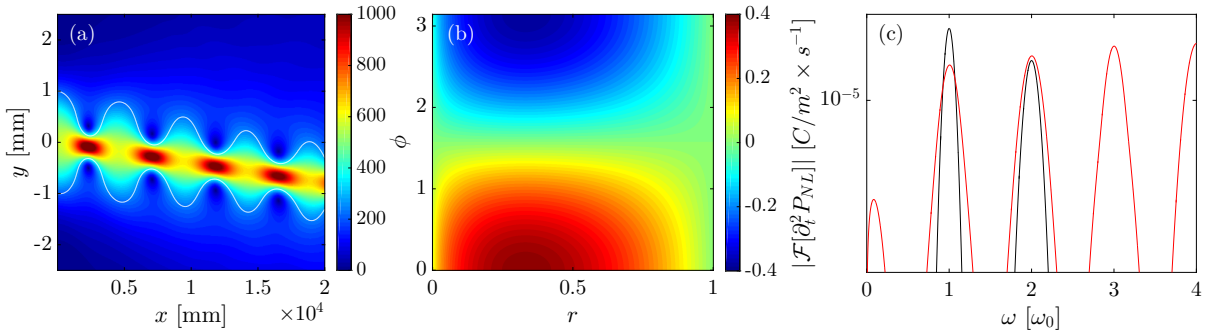

Figure 2.1: (a) Simulation results from a Kerr-driven nonlinear beam propagation method (BPM) split-step scheme [Agrawal 2012] with the laser pulse contour at $1/e$ (white line) over the intensity distribution. (b) Value of $(1-r)\sqrt{r}\cos\phi$ in the (r,ϕ) parameter space. (c) Typical radiated spectrum [Eq. (2.44)] due to the Kerr contribution (red line) generated by a two color laser field (black line).

For convenience, we will ignore the component oscillating at the third harmonic ($3\omega_0$). By using the same decomposition for the polarization,

$$P = \frac{1}{2}[\mathcal{P}\exp(ik_0x - i\omega_0t) + \mathcal{P}^*\exp(-ik_0x + i\omega_0t)], \tag{2.39}$$

we can identify the fundamental ω_0-oscillating component:

$$\mathcal{P}_{\mathrm{NL}} = \frac{3}{4}\epsilon_0\chi^{(3)}|\mathcal{E}|^2\mathcal{E}. \tag{2.40}$$

This expression can directly be used in the right-hand side of the propagation equation (2.22). Indeed, assuming only bound electrons ($J = 0$), and applying the paraxial approximation on the Laplacian operator, we find a nonlinear propagation equation for a monochromatic beam, resulting in the cubic Schrödinger equation:

$$\frac{\partial\mathcal{E}}{\partial x} = \frac{i}{2k_0}\nabla_\perp^2\mathcal{E} + \frac{i\omega_0}{c}n_2\mathcal{I}\mathcal{E} \tag{2.41}$$

after defining the Kerr index $n_2 \equiv 3\chi^{(3)}/4\epsilon_0 c n_0^2$ in cm^2/W and the intensity $\mathcal{I} \equiv \epsilon_0 c n_0|\mathcal{E}|^2/2$ expressed in $\mathrm{W/m}^2$ (c is the velocity of light in vacuum). The left-hand side term of Eq. (2.41) accounts for the propagation operator. In the right-hand side the transverse Laplacian operator describes wave diffraction in the (y, z) plane and the last term describes the nonlinear Kerr effect. The equation is solved in Fig. 2.1(a) where we can observe the succession of focusing-defocusing events (the white line delineates the $1/e$ intensity). Typically, plasma formation occurs around the hot spots where the laser intensity is maximum.

So far, the laser field has been viewed as being quasi-monochromatic, i.e., centered near a single fundamental frequency. However, laser setups nowadays routinely utilize several laser colors, e.g., a fundamental and its second harmonic generated by a doubling crystal or an optical parametric amplifier (OPA). In this context, the Kerr response of a gas generates a spectral continuum extending down to the THz range through the four wave-mixing process $\omega_0 + \omega_0 - 2\omega_0 \to 0$. To show this, let us choose a pulse comprising a fundamental (ω_0) and its second harmonic ($2\omega_0$) components with a relative phase shift ϕ. The parameter r is the

intensity ratio between the two components of the laser field and E_0 the amplitude entering:

$$E(t) = E_0[\sqrt{1-r}\cos(\omega_0 t) + \sqrt{r}\cos(2\omega_0 t + \phi)]. \tag{2.42}$$

The Kerr term scales as E^3, which expands as

$$\begin{aligned} E^3 = E_0^3\{&[\sqrt{1-r}\cos(\omega_0 t)]^3 + [\sqrt{r}\cos(2\omega_0 t + \phi)]^3 \\ &+ 3(1-r)\sqrt{r}\cos^2(\omega_0 t)\cos(2\omega_0 t + \phi) + 3r\sqrt{1-r}\cos(\omega_0 t)\cos^2(2\omega_0 t + \phi)\}. \end{aligned} \tag{2.43}$$

Using the trigonometric identities $\cos^2\theta = (1 + \cos(2\theta))/2$ and $\cos\theta\cos\psi = (\cos(\theta - \psi) + \cos(\theta + \psi))/2$, we readily identify the slow (direct-current or DC) component induced by the Kerr nonlinearity:

$$\widehat{\mathcal{P}}_{\mathrm{NL}}^{\mathrm{DC}} = \frac{3}{2}\epsilon_0\chi^{(3)}E_0^3(1-r)\sqrt{r}\cos\phi. \tag{2.44}$$

Therefore, the intensity ratio should approach 1/3 and the phase shift 0 for maximum generation of a DC (e.g. THz) field [Fig. 2.1(b)]. From Eq. (2.22) we can infer that the nonlinear polarization source term has a parabolic shape in the Fourier space ($\partial_t^2 \to -\omega^2$) if we neglect propagation effect. This characteristic signature of the Kerr effect has been first experimentally observed by Cook & Hochstrasser [2000] and verified by Xie *et al.* [2006]. Figure 2.1(c) displays a typical Kerr spectrum excited by a two-color laser. We indeed observe a contribution in the THz band but also third harmonic generation $\omega_0 + 2\omega_0 \to 3\omega_0$ [see Eq. (2.38)]. Along propagation, high-order harmonics can combine and strengthen the THz emission. Hence the propagated distance is also a key feature, for instance in increasing the coherence length of pulse harmonics ($L_n = \pi/\Delta k_n$). Kerr-driven THz pulse generation is expected to be efficient in the early stage of a self-focusing sequence whenever the pulse intensity does not exceed 10^{13} W/cm^2 for $\lambda_0 = 1$ μm. In the opposite situation, whenever the laser intensities exceeding few hundreds of TW/cm^2, photoionization prevails [Andreeva *et al.* 2016].

2.1.3 Photocurrent-Induced Radiation

This section is devoted to the generation of THz emission by the current modulations associated with photoionized electrons, the so-called "photocurrents". We first describe the process of field ionization through its different characteristic regimes depending on the laser intensity involved. Then useful (standard) ionization rates are derived to compute the generated photocurrent. The complete mechanism of THz generation in classical interaction regime is then exposed along with typical spectral signatures.

Field ionization

Photoionization happens when an electron bound to a nucleus is excited by an external electric field and freed by one or several photon(s). An ion and a free electron are then formed. Here, we do not take into account collisional ionization due to the relatively short timescale of the interaction (~ 100 fs) with respect to the typical electron-ion collision time, $\nu_{ei}^{-1} \simeq 500$ fs [Huba 2013]. A gas irradiated by an ultrashort, strong enough laser field turns into a partially or completely ionized plasma. In the classical regime (moderate intensities $< 10^{16}$ W/cm^2), the initial laser intensity is not necessary high enough to extract all electrons from the atom. As recalled above, the Kerr response induces a lens effect, focusing the laser beam and so increasing its intensity until plasma generation occurs. We first present the different photoionization regimes

depending on the so-called Keldysh parameter, and then discuss the corresponding ionization rates.

One can visualize the photoionization process as the deformation of the Coulomb potential barrier by a strong electric field. In a simplified 1D geometry, the overall potential can be expressed as

$$U(x) = -\frac{Ze^2}{4\pi\epsilon_0|x|} - eE_0x, \tag{2.45}$$

where the first term is the Coulomb barrier and the second term the contribution from a static, or slowly varying, field with amplitude E_0. Keldysh was the first to derive an ionization rate using the following adiabatic parameter, expressed below in atomic units ($\hbar = c = e = m_e = 1/4\pi\epsilon_0 = 1$) [Keldysh 1965]:

$$\gamma_K = \frac{\omega_0\sqrt{2U_i}}{E_0}, \tag{2.46}$$

where $\omega_0 \equiv 2\pi c/\lambda_0$ is the laser central frequency and U_i the potential energy of the irradiated atom (binding energy related to the Coulomb potential). The Keldysh parameter discriminates between the regime of multiphoton ionization at moderate laser intensities ($\gamma_K \gg 1$) and the regime of tunnel ionization at high enough intensities ($\gamma_K \ll 1$). Figure 2.2 plots Eq. (2.45) for a hydrogen atom and increasing values of I_0. The ground state ($I_0 = 0$ W/cm^2) is characterized by the electron potential energy $U_H = 13.6$ eV [Fig. 2.2(a)]. For an intense applied field ($I_0 = 10^{13}$ W/cm^2) the Coulomb barrier is deformed by the external electric field [Fig. 2.2(b)]. The electron can absorb several photons of energy $\hbar\omega_0$ to finally overcome the binding potential barrier; this is the so-called multiphoton ionization regime. Deforming even more the barrier ($I_0 = 10^{14}$ W/cm^2) increases the probability for the electron to tunnel across the potential barrier [Fig. 2.2(c)]. An extreme case is the over-barrier ionization (OBI) regime in which the Coulomb barrier can be completely suppressed [Fig. 2.2(d)].

Ionization rate

Since Keldysh's seminal work, improved theories have been developed to account for the Coulomb interaction between the excited electron and a parent ion. In this regard, the most accepted ionization theory for any value of γ_K (multiphoton and tunnel ionization) is due to Perelomov, Popov and Terent'ev (PPT theory) [Perelomov *et al.* 1966, 1967a,b]. In S.I. units, the PPT ionization rate reads as:

$$W_{\mathrm{PPT}}(\omega_0, E_0) = \frac{4\sqrt{2}}{\pi} C_{n^*,l^*,l,m} A_m(\omega_0) H_{n^*,m}(E_0)\omega_{\mathrm{au}}, \tag{2.47}$$

where $C_{n^*,l^*,l,m}$ is a function of the quantum number, $A_m(\omega_0)$ describes the MPI regime while $H_{n^*,m}(E_0)$ the tunneling regime. They are respectively given by:

$$C_{n^*,l^*,l,m} = \frac{2^{2n^*}(2l+1)(l+|m|)!}{2^{|m|}|m|!(l-|m|)!n^*\Gamma(n^*+l^*+1)\Gamma(n^*-l^*)}, \tag{2.48}$$

$$A_m(\omega_0) = \frac{\gamma_K^2}{1+\gamma_K^2} \times \sum_{\kappa=\langle K+1\rangle}^{+\infty} \Phi_m\left(\sqrt{\frac{2\gamma_K(\kappa-K)}{\sqrt{1+\gamma_K^2}}}\right) \exp\left[\left(\frac{2\gamma_K}{\sqrt{1+\gamma_K^2}} - 2\sinh^{-1}\gamma_K\right)\right], \tag{2.49}$$

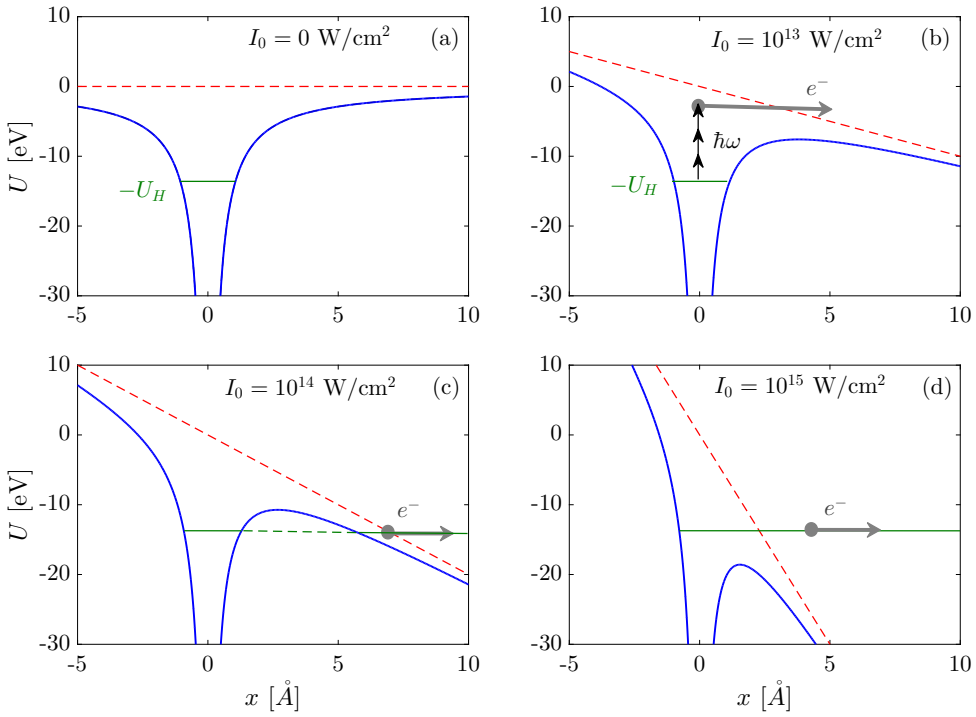

Figure 2.2: Total potential energetic well (blue line) deformed by an intense laser electric field (red dashed line) for the electron of an hydrogen atom. (a) No electric field, the electron is bounded, (b) a moderately intense electric field is applied and multiphoton ionization occurs corresponding to $\gamma_K \gg 1$, (c) The potential barrier is strongly altered and the electron can escape trough tunnel ionization ($\gamma_K \ll 1$) and (d) complete suppression of the barrier.

where

$$\Phi_m(z) = \frac{e^{-z^2}}{|m|!} \int_0^z (z^2 - \zeta^2)^{|m|} e^{\zeta^2} \, d\zeta \tag{2.50}$$

and

$$H_{n^*,m}(E_0) = \frac{U_i}{U_{\text{au}}} \left(\frac{2(2U_i U_{\text{au}}^{-1})^{\frac{3}{2}}}{E_0 E_{\text{au}}^{-1} \sqrt{1+\gamma_K^2}} \right)^{2n^* - \frac{3}{2} - |m|} \exp\left[-2K \left(\sinh^{-1}\gamma_K - \frac{\gamma_K \sqrt{1+\gamma_K^2}}{1+2\gamma_K^2} \right) \right]. \tag{2.51}$$

In the above expressions, $n^* = Z/\sqrt{2U_i U_{au}^{-1}}$ is the effective principal quantum number, $l^* = n^* - 1$, l is the angular quantum number and m the magnetic quantum number. The number of absorbed photons is represented by $K = (U_i/\hbar\omega_0)(1 + 1/2\gamma_K^2)$ from which the integer part is selected. The conversion factor from atomic to S.I. units are given by the atomic pulsation $\omega_{\text{au}} = mq^4/(\hbar^{3/2} 4\pi\epsilon_0)^2 \approx 4.13 \times 10^{16}$ Hz, the atomic energy $U_{\text{au}} = 2eU_H \approx 4.36 \times 10^{-18}$ J and the atomic field $E_{\text{au}} = m^2 q^5/(\hbar^{4/3} 4\pi\epsilon_0)^3 \approx 5.14 \times 10^{11}$ V/m. Note that the PPT rate holds for any Keldysh parameter from multiphoton to tunnel regime.

The multiphoton ionization regime is given by taking the limit of the PPT rate for $\gamma_K \to +\infty$. The ionization rate is a power function of the intensity of the form,

$$W_{\text{MPI}}(E_0) = \sigma_K E_0^{2K}, \tag{2.52}$$

where σ_K is the cross-section and K is the number of photons needed to unbound the electron. However, the short-pulse lasers considered for THz generation in gases commonly exceed the

10^{13} W/cm^2 intensity threshold. So let us now focus on the simplified PPT rate in the tunneling regime. The PPT theory in the strong field limit has been further revised by Ammosov, Delone and Krainov (ADK theory) [Ammosov *et al.* 1986]. The ADK rate can be obtained by taking the limit $\gamma_K \ll 1$ in the PPT rate and we have:

$$W_{\mathrm{ADK}}(E_0) = \sqrt{\frac{6}{\pi}} C_{n^*,l^*,l,m} H^{\mathrm{ADK}}_{n^*,m}(E_0)\omega_{\mathrm{au}}, \tag{2.53}$$

where

$$H^{\mathrm{ADK}}_{n^*,m}(E_0) = \frac{U_i}{U_{au}} \left(\frac{2(2U_i U_{\mathrm{au}}^{-1})^{\frac{3}{2}}}{E_0 E_{\mathrm{au}}^{-1}} \right)^{2n^* - \frac{3}{2} - |m|} \exp\left(\frac{2(2U_i U_{\mathrm{au}}^{-1})^{\frac{3}{2}}}{3E_0 E_{\mathrm{au}}^{-1}} \right). \tag{2.54}$$

Unfortunately, this expression does not account for the rapid variations of applied electric fields in the form $E(t) = E_0 \cos(\omega_0 t)$ as it is the case with UHI lasers. To do so, one can consider Eq. (2.53) as the time average of the instantaneous ADK rate over a laser period $2\pi/\omega_0$:

$$W_{\mathrm{ADK}}(E_0) = \frac{\omega_0}{2\pi} \int_0^{\frac{2\pi}{\omega_0}} W_{\mathrm{ADK-inst}}[E(\tau)]\, d\tau, \tag{2.55}$$

leading to

$$W_{\mathrm{ADK-inst}}[E(t)] = \sqrt{\frac{6}{\pi}} C_{n^*,l^*,l,m} H^{\mathrm{ADK-inst}}_{n^*,m}[E(t)]\omega_{\mathrm{au}}, \tag{2.56}$$

with

$$H^{\mathrm{ADK-inst}}_{n^*,m}[E(t)] = \frac{U_i}{U_{\mathrm{au}}} \left(\frac{2(2U_i U_{\mathrm{au}}^{-1})^{\frac{3}{2}}}{|E(t)|E_{\mathrm{au}}^{-1}} \right)^{2n^* - \frac{3}{2} - |m|} \exp\left(\frac{2(2U_i U_{\mathrm{au}}^{-1})^{\frac{3}{2}}}{3|E(t)|E_{\mathrm{au}}^{-1}} \right). \tag{2.57}$$

Following Ammosov *et al.* [1986], the dependence upon the magnetic quantum number m can be suppressed since $W^{m=0}_{\mathrm{ADK-inst}}/W^{m\neq 0}_{\mathrm{ADK-inst}} \gg 1$, to finally get the instantaneous ADK rate for a single ionization:

$$W_{\mathrm{ADK-inst}}[E(t)] = \frac{2^{\frac{8}{5}(n^*-1)}}{n^*\Gamma(2n^*)}(2l+1)\frac{\left[4(2U_i U_{\mathrm{au}}^{-1})^{\frac{5}{2}}\right]^{\frac{6n^*-1}{5}}}{(|E(t)|E_{au}^{-1})^{2n^*-1}} \exp\left[-\frac{2}{3}\frac{(2U_i U_{\mathrm{au}}^{-1})^{\frac{3}{2}}}{|E(t)|E_{\mathrm{au}}^{-1}} \right] \omega_{\mathrm{au}}. \tag{2.58}$$

From there we can also retrieve the classical Quasi-Static Tunneling (QST) ionization rate, first derived by Landau and Lifshitz [Landau & Lifshitz 1975]. This formula is valid for hydrogenoid atoms ($n^* = 1$, $l = 0$) and models single ionization only. It is given by

$$W_{\mathrm{QST}}[E(t)] = \frac{4(2U_i U_{\mathrm{au}}^{-1})^{\frac{5}{2}}}{|E(t)|E_{\mathrm{au}}^{-1}} \exp\left[-\frac{2}{3}\frac{(2U_i U_{\mathrm{au}}^{-1})^{\frac{3}{2}}}{|E(t)|E_{\mathrm{au}}^{-1}} \right] \omega_{\mathrm{au}}. \tag{2.59}$$

The QST and instantaneous ADK rates yield similar results despite some discrepancies in the slope of the curve $W([E(t)])$ which quantifies the ionization efficiency [González de Alaiza Martínez & Bergé 2014]. The QST rate will be used in Section 2.1.5 for laser intensities not exceeding 1 PW/cm^2.

The ionization rates presented so far (PPT, ADK, ADK-inst, QST) fail to describe multiple ionization (MI). However multiply-charged ions can be created using intense enough laser pulses. To model MI of an atom with atomic number Z, we shall use the instantaneous ADK rate for each electron shell ($1 \leq j \leq Z$). With the quantum numbers of the j-th shell l_j and $n_j^* = j/\sqrt{2U_i^j U_{au}^{-1}}$ where U_i^j is the binding energy of the electron shell j, we define the MI rate

based on the instantaneous ADK rate,

$$W_{\mathrm{MI}}^{j}[E(t)] = \frac{2^{\frac{8}{5}(n_j^*-1)}}{n_j^*\Gamma(2n_j^*)}(2l_j+1)\frac{\left[4(2U_i^j U_{\mathrm{au}}^{-1})^{\frac{5}{2}}\right]^{\frac{6n_j^*-1}{5}}}{(|E(t)|E_{\mathrm{au}}^{-1})^{2n_j^*-1}}\exp\left[-\frac{2}{3}\frac{(2U_i^j U_{\mathrm{au}}^{-1})^{\frac{3}{2}}}{|E(t)|E_{\mathrm{au}}^{-1}}\right]\omega_{\mathrm{au}}. \tag{2.60}$$

In the rest of the manuscript, we shall use the QST rate for academic purposes, or for describing single ionization events in the classical regime. By contrast, the MI rate will be preferred when relativistic intensities are employed to ionize atoms and describe different species with high atomic number Z.

Plasma generation

Knowing the rate W_{MI}^{j} we can introduce ionization effects in the equations describing the laser propagation. Over our time scales of interest (several tens of fs), ion motion can be neglected in non relativistic laser-gas interactions. We can also discard the kinetic aspect of the plasma and use a fluid description for the physical quantities of interest. The fluid quantities, e.g. the electron charge and current densities, correspond to the zeroth and first order averaged moments of the Vlasov equation, respectively (see Section 2.2.1). We also assume that the laser pulse is too short and its energy density too weak to yield significant plasma heating. Thus, thermal effects will be neglected in the fluid equations.

Let us consider a gas composed of atoms with atomic number Z. The ion distribution is modeled by $Z+1$ equations describing the depletion of the neutral atom (n_a) and the creation of the Z possible ions ($n_i^{(j)}$ with $1 \leq j \leq Z$). Each electronic shell j is characterized by its quantum number l_j and n_j^* defined above. The ionization rate is noted W_j for future convenience. The system of equations reads

$$\partial_t n_a = -W_1 n_a, \tag{2.61}$$

$$\partial_t n_i^{(j)} = W_j n_i^{(j-1)} - W_{j+1} n_i^{(j)}, \qquad 1 \leq j \leq Z-1 \tag{2.62}$$

$$\partial_t n_i^{(Z)} = W_Z n_i^{(Z-1)}. \tag{2.63}$$

The $Z+1$ initial conditions are:

$$n_a(t \to -\infty) = n_a^0, \tag{2.64}$$

$$n_i^{(j)}(t \to -\infty) = 0, \qquad 1 \leq j \leq Z. \tag{2.65}$$

During the ionization process the neutral and ion densities should fulfill matter conservation

$$n_a + \sum_{j=1}^{Z} n_i^{(j)} = n_a^0, \tag{2.66}$$

while the electron density is computed from the ion densities:

$$n_e = \sum_{j=1}^{Z} j n_i^{(j)}. \tag{2.67}$$

The system (2.61-2.63) models the generation of free electrons through photoionization. It will operate in the right hand side of the Vlasov equation as a source term (see Section 2.2.1). When

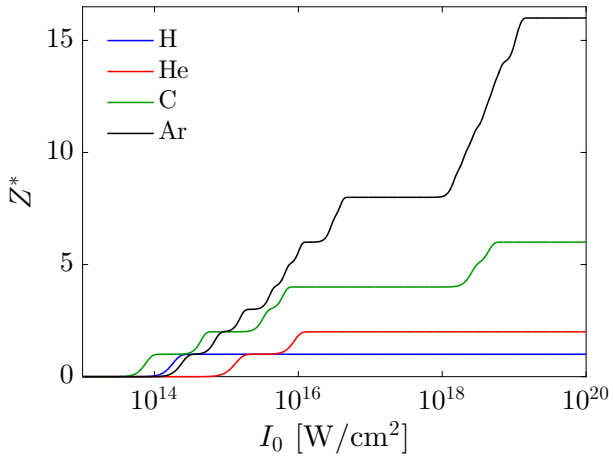

Figure 2.3: Ionization degree for different species Z^* as a function of the intensity for a single-color laser field ($\lambda_0 = 1$ μm) with FWHM duration $\tau_0 = 35$ fs and considering an instantaneous ADK ionization rate. Analytical model from Debayle *et al.* [2015].

the laser intensity is not too high, the medium is partially ionized and only single ionization occurs. In this context, as announced above, we use the QST rate and solve the simplified version of the electrons source equation:

$$\partial_t n_e = W_{\mathrm{QST}}(n_a^0 - n_e), \tag{2.68}$$

with the quantity of neutrals $n_a = n_a^0 - n_e$. The solution of Eq. (2.68) is

$$n_e(t) = n_a^0 \left[1 - \exp\left(-\int_{-\infty}^{t} W_{\mathrm{QST}}[E(t')]\, dt'\right)\right], \tag{2.69}$$

and can be employed to extract an analytical formulation of photocurrents [Babushkin *et al.* 2011]. One last useful quantity defining the ionization level of a plasma is the ionization degree Z^*:

$$Z^* = \frac{n_e(t \to +\infty)}{n_a^0}. \tag{2.70}$$

Usually, the ionization degree is computed numerically but a tractable approximate solution has been derived by Debayle *et al.* [2015] for a single-color laser based on the instantaneous ADK rate. This solution is dependent on the laser intensity I_0 and the pulse duration (FWHM) τ_0, and it can be extracted by solving $W_{\mathrm{MI}}^j(I_0) = \omega_0/\tau_0$. Figure 2.3 displays the ionization degree as a function of the laser intensity, inferred from a more elaborate version of the previous formula, for hydrogen, helium, carbon and argon atoms subject to a $\tau_0 = 35$ fs laser pulse. Significant ionization ($Z^* \geq 1$) is seen to occur for $I_0 \geq 10^{13-14}$ W/cm^2 in C, H and Ar atoms. This curve allows us to roughly foresee the final electron density when designing our simulations. For instance a relativistic laser pulse with 1 μm wavelength and 10^{18} W/cm^2 will be able to extract all electrons of an helium gas jet.

We are now able to compute the electron density released by an ultra-intense laser by solving the ionization system Eqs. (2.61-2.63) employing the adequate ionization rate. Let us then focus on the photocurrent mechanism responsible for THz generation, which is particularly efficient when two different laser frequencies co-propagate in the plasma.

Photocurrent mechanism and THz emission

The mechanism by which THz generation takes place through photoionization has been proposed by Kim *et al.* [2007, 2008], and experimentally tested by Li *et al.* [2012a] who changed the phase shift between the two harmonics of the laser and confirmed an optimum THz energy yield for the relative phase $\phi = \pi/2$. As an illustration, let us consider a two-color Gaussian electric field in time:

$$E_L(t) = E_0 \left(\sqrt{1-r}\cos(\omega_0 t) e^{-\left(\frac{t}{t_0}\right)^2} + \sqrt{r}\cos(2\omega_0 t + \phi) e^{-\left(\frac{\alpha t}{t_0}\right)^2} \right) \tag{2.71}$$

where the amplitude E_0 is linked to the laser intensity $I_0 = \epsilon_0 c E_0^2/2$. The laser field is characterized by its pulsation ω_0 and duration $t_0 = \tau_0/\sqrt{2\ln 2}$. Here, the second harmonic, usually created by a doubling crystal ($E_{2\omega_0} \propto E_{\omega_0}^2$), is taken to have a FWHM duration given by that of the fundamental divided by $\sqrt{2}$ ($\alpha = \sqrt{2}$)[2] with r the intensity ratio between the two harmonics. Figure 2.4(a) shows the photocurrent formation. When it is strong enough, the laser electric field E_L (blue line) ionizes the medium according to the ADK tunnel ionization rate. The resulting electron density n_e (green line) increases steplike at each field maxima (black dots). Once freed, electrons are accelerated by the laser electric field, which creates locally a transversally oscillating micro-current. The sum over all the ionization instants gives rise to a macroscopic current J_e (red line) oscillating at the laser pulsation ω_0 and containing also a slow component corresponding to THz frequencies. These so-called photocurrents act as a source term in the propagation equations (2.22), leading to the generation of THz radiation.

Note that the asymmetry in the time profile of the electric field critically matters. Indeed a Gaussian single-color laser with many optical cycles is essentially symmetric in time, so that the time-cumulated photocurrent tends to vanish. This can be easily demonstrated within a collisionless, nonrelativistic fluid description. A straightforward solution, assuming motionless ions, gives the equation satisfied by the electron current density J_e:

$$\partial_t J_e = \frac{e^2}{m_e} n_e E_L, \tag{2.72}$$

where n_e is the result of the photoionization system initiated by the laser field. Here the laser field is transversally polarized and so is the generated current. Then by integrating by part one has:

$$J_e(t) = \frac{e^2}{m_e} \int_{-\infty}^{t} n_e(t') E_L(t')\, dt' \tag{2.73}$$

$$= \frac{e^2}{m_e} \left[n_e \int_{-\infty}^{t} E_L(t')\, dt' - \int_{-\infty}^{t} \partial_t n_e(t') \left(\int_{-\infty}^{t'} E(t'')\, dt'' \right) dt' \right] \tag{2.74}$$

$$= -e n_e v_e + e \int_{-\infty}^{t} \partial_t n_e(t') v_e(t')\, dt' \tag{2.75}$$

by noting that

$$v_e(t) = -\frac{e}{m_e} \int_{-\infty}^{t} E_L(t')\, dt', \tag{2.76}$$

where we assumed that the electron is born at rest with $v_e(t \to -\infty) = 0$. The first term in Eq. (2.75) oscillates at the laser pulsation ω_0 while the second one contains low frequencies.

[2]Note that OPCPA techniques allow the second harmonic to be compressed to $\tau_0/2$, which is usually the value used in our simulations ($\alpha = 2$).

Indeed electron density jumps near the field maxima [see Fig. 2.4(a), green curve] can be well approximated by a succession of Heaviside functions:

$$n_e \simeq \sum_n \delta n_e^n H(t - t_n), \tag{2.77}$$

where t_n are the ionization instants, δn_e^n the successive density steps and H the standard Heaviside (step) function. Knowing that the time derivative of the Heaviside function is the Dirac function, the second term of Eq. (2.75) can be approximated by:

$$e \sum_n \delta n_e^n \int_{-\infty}^{t} \delta(t' - t_n) v_e(t')\, dt' = e \sum_n \delta n_e^n v_e(t_n). \tag{2.78}$$

This corresponds to a quasi-DC, i.e., low-frequency current source, which comes from the non-zero value of the velocity time integral evaluated around the ionization instants. Figure 2.4(b,c) shows the electric field E_L (blue line) and the electron velocity v_e (red line) computed from Eq. (2.76) for a single-color [Fig. 2.4(b)] and two-color [Fig. 2.4(c)] laser fields with $\tau_0 = 10$ fs and $\lambda_0 = 1$ μm [$\tau_0(2\omega_0) = 5$ fs and $\lambda_0(2\omega_0) = 0.5$ μm for the second harmonic of the two-color pulse]. The areas under the curve near field maxima are in light red. These areas cancel out for a single-color laser while the time-asymmetry of the two-color laser yields to a non-zero low frequency component in the photocurrent.

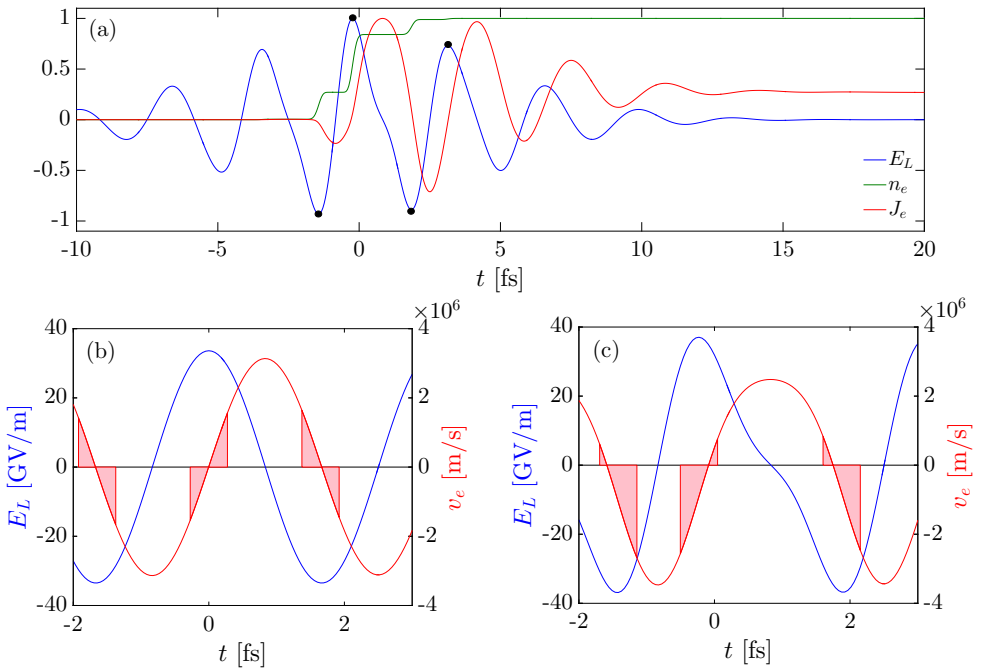

Figure 2.4: (a) Illustration of the photocurrent mechanism for a two-color laser pulse (blue line). The electron density (green line) follows a step like increase at each field maxima (black dots). Once freed, electrons participate to a macroscopic current (red line). Laser electric field E_L (blue line) and electron velocity v_e (red line) according to Eq. (2.76) for (b) a single-color laser and (c) a two-color laser. Light red areas show the time integral of the electron velocity around the field maxima demonstrating from Eq. (2.75) that the electronic current is maximized for time-asymmetric laser field. The laser pulse has a FWHM duration of $\tau_0 = 10$ fs and a carrier wavelength of $\lambda_0 = 1$ μm. The second harmonic parameters in the two-color setup are $\tau_0(2\omega_0) = 5$ fs and $\lambda_0(2\omega_0) = 0.5$ μm.

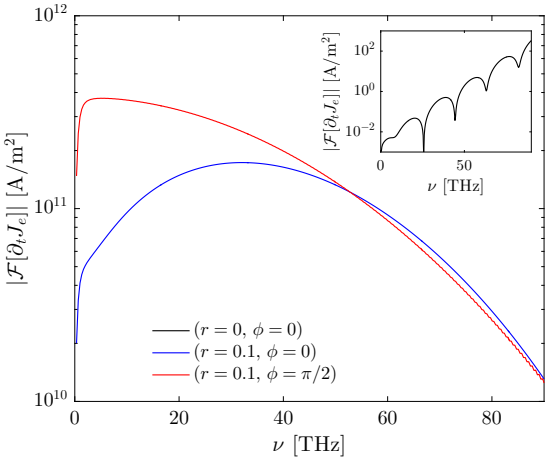

Figure 2.5: Typical photoionization source spectrum inferred from a 0D model for a one-color laser (inset, black line), a two-color laser ($r = 0.1$) with no phase-shift (blue line) and with $\pi/2$ phase-shift (red line). The total laser intensity is 150 TW/cm^2 with a carrier wavelength of $\lambda_0 = 1$ μm and a duration of $\tau_0 = 35$ fs propagating in argon at ambient pressure. The ionization rate is QST.

In the rest of the manuscript the two-color setup will be systematically used to study the so-called "Photocurrent Induced Radiation" (PIR) in the THz range. The (r, ϕ) parameters optimizing the time-asymmetry are $r \approx 0.3$ and $\phi = \pi/2$. Note that record values of $\sim 2\%$ in the laser-to-THz conversion efficiency in the classical photocurrent regime have been predicted by González de Alaiza Martínez *et al.* [2015] in the case of sawtooth waveforms generated by combining 4 or 5 laser harmonics with successive phase shifts $\pm\pi/2$. Finally the summation over the ionization instants can be viewed as an interference pattern between each electron radiated field, as proposed by Babushkin *et al.* [2011]. Indeed, the attosecond time scale over which each accelerated electron produces a large spectral content overlaps with that of electrons released a little bit earlier or later. The resulting THz band corresponds to constructive interferences between all fields emitted from ionization bursts in the low-frequency spectrum. Too many ionization instants, with a long pulse for instance, can deteriorate the interference figure and decrease the THz generation efficiency.

The photocurrent term along with the Kerr contribution, $\partial_t J_e \to \partial_t J_e + \partial_t^2 P_{\rm NL}$, can then be directly plugged into the wave equation (2.22) or the UPPE (2.32), to describe THz emission. The latter is characterized by extracting the low-frequency field component of the overall electric field (filtering the major laser component). Figure 2.5 displays typical THz spectra from the photocurrent source with different (r, ϕ) values. The generic spectral width scales as $1/\tau_0$ since τ_0 corresponds, roughly, to the duration of the ionization process. As expected, a many-cycle single-color laser ($r = 0$) delivers almost no THz signal (see inset), in contrast to an asymmetric laser ($r = 0.1$, blue line). The process is optimized with $\phi = \pi/2$ (red line) due to the $\sin\phi$ dependency of the THz field. Indeed, under small amplitude fields ($E_0 \ll E_{au}$) for which the QST ionization holds, Kim *et al.* [2008] suggest that:

$$E_{\rm THz} \propto \partial_t J_e \propto \sqrt{\frac{E_{au}}{E_\omega}} \exp\left(-\frac{2}{3}\frac{E_{au}}{E_\omega}\right) E_{2\omega} \sin\phi, \tag{2.79}$$

where E_ω and $E_{2\omega}$ are the amplitudes of the first and the second laser harmonics, respectively. This scaling is obtained by considering the low-frequency part of the photocurrent, Eq. (2.78),

where $v_f(t_n) \propto E_{2\omega} \sin\phi$, for a small r value, and δn_e^n is the solution of Eq. (2.69). Note that the phase shift rotates during the laser-plasma interaction, thereby modifying the photocurrent efficiency. Compared to the Kerr source term, the photoionization source is usually more efficient as soon as the medium is sufficiently ionized ($Z^* \approx 0.1$).

2.1.4 Electron plasma waves

A plasma is composed of ions and electrons interacting mutually through electromagnetic fields. When a particle is displaced from its equilibrium position, an electrostatic field grows which tends to pull the particle back to its original position.

An incident electromagnetic wave with frequency ω propagating in a plasma obeys the well-known dispersion relation [Jackson 1999]:

$$\omega^2 = c^2k^2 + \omega_{pe}^2, \tag{2.80}$$

where $\omega_{pe} = \sqrt{e^2 n_e / m_e \epsilon_0}$ is the classical plasma frequency and characterizes the time response ω_{pe}^{-1} of the plasma to a local perturbation while relativisic effects are neglected. From this, one can consider two different situations. When $\omega < \omega_{pe}$, the wave number k becomes complex, which leads to an evanescent wave in the so-called overdense plasma. If $\omega > \omega_{pe}$, the wave vector is real, and so the wave can propagate in the plasma, designated as underdense. Since the plasma frequency is linked to the electron density n_e, one can define a critical density n_c, based on the wavelength of the incident light,

$$n_c[\mathrm{cm}^{-3}] = \frac{\omega^2 m_e \epsilon_0}{e^2} \approx \frac{1.11 \times 10^{21}}{\lambda^2[\mu\mathrm{m}]} \mathrm{cm}^{-3}, \tag{2.81}$$

so that the plasma is opaque if $n_e > n_c$ and transparent when $n_e < n_c$. For laser wavelengths of the order of 1 μm, laser-gas interactions usually take place in the underdense regime. The refractive index of a plasma can be readily evaluated from Eq. (2.80) according to the defintion $\eta(\omega) = c/v_\phi = ck/\omega$ which gives

$$\eta(\omega) = \sqrt{1 - \frac{\omega_{pe}^2}{\omega^2}}. \tag{2.82}$$

The group velocity of the electromagnetic wave in the plasma satisfies the relation $v_g v_\phi = c^2$ such that $v_g = \eta c$.

Let us now consider the nonlinear plasma response to the ionizing electromagnetic field $(\mathbf{E}, \mathbf{B})$ within a cold-fluid limit. The conservation equations of both the averaged electron density n_e and of the averaged electron momentum $\mathbf{p}$ are, respectively (see Sec. 2.2.1):

$$\partial_t n_e + \boldsymbol{\nabla} \cdot (n_e \mathbf{v}) = S_{\mathrm{ext}}, \tag{2.83}$$

$$\partial_t \mathbf{p} + (\mathbf{v} \cdot \boldsymbol{\nabla})\mathbf{p} = -e\left(\mathbf{E} + \frac{\mathbf{p}}{\gamma m_e} \times \mathbf{B}\right) - \frac{\mathbf{p}}{n_e} S_{\mathrm{ext}}. \tag{2.84}$$

where $\mathbf{p} = \gamma m_e \mathbf{v}$ is the electron fluid momentum and $\gamma = (1 - v^2/c^2)^{-1/2}$ is the Lorentz factor that accounts for relativistic effects. The ionization source term is given by $S_{\mathrm{ext}} \equiv \sum_{j=1}^{Z} j \partial_t n_i^{(j)}$, and governs the creation of free electrons. Equations (2.83,2.84) will be also used to build 1D models for linear and nonlinear longitudinal waves excited in the wake of ultrashort laser pulses (see Section 2.2).

Equation (2.83) is equivalent to the well-known charge conservation equation

$$\partial_t \rho + \nabla \cdot \mathbf{J} = S_{\text{ext}}, \tag{2.85}$$

with $\rho = e(n_e + \sum_j n_i^{(j)})$ the free electron charge density. In turn, equation (2.84) can be recast to describe the evolution of the current density $\mathbf{J} = -en_e\mathbf{p}/\gamma m_e$ by first using Eq. (2.83) to include the photoionization source term:

$$n_e \partial_t \mathbf{p} + (n_e \mathbf{v} \cdot \boldsymbol{\nabla})\mathbf{p} = -en_e \left(\mathbf{E} + \frac{\mathbf{p}}{\gamma m_e} \times \mathbf{B} \right) - \mathbf{p}\partial_t n_e - \mathbf{p}\boldsymbol{\nabla} \cdot (n_e \mathbf{v}), \tag{2.86}$$

which gives:

$$\partial_t (n_e \mathbf{p}) + (n_e \mathbf{v} \cdot \boldsymbol{\nabla})\mathbf{p} + \mathbf{p}\boldsymbol{\nabla} \cdot (n_e \mathbf{v}) = -en_e \left(\mathbf{E} + \frac{\mathbf{p}}{\gamma m_e} \times \mathbf{B} \right). \tag{2.87}$$

In terms of the current density we obtain:

$$\partial_t (\gamma \mathbf{J}) = \frac{e^2}{m_e} n_e \mathbf{E} + \boldsymbol{\Pi} \tag{2.88}$$

$$\boldsymbol{\Pi} = -\frac{e}{m_e} \mathbf{J} \times \mathbf{B} + (\mathbf{J} \cdot \nabla) \left(\frac{\gamma \mathbf{J}}{e n_e} \right) + \left(\frac{\gamma \mathbf{J}}{e n_e} \right) (\nabla \cdot \mathbf{J}) \tag{2.89}$$

where $\boldsymbol{\Pi}$ gathers the ponderomotive forces exciting the plasma waves. $\boldsymbol{\Pi}$ can be decomposed into two parts, the Lorentz force and a convective term. Ponderomotive forces proportional to the gradient of the intensity lead to a nonzero averaged electron displacement. The effect of the ponderomotive force is strongly dependent on the laser intensity. For moderate classical interactions ($I_0 \leq 10^{13-14}$ W/cm^2) it is often discarded although it may generate radially-polarized low-frequency electromagnetic pulses as proposed by Sprangle *et al.* [2004]. This mechanism was further considered by D'Amico *et al.* [2007, 2008] to explain the THz generation in elongated plasma filaments with a single-color laser. In this case a finite longitudinal current propagates at the speed of light behind the ionization front. This current structure propagating at superluminal velocity emits radiation according to the Cherenkov effect. Rather than radial emission, the filament exhibits a forward conical shape. The ponderomotive force can be improved using tightly focused, few-cycle pulses leading to the creation of micro-plasmas. Even a single-color laser pulse can then create THz waves thanks to strong intensity gradients. The emission direction of these so-called micro-plasmas is almost orhogonal to the laser propagation axis [Buccheri & Zhang 2015], contrary to the elongated plasma filaments formed with either one or two-color lasers. The interplay between the ponderomotive force and the two-color driven photocurrents THz emissions have been studied in micro-plasmas by Thiele *et al.* [2016].

Let us now summarize on THz emitters in the classical regime. The Kerr effect, through four wave mixing, is able to produce THz waves. However, even if this nonlinearity is a key ingredient in driving the laser dynamics (self-focusing), Kerr-driven THz emission is weak compared with the radiation of the laser-generated plasma. The latter can be of micrometer scale or an elongated cm-long filament created by either single-color or two-colors laser. In the last few years the photocurrent scenario had emerged as the most effective way to produce THz waves at least along the laser propagation direction [Nguyen *et al.* 2017].

2.1.5 Analytical solutions and numerical results

Context

The approximate Unidirectional Pulse Propagation Equation (UPPE) is used to simulate laser filamentation over long propagation ranges. In past years, several research groups exploited it to model THz pulse generation with great success, in light of the good agreement met between numerical calculations and experiments [Andreeva *et al.* 2016]. Nevertheless, no thorough investigation was carried out to ensure the validity of the UPPE solution compared with that of the original wave equation (WE), e.g. Eq. (2.22). This remark particularly applies to the frequency range $\omega \leq \omega_{pe}$ in which the plasma becomes opaque. We propose to tackle this issue by first introducing an analytical model which reproduces the main features of the two approaches. We also use two 1D laser propagation codes, namely MAXFLU1D [González de Alaiza Martínez *et al.* 2016] and UPPE1D [Déchard *et al.* 2017], whose numerical implementation is presented in Appendix A. They are used to verify our theoretical predictions by solving the propagation equations (2.12) and (2.32), respectively. Here, our major result is an absolute convergence criterion, based on the propagated distance, which proves that solutions to the two models merge over long enough propagation distances. This criterion, inferred from theoretical calculations, is validated by numerical results.

As sketched in Fig. 2.6(a), an incident electromagnetic wave packet propagating in a preionized plasma ($n_e = cst$) experiences partial reflection at the plasma boundary ($x = 0$) depending on its frequency ω. The dielectric function of the plasma is given by Eq. (2.82) and models the response of the plasma to the incident wave packet. The transmitted wave corresponds to the real wave vector $k_T = \omega\sqrt{\epsilon(\omega)}/c$. This appears clearly when one considers the linear mode of the WE:

$$\widehat{\mathbf{E}}(x,\omega) \sim \exp\left[ikx\sqrt{1-\frac{\omega_{pe}^2}{\omega^2}}\right] \tag{2.90}$$

and that of the UPPE:

$$\widehat{\mathbf{E}}(x,\omega) \sim \exp\left[ikx\left(1-\frac{\omega_{pe}^2}{2\omega^2}\right)\right]. \tag{2.91}$$

Frequencies such that $\omega \leq \omega_{pe}$ propagate forward in an evanescent way over the plasma skin depth defined by $\delta_{pe} = c/\omega_{pe}$ [Jackson 1999]. Therefore, this spectral component is mainly reflected and forms a backward traveling wave. This phenomenon is correctly described by the WE, the solutions to which admit both forward and backward propagating waves [Nodland & McKinstrie 1997]. However, by construction, the UPPE equation cannot descrive reflection and wave evanescence since it always involves real refractive index. Indeed the two linear solutions match for $\omega \gg \omega_{pe}$ since $\sqrt{1-\omega_{pe}^2/\omega^2} \approx 1-\omega_{pe}^2/2\omega^2$, whereas plasma opacity is simply not present for the UPPE linear mode that always promotes oscillating modes at all frequencies. Hence one may ask how the UPPE deals with frequencies close to the plasma frequencies since, by construction, it does not take the plasma reflection into account. This is particularly problematic for THz wave propagation since ω_{pe} belongs to this frequency range.

Analytical framework

Although Nodland & McKinstrie [1997] solved exactly the WE for a homogeneous plasma, a number of important issues in nonlinear optics and plasma physics require source terms (Kerr effect, photocurrent) with time-dependent nonlinearities. Hence, we first propose an analytical

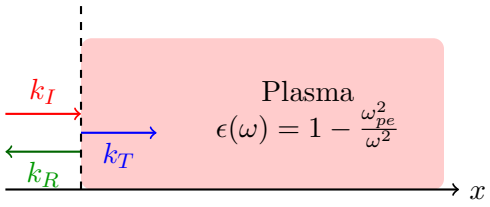

Figure 2.6: Incident (red), reflected (green) and transmitted (blue) wave vector on a vacuum-plasma interface. Frequencies $\omega \leq \omega_{pe}$ are damped in the plasma ($\sqrt{\epsilon} \in \mathcal{I}m$) while $\omega > \omega_{pe}$ are transmitted ($\sqrt{\epsilon} \in \mathcal{R}e$).

framework to treat the WE and the UPPE on the same ground. For the sake of simplicity, our study is confined to one dimension with a scalar electric field propagating in the x direction. In this geometry the above propagation equations can be recast as

$$(c\partial_x - \partial_t)(c\partial_x + \partial_t)E = c^2 Q, \tag{2.92}$$

for WE and

$$-2\partial_t(c\partial_x - \partial_t)E = c^2 Q, \tag{2.93}$$

for the UPPE where

$$Q = \mu_0(\partial_t J_e + \partial_t^2 P_{\mathrm{NL}}). \tag{2.94}$$

Here, linear dispersion is discarded and the nonlinear polarization is the instantaneous Kerr effect expresses as $P_{\mathrm{NL}} = \epsilon_0 \chi^{(3)} E^3$. The current J_e results from photoionization computed with Eq. (2.72) in which the electron density is solved with the QST rate for a single ionization Eq. (2.69). We focus on THz generation yielding weak radiation compared to the input laser pulse, so that we adopt a perturbative approach as proposed by Debayle *et al.* [2014]. The total electric field E is divided into the laser pulse E_L and a radiated part δE generated by interaction between the laser and the plasma, with $\delta E \ll E_L$. Also the laser is assumed unperturbed along its propagation, verifying the homogeneous propagation equation $(c^2\partial_x^2 - \partial_t^2)E_L = 0$. The source term Q is evaluated with E_L since we assumed that the radiated field δE is too weak to trigger nonlinear effects. Hence we obtain for the WE:

$$[(c\partial_x - \partial_t)(c\partial_x + \partial_t) - \omega_{pe}^2]\delta E = c^2 Q(E_L) = \omega_{pe}^2 E_L + \chi^{(3)}\partial_t^2 E_L^3 \tag{2.95}$$

and for the UPPE:

$$[-2\partial_t(c\partial_x + \partial_t) - \omega_{pe}^2]\delta E = c^2 Q(E_L). \tag{2.96}$$

Next we change the coordinate system to the co-moving laser frame

$$\xi = x - ct, \tag{2.97}$$
$$\tau = t, \tag{2.98}$$

in order to seek a forward-propagating solution such that the laser pulse and the laser-generated free electron density are functions of ξ only. We then have

$$\text{WE: } [\partial_\tau(2c\partial_\xi - \partial_\tau) - \omega_{pe}^2]\delta E = c^2 Q(E_L), \tag{2.99}$$
$$\text{UPPE: } [\partial_\tau(2c\partial_\xi - 2\partial_\tau) - \omega_{pe}^2]\delta E = c^2 Q(E_L), \tag{2.100}$$

with initial conditions reduced to $\delta E(\tau = 0, \xi) = \delta E(\tau, \xi = 0) = 0$. For the WE, we now apply the Laplace transform $\widetilde{f}(p) = \int_0^{+\infty} f(\tau) e^{-p\tau} d\tau$ onto Eq. (2.99) and obtain the following partial differential equation over ξ:

$$\left[-p^2 + 2cp\partial_\xi - \omega_{pe}^2(\xi)\right] \widetilde{\delta E} = \frac{c^2 Q(\xi)}{p}. \tag{2.101}$$

The solution is straightforward:

$$\widetilde{\delta E}_{\mathrm{WE}}(p, \xi) = \int_0^\xi \left\{ \frac{cQ}{2p^2} \exp\left[-\int_\xi^{\xi'} \frac{1}{2cp} \left(p^2 + \omega_{pe}^2\right) d\xi'' \right] \right\} d\xi'. \tag{2.102}$$

The inverse Laplace transform of the previous expression allows us to find the solution in the co-moving coordinates [Abramovitz & Stegun 1972]:

$$\delta E_{\mathrm{WE}}(\tau, \xi) = \frac{c}{2} \int_0^\xi Q(\xi') \sqrt{\frac{2c\tau + \xi - \xi'}{G(\xi, \xi')}} J_1 \left[\frac{\sqrt{G(\xi, \xi')}}{c} \sqrt{2c\tau + \xi - \xi'} \right] d\xi', \tag{2.103}$$

where J_1 is the Bessel function of the first kind and

$$G(\xi, \xi') = \int_\xi^{\xi'} \omega_{pe}^2(u) du \tag{2.104}$$

is positive ($\xi < 0$ and $\xi' \geq \xi$). In the original frame variables, this solution expresses as

$$\delta E_{\mathrm{WE}}(x, t) = \frac{c}{2} \int_0^{x-ct} Q(\xi') \sqrt{\frac{x + ct - \xi'}{\int_{x-ct}^{\xi'} \omega_{pe}^2(u) du}} J_1 \left[\frac{1}{c} \sqrt{\int_{x-ct}^{\xi'} \omega_{pe}^2(u) du \, (x + ct - \xi')} \right] d\xi', \tag{2.105}$$

and its spectrum is obtained after taking the Fourier transform in time t.

Applying the same treatment to Eq. (2.100), we get

$$\left[-2p^2 + 2cp\partial_\xi - \omega_{pe}^2(\xi)\right] \widetilde{\delta E} = \frac{c^2 Q(\xi)}{p}, \tag{2.106}$$

yielding

$$\delta E_{\mathrm{UPPE}}(x, t) = \frac{c}{\sqrt{2}} \int_0^{x-ct} Q(\xi') \sqrt{\frac{x - \xi'}{\int_{x-ct}^{\xi'} \omega_{pe}^2(u) du}} J_1 \left[\frac{\sqrt{2}}{c} \sqrt{\int_{x-ct}^{\xi'} \omega_{pe}^2(u) du \, (x - \xi')} \right] d\xi'. \tag{2.107}$$

The nonlinear source term Q triggers the first THz cycle over the laser pulse length. At later times, plasma oscillations at ω_{pe}^{-1} dictated by the partial convolution product with the Bessel function occur. This emission structure is characteristic of THz emission at moderate laser intensity ($I_0 \sim 10^{13} - 10^{15}$ W/cm^2), and is driven by the photocurrent source term.

Since the unidirectional approach modifies the propagator operator, we compare the linear kernels of Eqs. (2.105) and (2.107). The WE solution argument is $\sqrt{x + ct - \xi'}$ while the UPPE one is $\sqrt{2(x - \xi')}$, where the integration variable ξ' runs from 0 to $\xi'_{min} = x_{min} - ct_{max}$, x_{min} and t_{max} being fixed by the boundary of the simulation domain ($x_{min} = 0$ μm and $t_{max} = 3.3$ ps here). Assuming $x \gg \xi'$ we obtain $\sqrt{x + ct - \xi'} \approx \sqrt{2x}\sqrt{(x + ct)/(2x)}$ for the WE and $\sqrt{2}\sqrt{x - \xi'} \approx \sqrt{2x}$ for the UPPE. The $\sqrt{(x + ct)/(2x)}$ factor highlights the fact that the

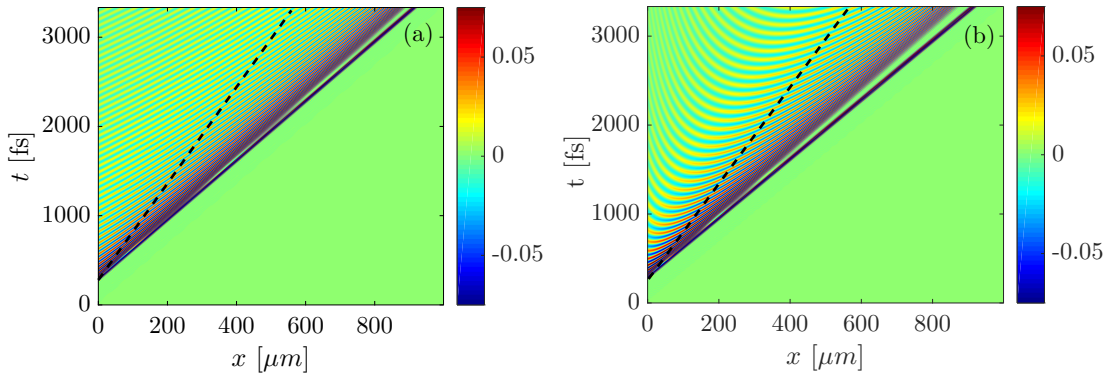

Figure 2.7: (x,t) maps of the full analytical solutions (a) Eq. (2.105) and (b) Eq. (2.107) with a source term driven by two-color 50-fs pulse with 150 TW/cm^2 total intensity ionizing argon at ambient pressure. The black dashed lines delimit the convergence domain of the WE and UPPE solutions, which increases with the coordinate x.

backward traveling wave is not accounted for in the UPPE model and it seems logical to recover this feature in our analytic solutions. Finally, if we consider $x \gg |x-ct|$, the two solutions converge to each other in the laser-filled region $x \gg |x-ct| > |\xi'|$.

Figures 2.7(a,b) show the solution of Eqs. (2.105) and (2.107), respectively, as a function of x and t, accounting for plasma generation alone in argon at ambient pressure. The lower-right part ($x > ct$), in which our solutions are not defined, is set to zero for causality reason. The WE and UPPE solutions coincide as long as $x \gg |x-ct|$, which includes the laser region. By contrast, they depart from each other in the opposite limit $ct \gg x$, which is associated with linear propagation. The WE and UPPE solutions indeed converge to each other near the laser head, where they are dominated by photocurrents. Far from the laser head, they are mainly driven by plasma oscillations modulated by their proper linear propagators that behave differently over large times. As a result the UPPE plasma oscillations appear to be longer by a $\sqrt{2}$ factor (hyperbolic contours), solely due to the omission of the backward traveling wave. However, the larger the propagated distance x, the broader the convergence domain, which spans a cone in the (x,t) plane [see dashed lines in Fig. 2.7(a,b)].

To get better insight into the analytical solutions and be able to compare them with numerical solutions, we compute the temporal Fourier spectrum of the field at $x = 100$ μm and $x = 1$ mm, and apply a low-pass filter in the frequency window $\nu \equiv \omega/2\pi \leq 90$ THz. The time signal of the THz field at these two locations is obtained through an inverse Fourier transform. Figures 2.8(a,b) show analytical WE/UPPE spectra and fields for the same two-color Gaussian pulse parameters ($\tau_0 = 50$ fs and $I_0 = 150$ TW/cm^2). One can observe that the spectral region $\nu < \nu_{pe} \equiv \omega_{pe}/2\pi$ becomes depleted as x increases while the minimum frequency marking the UPPE spectrum, ν_{min}, increases in turn. Accordingly, longer periods develop in the rear part of the pulse for the UPPE linear mode [see inset of Fig. 2.8(a)].

Our theoretical expectations are tested by running the MAXFLU1D and UPPE1D codes. For both codes the input condition at $x = 0$ is the two-color Gaussian pulse. The pump intensity is alternatively set to 50, 150 and 1000 TW/cm^2 in order to investigate various ionization degrees. The phase angle ϕ is equals to $\phi = 0$ to enhance the Kerr effect in the 50 TW/cm^2 case and $\pi/2$ otherwise. For Gaussian pulses with moderate laser intensity, from 50 TW/cm^2 to 150 TW/cm^2, and inducing single ionization, we employ the QST rate [Eq. (2.59)]. Alternatively, when dealing with 1 PW/cm^2 pulses, multiple ionization will be described from the multi-ion

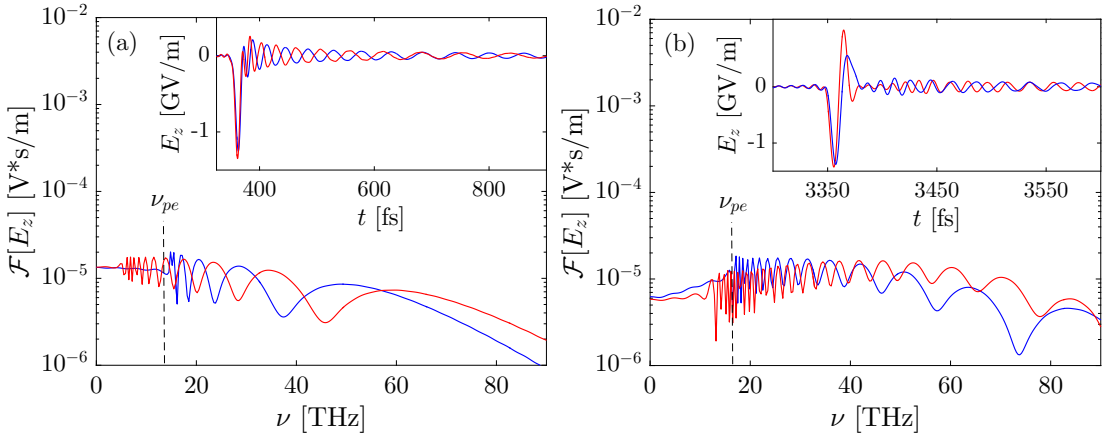

Figure 2.8: Spectra at (a) $x = 100$ μm and (b) $x = 1$ mm plotted from the analytical solutions (2.105) (WE, blue curves) and (2.107) (UPPE, red curves) for a two-color Gaussian pulse with mean pump intensity of 150 TW/cm^2 and FWHM duration of 50 fs interacting with argon. Note the oscillations in the UPPE spectrum for $\nu \leq \nu_{pe}$ and the growth in ν_{min} as x increases.

model [Eqs. (2.61)-(2.63)] employing the field-dependent PPT ionization rate [Eq. (2.47)].

To start with, only the Kerr response with rather weak intensity ($I_0 = 50$ TW/cm^2) and zero phase shift angle ($\phi = 0$) is accounted for (no plasma, no collision). As a result, the four-wave mixing (Kerr) mechanism is the unique conversion process. The nonlinear refractive index in argon is given by $n_2 = 3\chi^{(3)}/4\epsilon_0 c = 1 \times 10^{-19}$ cm^2/W. Figure 2.9 shows the spectra of the THz fields produced in argon by a 50-fs two-color pulse with 1-μm fundamental pump at increasing propagation distances, when using MAXFLU1D and the UPPE1D codes. Although the WE and UPPE solution spectra may not perfectly match over short propagation distances, i.e., $x = 10$ μm, excellent agreement is found at large distances $x \geq 50$ μm. These simulations show that, in the absence of plasma generation, the WE and UPPE solutions match in the whole spectral domain over relatively short distances ≈ 10 μm. The observed minor early-times discrepancies arise from small differences in the initialization of the numerical codes. The convergence speed between the WE and UPPE spectra driven by a Kerr response alone thus does not depend on the propagated distance. This behavior is rather logical, as the Kerr nonlinearity is just treated as a perturbation in the source term Q, and does not impact the frequency range of the linear modes in equations (2.90) and (2.91).

Next, in Fig. 2.10, only plasma generation is taken into account, similarly to Fig. 2.8. So, the Kerr response is set equal to zero. The selected intensity level is $I_0 = 150$ TW/cm^2. At short distances [Fig. 2.10(a,b)], the UPPE spectra shows oscillatory structures for $\nu < \nu_{pe}$, while the WE spectra are peaked around the plasma frequency. Those modulations, which are ascribed to improper modeling of plasma opacity effects, translate into longer oscillations in the time-domain UPPE field. After a few plasma skin depths [here, $\delta_{pe} = 3.3\,\mu$m], the transverse plasma wave oscillation develops behind the laser head (as described by the Bessel function in the analytical solutions), so that photocurrents govern the THz generation. As a result, the THz field amplitude reaches higher value than 1 GV/m and both solutions begin to merge. By doing so the minimum frequency of the oscillations in the UPPE spectrum increases until reaching the plasma frequency, as already observed in the analytical solutions.

Similar convergence of the two models is found in configurations favoring either a weaker plasma response (thus a more efficient Kerr effect) at smaller intensities or a stronger plasma response achieved at higher intensities. Figures 2.11(a) and (b) display the evolution of the

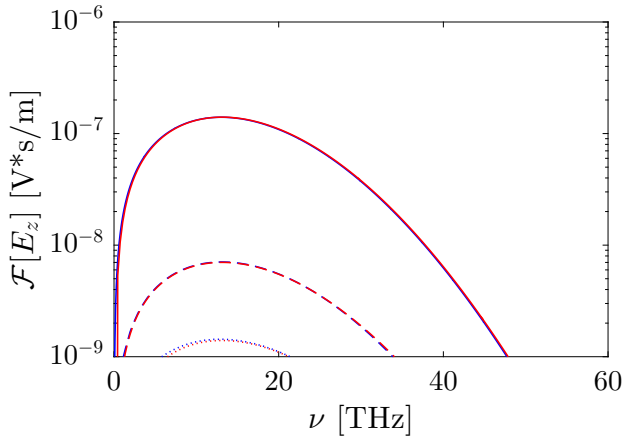

Figure 2.9: THz spectra at $x = 10$ μm (dotted line), $x = 50$ μm (dashed line) and $x = 1$ mm (solid line) from the MAXFLU1D code (blue lines) and the UPPE1D code (red curves) for 50 TW/cm^2 laser intensity using a two-color 50 fs Gaussian pulse with zero phase difference.

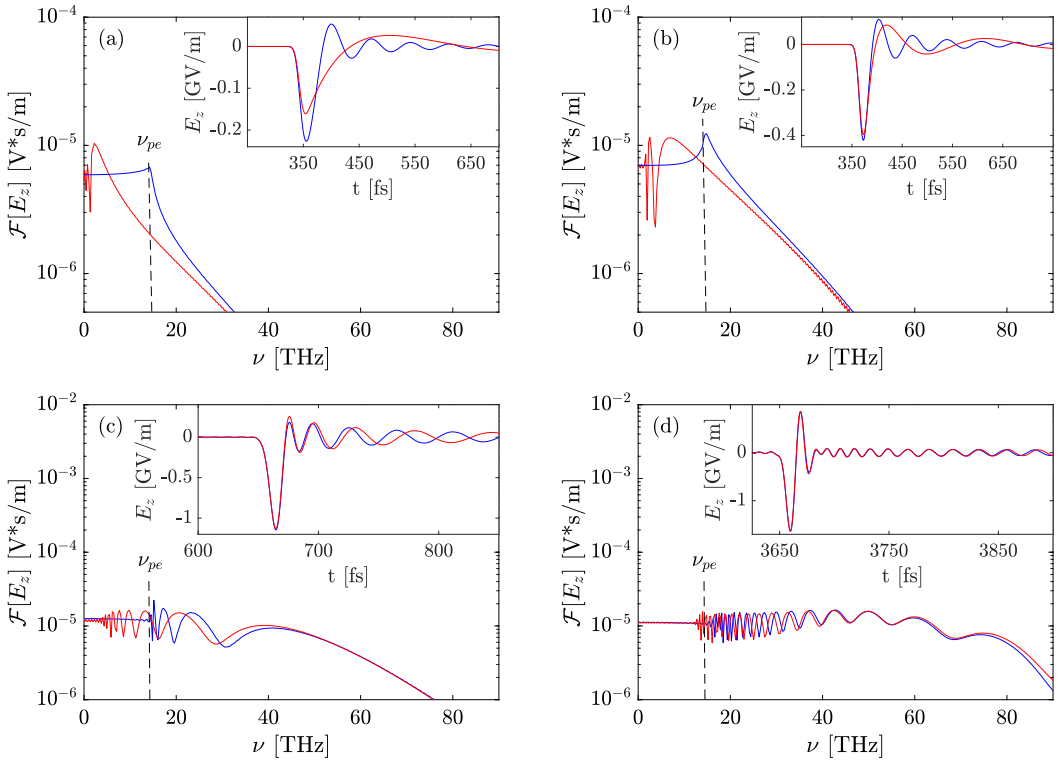

Figure 2.10: THz spectra and fields (see insets) at different propagation distances computed from the MAXFLU1D code (blue curves) and the UPPE1D code (red curves) for a two-color 50-fs Gaussian pulse with 150 TW/cm^2 intensity: (a) $x = 3$ μm (corresponding to almost one plasma skin depth δ_{pe}), (b) $x = 10$ μm, (c) $x = 100$ μm, and (d) $x = 1$ mm. Vertical dashed lines indicate $\nu = \nu_{pe}$.

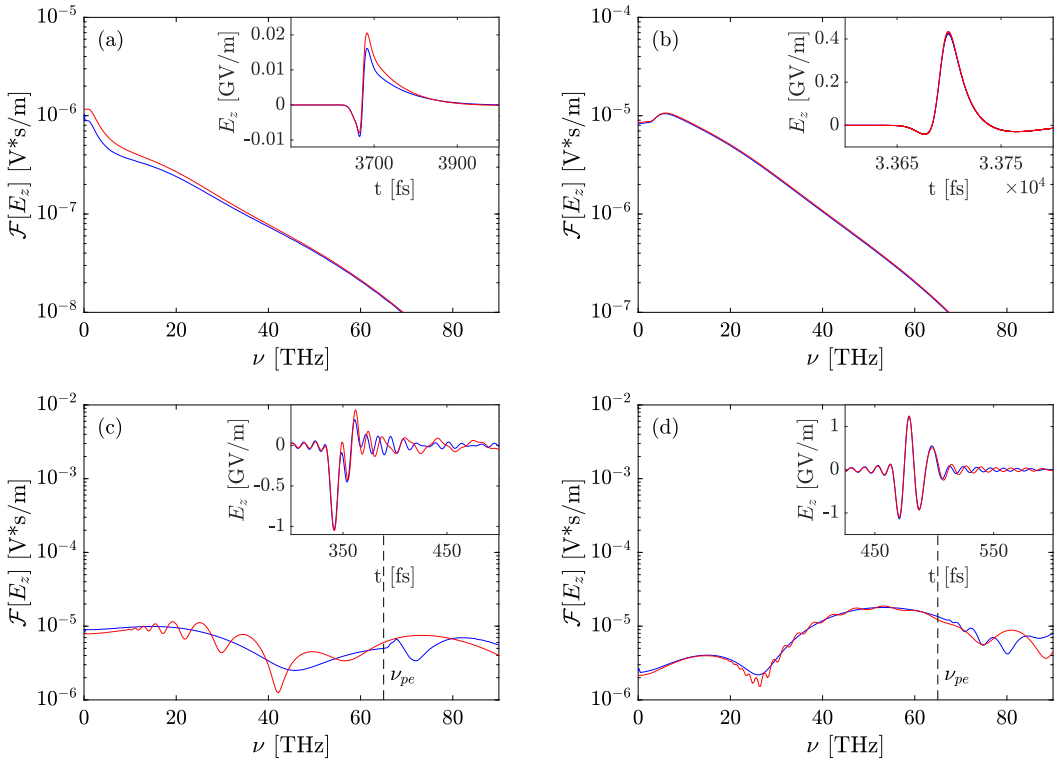

Figure 2.11: Same as in Fig. 2.10 with same color plotstyle but with the Kerr term included for $I_0 = 50$ TW/cm^2 at (a) $x = 1$ mm, (b) $x = 1$ cm and $I_0 = 1$ PW/cm^2 at (c) $x = 10$ μm and (d) $x = 50$ μm. Insets show the corresponding THz fields.

same two-color pulse having an input intensity of 50 TW/cm^2. The pulse is undergoing an effective Kerr response combined with plasma generation in argon. The corresponding plasma frequency is very weak, $\nu_{pe} = 0.53$ THz corresponding to a long plasma skin depth $\delta_{pe} = 90$ μm. The accumulation process due to the combined plasma and Kerr effects is clearly visible as the maximum field amplitude increases from 0.02 GV/m at $x = 1$ mm to 0.4 GV/m at $x = 1$ cm (see insets). Contrary to Fig. 2.9, the two numerical solutions no longer merge at $x = 1$ mm [Fig. 2.11(a)], which we attribute to the plasma contribution, although very weak. This confirms the important role of the plasma skin depth in the matching process. The numerical UPPE/WE spectra merge from $x = 5$ mm until perfectly overlapping at 1 cm [Fig. 2.11(b)]. At higher pulse intensities, $I_0 = 1$ PW/cm^2, the peak plasma density increases and the plasma skin depth becomes much shorter, $\delta_{pe} \approx 0.75$ μm for $\nu_{pe} \approx 65$ THz. We thus expect a quicker convergence between the UPPE and WE solutions, which is indeed achieved at about $z = 50$ μm, i.e., over a few tens of δ_{pe} [Figs. 2.10(c,d)].

For the same high intensity level, as recalled above, photocurrents are expected to dominate THz generation, provided that the pulse is only a few-cycle long Thiele *et al.* [2016]. The same trends have been observed in our simulation (not shown). However, the pulse was found to be strongly distorted along propagation, which impacted the ionization degree and so the effective plasma skin depth. The latter mays thus vary along the optical path. This justifies that the number of skin depths needed for matching the two solutions is not universal, and may change as the pulse propagates in a non-fully ionized medium.

To conclude, we demonstrated that, in a one-dimensional geometry, the UPPE model, which only describes the forward-propagating pulse component, provides similar THz spectra to an exact Maxwell-fluid model over distances of several plasma skin depths, along which Kerr non-

linearities as well as photocurrents drive THz pulse generation. Analytical solutions gave insight into the convergence dynamics of the two models in the (x, t) plane. Both numerical solutions highlighted the role of the time-varying plasma skin depth in controlling the THz radiation properties. This is the first original result of the present thesis. Further studies should aim at testing this property in full 3D propagation geometries.

2.2 Relativistic laser-plasma interaction

From now on we shall consider only relativistic laser intensities ($I_0 \geq 1.4 \times 10^{18}$ W/cm^2 for $\lambda_0 = 1$ μm). Such ultrahight intensities were made available to the scientific community after the invention of the chirped-pulse amplification (CPA) technique [Strickland & Mourou 1985], in the form of ultrashort ($\sim$ 10 fs - 1ps), high peak power ($\sim$ 100 TW - 10 PW) pulses. Through the triggering of extremely nonlinear plasma processes, these lasers are being exploited to drive compact high-energy particle and radiation sources (THz, X and γ rays). The different physical phenomena promoted by these light pulses are dictated by the density of the target. Underdense plasmas give rise to wakefield acceleration, relativistic self-focusing or parametric instabilities. In an overdense target, by contrast, the laser pulse is mainly reflected, but it may also be efficiently converted into energetic electron through various mechanisms which break the adiabatic motion of particles (e.g. anharmonic oscillations, vacuum heating). This energetic electron population is responsible, for instance, for the in-depth target heating and ion acceleration.

2.2.1 Modeling and numerical tools

Relativistic laser-plasma interaction triggers a wealth of phenomena which, in principle, can only be described by kinetic plasma theory, accounting for every particle information coupled to the Maxwell equations. However, despite the remarkable computing resources available nowadays, supercomputers are still incapable of following each particle at the microscopic level. Thus techniques have been developed to model properly the kinetics of laser-driven plasmas. One of them is the Particle-In-Cell (PIC) method pioneered by Birdsall & Langdon [1985], which we will introduce after reviewing the basics of plasma theory.

From Klimontovich to Vlasov equation

Let us consider a plasma composed of different species, labeled s, with N_s particles. Each particle is characterized by its position $\mathbf{r}$ and momentum $\mathbf{p} = \gamma m_s \mathbf{v}$ at instant t. The plasma state is thus defined as a point of $6\sum_s N_s$ coordinates in a phase space of dimensions $6\sum_s N_s$. The exact number of particles for the species s at the location $\mathbf{r}_i$ with momentum $\mathbf{p}_i$ is

$$\mathcal{N}_s(\mathbf{r},\mathbf{p},t) = \sum_{i=1}^{N_s} \delta(\mathbf{r}-\mathbf{r}_i(t))\delta(\mathbf{p}-\mathbf{p}_i(t)), \tag{2.108}$$

while the total number of particles is

$$\mathcal{N}(\mathbf{r},\mathbf{p},t) = \sum_s \mathcal{N}_s(\mathbf{r},\mathbf{p},t). \tag{2.109}$$

The point-like particles are represented by Dirac functions centered at the coordinates $(\mathbf{r}_i, \mathbf{p}_i)$. The momentum of the i-th particle of species s evolves according to the Lorentz force exerted by the microscopic fields $(\mathbf{E}^m, \mathbf{B}^m)$:

$$\frac{d\mathbf{p}_i(t)}{dt} = q_s \left\{ \mathbf{E}^m[\mathbf{r}_i(t),t] + \frac{\mathbf{p}_i(t)}{\gamma m_s} \times \mathbf{B}^m[\mathbf{r}_i(t),t] \right\} \tag{2.110}$$

The microscopic fields result from the superposition of the particle self-field, attached to the moving particle, plus the interaction field of the $\mathcal{N}-1$ other particles at given time t. These highly fluctuating fields are solutions to the Maxwell's equations with the charge and current

density source terms

$$\rho^m(\mathbf{r},t) = \sum_s q_s \int \mathcal{N}_s(\mathbf{r},\mathbf{p},t)\, d^3\mathbf{p}, \tag{2.111}$$

$$J^m(\mathbf{r},t) = \sum_s q_s \int \frac{\mathbf{p}}{\gamma(\mathbf{p})m_s}\mathcal{N}_s(\mathbf{r},\mathbf{p},t)\, d^3\mathbf{p}. \tag{2.112}$$

Since we do not consider any particle annihilation or creation, the distribution function $\mathcal{N}_s$ has to be conserved along the time evolution of the plasma, or a particle path, meaning that

$$\frac{D}{Dt}\mathcal{N}_s(\mathbf{r},\mathbf{p},t) = 0. \tag{2.113}$$

Hence using the properties of the differential and the Dirac function along with Eq. (2.110), it is easy to find:

$$\frac{D}{Dt}\mathcal{N}_s(\mathbf{r},\mathbf{p},t) = \frac{\partial \mathcal{N}_s(\mathbf{r},\mathbf{p},t)}{\partial t} + \frac{\partial \mathcal{N}_s(\mathbf{r},\mathbf{p},t)}{\partial \mathbf{r}}\cdot\frac{d\mathbf{r}}{dt} + \frac{\partial \mathcal{N}_s(\mathbf{r},\mathbf{p},t)}{\partial \mathbf{p}}\cdot\frac{d\mathbf{p}}{dt} = 0 \tag{2.114}$$

$$= \frac{\partial \mathcal{N}_s(\mathbf{r},\mathbf{p},t)}{\partial t} + \frac{\mathbf{p}}{\gamma m_s}\cdot\frac{\partial \mathcal{N}_s(\mathbf{r},\mathbf{p},t)}{\partial \mathbf{r}} + q_s\left(\mathbf{E}^m + \frac{\mathbf{p}}{\gamma m_s}\times\mathbf{B}^m\right)\cdot\frac{\partial \mathcal{N}_s(\mathbf{r},\mathbf{p},t)}{\partial \mathbf{p}}. \tag{2.115}$$

As a result, we obtain the so-called Klimontovich equation:

$$\frac{\partial \mathcal{N}_s}{\partial t} + \frac{\mathbf{p}}{\gamma m_s}\cdot\nabla\mathcal{N}_s + q_s\left(\mathbf{E}^m + \frac{\mathbf{p}}{\gamma m_s}\times\mathbf{B}^m\right)\cdot\nabla_p\mathcal{N}_s = 0. \tag{2.116}$$

This description of the plasma dynamics is exact because of the singular feature of the distribution function (Dirac). It has to be coupled to the evolution of the micro-fields governed by Maxwell equations. However one has to be aware that this set of equations cannot be solved because it models all particle motions constituting the plasma at each point of space-time. In practice we have neither access to such a resolution, nor the computational power to simulate all particles in a plasma.

A solution is thus to pass from singular to continuous functions by averaging the particle distribution over a small phase space volume ΔV to get:

$$f_s(\mathbf{r},\mathbf{p},t) = \langle \mathcal{N}_s(\mathbf{r},\mathbf{p},t)\rangle = \frac{1}{\Delta V}\int_{\Delta V}\mathcal{N}_s(\mathbf{r},\mathbf{p},t)\, dV \tag{2.117}$$

with $\Delta V = \Delta x\Delta y\Delta z\Delta p_x\Delta p_y\Delta p_z$. The distribution function f_s represents the probability density to find at time t particles located in a ΔV volume around $(\mathbf{r},\mathbf{p})$. In the same way we can split fields into averaged and fluctuating components:

$$\mathcal{N}_s = \langle\mathcal{N}_s\rangle + \delta\mathcal{N}_s = f_s + \delta\mathcal{N}_s \tag{2.118}$$

$$\mathbf{E}^m = \langle\mathbf{E}^m\rangle + \delta\mathbf{E}^m = \mathbf{E} + \delta\mathbf{E}^m \tag{2.119}$$

$$\mathbf{B}^m = \langle\mathbf{B}^m\rangle + \delta\mathbf{B}^m = \mathbf{B} + \delta\mathbf{B}^m \tag{2.120}$$

where, by definition, $\langle\delta\mathcal{N}_s\rangle = \langle\delta\mathbf{E}^m\rangle = \langle\delta\mathbf{B}^m\rangle = 0$. The averaged Klimontovich equation is thus a plasma kinetic equation expressed as:

$$\frac{\partial f_s}{\partial t} + \frac{\mathbf{p}}{\gamma m_s}\cdot\nabla f_s + q_s(\mathbf{E} + \frac{\mathbf{p}}{\gamma m_s}\times\mathbf{B})\cdot\nabla_p f_s = -q_s\langle(\delta\mathbf{E}^m + \frac{\mathbf{p}}{\gamma m_s}\times\delta\mathbf{B}^m)\cdot\nabla_p\,\delta\mathcal{N}_s\rangle. \tag{2.121}$$

The left-hand side of the previous equation accounts for large-scale collective effects whereas the right-hand side models collisional effects resulting from the rapid variations of the short-scale fields. Neglecting the collisional term yields the Vlasov equation:

$$\frac{\partial f_s}{\partial t} + \mathbf{v} \cdot \nabla f_s + q_s(\mathbf{E} + \frac{\mathbf{p}}{\gamma m_s} \times \mathbf{B}) \cdot \nabla_v f_s = 0. \tag{2.122}$$

The Vlasov equation is a kinetic equation for the distribution function f_s. In the following, it will be solved numerically by the PIC method (see Section 2.2.1). In the context of THz generation, the photoionization process needs to be included to describe the photocurrent source. To do so the source term S_{ext} is added on the right-hand side of the Vlasov equation.

A fluid description of plasmas

Starting from the Vlasov equation (2.122), it is possible to model the plasma as a fluid by taking the different moments of n-th order ($n \geq 0$) of this equation [Kruer 1988]. The 0^{th} moment ($\int d^3\mathbf{p}$) corresponds to the density conservation (or continuity equation):

$$\partial_t n_s + \nabla(n_s \mathbf{v}_s) = S_{\text{ext}} \tag{2.123}$$

where we define the density of species s by

$$n_s(\mathbf{r}, \mathbf{p}, t) = \int f_s(\mathbf{r}, \mathbf{p}, t)\, d^3\mathbf{p}, \tag{2.124}$$

and the fluid momentum $\mathbf{p}_s$ by

$$\mathbf{p}_s(\mathbf{r}, \mathbf{v}, t) = \frac{1}{n_s} \int \mathbf{p} f_s(\mathbf{r}, \mathbf{p}, t)\, d^3\mathbf{p}. \tag{2.125}$$

In a similar manner the 1^{st} moment ($\int \mathbf{v}\, d^3\mathbf{p}$) gives the momentum conservation equation

$$\partial_t(n_s \mathbf{p}_s) + \nabla \cdot \Psi + \nabla \cdot (n_s \mathbf{v}_s \otimes \mathbf{p}_s) = -e n_s(\mathbf{E} + \frac{\mathbf{p}_s}{\gamma m_s} \times \mathbf{B}) - \mathbf{p}_s S_{\text{ext}}, \tag{2.126}$$

with Ψ being the kinetic pressure tensor. Note that the equation governing the n-th order moment involves a $n+1$ order moment. For instance the momentum conservation requires the knowledge of the plasma pressure to be solved. Hence we need a closure condition to truncate the infinite set of moment equations. In our case the fluid equations will be only used in underdense plasmas, the temperature of which can be neglected and hence we will take $\Psi = 0$. This cold-fluid limit allows us to have a complete description through the fluid quantities $n_s, \mathbf{p}_s$ and their conservation equations (2.123), (2.126). Of course this approach discards completely any kinetic effect since the fluid has, for each given position $\mathbf{r}(t_0)$ and momentum $\mathbf{p}_s(t_0)$, a single value in the phase space.

To summarize, non-collisional plasmas can be described by the coupled Vlasov-Maxwell equations, which, for analytical purposes, will be reduced to a set of fluid-Maxwell equations evaluated in the cold limit. Nevertheless, even if this description has been simplified there is still too much information to handle. The next section shows how PIC codes are built in order to numerically describe such complex behaviors in plasma physics.

Particle-In-Cell code

The PIC method was popularized in the late 60's thanks to its efficiency and simplicity [Birdsall & Langdon 1985]. Since the particle distribution is conserved in the phase space (Liouville theorem) the Vlasov equation is solved through the method of characteristics. The density function f_s is then discretized over N_m points localized at coordinate $(\mathbf{r}_j, \mathbf{v}_j)$ at time t in the $6N_s$ phase space leading to:

$$f_s = \sum_{j=1}^{N_m} \Gamma_j S_\alpha(\mathbf{r} - \mathbf{r}_j(t))\delta(\mathbf{v} - \mathbf{v}_j(t)). \tag{2.127}$$

Compared to Eq. (2.108), the Dirac functions have been replaced by spatially extended splines (or shape functions S). Also, each numerical particle (or macro-particle) now represents a finite (large) number of physical particles as measured by Γ_j. As time goes by, the macro-particles follow a trajectory in the phase space given by $(\mathbf{r}_j(t), \mathbf{v}_j(t))$. At a given instant the charge and current densities are:

$$\rho(\mathbf{r}, t) = \sum_s \sum_{j=1}^{N_m} q_s \Gamma_j S_\alpha(\mathbf{r} - \mathbf{r}_j(t)), \tag{2.128}$$

$$\mathbf{J}(\mathbf{r}, t) = \sum_s \sum_{j=1}^{N_m} q_s \mathbf{v}_s \Gamma_j S_\alpha(\mathbf{r} - \mathbf{r}_j(t)). \tag{2.129}$$

These quantities are then projected on mesh nodes to compute, through Maxwell's equations, the discretized $(\mathbf{E}, \mathbf{B})$ fields at the next time step, while satisfying, at the same time, the charge conservation law Eq. (2.85). Once this is done, the new fields are interpolated from the mesh nodes to the macro-particle $(\mathbf{r}_j, \mathbf{v}_j)$. The momenta and positions of the particles are then advanced by solving the equation of motion (the so-called pusher step). By doing so the charge and current densities at the particle positions are modified. Finally, one time step later, $(\rho, \mathbf{J})$ are projected once again from the particle positions the to mesh nodes. This loop is the core of the PIC method and is repeated at each time step. To sum it up, starting from an initial distribution, we have to:

(1) Project $(\rho, \mathbf{J})$ from the macro-particle positions to the mesh nodes

(2) Solve the discretized Maxwell's equations

(3) Interpolate $(\mathbf{E}, \mathbf{B})$ from the grid nodes to the macro-particle positions

(4) Push the macro-particles subject to the Lorentz force

The projection (1) and interpolation (2) steps make use of the shape function S_α. Generally, S_α is taken to be a piecewise α-th order polynomial function, defined as the α-th order auto convolution of the nearest-grid point (NGP) function:

$$S_\alpha(x) = S_{\alpha-1}(x) * S_0(x) = \underbrace{S_0(x) * S_0(x) * \cdots * S_0(x)}_{\times(\alpha+1)}, \tag{2.130}$$

where

$$S_0(x) = H\left(\frac{x}{\Delta x} + \frac{1}{2}\right) H\left(\frac{x}{\Delta x} - \frac{1}{2}\right) \tag{2.131}$$

is the NGP function. Nowadays, PIC codes commonly employ 4^{th} order shape functions, which reduce the numerical noise and improve energy conservation, through at the cost of an increased simulation time. Usually, the same shape function is used for the projection and the interpolation stages. Moreover, to ensure that the electric field advanced from Maxwell-Ampère's equation [Eq. (2.3)] automatically satisfies Maxwell-Gauss's equation [Eq. (2.2)], the current density is not projected according to Eq. (2.129) but is computed from the continuity equation using the projected charge densities at two successive time step [Esirkepov 2001].

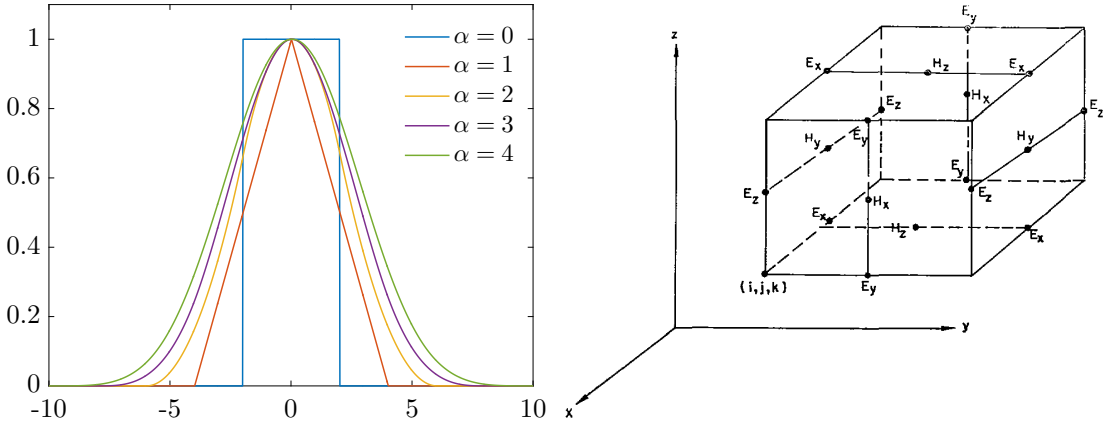

Figure 2.12: Shape functions of different orders. Position of various field comopnents in the Yee grid, *extract from* Yee [1966].

Knowing the current density at the mesh nodes, the $(\mathbf{E}, \mathbf{B})$ fields can be advanced through Maxwell-Ampère's [Eq. (2.3)] and Maxwell-Faraday's [Eq. (2.4)] equations. This is done using a finite-difference time domain scheme proposed by [Yee 1966]. This explicit solver considers a Cartesian grid with nodes located at $(x, y, z = i\Delta x,\, j\Delta y,\, k\Delta z)$ and discretized instants $t = n\Delta t$ (see Fig. 2.12). In a 3D geometry, the fields are advanced through

$$\frac{E_x|^{n+1}_{i+\frac{1}{2},j,k} - E_x|^{n}_{i+\frac{1}{2},j,k}}{c^2\Delta t} = \frac{B_z|^{n+\frac{1}{2}}_{i+\frac{1}{2},j+\frac{1}{2},k} - B_z|^{n+\frac{1}{2}}_{i+\frac{1}{2},j-\frac{1}{2},k}}{\Delta y} - \frac{B_y|^{n+\frac{1}{2}}_{i+\frac{1}{2},j,k+\frac{1}{2}} - B_y|^{n+\frac{1}{2}}_{i+\frac{1}{2},j,k-\frac{1}{2}}}{\Delta z} - \mu_0 J_x|^{n+\frac{1}{2}}_{i+\frac{1}{2},j,k} \tag{2.132}$$

$$\frac{E_y|^{n+1}_{i,j+\frac{1}{2},k} - E_y|^{n}_{i,j+\frac{1}{2},k}}{c^2\Delta t} = \frac{B_x|^{n+\frac{1}{2}}_{i,j+\frac{1}{2},k+\frac{1}{2}} - B_x|^{n+\frac{1}{2}}_{i,j+\frac{1}{2},k-\frac{1}{2}}}{\Delta z} - \frac{B_z|^{n+\frac{1}{2}}_{i+\frac{1}{2},j+\frac{1}{2},k} - B_z|^{n+\frac{1}{2}}_{i-\frac{1}{2},j+\frac{1}{2},k}}{\Delta x} - \mu_0 J_y|^{n+\frac{1}{2}}_{i,j+\frac{1}{2},k} \tag{2.133}$$

$$\frac{E_z|^{n+1}_{i,j,k+\frac{1}{2}} - E_z|^{n}_{i,j,k+\frac{1}{2}}}{c^2\Delta t} = \frac{B_y|^{n+\frac{1}{2}}_{i+\frac{1}{2},j,k+\frac{1}{2}} - B_y|^{n+\frac{1}{2}}_{i-\frac{1}{2},j,k+\frac{1}{2}}}{\Delta x} - \frac{B_x|^{n+\frac{1}{2}}_{i,j+\frac{1}{2},k+\frac{1}{2}} - B_x|^{n+\frac{1}{2}}_{i,j-\frac{1}{2},k+\frac{1}{2}}}{\Delta y} - \mu_0 J_z|^{n+\frac{1}{2}}_{i,j,k+\frac{1}{2}} \tag{2.134}$$

$$\frac{B_x|^{n+\frac{1}{2}}_{i,j+\frac{1}{2},k+\frac{1}{2}} - B_x|^{n-\frac{1}{2}}_{i,j+\frac{1}{2},k+\frac{1}{2}}}{\Delta t} = -\frac{E_z|^{n}_{i,j+1,k+\frac{1}{2}} - E_z|^{n}_{i,j,k+\frac{1}{2}}}{\Delta y} + \frac{E_y|^{n}_{i,j+\frac{1}{2},k+1} - E_y|^{n}_{i,j+\frac{1}{2},k}}{\Delta z} \tag{2.135}$$

$$\frac{B_y|^{n+\frac{1}{2}}_{i+\frac{1}{2},j,k+\frac{1}{2}} - B_y|^{n-\frac{1}{2}}_{i+\frac{1}{2},j,k+\frac{1}{2}}}{\Delta t} = -\frac{E_x|^{n}_{i+\frac{1}{2},j,k+1} - E_x|^{n}_{i+\frac{1}{2},j,k}}{\Delta z} + \frac{E_z|^{n}_{i+1,j,k+\frac{1}{2}} - E_z|^{n}_{i,j,k+\frac{1}{2}}}{\Delta x} \tag{2.136}$$

$$\frac{B_z|^{n+\frac{1}{2}}_{i+\frac{1}{2},j+\frac{1}{2},k} - B_z|^{n-\frac{1}{2}}_{i+\frac{1}{2},j+\frac{1}{2},k}}{\Delta t} = -\frac{E_y|^{n}_{i+1,j+\frac{1}{2},k} - E_y|^{n}_{i,j+\frac{1}{2},k}}{\Delta x} + \frac{E_x|^{n}_{i+\frac{1}{2},j+1,k} - E_x|^{n}_{i+\frac{1}{2},j,k}}{\Delta y} \tag{2.137}$$

Note that the field components are located at integer or half-integer nodes and known at integer and half-integer instants, thus ensuring centered finite differences in both space and time, of second order accuracy. The discretized magnetic field has a vanishing divergence, as it should be.

The stability of the Yee's scheme is given by the Courant-Friedrichs-Lewy (CFL) condition,

$$c\Delta t \leq \sqrt{\frac{1}{\frac{1}{\Delta x^2}+\frac{1}{\Delta y^2}+\frac{1}{\Delta z^2}}}. \tag{2.138}$$

One shortcoming of the Yee's scheme is that it gives rise to wave phase velocities lower than the speed of light c for electromagnetic waves propagating along the grid axes. A Van Newman analysis of Eqs. (2.132-2.137) indeed gives

$$v_\phi = \frac{\omega}{k} = \frac{2}{k\Delta t}\arcsin\left(\sqrt{\frac{c^2\Delta t^2}{\Delta x^2}\sin^2\left(\frac{k_x\Delta x}{2}\right)+\frac{c^2\Delta t^2}{\Delta y^2}\sin^2\left(\frac{k_y\Delta y}{2}\right)+\frac{c^2\Delta t^2}{\Delta z^2}\sin^2\left(\frac{k_z\Delta z}{2}\right)}\right), \tag{2.139}$$

with $k=\sqrt{k_x^2+k_y^2+k_z^2}$. This may impact simulations involving ultrarelativistic particles moving at $v > v_\phi$, thus experiencing a numerical variant of the Cherenkov instability (i.e., emitting non physical radiation). Various methods have been proposed to mitigate this defect. Among them the Yee scheme can be tuned by an *ad-hoc* coefficient in order to have a better numerical dispersion relation. In the following we adopt this improved numerical scheme.

Next, the value of the $(\mathbf{E},\mathbf{B})$ fields at mesh nodes is interpolated to the macro-particle positions thanks to the shape function described above. At the end of this step, each macro-particle is subject to a local electromagnetic field. By means of the equation of motion we can advance their momentum and position:

$$\frac{d\mathbf{p}}{dt} = q_s(\mathbf{E}+\frac{\mathbf{p}}{\gamma m_s}\times\mathbf{B}), \tag{2.140}$$

$$\frac{d\mathbf{r}}{dt} = \frac{\mathbf{p}}{\gamma m_s}. \tag{2.141}$$

To do so we resort to the Boris pusher [Boris 1970] which splits the action of the Lorentz force according to:

- During a half time step the particle is accelerated by the electric field:

$$\mathbf{p}^- = \mathbf{p}^{n-1/2} + \frac{\Delta t}{2}\frac{q_s\mathbf{E}^n}{m_s} \tag{2.142}$$

- Then the magnetic rotation is described during a complete time step:

$$\mathbf{p}^+ = \frac{2}{1+b^2}\begin{pmatrix} -b_y^2-b_z^2 & b_z+b_xb_y & -b_y+b_xb_z \\ -b_z+b_x+b_y & -b_x^2-b_z^2 & b_x+b_yb_z \\ b_y+b_xb_z & -b_x+b_yb_z & -b_x^2-b_y^2 \end{pmatrix}\mathbf{p}^- \tag{2.143}$$

  where $\mathbf{b}=\Delta t q_s\mathbf{B}^n/2m_s$ is the normalized $\mathbf{B}$ field obtained by linear interpolation $\mathbf{B}^n = (\mathbf{B}^{n+1/2}+\mathbf{B}^{n-1/2})/2$.

- The final momentum is given by the second half time step electric acceleration:

$$\mathbf{p}^{n+1/2} = \mathbf{p}^{+} + \frac{\Delta t}{2}\frac{q_s \mathbf{E}^n}{m_s} \tag{2.144}$$

- Once the new momentum is known, we can use it to find the new particle position:

$$\mathbf{r}^{n+1} = \mathbf{r}^{n} + \mathbf{v}^{n+1/2}\Delta t, \tag{2.145}$$

with

$$\mathbf{v}^{n+1/2} = \frac{\mathbf{p}^{n+1/2}}{m_s \gamma^{n+1/2}}. \tag{2.146}$$

The PIC method allows to study a wide range of physical situations from laser-plasma interactions to astrophysical scenarios. Besides describing the collective dynamics of a kinetic plasma, it can also model various effects expected in non-ideal plasmas. The PIC code CALDER used during this PhD can thus model elastic and inelastic collisions, high energy processes such as Bremsstrahlung, pair creation as well as field ionization with the instantaneous multi-ion ADK rate (2.60).

Parallelized using the MPI library, the CALDER code can take advantage of the computing power of thousands of CPUs. To give an order of magnitude, a standard simulation done during this PhD was run over 1000 processors during 24 hours, hence more than two years and a half of computations on one CPU is condensed into one day of intense computing. The simulation domain is usually 100 μm long in each direction with mesh size resolving the the laser wavelength, $\Delta x \sim \lambda_0/100$ leading to hundreds of millions of cells in a 2D geometry. The plasma can be composed of several species with tens of millions of macro-particles.

Cylindrical geometry

When a 3D geometry turns out to be mandatory to capture the physics, we have made use of the CALDER-CIRC code [Davoine 2009; Lifschitz *et al.* 2009]. Based on a cylindrical geometry and truncated angular Fourier expansion, this tool allows the simulation time to be greatly reduced compared to full 3D Cartesian simulation. Precisely, the Cartesian system (x, y, z) is replaced by (r, θ, x) and fields are Fourier expanded along the θ coordinate while macro-particles quantities $(\mathbf{r}, \mathbf{p})$ are still computed over a Cartesian grid. For a given field F representing one of the field $\mathbf{E}, \mathbf{B}, \mathbf{J}$ or ρ, their Fourier expansion expresses as:

$$F(r, \theta, x) = \sum_{m=-\infty}^{+\infty} \widehat{F}^m(r, x) e^{-im\theta}, \tag{2.147}$$

with

$$\widehat{F}^m(r, x) = \frac{1}{2\pi}\int_0^{2\pi} F(r, \theta, x) e^{im\theta}. \tag{2.148}$$

Equation (2.147) can be simplified since our fields are all real quantities. Hence $\widehat{F}^m(r, x)$ is equal to its conjugate:

$$F(r, \theta, x) = \widetilde{F}^0(r, x) + \sum_{m=1}^{+\infty} \mathcal{R}e[\widetilde{F}^m(r, x) e^{-im\theta}], \tag{2.149}$$

with

$$\widetilde{F}^0(r,x) = \widehat{F}^0(r,x) \tag{2.150}$$

$$\widetilde{F}^m(r,x) = 2\widehat{F}^m(r,x) \qquad \text{for } m \geq 1. \tag{2.151}$$

For a given mode m, the code computes the corresponding field components in cylindrical coordinates as

$$\frac{1}{c^2}\frac{\partial \widetilde{E}_r^m}{\partial t} = -\frac{im}{r}\widetilde{B}_x^m - \frac{\partial \widetilde{B}_\theta^m}{\partial x} - \mu_0 \widetilde{J}_r^m \tag{2.152}$$

$$\frac{1}{c^2}\frac{\partial \widetilde{E}_\theta^m}{\partial t} = \frac{\partial \widetilde{B}_r^m}{\partial x} - \frac{\partial \widetilde{B}_x^m}{\partial r} - \mu_0 \widetilde{J}_\theta^m \tag{2.153}$$

$$\frac{1}{c^2}\frac{\partial \widetilde{E}_x^m}{\partial t} = \frac{1}{r}\frac{\partial (r\widetilde{B}_\theta^m)}{\partial r} + \frac{im}{r}\widetilde{B}_r^m - \mu_0 \widetilde{J}_x^m \tag{2.154}$$

$$\frac{\partial \widetilde{B}_r^m}{\partial t} = \frac{im}{r}\widetilde{E}_x^m + \frac{\partial \widetilde{E}_\theta^m}{\partial x} \tag{2.155}$$

$$\frac{\partial \widetilde{B}_\theta^m}{\partial t} = -\frac{\partial \widetilde{E}_r^m}{\partial x} + \frac{\partial \widetilde{E}_x^m}{\partial r} \tag{2.156}$$

$$\frac{\partial \widetilde{B}_x^m}{\partial t} = -\frac{1}{r}\frac{\partial (r\widetilde{E}_\theta^m)}{\partial r} - \frac{im}{r}\widetilde{E}_r^m, \tag{2.157}$$

where we have used the fact that, for any field $\widetilde{F}(r,x)$:

$$\partial_\theta \left[\widetilde{F}^m(r,x)e^{-im\theta}\right] = -im\widetilde{F}^m(r,x)e^{-im\theta}. \tag{2.158}$$

These modes are coupled through the Vlasov equation which is nonlinear. In practice, the system is truncated to $m_{\max}$, assuming that higher modes do not affect the simulated physics. Thus, a 3D computation is here replaced by $(m_{\max}+1)$ 2D simulations. Usually two modes ($m_{\max} = 1$) are sufficient to describe the interaction of an intense laser with an underdense gas within a good accuracy. The $m = 0$ mode represents axisymmetric fields (independent of θ) such as the plasma wakefield. Linearly polarized fields need at least $m = 1$ to be properly described. Indeed, a laser polarized in the y direction can be decomposed over the r and θ variables and related directions according to:

$$\mathbf{E}(r,\theta,x) = E(r,x)\mathbf{e_y} = E(r,x)\cos(\theta)\mathbf{e_r} - E(r,x)\sin(\theta)\mathbf{e_\theta}, \tag{2.159}$$

$$\mathbf{B}(r,\theta,x) = B(r,x)\mathbf{e_z} = B(r,x)\sin(\theta)\mathbf{e_r} + B(r,x)\cos(\theta)\mathbf{e_\theta}. \tag{2.160}$$

Thus, the laser components correspond to $m = 1$ mode [see Eq. (2.149)]:

$$\widetilde{E}_r^1 = E(r,x) \tag{2.161}$$

$$\widetilde{E}_\theta^1 = -iE(r,x) \tag{2.162}$$

$$\widetilde{B}_r^1 = iE(r,x) \tag{2.163}$$

$$\widetilde{B}_\theta^1 = E(r,x). \tag{2.164}$$

By contrast, the Vlasov equation solving the plasma dynamics is still integrated over a Cartesian grid. Yet, the projection step of the charge and current densities from the macro-particles positions (x,y,z) to the mesh nodes in the (r,θ,x) coordinate system is modified to take into account the angular expansion. This operation is repeated $m_{\max}$ times. The interpolation

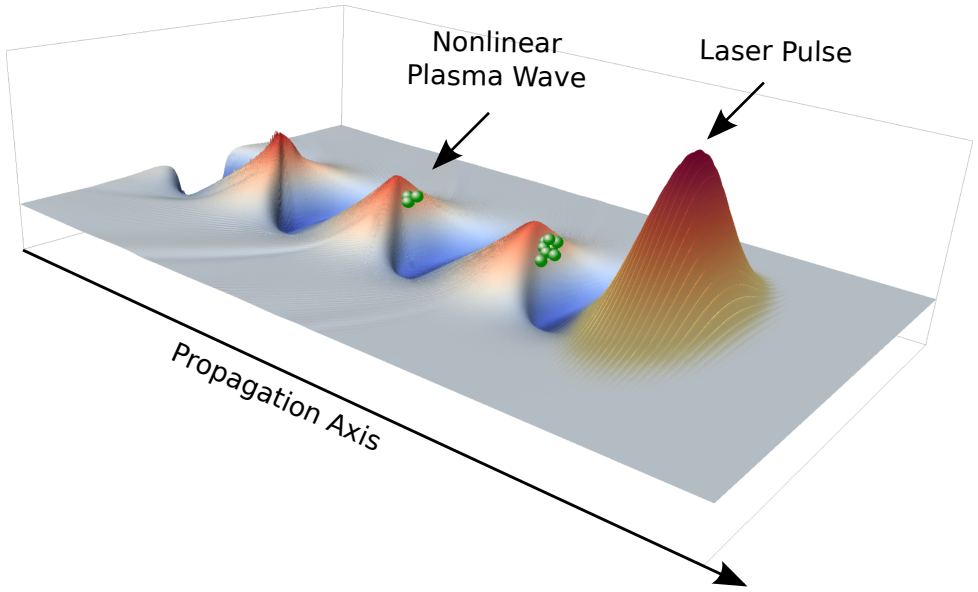

Figure 2.13: Generation of a plasma wakefield by an ultrashort intense laser pulse. The figure plots the longitudinal electric field (red-blue colormap) and the accelerated trapped electrons (green spheres).

step follows the same procedure. Moreover *ad-hoc* boundary conditions in $r = 0$ are used.

CALDER-CIRC has been benchmarked against 3D Cartesian simulations in Lifschitz *et al.* [2009]. The typical gain in computational time is of about ~ 50. In this manuscript, CALDER-CIRC will be only used for underdense plasmas since the interaction is then mainly axisymmetric.

2.2.2 Laser-Plasma Wakefield Accelerator

Physical mechanism

When an ultrashort and ultra-intense laser pulse propagates in an underdense gas, the atoms are ionized in the pulse front. Then the ponderomotive force acts on freed electrons and push them (longitudinally and transversally) away from the high intensity regions. Displaced from their equilibrium position, the electrons are pulled back by their parent ions, which induces an electrostatic electron plasma wave oscillating at the plasma frequency ω_{pe}, and co-propagating with the laser. When the laser length is shorter than the plasma wavelength $\lambda_{pe} \sim c/\omega pe$, the plasma wave develops mostly in its wake, hence its designation as a "wakefield" [Tajima & Dawson 1979]. Figure 2.13 shows an illustration of a nonlinear plasma wave in the wake of an ultra-intense laser.

For moderate laser intensities ($< 10^{18}$ W/cm^2 at $\lambda_0 = 1$ μm), the ponderomotive force is weak, so that the wakefield is well described by a sinusoidal modulation at ω_{pe}.

At high laser intensity ($> 10^{18}$ W/cm^2 at $\lambda_0 \simeq 1$ μm), the wakefield may become strong enough to trap part of the plasma electrons and accelerate them to high energies. This mechanism is similar to that of a strong wave accelerating a surfer initially at rest. This so-called injection phenomenon is able to accelerate particles over much shorter distances than conventional accelerators thanks to much stronger accelerating fields. To give some illustrative numbers, the longest linear accelerator at the Stanford Linear Accelerator Center (SLAC) is 2.6 km long and generates accelerating fields of 0.1 GV/m, thus delivering electron beams at 20 GeV energy. A plasma of few millimeters long can sustain electric fields of about 100 GV/m, hence three

orders of magnitude higher. As a result, GeV energies can be attained over much smaller distance. Considerable progress have been made experimentally since the concept of laser wakefield accelerator (LWFA) was proposed by [Tajima & Dawson 1979]. The first quasi-monoenergetic electron bunches were produced in 2004 with 100 MeV energy [Faure *et al.* 2004; Geddes *et al.* 2004; Mangles *et al.* 2004]. Ten years later a record energy of 4.2 GeV was achieved by means of capillary-discharge-waveguides [Leemans *et al.* 2014]. The same technique now delivers 8 GeV energetic bunches [Gonsalves *et al.* 2019]. Note that the betatron [Esarey *et al.* 2002; Rousse *et al.* 2004; Corde *et al.* 2013] or Compton based radiation by electron beams in LWFA is also an active field of research.

To put this physical process into equations, we first recall the origin of the ponderomotive force acting on electrons. Then the 1D fluid equations of the plasma wave in the quasilinear and nonlinear regime are derived. Using a Hamiltonian approach, a criterion for electron injection can be modeled in various situations. Optimizing the electron injection process then must be extended in three dimensions due to the underlying physics. Therefore, we shall give scaling laws reported in the literature as inferred from PIC simulations and experiments. We will also show that the plasma wave can significantly impact the laser propagation through the density dependence of the plasma refractive index. Finally, current limitations in particle acceleration will be discussed.

Transverse canonical momentum and ponderomotive force

In order to introduce meaningful quantities let us first consider the motion of a single electron subject to an electromagnetic wave in vacuum. The $(\mathbf{E}, \mathbf{B})$ fields are completely characterized by the vector potential $\mathbf{A}$:

$$\mathbf{E} = -\frac{\partial \mathbf{A}}{\partial t}, \tag{2.165}$$

$$\mathbf{B} = \nabla \times \mathbf{A}, \tag{2.166}$$

with vanishing scalar potential. The equation of motion for the electron is

$$\frac{d\mathbf{p}}{dt} = -e(\mathbf{E} + \frac{\mathbf{p}}{\gamma m} \times \mathbf{B}) \tag{2.167}$$

with $\gamma = \sqrt{1 + p^2/(mc)^2}$ denoting the Lorentz factor. By expressing fields in terms of the vector potential, and using the fact that $\partial_t \mathbf{A} = d_t \mathbf{A} - (\mathbf{v} \cdot \nabla)\mathbf{A}$, we have:

$$\frac{d}{dt}(\mathbf{p} - e\mathbf{A}) = -e\left[(\mathbf{v} \cdot \nabla)\mathbf{A} + \mathbf{v} \times (\nabla \times \mathbf{A})\right]. \tag{2.168}$$

The vector identity $\mathbf{v} \times (\nabla \times \mathbf{A}) = (\nabla \mathbf{A}) \cdot \mathbf{v} - (\mathbf{v} \cdot \nabla)\mathbf{A}$ allows us to obtain:

$$\frac{d}{dt}(\mathbf{p} - e\mathbf{A}) = -e(\nabla \mathbf{A}) \cdot \mathbf{v}. \tag{2.169}$$

Moreover, energy conservation equation for the electron reads

$$\frac{d}{dt}\gamma m_e c^2 = -e\mathbf{v} \cdot \mathbf{E} = e\mathbf{v} \cdot \frac{\partial \mathbf{A}}{\partial t}. \tag{2.170}$$

Now if we consider a simple plane wave propagating along the x axis and being linearly polarized in the transverse plane, we can project Eq. (2.169) to get:

$$\frac{d}{dt}(\mathbf{p}_\perp - e\mathbf{A}_\perp) = \mathbf{0}, \tag{2.171}$$

$$\frac{d}{dt}p_x = -e\mathbf{v}_\perp \cdot \frac{\partial \mathbf{A}}{\partial x}. \tag{2.172}$$

Since the electron is initially at rest before the arrival of the laser wave, Eq. (2.171) gives the conservation of the transverse canonical momentum,

$$\mathbf{p}_\perp = e\mathbf{A}_\perp, \tag{2.173}$$

hence the electron acquires a transverse momentum supplied by the potential vector of the wave. An important consequence of Eq. (2.173) is that, after the interaction with a finite duration laser pulse, the transverse momentum recovers its initial vanishing value

We deduce the transverse velocity $\mathbf{v}_\perp = e\mathbf{A}/\gamma m_e$ and replace it in Eqs. (2.170, 2.172):

$$\frac{d}{dt}\gamma m_e c^2 = \frac{e^2}{\gamma m_e} A \frac{\partial A}{\partial t} = \frac{e^2}{2\gamma m_e}\frac{\partial A^2}{\partial t}, \tag{2.174}$$

$$\frac{d}{dt}p_x = -\frac{e^2}{\gamma m_e} A \frac{\partial A}{\partial x} = -\frac{e^2}{2\gamma m_e}\frac{\partial A^2}{\partial x}. \tag{2.175}$$

Equation (2.175) involves an effective force along the x axis, $-e^2/(2\gamma m_e)\partial A^2/\partial x$, called the ponderomotive force. This longitudinal force is due to the magnetic component of the Lorentz force and thus comes into play when $v \sim c$. For a realistic laser pulse with longitudinal and transverse spatial extent, a three dimensional ponderomotive force is thus applied on electrons.

By subtracting the last two equations and passing into the pulse referential phase frame we obtain, after integration with $p_x(0) = \gamma(0) = 0$,

$$\gamma = 1 + p_x/m_e c, \tag{2.176}$$

which, combined to the classical definition of $\gamma = \sqrt{1 + (p/m_e c)^2}$, leads to:

$$\frac{p_x}{m_e c} = \frac{1}{2}\left(\frac{e\mathbf{A}}{m_e c}\right)^2 \tag{2.177}$$

$$\gamma = 1 + \frac{1}{2}\left(\frac{e\mathbf{A}}{m_e c}\right)^2. \tag{2.178}$$

This allows us to define the normalized laser amplitude $a_0 = e|\mathbf{A}|/m_e c = eE_0/m_e c\omega_0$ along with the normalized momentum $\tilde{\mathbf{p}} = \mathbf{p}/m_e c$ such that $\tilde{p}_x = a_0^2/2$ and $\gamma = 1 + a_0^2/2$. The factor $1/2$ in the expression of γ is due to the linear polarization of the pulse[3]. For a circular polarization the ponderomotive force is increased and $\gamma = 1 + a_0^2$. In the following we will only consider linearly polarized laser pulses. The relativistic regime is reached when $\tilde{p} \gtrsim 1$ hence for $a_0 \gtrsim 1$.

[3] A general expression for the laser vector potential is $A(x,t) = \frac{A_0(x,t)}{1+\epsilon^2}(\mathbf{e_z}\cos\omega_0 t + \mathbf{e_y}\epsilon\sin\omega_0 t)$, with ϵ the ellipticity of the wave. Hence, for $\epsilon = 0$ the laser is linearly polarized along z while for $\epsilon = 1$ we obtain a circularly polarized laser field.

A convenient expression of a_0 is

$$a_0 = \left(\frac{e^2}{2\pi^2\epsilon_0 m_e^2 c^5} I_0 \lambda_0\right)^2 = 0.85\sqrt{I_{18}}\lambda_{\mu m}, \tag{2.179}$$

where $I_0 = \epsilon_0 c E_0^2/2$ is the laser intensity (I_{18} is I_0 in 10^{18} W/cm^2) and λ_0 is the laser wavelength ($\lambda_{\mu m}$ is λ_0 in micrometers). Hence the relativistic threshold $a_0 = 1$ corresponds to an intensity $I_0 = 1.4 \times 10^{18}$ W/cm^2 for a wavelength $\lambda_0 = 1$ μm.

1D plasma wave

We now analyze the response of a plasma considered as a fluid, subject to an intense propagating electromagnetic wave. An exact analytical calculation is only possible in 1D geometry, assuming a cold pre-ionized plasma with immobile ions. Indeed the electron thermal velocity is small compared to the oscillation velocity ($\sim c$) in the laser field and the mass of ions is several orders of magnitude higher than the electron one, resulting in a negligible motion. In this chapter, the fluid equations (2.123) and (2.126) for electrons will be employed following the standard literature, most of which ignores the influence of photoionization [Akhiezer & Polovin 1956; Sprangle *et al.* 1990; Esarey *et al.* 2009]. The laser is propagating along the x direction, polarized in the transverse plane and described by the vector potential $\mathbf{A}_\perp(x,t)$. The plasma is initially neutral with an ambient density n_0 subject to an electronic perturbation δn_e. Thus, the electron ($n_e = n_0 + \delta n_e$) and ion ($n_i = n_0$) densities satisfy the Gauss law, expressed with the scalar potential $\Phi(x,t)$ as

$$\frac{\partial^2 \Phi}{\partial x^2} = \frac{e(n_e - n_i)}{\epsilon_0}. \tag{2.180}$$

Introducing the ambient plasma frequency $\omega_{pe} = \sqrt{e^2 n_0/m_e\epsilon_0} \equiv c k_{pe}$ and the normalized scalar potential $\phi = e\Phi/m_e c^2$, we obtain:

$$\frac{\partial^2 \phi}{\partial x^2} = k_{pe}^2 \left(\frac{n_e}{n_0} - 1\right). \tag{2.181}$$

Moreover, the continuity and momentum Eqs. (2.123) and (2.126) can be written as

$$\frac{\partial n_e}{\partial t} + c\frac{\partial}{\partial x}(n_e \beta_x) = 0, \tag{2.182}$$

$$\left(\frac{\partial}{\partial t} + v_x \frac{\partial}{\partial x}\right) p_x = -e\left(E_x + \frac{p_\perp}{\gamma m_e} B_\perp\right) = e\frac{\partial \Phi}{\partial x} - \frac{e^2}{2\gamma m_e}\frac{\partial A_\perp^2}{\partial x}, \tag{2.183}$$

$$\left(\frac{\partial}{\partial t} + v_x \frac{\partial}{\partial x}\right) p_\perp = -e\left(E_\perp - \frac{p_x}{\gamma m_e} B_y\right) = \left(\frac{\partial}{\partial t} + v_x \frac{\partial}{\partial x}\right) e A_\perp. \tag{2.184}$$

The ionization term is not taken into account in Eq. (2.182) since we consider a pre-ionized plasma. The inclusion of photoionization will be addressed in Chapter 3 where we shall consider THz pulse generation by photocurrents in relativistic plasmas hosting nonlinear plasma waves. We retrieve in Eq. (2.183) the relativistic ponderomotive force $-e^2/(2\gamma m_e)\partial A_\perp^2/\partial x$ expressed above in Eq. (2.175) but now it is balanced by the electrostatic restoring force $e\partial\Phi/\partial x$ due to the presence of ions. Note that, due to the 1D geometry, the (fluid) transverse canonical momentum is still preserved [Eq. (2.184)]. Before proceeding, we change to normalized quantities: $\mathbf{p} \to \mathbf{p}/m_e c$, $\mathbf{v} \to \mathbf{v}/c$, $n_e \to n_e/n_c$, $x \to \omega_0 x/c$, $t \to \omega_0 t$, $\mathbf{A} \to e\mathbf{A}/m_e c$ and $\phi \to e\Phi/m_e c^2$. The

momentum equations then become:

$$\left(\frac{1}{c}\frac{\partial}{\partial t}+\beta_x\frac{\partial}{\partial x}\right)p_x=\frac{\partial\phi}{\partial x}-\frac{1}{2\gamma}\frac{\partial\, a_\perp^2}{\partial x} \tag{2.185}$$

$$\frac{d}{dt}(p_\perp-a_\perp)=0 \tag{2.186}$$

where $\beta_x=v_x/c$ and $a_\perp=eA_\perp/m_ec$ is the normalized vector potential.

A change in the coordinates to the co-moving reference frame of the laser allows us to simplifies the problem. Once again we use $(\xi,\tau)=(x-v_gt,t)$ whith $v_g\equiv c\beta_g$ the effective group velocity of the laser pulse in the plasma. The derivatives are then given by $\partial_x=\partial_\xi$ and $\partial_t=\partial_\tau-c\beta_g\partial_\xi$. The front of the laser pulse is localized at $\xi=0$ and lies in the domain $\xi\leq 0$, hence, for $\xi\geq 0$ the plasma is unperturbed ($a_\perp=0, n_e=n_0, \beta_x=1, \gamma=1$). The Gauss law (2.181) and fluid equations (2.182, 2.185) become:

$$\frac{\partial^2\phi}{\partial\xi^2}=k_{pe}^2\left(\frac{n_e}{n_0}-1\right), \tag{2.187}$$

$$\frac{\partial}{\partial\xi}[(\beta_g-\beta_x)]n_e=\frac{1}{c}\frac{\partial n_e}{\partial\tau}, \tag{2.188}$$

$$\left[\frac{1}{c}\left(\frac{\partial}{\partial\tau}-c\beta_g\frac{\partial}{\partial\xi}\right)+\beta_x\frac{\partial}{\partial\xi}\right]p_x=\frac{\partial\phi}{\partial\xi}-\frac{1}{2\gamma}\frac{\partial\, a_\perp^2}{\partial\xi^2}. \tag{2.189}$$

We further assume that the electron plasma response is quasi-stationary in the co-moving frame ($\omega_{pe}\ll\omega_0$) such that $\partial_\tau\simeq 0$, which gives

$$\frac{\partial}{\partial\xi}[(\beta_g-\beta_x)n_e]=0, \tag{2.190}$$

$$(\beta_x-\beta_g)\frac{\partial p_x}{\partial\xi}=\frac{\partial\phi}{\partial\xi}-\frac{1}{2\gamma}\frac{\partial\, a_\perp^2}{\partial\xi^2}. \tag{2.191}$$

The longitudinal momentum equation can be recast in order to express energy conservation as in Eq. (2.170). Thanks to transverse momentum conservation Eq. (2.186), $\gamma^2=1+p_\perp^2+p_x^2=1+a_\perp^2+p_x^2$, leading to

$$-\beta_g\frac{\partial p_x}{\partial\xi}=\frac{\partial\phi}{\partial\xi}-\frac{1}{2\gamma}\frac{\partial\, a_\perp^2}{\partial\xi^2}+\frac{p_x}{\gamma}\frac{\partial p_x}{\partial\xi} \tag{2.192}$$

$$=\frac{\partial\phi}{\partial\xi}-\frac{1}{2\gamma}\frac{\partial}{\partial\xi^2}(a_\perp^2+p_x^2) \tag{2.193}$$

$$=\frac{\partial}{\partial\xi}(\phi-\gamma), \tag{2.194}$$

where the ponderomotive force is represented by the $-\partial_\xi\gamma$ term. Integration of the density equation (2.190) and the momentum equation (2.194) over the range $[\xi,+\infty[$ leads to:

$$\frac{n_e}{n_0}=\frac{\beta_g}{\beta_g-\beta_x}, \tag{2.195}$$

$$\gamma(1-\beta_g\beta_x)=1+\phi. \tag{2.196}$$

From these expressions we see that the density variation n_e/n_0 can reach infinity (due to the 1D geometry) when the electron velocity tends to the laser wave group velocity $\beta_x \to \beta_g$. The plasma fluid quantities (n_e/n_0, β_x, γ) are then governed by

$$\frac{n_e}{n_0} = \gamma_g^2 \beta_g \left[\left(1 - \frac{1+a_\perp^2}{\gamma_g^2 (1+\phi)^2} \right)^{-1/2} - \beta_g \right], \tag{2.197}$$

$$\beta_x = \gamma_g^2 (1+\phi) \left[\beta_g - \left(1 - \frac{1+a_\perp^2}{\gamma_g^2 (1+\phi)} \right)^{1/2} \right], \tag{2.198}$$

$$\gamma = \gamma_g^2 (1+\phi) \left[1 - \beta_g \left(1 - \frac{1+a_\perp^2}{\gamma_g^2 (1+\phi)} \right)^{1/2} \right], \tag{2.199}$$

where $\gamma_g = (1-\beta_g^2)^{-1/2}$. By injecting n_e/n_0 in Eq. (2.187) we finally obtain the nonlinear equation satisfied by the scalar potential ϕ as a function of the laser field $a_\perp$ [Akhiezer & Polovin 1956; Berezhiani & Murusidze 1992; Esarey *et al.* 1996]:

$$\frac{\partial^2 \phi}{\partial \xi^2} = k_{pe}^2 \gamma_g^2 \left[\beta_g \left(1 - \frac{1+a_\perp^2}{\gamma_g^2 (1+\phi)^2} \right)^{-1/2} - 1 \right]. \tag{2.200}$$

In general, this nonlinear equation must be solved numerically.

To close our equations system we must consider the evolution of the laser pulse into the plasma. The electromagnetic wave equation Eq. (2.12) can be recast in terms of the normalized vector potential $a_\perp$ leading to

$$\left(\frac{\partial^2}{\partial x^2} - \frac{1}{c^2} \frac{\partial^2}{\partial t^2} \right) a_\perp = k_{pe}^2 \frac{n_e}{n_0} \frac{p_\perp}{\gamma}. \tag{2.201}$$

In (ξ, τ) coordinates we obtain [Sprangle *et al.* 1990]:

$$\left(\frac{1}{\gamma_g^2} \frac{\partial^2}{\partial \xi^2} + \frac{2\beta_g}{c} \frac{\partial^2}{\partial \xi \partial \tau} - \frac{1}{c^2} \frac{\partial^2}{\partial \tau^2} \right) a_\perp = k_{pe}^2 \frac{n_e}{n_0} \frac{p_\perp}{\gamma}. \tag{2.202}$$

The effect of the plasma wave on the laser field is studied in more detail below. Note that the transverse momentum in the right-hand side is equal to the transverse potential vector only in a pre-ionized plasma ($p_\perp = a_\perp$ with zero boundary conditions) which is the case here.

If the plasma is very underdense we can assume $\beta_g \ll 1$, and simplify the plasma fluid and laser equations into [Esarey *et al.* 2009]:

$$\frac{n_e}{n_0} = \frac{1 + a^2 + (1+\phi)^2}{2(1+\phi)^2}, \tag{2.203}$$

$$\beta_x = \frac{1 + a^2 - (1+\phi)^2}{2(1+\phi)}, \tag{2.204}$$

$$\gamma = \frac{1 + a^2 + (1+\phi)^2}{2(1+\phi)}, \tag{2.205}$$

$$\frac{\partial^2 \phi}{\partial \xi^2} = \frac{k_{pe}^2}{2} \left[\frac{1+a^2}{(1+\phi)^2} - 1 \right], \tag{2.206}$$

$$\left(\frac{2}{c} \frac{\partial}{\partial \xi} - \frac{1}{c^2} \frac{\partial}{\partial \tau} \right) \frac{\partial a_\perp}{\partial \tau} = k_{pe}^2 \frac{a_\perp}{1+\phi}. \tag{2.207}$$

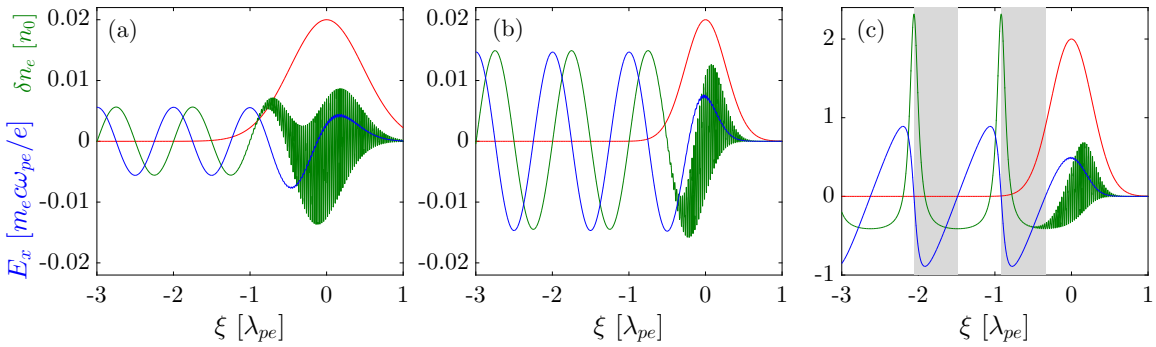

Figure 2.14: Longitudinal electric field (blue) and electron density perturbation (green) as obtained from the nonlinear equation (2.200) in a plasma with ambient density of 2.75×10^{18} cm^{-3} for different laser configurations (a) $a_0 = 0.2$ and $k_{pe}\sigma_0 = 2.12$, (b) $a_0 = 0.2$ and $k_{pe}\sigma_0 = 1.18$, and (c) $a_0 = 2$ and $k_{pe}\sigma_0 = 1.18$. The acceleration zone (in grey) corresponds to $E_x < 0$.

To make analytical progress, we assume a moderately relativistic laser field, $a_\perp \ll 1$, so that $\phi \ll 1$. Linearizing Eq. (2.206) gives:

$$\frac{\partial^2 \phi}{\partial \xi^2} + k_{pe}^2 \phi = k_{pe}^2 \frac{a_\perp^2}{2}. \tag{2.208}$$

This equation describes a forced harmonic oscillator, and can be readily solved as

$$\phi(\xi) = \frac{k_{pe}^2}{2} \int_\xi^{+\infty} a_\perp^2(\xi') \sin[k_{pe}(\xi - \xi')]\, d\xi'. \tag{2.209}$$

For a Gaussian laser pulse of FWHM τ_0 the resonance between the ponderomotive force and the plasma wave oscillations arises for $k_{pe}\sigma_0 \simeq 1$ where $\sigma_0 = c\tau_0/2\sqrt{2\ln 2}$. Figure 2.14 shows the solution of the nonlinear plasma wave equation for different laser configurations. For small amplitude ($a_0^2 \ll 1$) pulses with two different durations, the density perturbation remains small ($\delta n_e/n_0 \ll 1$). The wakefield $E_x = -\partial_\xi \phi$ has a harmonic profile oscillating over λ_{pe} with higher amplitude when resonance occurs [Fig. 2.14(a,b)]. If we increase the laser intensity above the relativistic threshold ($a_0 > 1$) the wakefield becomes sharper with a sawtooth-like shape [Fig. 2.14(c)]. The acceleration zone, where the E_x field is negative, has a length $\sim \lambda_{pe}/2$ (see grey areas). Note that the period of the plasma wave is longer, $2\pi/\omega_{pe} \to 2\pi\sqrt{\gamma}\ /\omega_{pe}$, because of the increased relativistic inertia of electrons.

The computed plasma wave is not able to describe the injection process since fluid quantities have been used throughout the derivation. Nevertheless we can study the acceleration of a test particle released in a preformed wakefield using a Hamiltonian approach in the (ξ, p_x) phase space. The Hamiltonian in normalized units reads as [Esarey & Pilloff 1995]:

$$H(\xi) = \sqrt{1 + a_\perp^2 + p_x^2} - \phi - \beta_g p_x, \tag{2.210}$$

where ϕ is obtained from solving Eq. (2.200) as a function of the (known) laser profile $a_\perp(\xi)$ Since the Hamiltonian depends only on ξ, it is conserved and so is the electron energy. As a result an electron with initial energy H_0 has a trajectory defined by

$$p_x(\xi) = \beta_g \gamma_g^2 (H_0 + \phi) \pm \gamma_g \sqrt{\gamma_g^2 (H_0 + \phi)^2 - (1 + a_\perp^2)}. \tag{2.211}$$

For the preceding case ($n_e = 2.5 \times 10^{-3} n_c$, $a_0 = 2$, $\tau = 30$ fs), Fig. 2.15 displays three different types of trajectory: fluid, separatrix and trapped orbits. An initially electron at rest has $p_\perp \equiv a_\perp = 0$, $p_x = 0$, $\phi = 0$ so that Eq. (2.210) corresponds to the fluid Hamiltonian value $H_{\rm flu} = 1$. These plasma background electrons follow the so-called fluid orbit and oscillate in the wakefield without being trapped (geen line). The separatrix orbit distinguishes untrapped from trapped orbits. It is defined by setting that the electron velocity equates the group velocity of the plasma wave ($\beta_x = \beta_g$) at the location of the minimum value of the potential $\phi(\xi_{\rm min}) = \phi_{\rm min}$. Thus the separatrix orbit has the Hamiltonian value:

$$H_{\rm sep} = \frac{\sqrt{1 + a_\perp^2(\xi_{\rm min})}}{\gamma_g} - \phi_{\rm min}. \tag{2.212}$$

The red line of Fig. 2.15 (bottom) shows the separatrix orbit which is closed. Blue dashed lines are trapped (closed) orbits corresponding to electrons with initial kinetic energy above the trapping threshold defined by [Faure 2016]

$$E_{\rm trap} = m_e c^2 (\sqrt{1 + p_{x,\rm sep}^2(\xi \to +\infty)} - 1). \tag{2.213}$$

This threshold is defined when the electron velocity is higher than the initial velocity corresponding to the separatrix orbit. Electrons just crossing the separatrix are injected into the plasma wave and gradually overtake it. By doing so they move away from the accelerating zone ($\phi = \phi_{\rm min}$) and decelerate, becoming out of phase with the plasma wave ($\phi = \phi_{\rm max}$). This takes place over a dephasing length for electrons equal to [Esarey *et al.* 2009]

$$L_{\rm deph} \approx \gamma_g^2 \lambda_{pe}. \tag{2.214}$$

The greater the dephasing length, the larger the energy gain for trapped electrons since $\Delta E = m_e c^2 \times 2\gamma_g^2(\phi_{\rm max} - \phi_{\rm min})$. For a typical plasma density of $n_e = 2.5 \times 10^{-3} n_c = 2.75 \times 10^1 8$ cm^{-3} and $\gamma_g = 20$, we get a dephasing length of about $L_{\rm deph} \approx 3$ mm such that electrons dephase slowly with respect to the plasma wave.

Injection and beam loading

Different schemes exist to inject electrons in a plasma wave. The simplest one is the so-called self-injection, which relies on the nonlinear evolution of the laser pulse in the plasma as a result of the wakefield generation and relativistic effects [Kalmykov *et al.* 2009]. These processes are induced in the refractive index of the plasma. Its expression is given by Eq. (2.82), modified by the γ factor following the relativistic description of $a_\perp$ [see Eq. (2.201)]:

$$\eta = \sqrt{1 - \frac{\omega_{pe}^2}{\omega_0^2 \gamma}}. \tag{2.215}$$

The influence of the plasma wave is accounted for in the plasma frequency. We define the total electron density as $n_e = n_e^0 + \delta n_e$, where n_e^0 is the unperturbed density and δn_e the density perturbation associated with the wakefield. The plasma frequency can be written as $\omega_{pe} = \omega_{pe,0}\sqrt{n_e/n_0}$ and the Lorentz factor is $\gamma = \sqrt{1 + a_\perp^2/2}$. In the limits $\omega_{pe,0} \ll \omega_0$, $a_0 \ll 1$

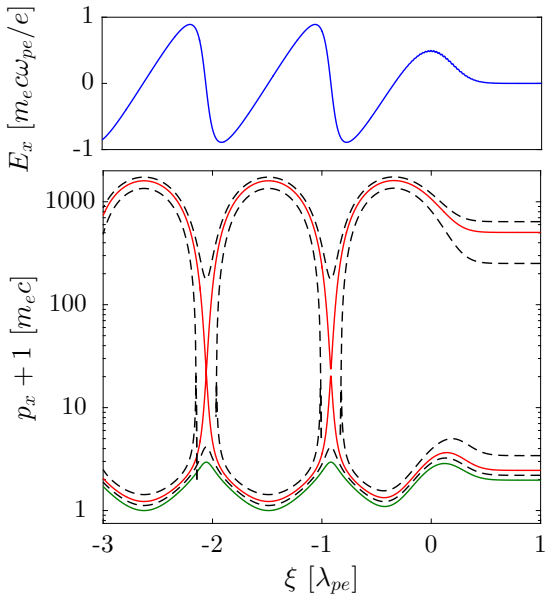

Figure 2.15: (Top) Wakefield in a pre-ionized plasma with an background electron density of 2.75×10^{18} cm^{-3} with laser parameters $a_0 = 2$ and $k_{pe}\sigma_0 = 1.18$ corresponding to a 30 fs pulse duration. (Bottom) Different electron trajectories in the phase space computed from Eq. (2.211). The fluid orbit is the green line, the separatrix is the red line.

and $\delta n_e \ll n_e^0$, successive Taylor expansions lead to [Esarey *et al.* 1996; Mori 1997]:

$$\eta = 1 - \frac{1}{2}\frac{\omega_{pe,0}^2}{\omega_0^2}\left(1 - \frac{\langle a_\perp^2 \rangle}{2} + \frac{\delta n_e}{n_0}\right). \tag{2.216}$$

The first source of nonlinearity is the density perturbation $\delta n_e/n_0$ induced by the laser ponderomotive force. Then the term in $\langle a_\perp^2 \rangle/2$ describes the variations of the relativistic electron inertia, where $\langle \cdot \rangle$ represents averaging over the fast laser oscillations. The phase velocity of the wave is $v_\phi = c\eta^{-1}$ such that it can be modulated by a change in either the density or the laser intensity profile.

Let us consider a laser pulse with a Gaussian transverse intensity profile of the form

$$a_\perp(\tau) = \left(\frac{a_0 w_0}{w(\tau)}\right)^2 \exp\left[-2\left(\frac{r}{w}\right)^2\right], \tag{2.217}$$

using the light-frame coordinates (ξ, τ). Hence, the laser intensity is maximum on-axis resulting in a local increase in the refractive index according to Eq. (2.216). The wave phase velocity is then altered ($v_\phi = c\eta^{-1}$) as illustrated in Fig. 2.16. The relativistic variations in v_ϕ over the laser waist w_0 cause the wave front to bend forward at an angle $\Delta\theta \simeq [v_\phi(w_0) - v_\phi(0)]\Delta t/w_0 \simeq -\partial w/\partial\tau$. Differentiating with respect to time and injecting the expression of v_ϕ, depending only on the relativistic term, yields the variation of the spot size as a result of relativistic self-focsuing:

$$\frac{\partial^2 w}{\partial \tau^2} = -\frac{1}{8}\frac{\omega_{pe}^2}{\omega_0^2}\frac{c^2}{w}a_0^2. \tag{2.218}$$

Moreover, the Gaussian beam is subject to diffraction such that the waist evolution is given by $w(\tau) = w_0\sqrt{1 + c^2\tau^2/Z_R^2}$, where $Z_R = k_0 w_0/2$ is the Raylength length. Differentiating twice

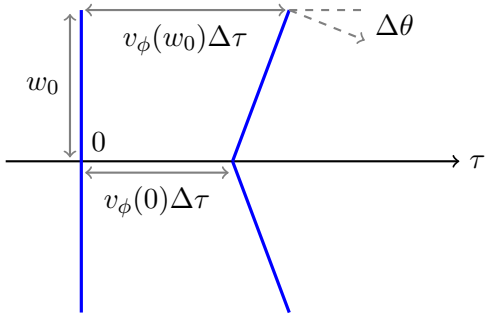

Figure 2.16: Scheme of relativistic self-focusing. The radial phase velocity difference causes the wave front to bend in high intensity region.

this evolution law, we obtain:

$$\frac{\partial^2 w}{\partial \tau^2} \approx \frac{4}{k_0^2 w_0^3}. \tag{2.219}$$

Combining Eqs. (2.218) and (2.219) gives the equation for the laser waist evolution:

$$\frac{\partial^2 w}{\partial \tau^2} = \frac{4}{k_0^2 w_0^3}\left(1 - \frac{a_0^2}{32}\frac{\omega_{pe}^2}{c^2}w_0^2\right), \tag{2.220}$$

so that self-focusing takes place if $a_0^2\omega_{pe}^2 w_0^2/32c^2 > 1$, which can be recast as a condition on the laser power

$$P > P_c\,[\mathrm{GW}] = 17(\omega_0/\omega_{pe})^2, \tag{2.221}$$

as demonstrated by Sun *et al.* [1987]; Sprangle *et al.* [1987] with more elaborated techniques. In addition, the density perturbation has an opposite sign in the expression of the refractive index such that it is defocusing where the plasma modulation is strong, that is to say on-axis. Therefore, it can balance the self-focusing effect in the front of the laser pulse. Laser self-focusing is primordial to accelerate electrons since it enables guided laser propagation over distances much larger than the Rayleight length, approaching the dephasing length associated with the maximum energies.

Moreover, when the laser spot size shrinks, the transverse ponderomotive force is increased expelling electrons further away from the propagation axis. This leads to a slow expansion of the electron depletion zone easing electron injection [Kalmykov *et al.* 2009; Yi *et al.* 2010; Kostyukov *et al.* 2010]. This corresponds to a regime where the separatrix is lowered and merges with the fluid orbit in the phase space, i.e., electrons are thus "self-injected". The plasma wave amplitude is then reduced since the negative charge produces a strong electrostatic field, and the separatrix goes up, leading to a self-regulated process.

Other injection techniques take advantage of the slowing down of the plasma wave phase velocity in downward density ramps [Bulanov *et al.* 1998; Geddes *et al.* 2008]. The accelerating zone increases, rendering easier the injection. One may also want to alter the electromagnetic force felt by electrons using a second laser pulse. Such colliding-beam setups [Umstadter *et al.* 1996; Esarey *et al.* 1997] have been shown to dramatically increase the amount of injected charge. Nevertheless the experimental difficulties (beam alignment) complicate their realization. Finally the injection by ionization allows electrons to be injected at a precise phase in the plasma wave [Pak *et al.* 2010; McGuffey *et al.* 2010; Chen *et al.* 2012]. They are freed at rest but above the separatrix (see Fig. 2.15) in order to be directly injected. This technique uses gas mixture of low and high Z gases (typically hydrogen and nitrogen) with percent level of high Z-gas

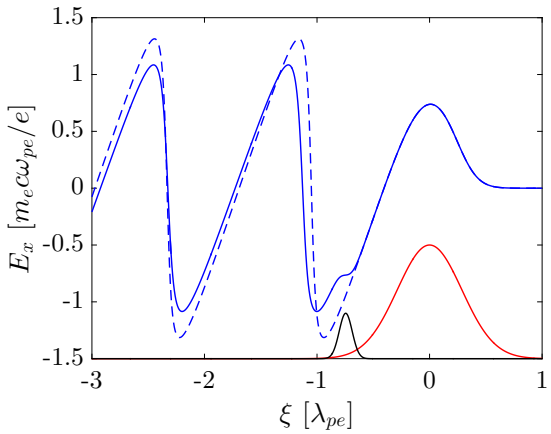

Figure 2.17: Solution of Eq. (2.222) taking into account the influence of beamloading. Red and black line are the laser envelope and the beam electron density, respectively. Blue lines is the longitudinal laser wakefield computed for negligible charge (dashed line) and for $n_b^0 = 0.4n_0$ (solid line). The duration of the laser pulse ($a_0 = 2$) and the electron beam are 16 fs and 2.6 fs, respectively. The background plasma density is set to 10^{19} cm^{-3}.

whose electrons will be freed at the maximum of the laser field when the plasma wave is already sustained by hydrogen electrons. In the following we will rely on self-injection and on the density down-ramp technique (at the exit of the plasma channel). Also since the THz generation involves ionization based mechanism, the injection by ionization may also occur. The injected electron population thus results in a mix between these different processes.

In addition to laser energy depletion and dephasing with the plasma wave, electron acceleration can be limited by the accelerated bunch itself. Indeed, electromagnetic fields created by this amount of charged particles is able to disrupt the longitudinal wakefield by forming a secondary wake. This effect, known as beamloading, limits naturally the electron energy gain. In order to demonstrate it, we resort to Eq. (2.200), augmented by an additional term $n_b(\xi)/n_0$ modeling the density of the accelerated beam:

$$\frac{\partial^2 \phi}{\partial \xi^2} = k_{pe}^2 \gamma_g^2 \left[\beta_g \left(1 - \frac{1 + a_\perp^2}{\gamma_g^2 (1+\phi)^2} \right)^{-1/2} - 1 \right] + \frac{n_b(\xi)}{n_0}. \tag{2.222}$$

Figure 2.17 shows the result of Eq. (2.222) for a Gaussian electron bunch with 2.6 fs duration and a density corresponding to $0.4n_0$. The original wakefield (dashed blue line) is modified by the presence of the electron beam. Electrons in the front experience the unperturbed field while those at the back are decelerated since the laser wake overlaps with the beam wake and neutralize the accelerating field. The overall result is a decrease in the total wakefield amplitude preventing further energy gain or particle injection.

3D scaling laws

By nature a LWFA is a three-dimensional process. The above 1D nonlinear analytical framework just provides first physical insights into the process. However, to predict accurately experimental behaviours, one has to resort to 3D simulations. Yet, state-of-the-art supercomputers can barely handle full 3D simulations. The laser-plasma community have tackled this issue by proposing scaling laws inferred from 2D PIC simulations and simplified models of specific acceleration regime. A ultrashort laser pulse with a normalized potential vector $a_0 \gg 1$ can ponderomotively

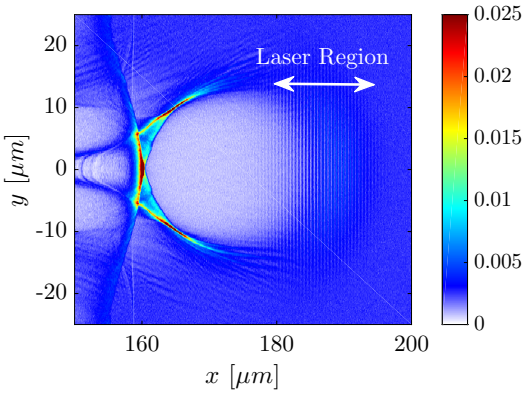

Figure 2.18: Snapshot of the electron density as computed by a 2D PIC simulation. The laser spatial extent is indicated by the double white arrow. The ambient plasma density is $n_e = 2.5 \times 10^{-3} n_c = 2.75 \times 10^{18}$ cm^{-3} interacting with a near-infrared ($\lambda_0 = 1$ μm) laser at $a_0 = 4$ amplitude ($I_0 = 2.2 \times 10^{19}$ W/cm^2).

expels all the electrons on is way, forming an ion cavity (see Fig. 2.18). If the spatial extent of the laser matches resonance conditions then the ion cavity is spherical: This is the so-called blow-out regime [Lu *et al.* 2006a,b, 2007] or bubble regime [Pukhov & Meyer-ter Vehn 2002; Gordienko & Pukhov 2005]. Electrons are eventually injected at the end of the ion cavity. In the following, we will base our analysis on the scaling laws given by Lu *et al.* [2007]. For an ultra-intense laser ($a_0 > 4$) a quasi-spherical ion cavity with radius R can be formed if the transverse ponderomotive force is balanced by the restoring force (this is a generalization of the 1D process presented below). This requires the following matching condition (inferred from 2D PIC simulations) to be fulfilled:

$$k_{pe} R \simeq k_{pe} w_0 = 2\sqrt{a_0}, \tag{2.223}$$

where w_0 is the FWHM intensity spot. This expression guarantees also good self-focusing conditions in the plasma since it can be recast as $a_0 \approx 2(P/P_c)^{1/3}$ (for Gaussian pulses). If we assume a spherical ion cavity completely depleted of electrons, the accelerating and focusing fields inside the cavity are given by the longitudinal and the transverse components of the Lorentz force:

$$E_{\text{acc.}} = \frac{E_x}{E_0} = \frac{k_{pe}\zeta}{2}, \tag{2.224}$$

$$E_{\text{foc.}} = \frac{E_r - cB_\theta}{E_0} = \frac{k_{pe} r}{2}, \tag{2.225}$$

where ζ is the distance from the center of the cavity and $E_0 = m_e c \omega_{pe}/e$. Hence, the injected electrons at the backside of the cavity ($\zeta = -R/2$) can be accelerated up to $\zeta = 0$. When electrons outrun the center of the bubble ($\zeta > 0$) they get decelerated. However the wakefield is always focusing for the confined electrons. Alternatively the laser can be depleted in energy due to the wakefield formation. The electron dephasing and laser depletion, which both limit the final energy acquired by the electron bunch, are characterized by two lengths, the dephasing length and the depletion length, respectively.

The laser front is depleted in energy by setting the electrons into motion, inducing the plasma wakefield. Based on 1D theory (hence neglecting diffraction effects), Decker *et al.* [1996]

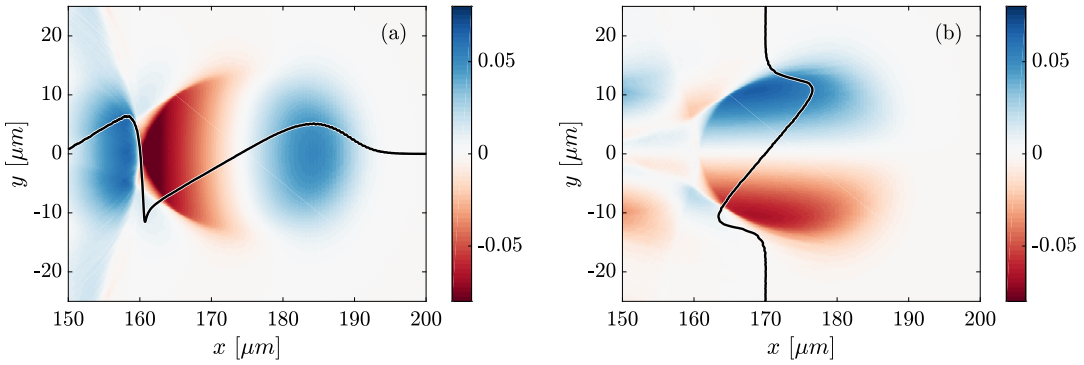

Figure 2.19: Same simulation and instant than Fig. 2.18. (a) Longitudinal field E_x $[m_e c\omega_0/e]$ (colormap) and on-axis profile (black line) of the electronic bubble. (b) Transverse force $E_y - cB_z$ $[m_e c\omega_0/e]$ (colormap) and transverse profile at $x = 170$ μm (black line).

computed the etching velocity of the laser front, $v_{\text{etch}} = c\omega_{pe}^2/\omega_0^2$ and therefore the laser depletion length,

$$L_{\text{depl}} = \frac{c}{v_{\text{etch}}} c\tau_0 = \frac{\omega_0^2}{\omega_{pe}^2} c\tau_0. \tag{2.226}$$

The effective phase velocity of the plasma wave is thus $v_{\text{wake}} = v_g - v_{\text{etch.}} = c(1 - 3\omega_{pe}^2/2\omega_0^2)$.

In the bubble model the dephasing length before trapped electrons outrun the wave differs from its 1D evaluation. It is given by the identity $cR = (c - v_{\text{wake}})L_{\text{deph}}$ leading to

$$L_{\text{deph}} = \frac{2\omega_0^2}{3\omega_{pe}^2} R. \tag{2.227}$$

As a result the acceleration distance is $L_{\text{acc}} = \min(L_{\text{depl}}, L_{\text{deph}})$. Alternatively, we can set these two characteristic lengths to be equal in order to optimize the process. Doing so, we find a second condition linking the transverse and the spatial extent of the laser:

$$c\tau_0 \simeq \frac{2}{3} R \simeq \frac{2}{3} w_0. \tag{2.228}$$

For an intense laser field ($a_0 > 2$), fulfilling Eqs. (2.223) and (2.228), we can extract a scaling law for the net energy gain acquired by the trapped electrons. Indeed the work developed by the accelerating field E_{acc} is:

$$\Delta E = e\langle E_{\text{acc}} \rangle L_{\text{acc}}, \tag{2.229}$$

with $\langle E_{\text{acc}} \rangle \approx E_{\text{acc}}/2$ being the mean value of the accelerating field. The latter is given by Eq. (2.224) which, combined to the blow-out matching condition Eq. (2.223), leads to [Lu *et al.* 2007]

$$\Delta E = m_e c^2 \frac{2}{3} \frac{\omega_0^2}{\omega_{pe}^2} a_0, \tag{2.230}$$

or equivalently,

$$\Delta E \text{ [GeV]} = 1.7 \left(\frac{P \text{ [TW]}}{100} \right)^{1/3} \left(\frac{10^{18}}{n_e \text{ [cm}^{-3}]} \right)^{2/3} \left(\frac{0.8}{\lambda_0 \text{ [}\mu\text{m]}} \right)^{4/3}. \tag{2.231}$$

In the self-injection process, the amount of accelerated charge is directly linked to the energy

carried by the plasma wave. For a large enough bubble ($k_{pe}R > 4$), one might expect:

$$Q\ [\mathrm{nC}] = 2.5 \times 10^9 \frac{\lambda_0\ [\mu\mathrm{m}]}{0.8} \sqrt{\frac{P\ [\mathrm{TW}]}{100}}. \tag{2.232}$$

The above scaling laws provide useful estimates for the expected acceleration length, final electron energy and charge in a specific regime. In the remainder of the manuscript they will be used to design simulations and give some general trends.

2.3 Transition Radiation

The previous sections presented conversion mechanisms of THz generation in the classical regime (Sec. 2.1) and the physics involved in the relativistic laser-gas interaction (Sec. 2.2). We now pass to the description of the main phenomenon studied during this PhD work, namely transition radiation. We first give a physical interpretation of this mechanism along with key parameters (Sec. 2.3.1). Then we consider the ideal situation in which a single electron crosses a perfect conductor-vacuum interface, as historically done (Sec. 2.3.2). We finally focus on a plasma-vacuum interface with general dielectric function $\epsilon(\omega) = 1 - \omega_{pe}^2/\omega^2$ for the plasma, which is the situation of physical interest when considering wakefield-accelerated electrons (Sec. 2.3.3).

2.3.1 Principle

Transition radiation (TR) has been theoretically predicted in 1945 by Ginzburg & Frank [1945]. This field emission arises when a charged particle with constant velocity goes across the boundary between two media having different optical properties (or dispersion relation). The radiation takes place toward both the front and the back sides of the interface. This theoretical prediction was experimentally demonstrated by Goldsmith & Jelley [1959]. They studied the TR emission of 5 MeV protons, generated by a Van de Graaf accelerator, impacting three different targets being aluminum, silver and gold. The transition radiation has been identified by plotting the measured energy yield as a function of the polarization orientation (dipole orientation) and of the proton energy (linear scaling). Since then, many theoretical works have been done considering arbitrary dispersive materials or dielectric constant properties [Garibian 1958], smooth boundary transitions [Galeev 1964; Lepore & Riddell 1976], finite-thickness media [Garibian & Chalikian 1958], the effect of multiple interfaces with periodic or arbitrary spacing [Bass & Yakovenko 1965] and even in a non-stationay medium [Ginzburg & Tsytovich 1974]. More information on these issues can be found in the reviews by Bass & Yakovenko [1965]; Ter-Mikaelian [1972]. From the application point of view, TR has been widely used as a diagnostic in the particle accelerator community, where it is commonly referred to as optical transition radiation (OTR), since its intensity is proportional to the γ factor of the charged particles [Dolgoshein 1993].

The TR effect can be understood in many different ways. We present some of them below and give a physical interpretation of the phenomenon. We consider the simplest situation in which an electron emerges from medium 1 into medium 2, e.g., from a metal to vacuum. Alternatively, one may want to rather study the electron going in the opposite direction (from vacuum to the metal boundary). As we will see later, both situations are equivalent. Generally, a single charged particle in constant motion near the speed of light is surrounded by an electrostatic field perceived in the laboratory frame as an electromagnetic field ($\mathbf{B} \neq \mathbf{0}$). We quickly recall the transformation of electromagnetic fields between two inertial frames. Let us define by $\mathcal{R}'(x', y', z', t')$ the co-moving frame traveling with the relativistic velocity v of an electron beam along the x axis.

$\mathcal{R}(x, y, z, t)$ is the fixed laboratory frame. Passing from the moving coordinate system to the fixed coordinate system expresses through the set of Lorentz-transformed variables:

$$x' = \gamma(x - vt) \tag{2.233}$$
$$y' = y \tag{2.234}$$
$$z' = z \tag{2.235}$$
$$t' = \gamma(t - vx/c^2) \tag{2.236}$$

and transforms the parallel (to the velocity direction) and the orthogonal electromagnetic field components into

$$E_{\parallel} = E'_{\parallel}, \tag{2.237}$$
$$B_{\parallel} = B'_{\parallel}, \tag{2.238}$$
$$\mathbf{E}_{\perp} = \gamma(\mathbf{E}'_{\perp} - \mathbf{v} \times \mathbf{B}'_{\perp}), \tag{2.239}$$
$$\mathbf{B}_{\perp} = \gamma(\mathbf{B}'_{\perp} + \mathbf{v} \times \mathbf{E}'_{\perp}/c^2). \tag{2.240}$$

The charge moves with v_e along the x axis and creates in its own frame the electrostatic field:

$$\mathbf{E}' = \frac{-e}{4\pi\epsilon_0}\frac{\mathbf{R}'}{R'^3}, \tag{2.241}$$
$$\mathbf{B}' = \mathbf{0}, \tag{2.242}$$
$$\mathbf{A}' = \mathbf{0}, \tag{2.243}$$
$$V' = \frac{-e}{4\pi\epsilon_0 r'}, \tag{2.244}$$

where $R' \equiv (x'^2 + y'^2 + z'^2)^{3/2}$. In the laboratory frame the field components express as [Jackson 1999]

$$E_x = \frac{-e}{4\pi\epsilon_0}\frac{x'}{R'^3} = \frac{-e}{4\pi\epsilon_0\gamma^2}\frac{x - vt}{[(x - vt)^2 + (1 - \beta^2)(y^2 + z^2)]^{3/2}}, \tag{2.245}$$
$$E_y = \gamma E'_y = \frac{-e}{4\pi\epsilon_0\gamma^2}\frac{y}{[(x - vt)^2 + (1 - \beta^2)(y^2 + z^2)]^{3/2}}, \tag{2.246}$$
$$E_z = \gamma E'_z = \frac{-e}{4\pi\epsilon_0\gamma^2}\frac{z}{[(x - vt)^2 + (1 - \beta^2)(y^2 + z^2)]^{3/2}}, \tag{2.247}$$

where $\beta = v/c$. Similarly the magnetic field components express as

$$B_x = 0, \tag{2.248}$$
$$B_y = -\frac{v}{c^2}(\gamma E'_x), \tag{2.249}$$
$$B_z = \frac{v}{c^2}(\gamma E'_y). \tag{2.250}$$

Equations (2.246) and (2.247) define the particle self-field (SF), i.e., the field attached to the particle. Note that the SF is not a radiated field with a classical $1/R$ amplitude decay as it decays rapidly in $1/R^2$ (see Chapter 3) [Jackson 1999]. As a charged particle travels in the first medium, its SF excites adjacent volumes on the way inducing a time-dependent polarization, for a dielectric, or a time-dependent current, for an ionized medium. As already underlined, the time derivative of the polarization and the current are the source terms of the Maxwell equations.

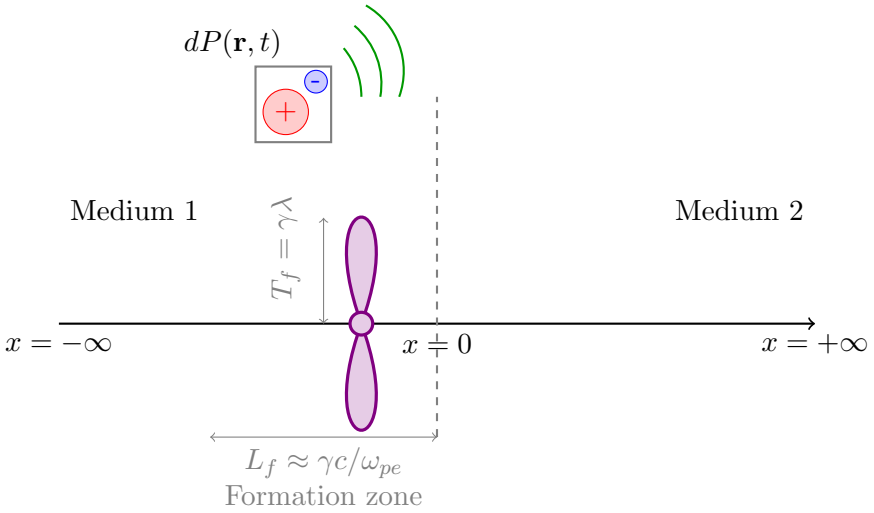

Figure 2.20: Scheme of the transition radiation mechanism. The particle self-field (violet) excites around its path a small volume. The time-dependent polarization emits a dipole-like radiated field. Over the formation length L_f, the emission by sub-volumes add coherently leading to the transition radiation at the boundary $x = 0$ separating medium 1 from medium 2.

Thus radiations are emitted in the neighborhood of the particle path. When approaching the boundary $x = 0$, the radiations emitted by different points in space sum up coherently and build up the TR field.

The length over which phase coherence occurs and promotes an efficient field emission is the formation length L_f. It is defined by setting the phase difference between two emitting points A and B equal to 2π [see Fig. 2.21]. By doing so we have:

$$|\phi_A - \phi_B| = |kL_f \cos\theta - \omega t| = |\frac{\omega}{c}\sqrt{\epsilon(\omega)}L_f \cos\theta - \frac{\omega}{v}L_f| \tag{2.251}$$

$$= L_f \frac{\omega}{c}|\sqrt{\epsilon(\omega)} - \frac{1}{\beta}| = 1\ [2\pi], \tag{2.252}$$

such that:

$$L_f(\omega) = \frac{\beta\omega/c}{1 - \beta\sqrt{\epsilon(\omega)}\cos\theta}. \tag{2.253}$$

In the case of a perfect conductor $\epsilon \to -\infty$, the formation length tends to zero. In contrast, when considering a plasma with finite permittivity, $\epsilon(\omega) = 1 - \omega_{pe}^2/\omega^2$, the formation length is significantly increased. In this case we can simplify the expression of the formation length by assuming a relativistic motion. By doing so we consider that $\beta^{-1} \approx 1 + 1/2\gamma^2$ so that we obtain:

$$L_f(\omega) = \frac{2\gamma c}{\omega_{pe}} \frac{1}{\frac{\omega}{\gamma\omega_{pe}} + \frac{\gamma\omega_{pe}}{\omega}}, \tag{2.254}$$

which admits a maximum in $\omega = \gamma\omega_{pe}$. In the rest of the manuscript we will consider the formation length null when dealing with perfect conductor or metallic foil. For plasma-vacuum interface we will take the upper limit of the formation length

$$L_f^{\max} \approx \gamma c/\omega_{pe}. \tag{2.255}$$

As demonstrated by Yuan *et al.* [1970] for GeV positron beams on aluminium foils, TR is lowered when the foil thickness is smaller than the formation length. Hence one must ensure that the

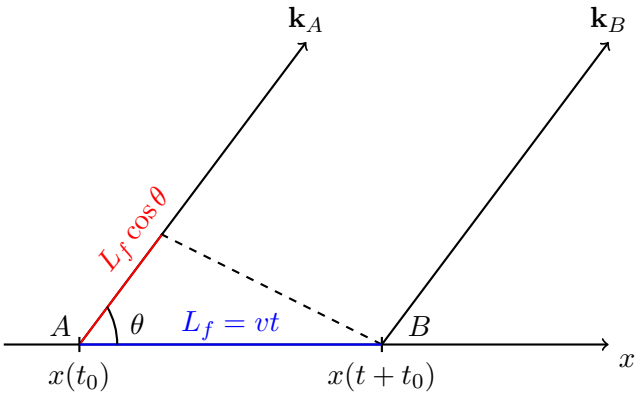

Figure 2.21: Wave coming from point A at $t = t_0$ and interfering with the wave emitted in point B at $t = t + t_0$. Coherence occurs for $|\phi_A - \phi_B| = 1\ [2\pi]$.

distance propagated by the particle corresponds, at least, to the formation length.

The excitation of the surrounding medium by the particle self-field is limited by the transverse extent of the field which is given by $T_f = \gamma\lambda$ where λ is the considered radiated wavelength. Hence for low frequency emission, i.e. long wavelength, this distance is usually greater than the transverse size of the plasma channel and does not affect the transition radiation itself. However the particle self-field can be subject to diffraction if the interface presents a finite transverse extent. In this case one should add a function modeling the diffraction in the TR formula and reducing the amplitude of the latter [Schroeder *et al.* 2004]. In the rest of the manuscript we do not consider diffraction for the sake of simplicity, since it is a second-order correction to the ideal case.

In the following we always consider a sharp interface, meaning that the period $T = 2\pi/\omega$ of the emitted wave is small in comparison to the formation time $t_f = L_f/v$. After crossing the interface the particle SF adapts itself to the new permittivity and the TR expands as a spherical wave. TR theories seek to determine the radiated energy per solid angle (Ω) per angular frequency (ω) in the far field. The energy collected by solid angle unit is:

$$\frac{d\mathcal{E}}{d\Omega} = c\epsilon_0 R^2 \int_{-\infty}^{+\infty} \mathbf{E}_{\text{rad.}}^2 \, dt \tag{2.256}$$

where $\mathbf{E}_{\text{rad.}}$ is the radiated field. By using the inverse Fourier transform of the radiated field and interchanging time and frequency integration (Parseval's theorem) we obtain:

$$\frac{d\mathcal{E}}{d\Omega} = c\epsilon_0 R^2 \int_{-\infty}^{+\infty} \widehat{\mathbf{E}}_{\text{rad.}}^2 \, d\omega. \tag{2.257}$$

This quantity can be recovered in various situations and, after integration, leads to the total radiated energy by TR. In the next two sections we study two cases of interest. The first one is academic and considers a single particle emerging normally from a perfect conductor into vacuum. We make use of the charge image method [see Fig. 2.23] to find the radiated energy as done in the pioneering work by Ginzburg & Frank [1945]. In the second case, we derive the radiated energy due to a single electron going from medium 1 to medium 2 with arbitrary permittivity before applying it to the plasma-vacuum interface as established by Garibian [1958]. We finally consider the effect of a bunch of electrons, as created in laser-plasma accelerators, on the emitted radiation.

2.3.2 Perfect boundary and charge image method

It is well-known that a single charged particle with constant velocity does not radiate: It has to accelerate ($\dot{\beta}$) or follow a curvilinear trajectory (synchrotron radiation) to emit a $(\mathbf{E}, \mathbf{B})$ fields according to [Jackson 1999]:

$$\mathbf{E}(\mathbf{r}, t) = \frac{-e}{4\pi\epsilon_0} \left\{ \left[\frac{\mathbf{n} - \boldsymbol{\beta}}{\gamma^2 (1 - \boldsymbol{\beta} \cdot \mathbf{n})^3 R^2} \right]_{\text{ret.}} + \frac{1}{c} \left[\frac{\mathbf{n} \times \{(\mathbf{n} - \boldsymbol{\beta}) \times \dot{\boldsymbol{\beta}}\}}{(1 - \boldsymbol{\beta} \cdot \mathbf{n})^3 R} \right]_{\text{ret.}} \right\}, \tag{2.258}$$

$$\mathbf{B} = [\mathbf{n} \times \mathbf{E}]_{\text{ret.}}, \tag{2.259}$$

where "ret." means that the quantity is evaluated at the retarded time $t' = t - R/c$ with $R \equiv |\mathbf{r} - \mathbf{r'}|$ being the distance between the moving source point and the observer and $\mathbf{n}$ is a unit vector in the radiation direction (see Fig. 2.22). The first term is usually called "velocity field" and the second the "acceleration field" because the former depends on $\boldsymbol{\beta}$ and the latter on the time derivative $\dot{\boldsymbol{\beta}}$. Since they fall as R^{-2}, velocity fields are considered as static (non-propagating) fields, in contrast to the R^{-1} decaying acceleration fields, which are considered as radiative and are able to propagate far away. In short, the electron SF belongs to the first category and TR to the second one. Surprisingly, even if the particle has a constant velocity ($\dot{\boldsymbol{\beta}} = \mathbf{0}$) a radiated field can still appear at the interface.

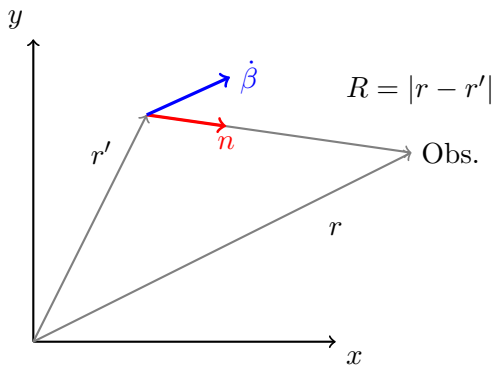

Figure 2.22: Scheme of a charged particle in acceleration motion along $\dot{\boldsymbol{\beta}}$ with position $\mathbf{r'}$ and radiating in the $\mathbf{n}$ direction. The observer is located at position $\mathbf{r}$. The distance between the moving source and the observer is $\mathbf{R} \equiv |\mathbf{r} - \mathbf{r'}|$.

In the case of a perfect conductor-vacuum interface, this apparent contradiction is not relevant since, from the observer point of view, the electron field is completely screened before emerging from the conductor. However, just after the boundary, the observer sees the sudden appearance of a moving charge with $\boldsymbol{\beta}$ hence $\dot{\boldsymbol{\beta}} \neq \mathbf{0}$ and Eq. (2.258) correctly describes TR with $\boldsymbol{\beta}(t') = \boldsymbol{\beta}_0 H(t' - t_0)$ with H denoting the Heaviside function and t_0 the interface-crossing instant. One can retain only the radiation term to compute the TR field. However surface currents on the interface ensuring the neutralization of internal fields in the escape plane of the charged particles are not taken into account. This shielding effect is modeled by the image charge method, according to which the induced current on the surface radiates exactly like an "imaginary" particle of opposite charge and propagating in the opposite direction [see Fig. 2.23(b)].

Therefore, here, one has to consider a suddenly moving pair of particles, i.e. electron-positron, to model (i) the sudden appearance of the exiting electron and (ii) ensure correct boundary conditions (vanishing fields parallel to the surface). In this framework, let us imagine an incident electron with charge e and velocity $\mathbf{v}_{e,1} = \mathbf{0}$ in the perfect conductor and $v_{e,2} = v\mathbf{e}_x$

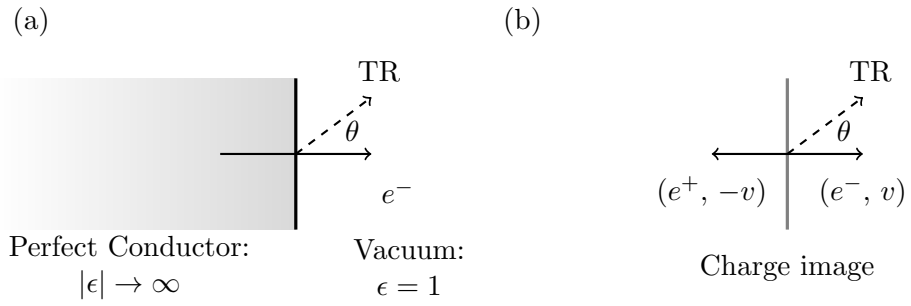

Figure 2.23: Schemes of TR calculation where we consider (a) a perfect conductor-vacuum interface crossed by a single electron emitting TR in the θ direction and (b) the charge image formalism satisfying the boundary conditions at the interface between the two media.

in vacuum and, similarly, a positron with charge $-e$ with velocity $v_{p,1} = -v\mathbf{e}_x$ before and $\mathbf{v}_{p,2} = \mathbf{0}$ after the interface. The radiated energy, computed from Eqs. (2.257), (2.258), gives [Ginzburg 1982, 1964; Bae & Cho 2015]:

$$\frac{d^2\mathcal{E}}{d\Omega d\omega} = \frac{1}{16\pi^3\epsilon_0 c^3}\left[\sum_{i=\{e,p\}} q_i\left(\frac{\mathbf{v}_{i,2}\times\mathbf{n}}{1-\mathbf{n}\cdot\beta_{i,2}} - \frac{\mathbf{v}_{i,1}\times\mathbf{n}}{1-\mathbf{n}\cdot\beta_{i,1}}\right)\right]^2, \tag{2.260}$$

with $\mathbf{n}$ the unit vector in the radiated direction. The above expression simplifies into:

$$\frac{d^2\mathcal{E}}{d\Omega d\omega} = \frac{1}{16\pi^3\epsilon_0 c^3}\left[e\left(-\frac{v\sin\theta}{1-\beta\cos\theta}\right) + e\left(\frac{-v\sin\theta}{1-\beta\cos\theta}\right)\right]^2 \tag{2.261}$$

$$= \frac{e^2}{4\pi^3\epsilon_0 c}\frac{\beta^2\sin^2\theta}{(1-\beta^2\cos^2\theta)^2}. \tag{2.262}$$

This approach is the classical one proposed by Ginzburg & Frank [1945]. Equation (2.262) is the well-known radiated energy of an electron going out of a perfect conductor. The symmetry of the image charge problem shows that the reverse situation, e.g. an electron going from vacuum to the metal, can be described in the same way. We see that the radiated energy is not a function of the frequency ω since we consider a point-like particle with a zero acceleration time setting no time scale. Therefore, all frequencies are present with equal strength. In practice, the emitted radiation is limited by the physical dimension of the source (for instance an electron bunch accelerated by laser wakefield). Figure 2.24(a) represents the angular distribution for different γ value. Just like other radiations emitted by relativistic particles (Cherenkov radiation or synchrotron radiation [Jackson 1999]) the field vanishes on axis. Also the maximum emission is given for $\sin\theta \sim 1/\gamma$ as expected. An integration over the solid angle $d\Omega = \sin\theta d\theta d\phi$ yields [Ginzburg 1982; Schroeder *et al.* 2004]

$$\frac{d\mathcal{E}}{d\omega} = \frac{e^2}{4\pi^2\epsilon_0 c}\left(\frac{1+\beta^2}{2\beta}\ln\frac{1+\beta}{1-\beta} - 1\right). \tag{2.263}$$

As shown by Fig. 2.24(b) the integration of Eq. (2.262) in θ (blue line) follows a logarithmic law (red dashed line).

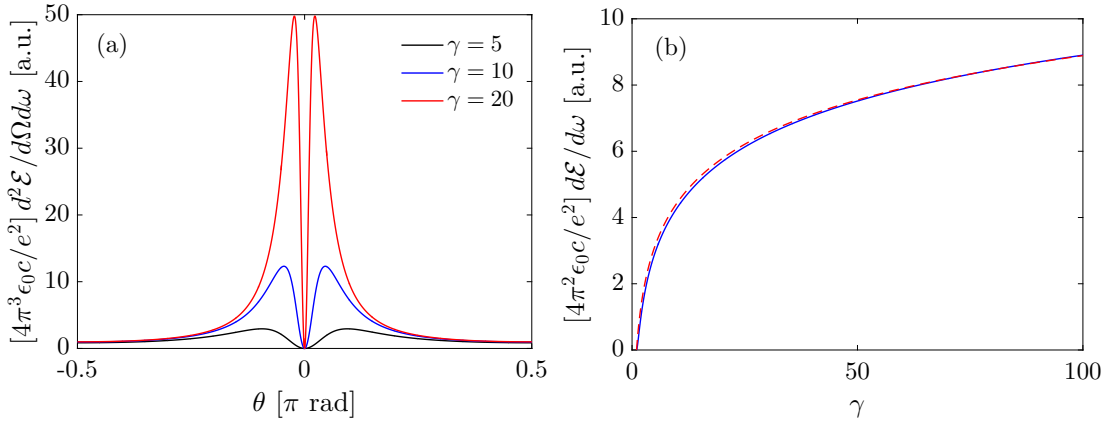

Figure 2.24: (a) Angular emission of TR according to Eq. (2.262) emitted by an electron exiting a perfect conductor for different γ factor. (b) Integration over θ angle of the radiated energy (blue line) with a $\ln(\gamma)$ law (red dashed line).

2.3.3 Transition radiation by plasma-vacuum interface

In order to treat more realistic scenarios, one needs to solve Maxwell equations in the two media and impose matching boundary conditions. We now consider the transition between two media with arbitrary permittivity ϵ_1 and ϵ_2. A single electron coming from infinity in medium 1 along the x axis is accompanied by its SF resulting from the heterogeneous solution of Maxwell's equations in medium 1. Similarly, after crossing the interface and far from it, the same electron in medium 2 will be surrounded by its SF modified by the change in the medium permittivity. To connect these two fields at the interface, boundary conditions must be satisfied: the tangential component of $\mathbf{E}$ and the normal component of $\mathbf{D}$ have to be continuous. Obviously these conditions cannot be verified by the particle's field alone. We have to add an homogeneous solution which, by definition, is a radiated field. Mathematically, the TR is the homogeneous solution needed to satisfy boundary conditions at the interface between two media. This resolution method has been proposed by Garibian [1958], the complete derivation is performed in Appendix B for the interested reader. Here we give only the major steps for its calculation:

(1) Find the heterogeneous solution corresponding to the particle self-field,

(2) Express a homogeneous solution in Fourier domain with unknown coefficient,

(3) Apply boundary conditions to the total field in order to determine the Fourier component of the homogeneous field,

(4) Compute the Fourier integral of the radiated field (homogeneous solution) using an asymptotic Bessel expansion and the saddle point method,

(5) Express the radiated energy thanks to Eq. (2.257).

Let us proceed with the first step. The heterogeneous solution is given by the propagation equation in which a specified current mimics the electron motion $\mathbf{J} = e\mathbf{v}\delta(\mathbf{r} - \mathbf{v}t)$. Maxwell's

equations in real domain are:

$$\nabla \times \mathbf{H}_{1,2} = \frac{\partial \mathbf{D}_{1,2}}{\partial t} + e\mathbf{v}\delta(\mathbf{r} - \mathbf{v}t), \tag{2.264}$$

$$\nabla \times \mathbf{E}_{1,2} = \frac{\partial \mathbf{B}_{1,2}}{\partial t}, \tag{2.265}$$

$$\nabla \cdot \mathbf{B}_{1,2} = 0, \tag{2.266}$$

$$\nabla \cdot \mathbf{D}_{1,2} = e\delta(\mathbf{r} - \mathbf{v}t), \tag{2.267}$$

where subscript 1, 2 refers to medium 1 and medium 2, respectively. We define the spatial Fourier transform as:

$$\mathbf{E}_{1,2}(\mathbf{r}, t) = \int \mathbf{E}_{1,2}(\mathbf{k}, t) e^{i(\mathbf{k}\cdot\mathbf{r} - \omega t)} d^3\mathbf{k} \tag{2.268}$$

with $\omega = \mathbf{k} \cdot \mathbf{v} = k_x v$, $\mathbf{D}_{1,2} = \epsilon_{1,2}(\omega)\mathbf{E}_{1,2}$ and $\mathbf{B}_{1,2} = \mu_{1,2}(\omega)\mathbf{H}_{1,2}$. By combining Maxwell's equations we obtain the propagation equation:

$$\nabla^2 \mathbf{E}_{1,2} - \nabla(\nabla \cdot \mathbf{E}_{1,2}) = \chi_{1,2} \frac{\partial^2 \mathbf{E}_{1,2}}{\partial t^2} + \mu_{1,2} e\mathbf{v} \frac{\partial \delta(\mathbf{r} - \mathbf{v}t)}{\partial t} \tag{2.269}$$

with $\chi_{1,2} = \epsilon_{1,2}\mu_{1,2}$. We solve the equation in Fourier domain, leading to:

$$\mathbf{E}_{1,2}(\mathbf{k}, \omega) = \frac{ie}{(2\pi)^3} \frac{1}{\epsilon_{1,2}} \frac{\omega\chi_{1,2}\mathbf{v} - \mathbf{k}}{k^2 - \omega^2\chi_{1,2}}, \tag{2.270}$$

with the magnetic field:

$$\mathbf{H}_{1,2} = \frac{\mathbf{k} \times \mathbf{E}_{1,2}}{\mu_{1,2}\omega}. \tag{2.271}$$

The electric field (2.270) does not satisfy the continuity equations at the interface $x = 0$. As done previously, we express the homogeneous solution $\mathbf{E'}_{1,2}$ in both medium through its Fourier component such that:

$$\mathbf{E'}_{1,2}(\mathbf{r}, t) = \int \mathbf{E'}_{1,2}(\mathbf{k}) e^{i(\mathbf{k}\cdot\mathbf{r} - \omega t)} d^3\mathbf{k} \tag{2.272}$$

$$= \int \mathbf{E'}_{1,2}(\mathbf{k}) e^{i(\boldsymbol{\kappa}\boldsymbol{\rho} + k_z z - \omega t)} d^3\mathbf{k} \tag{2.273}$$

$$= \int \mathbf{E'}_{1,2}(\mathbf{k}) e^{i(\boldsymbol{\kappa}\boldsymbol{\rho} + \lambda_{1,2} x - \omega t)} d^3\mathbf{k} \tag{2.274}$$

with $\mathbf{r} = (\boldsymbol{\rho}, x)$, $\mathbf{k} = (\boldsymbol{\kappa}, k_x)$ and $\lambda_{1,2}^2 = \omega^2\chi_{1,2} - \kappa^2$. The magnetic field of the radiation is then given by:

$$\mathbf{H}_{1,2} = \frac{\mathbf{k} \times \mathbf{E}_{1,2}}{\mu_{1,2}\omega} = \frac{1}{\mu_{1,2}\omega}(\boldsymbol{\kappa} + \lambda_{1,2}\mathbf{n}) \times \mathbf{E}_{1,2}, \tag{2.275}$$

where $\mathbf{n}$ is the unit vector parallel to the radiated field direction.

We can now apply the continuity equations at $x = 0$ to the tangential component of $\mathbf{E}$ and the normal component of $\mathbf{D}$ (no surface charge density). In the following subscript t (resp. n) will denote the tangential (resp. normal) component of a given field. Hence we have,

$$\begin{cases} \mathbf{E_{t}}_1 + \mathbf{E'_{t}}_1 = \mathbf{E_{t}}_2 + \mathbf{E'_{t}}_2 \\ D_{n1} + D'_{n1} = D_{n2} + D'_{n2}. \end{cases} \tag{2.276}$$

Our goal is to express $\mathbf{E'_{1t}}$. However, two independent equations are missing. The ho-

mogeneous Maxwell equation $\nabla \cdot \mathbf{E'}_{1,2} = 0$ writes in Fourier space $\mathbf{k} \cdot \mathbf{E'}_{1,2} = 0$, leading to $\boldsymbol{\kappa}\mathbf{E'_{1,2t}} + sign(\mathcal{R}e\,[\lambda_{1,2}])\lambda_{1,2}E'_{1,2n} = 0$. Assuming that the $\boldsymbol{\kappa}$ vector is parallel to $\mathbf{E'_{1,2t}}$, we get two additional equations:

$$\begin{cases} \kappa E'_{1t} - \lambda_1 E'_{1n} = 0 \\ \kappa E'_{2t} + \lambda_2 E'_{2n} = 0 \end{cases} . \tag{2.277}$$

We can now solve the two systems (2.276) and (2.277) for the transverse radiated field in medium 1. After a few computations [see Eq. (B.33) of Appendix B] the solution reads as:

$$E'_{1t} = \frac{ie}{(2\pi)^3}\frac{\kappa\lambda_1}{\xi}\eta, \tag{2.278}$$

with

$$\xi = \lambda_1\epsilon_2 + \lambda_2\epsilon_1, \tag{2.279}$$

and

$$\eta = \left(\frac{\frac{\epsilon_2}{\epsilon_1} - \lambda_2\frac{v}{\omega}}{k^2 - \omega^2\chi_1}\right) + \left(\frac{-1 + \lambda_2\frac{v}{\omega}}{k^2 - \omega^2\chi_2}\right). \tag{2.280}$$

The normal field in medium 1 is easily found thanks to the previous relations (2.277) [see also Eq. (B.36) in Appendix B]:

$$E'_{1n} = -\frac{\kappa}{\lambda_1}E'_{1t} = -\frac{ie}{(2\pi)^3}\frac{\kappa^2}{\xi}\eta. \tag{2.281}$$

Radiation fields in the second medium can be obtained by interchanging subscripts 1 and 2. Note that the radiation field vanishes if we set $\mu_1 = \mu_2$ and $\epsilon_1 = \epsilon_2$. From now on we consider the case in which medium 1 is a plasma with permittivity $\epsilon_1 = \epsilon(\omega) = 1 - \omega_{pe}^2/\omega^2$, and medium 2 is vacuum with $\epsilon_2 = 1$. The solution in real domain can be obtained by inserting the Fourier component into Eq. (2.274). To do so the integration in the spectral plane is performed through the saddle point method [Bender & Orszag 1999]. At the end of the process one eventually gets the transverse field in medium 2 since it is the field of interest:

$$E'_{t,2} = \frac{e\beta^2}{4\pi\epsilon_0 vR}\int \sin\theta\cos^2\theta\xi e^{i\omega(R/c-t)}d\omega \tag{2.282}$$

with

$$\xi = \frac{1}{\epsilon\cos\theta + \sqrt{\epsilon - \sin^2\theta}} \times \left(\frac{\epsilon + \beta\sqrt{\epsilon - \sin^2\theta}}{1 - \beta^2\cos^2\theta} - \frac{1}{1 - \beta\sqrt{\epsilon - \sin^2\theta}}\right), \tag{2.283}$$

while the normal component of the radiated field is:

$$E'_{n,2} = \frac{e\beta^2}{4\pi\epsilon_0 vR}\int \sin^2\theta\cos\theta\xi e^{i\omega(R/c-t)}d\omega. \tag{2.284}$$

The total radiated field in vacuum is:

$$E'_2 = E'_{t,2}\cos\theta + E'_{n,2}\sin\theta = \frac{e\beta^2}{4\pi\epsilon_0 vR}\int \sin\theta\cos\theta\xi e^{i\omega(R/c-t)}d\omega \tag{2.285}$$

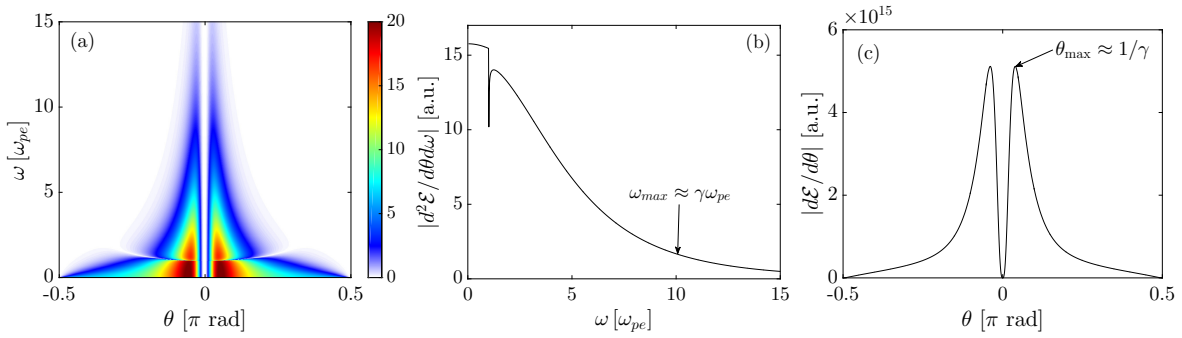

Figure 2.25: (a) Radiated energy per angle unit ($d\theta$) and per angular frequency unit ($d\omega$) given by Eq. (2.286), with $d\Omega = 2\pi \sin\theta d\theta$, for $\gamma = 10$ and a plasma density of $n_0 = 10^{18}$ cm^{-3}. The ω dependency is solely due to the plasma permittivity $\epsilon(\omega) = 1 - \omega_{pe}^2/\omega^2$. (b) Cut for $\theta = \theta_{max} \approx 1/\gamma$. The spectral content extends up to approximately $\omega_{max} \approx \gamma\omega_{pe}$ while a discontinuity occurs for $\omega = \omega_{pe} \to \epsilon = 0$. (c) Angular distribution of the radiated energy after integration over the frequencies ω.

Finally, by using Eq. (2.257) we obtain the radiated energy [Garibian 1958]:

$$\frac{d^2\mathcal{E}}{d\Omega d\omega} = \frac{e^2}{4\pi^3\epsilon_0 c}\frac{\beta^2\sin^2\theta\cos^2\theta}{(1-\beta^2\cos^2\theta)^2} \times \left|\frac{(\epsilon-1)(1-\beta^2-\beta\sqrt{\epsilon-\sin^2\theta})}{(\epsilon\cos\theta+\sqrt{\epsilon-\sin^2\theta})(1-\beta\sqrt{\epsilon-\sin^2\theta})}\right|^2 . \tag{2.286}$$

Formula (2.286) describes the radiated energy in the wave zone, far from the interface. Thus in the spatial region close to the particle trajectory where the radiation is in formation, this expression does not give the right evaluation. The vacuum-plasma case can be simply obtained by replacing β by $-\beta$ whereas the perfect conductor-vacuum situation is recover when, after factorization, one takes the limit $|\epsilon| \to \infty$. Note that the radiated energy is proportional to the dielectric constant difference squared $|\epsilon - 1|^2$ such that the TR is stronger for steep permittivity step. The radiated field is radially polarized for a normally incident particle since the material response has a radial symmetry along the particle path. The TR field oscillates in the radiation plane defined by the target normal direction and the observation direction. For an arbitrary incident particle the TR field has a component normal to the radiation plane [Ter-Mikaelian 1972]. This property can be used as a diagnostic to estimate the divergence or the dynamics of an electron beam at the rear side of a foil irradiated by an intense laser [Bellei *et al.* 2010, 2012; Liao *et al.* 2016b].

As an example Fig. 2.25(a) shows the radiated energy distribution resolved in angle and in frequency for an electron with $\gamma = 10$ emerging from a plasma with an ambient density of $n_0 = 10^{18}$ cm^{-3}. The spectral extention is roughly given by $\gamma\omega_{pe}$ as illustrated by Fig. 2.25(b) for $\theta = \theta_{max} \approx 1/\gamma$. Thus for the considered density the upper spectral limit is $\gamma\omega_{pe} \sim 100$ THz. Higher energetic electrons will lead to optical transition radiation or even X-ray emission [Garibian 1971]. The spatial distribution still presents extinction along the propagation axis ($\theta = 0$) while it is peaked for $\theta_{\max} \sim 1/\gamma$ [see Fig. 2.25(c)].

2.3.4 Coherence effect for electron bunch

Electromagnetic fields created by an electron beam are obtained by the superposition of point particle field expressions. The radiated energy derived so far is valid for one electron. In practice accelerated particles are bunched and they exhibit a certain spatial extent. We can deal with this issue by multiplying the radiated energy per particle by the Fourier transform of the particle

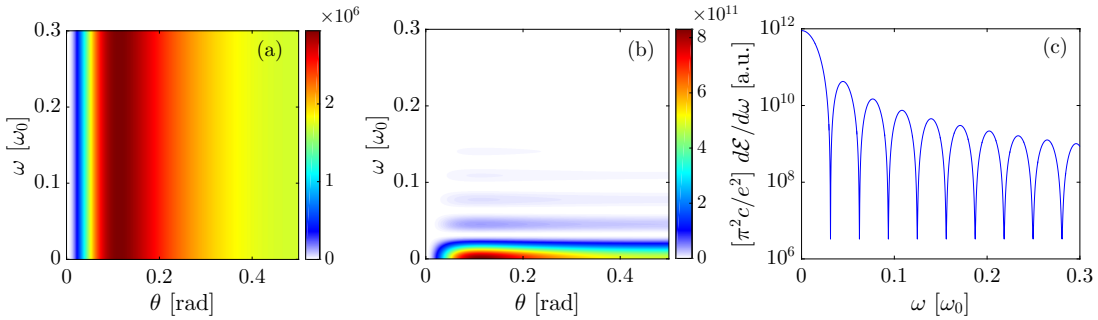

Figure 2.26: Radiated energy per solid angle unit ($d\Omega$) and per angular frequency unit ($d\omega$) for $\gamma = 10$ and a bunch length of $L_b = 3$ μm for (a) the incoherent part and (b) the coherent part of the radiation Eq. (2.289). (c) Integration over the θ angle of the total radiated intensity (incoherent and coherent contributions). Note that $\omega_0 = 2\pi c/\lambda_0$ with $\lambda_0 = 1$ μm.

bunch distribution as suggested in Zheng *et al.* [2002, 2003] and Schroeder *et al.* [2004]. For an electron bunch with length L_b composed of N_e electrons and zero transverse size, this is equivalent to consider the succession of electrons along the length L_b. Each of them will radiate a TR field with a given phase. Their radiations add coherently for radiated wavelength longer than L_b, otherwise the radiation is incoherent. We thus distinguish the coherent transition radiation (CTR) proportional to N_e^2 and affected by the bunch form factor, from the incoherent transition radiation (ITR) which is only proportional to N_e:

$$\frac{d^2\mathcal{E}_{\mathrm{CTR}}}{d\Omega d\omega} = N_e(N_e-1)\frac{e^2}{4\pi^3\epsilon_0 c}\frac{\beta^2\sin^2\theta}{(1-\beta\cos^2\theta)^2}\times\int d\omega F_{//}(\omega)F_{\perp}(\omega), \tag{2.287}$$

$$\frac{d^2\mathcal{E}_{\mathrm{ITR}}}{d\Omega d\omega} = N_e\frac{e^2}{4\pi^3\epsilon_0 c}\frac{\beta^2\sin^2\theta}{(1-\beta\cos^2\theta)^2}, \tag{2.288}$$

$$\frac{d^2\mathcal{E}}{d\Omega d\omega} = \frac{d^2\mathcal{E}_{\mathrm{CTR}}}{d\Omega d\omega}+\frac{d^2\mathcal{E}_{\mathrm{ITR}}}{d\Omega d\omega} = N_e\frac{e^2}{4\pi^3\epsilon_0 c}\frac{\beta^2\sin^2\theta}{(1-\beta\cos^2\theta)^2}\left[1+(N_e-1)\int d\omega F_{//}(\omega)F_{\perp}(\omega)\right] \tag{2.289}$$

where $F_{//}(\omega)$ and $F_{\perp}(\omega)$ are the Fourier transforms of the longitudinal and transverse electron bunch distribution, respectively.

Figure 2.26 shows an example of the radiated energy for a 3 μm rectangular electron bunch with a γ factor of 10. The incoherent contribution [Fig. 2.26(a)] is ω-independent since, as it is the case for the single electron calculation, no time scale is introduced. The coherent contribution displays higher intensity values due to the additional $(N_e - 1)$ factor and spectral oscillations occur [Fig. 2.26(b)]. The latter are due to the Fourier transform of the bunch form factor. Indeed a rectangular shape corresponds to a sinc function in Fourier space. Integration over θ angle clearly identifies the oscillation period corresponding to the inverse of the bunch length $2\pi c/L_b$ [Fig. 2.26(c)]. In the Garibian formula (2.286) the ω dependency is imposed by the dielectric function of the plasma whereas, here, it is imposed by the dimension of the electron bunch. Note that if the perfect conductor assumption does not apply, we can also compute the TR of an electron packet with the Garibian formula.

Conclusion

This Chapter has provided a concise summary of the involved physics for the generation of THz pulses either in classical or relativistic regime. We thus pointed out general processes (Kerr

effect, photocurrents, laser wakefield, transition radiation) having a crucial, direct or indirect, role in THz emission.

We first began by presenting the propagation equation of an electric field in a partially ionized medium. Two approaches were retained, the standard wave equation [Eq. (2.22)] and the unidirectional pulse propagation equation (UPPE) [Eq. (2.32)]. Their source terms, namely Kerr effect and photocurrents, were derived and their contribution to the generation of low frequencies have been demonstrated. Then, an analytical framework encompassing the two propagation models, with the nonlinear source terms, was derived to study the influence of the unidirectional approximation on the THz generation. We showed that both approaches exhibit similar spectral signature once the propagated distance reaches a few plasma skin depth. We thus validated the use of UPPE type equations for theoretical studies and interpretations of experiments.

The next section focused on laser-gas interactions in the relativistic regime. The Vlasov equation [Eq. (2.122)] governing the plasma dynamics was presented as well as the PIC code CALDER used during this PhD work. After deriving the nonlinear equation satisfied by the wakefield, we described the processes of electron trapping and acceleration by means of a Hamiltonian approach. We finally gave a 3D description of the laser wakefield accelerator concept with some of its limitations.

In this context, an alternative THz generation scheme, proposed by Leemans *et al.* [2003], relies on the radiated field emitted by a charged particle crossing the interface between two media having different optical properties. This so-called transition radiation has been extensively studied in the particle accelerator community to design particle detectors. We gave a rapid review of the theory in two situations of interest: the perfect conductor-vacuum interface and the plasma-vacuum interface. We also underlined the effect of coherent emission due to the spatial extent of the wakefield-accelerated electron bunch.

Chapter 3

Coherent Transition Radiation for the generation of THz pulses

Contents

This chapter deals with THz emission in relativistic underdense plasmas. First, in Section 3.1, the photocurrent model for THz pulse generation is extended to the coupling with the nonlinear wakefield dynamics. Simulating two-color ultra-intense pulses, we describe in 1D plasma geometry the photocurrent-induced radiation (PIR) in relativistic regime and report new periodic bursts of THz emission occurring at the relativistic plasma frequency along the laser polarization axis. Then, Section 3.2 compares the result of this model to 3D PIC simulations in the LWFA scenario and emphasizes the 3D features impacting the plasma bubble dynamics. We also demonstrate that transition radiation induced by wakefield-accelerated electrons is a relevant THz emission mechanism. A parametric study testing the robustness of this mechanism is assessed in Section 3.3 for an electron density increased from under- to near-critical levels, keeping a constant product between the latter and the plasma length.

3.1 Photocurrent model in the relativistic regime

The photocurrent model for THz generation in classical regime has been described in Section 2.1.3 and a semi-analytical formulation of the radiated field has been given in Section 2.1.5 for either the wave equation or the UPPE. We now seek a solution of the electromagnetic transverse field radiated from a relativistic laser pulse propagating in an underdense plasma and triggering a nonlinear plasma wake as studied in Section 2.2. Within a 1D quasi-static description, we first propose to couple the photocurrent-induced radiation (PIR) with the nonlinear plasma wave and taking into account the rate equations for the ion species. The plasma wave is numerically solved in terms of momenta and plugged as the source term into the PIR formula. The related fluid system is derived in Section 3.1.1 while the PIR field integrated in Section 3.1.2 will be exploited in Section 3.2.

3.1.1 Nonlinear plasma waves in the quasi-static approximation

We consider an underdense gas with neutral density n_a^0. At relativistic intensities (high fields), atoms are rapidly ionized along the propagation of the ultra-intense laser pulse, so that the nonlinearities associated to bounded electrons are inefficient and thus the Kerr effect can be fairly neglected. Over the short interaction time scale considered (~ 100 fs) the ions are viewed as immobile. Collisional as well as thermal effects are discarded due to the relativistic motion of electrons and to the short pulse duration leading to negligible heating, respectively. Under these assumptions we can make use of the density and momenta conservation equations accounting for ionization given by Eqs. (2.123), (2.126):

$$\partial_t n_e + \nabla(n_e \mathbf{v}) = S_{\text{ext}}, \tag{3.1}$$

$$\partial_t \mathbf{p} + (\mathbf{v}\cdot\nabla)\mathbf{p} = -e\left(\mathbf{E} + \frac{\mathbf{p}}{\gamma m_e}\times\mathbf{B}\right) - \frac{\mathbf{p}}{n_e}S_{\text{ext}}, \tag{3.2}$$

where we recall that $S_{\text{ext}} = \sum j\partial_t n_i^{(j)}$ is the ionization term resulting from the solution of the ion evolution system (2.61), (2.63). Again, we restrict our model to one spatial dimension being the propagation axis x while the laser is assumed linearly polarized in the y direction. We also consider $E_z = 0$ such that $(\mathbf{E},\mathbf{B}) = (E_x, E_y, B_z)$. After projection over the longitudinal and transverse direction we obtain:

$$\partial_t n_e + \partial_x(n_e v_x) = S_{\text{ext}}, \tag{3.3}$$

$$\partial_t p_x + v_x\partial_x p_x = -e\left(E_x + \frac{p_y}{\gamma m_e}B_z\right) - \frac{p_x}{n_e}S_{\text{ext}}, \tag{3.4}$$

$$\partial_t p_y + v_x\partial_x p_y = -e\left(E_y - \frac{p_x}{\gamma m_e}B_z\right) - \frac{p_y}{n_e}S_{\text{ext}}. \tag{3.5}$$

Then we adopt a perturbative approach assuming that the radiated field δE_y is small in front of the laser field E_y^L. In term of potentials and by using the Coulomb gauge $\nabla\cdot\mathbf{A} = \partial_x A_x = 0 \rightarrow A_x = 0$, the electromagnetic field components are given by:

$$\mathbf{E} = \begin{pmatrix} E_x \\ E_y^L + \delta E_y \\ E_z \end{pmatrix} = \begin{pmatrix} -\partial_x\Phi \\ -\partial_t A_y^L - \partial_t \delta A_y, \\ 0 \end{pmatrix}. \tag{3.6}$$

If we inject this decomposition into the momenta equations we get:

$$\partial_t p_x + \frac{p_x}{\gamma m_e}\partial_x p_x = -e\left(-\partial_x \Phi + \frac{p_y}{\gamma m_e}\partial_x A_y\right), \tag{3.7}$$

$$n_e\left(\partial_t p_y + \frac{p_x}{\gamma m_e}\partial_x p_y\right) = -e n_e\left(-\partial_t A_y - \frac{p_x}{\gamma m_e}\partial_x A_y\right) - p_y S_{\text{ext}}. \tag{3.8}$$

where we neglect the influence of ionization in the longitudinal momentum equation p_x. Photoionization is indeed supposed to be negligible for near-infrared laser [Chen *et al.* 2012] as for $\lambda_0 = 0.8 - 1$ μm a relativistic amplitude with laser intensity of about 10^{19} W/cm^2 triggers ionization in the beginning of the laser pulse where the vector potential is small. This contribution will be taken into account in the next chapter where CO_2 lasers will be considered. Once again it is convenient to change the coordinate system in the laser reference frame ($\xi = x - ct, \tau = t$) assuming plasma quantities remaining function of ξ only. Here we suppose that $v_g \approx c$ since an underdense plasma ($\omega_{pe} \ll \omega_0$) is considered. The (x, t) derivatives are given by $\partial_x = \partial_\xi$ and $\partial_t = \partial_\tau - c\partial_\xi$, respectively. The quasi-static approximation, $\partial_\tau = 0$, is thus applied to the fluid quantities for which it remains valid when we consider an unperturbed laser with slow electron oscillations ($\omega_{pe} \ll \omega_0$) [Sprangle *et al.* 1990]. After this change of coordinates, the momenta equations read as:

$$\left(\frac{p_x}{\gamma m_e c} - 1\right)\partial_\xi p_x = \frac{e}{c}\left(\partial_\xi \Phi - \frac{p_y}{\gamma m_e}\partial_\xi A_y^L\right), \tag{3.9}$$

$$n_e\left(\frac{p_x}{\gamma m_e c} - 1\right)\partial_\xi p_y = e n_e\left(\frac{p_x}{\gamma m_e c} - 1\right)\partial_\xi A_y^L - \frac{p_y S_{\text{ext}}}{c}. \tag{3.10}$$

where $\partial_\xi A_y \approx \partial_\xi A_y^L$ is computed with the laser field only as we assume a weak radiated field. Dividing by $m_e c$ allows us to use normalized quantities $p_i/m_e c \to p_i$, $e\Phi/m_e c^2 \to \phi$ and $eA_y^L/m_e c \to a_y^L$ to re-express the above equation set as:

$$\left(\frac{p_x}{\gamma} - 1\right)\partial_\xi p_x = \partial_\xi \phi - \frac{p_y}{\gamma}\partial_\xi a_y^L, \tag{3.11}$$

$$\partial_\xi(p_y - a_y^L) = -\frac{p_y}{c n_e\,(p_x/\gamma - 1)} S_{\text{ext}}, \tag{3.12}$$

with $S_{\text{ext.}} = \sum_j j\partial_t n_i^{(j)} = -c\sum_j j\partial_\xi n_i^{(j)}$. We remark that, unlike the derivation established in Chapter 2, the canonical transverse momentum is not conserved any longer due to the photoionization source term $S_{\text{ext.}}$. Electrons acquire a residual transverse momentum equal to the laser vector potential at the ionization instant. This additional transverse momentum is then kept by the particle [see Eq. (2.184)]. The Lorentz factor $\gamma = \sqrt{1 + p_x^2 + p_y^2}$ couples the longitudinal and transverse momentum such that Eqs. (3.11) and (3.12) form a coupled and closed system which can be numerically solved for a given laser profile a_y^L. The ionization system Eqs. (2.61), (2.63), computed with the multiple ionization ADK rate [Eq. (2.60)], gives the ion densities for the photoionization source term S_{ext} and the electron density n_e needed in Eq. (3.12). The latter is obtained thanks to the conservation equation (3.3) in the (ξ, τ) frame subject in turn to the quasi-static approximation:

$$-\partial_\xi n_e + \partial_\xi \frac{n_e p_x}{\gamma m_e c} = -\sum_{j=1}^{Z} j\partial_\xi n_i^{(j)}, \tag{3.13}$$

which, after integration over ξ in terms of the previous normalized quantities, leads to:

$$n_e = \frac{\sum_{j=1}^{Z} j n_i^{(j)}}{1 - p_x/\gamma}. \tag{3.14}$$

The numerator describes the steplike increase of the electron density in the ionization front that directly enters the plasma frequency $\omega_{pe}^0 = \sqrt{e^2 n_e^0/\epsilon_0 m_e}$ with

$$n_e^0 = \sum_j j n_i^{(j)}. \tag{3.15}$$

This last quantity also defines the ionization degree $Z^* = n_e^0(\xi \to -\infty)/n_a^0$. The denominator is responsible for the density oscillations imposed by the plasma wave such that, for strong enough p_x, the denominator tends to 0 and density spikes occur periodically over the relativistic plasma period $\omega_{pe}^0/\sqrt{\gamma}$.

Eventually the last needed quantity is the scalar potential ϕ of the plasma wave modeling the ion restoring force (Coulomb potential) in Eq. (3.11). Poisson equation expresses as

$$\partial_x E_x = -\partial_x^2 \Phi = \frac{e(n_z^0 - n_e)}{\epsilon_0}, \tag{3.16}$$

or equivalently in ξ coordinates as

$$\partial_\xi^2 \phi = \frac{\omega_{pe}^2}{c^2} \frac{p_x}{\gamma - p_x}. \tag{3.17}$$

The longitudinal electrostatic field E_x is straightforwardly inferred from $E_x = -\partial_\xi \Phi$. The plasma wave system is composed of the ionization system (2.61), (2.63), the momenta equations (3.11), (3.12) and the scalar potential equation (3.17). It is solved by a 4^{th}-order Runge-Kutta solver for a given set of laser-plasma parameters. The numerical solution of this computation step provides the transverse momentum p_y and the electron density oscillations n_e/γ which are necessary to find out the semi-analytical radiated transverse field derived in the next Section.

Figure 3.1 shows illustrative solutions of Eqs. (3.11), (3.14) and (3.17) for three laser intensities ($\lambda_0 = 1$ μm, $\tau_0 = 20$ fs) increased from classical to relativistic regime. The initial gas cell is composed of helium with a neutral density of $n_a^0 = 5 \times 10^{-3} n_c \approx 5.5 \times 10^{18}$ cm^{-3}. The second electronic shell of helium is ionized for a laser intensity higher than $I_0 = 8.78 \times 10^{15}$ W/cm^2 (see Fig. 2.3) corresponding to the ionization potential $U(\text{He}^{2+}) = 54.4$ eV. Therefore, the first laser intensity considered is set to $I_0 = 1.4 \times 10^{16}$ W/cm^2 ($a_0 = 0.1$) in Fig. 3.1(a, b, c) in order to extract all electrons from helium (He) while staying below the relativistic intensity threshold. In this situation the oscillations of the longitudinal momentum p_x remains very small [see Fig. 3.1(a)] and the plasma wave E_x exhibits a harmonic profile [see Fig. 3.1(b)] as underlined in Section 2.2. Figure 3.1(c) clearly displays the steplike increase of the electronic density with the two sequential ionizations, ensuring that helium atoms are fully ionized ($Z^* = 2$). The characteristic oscillation period is $\lambda_{pe} = 2\pi\sqrt{n_c/n_e} = 62.8\, c\omega_0^{-1}$ with the unperturbed electron density $n_e \approx n_e^0$ due to the weak wakefield.

Then we increase the laser intensity to the relativistic limit $I_0 = 1.4 \times 10^{18}$ W/cm^2 ($a_0 = 1$) in Fig. 3.1(d,e,f). The longitudinal momentum and plasma wave amplitudes become enhanced by a factor 50. However, in this marginally relativistic regime, plasma oscillations are barely affected by relativistic effects and the oscillations still remain linear [see Fig. 3.1(d,e)]. Nevertheless,

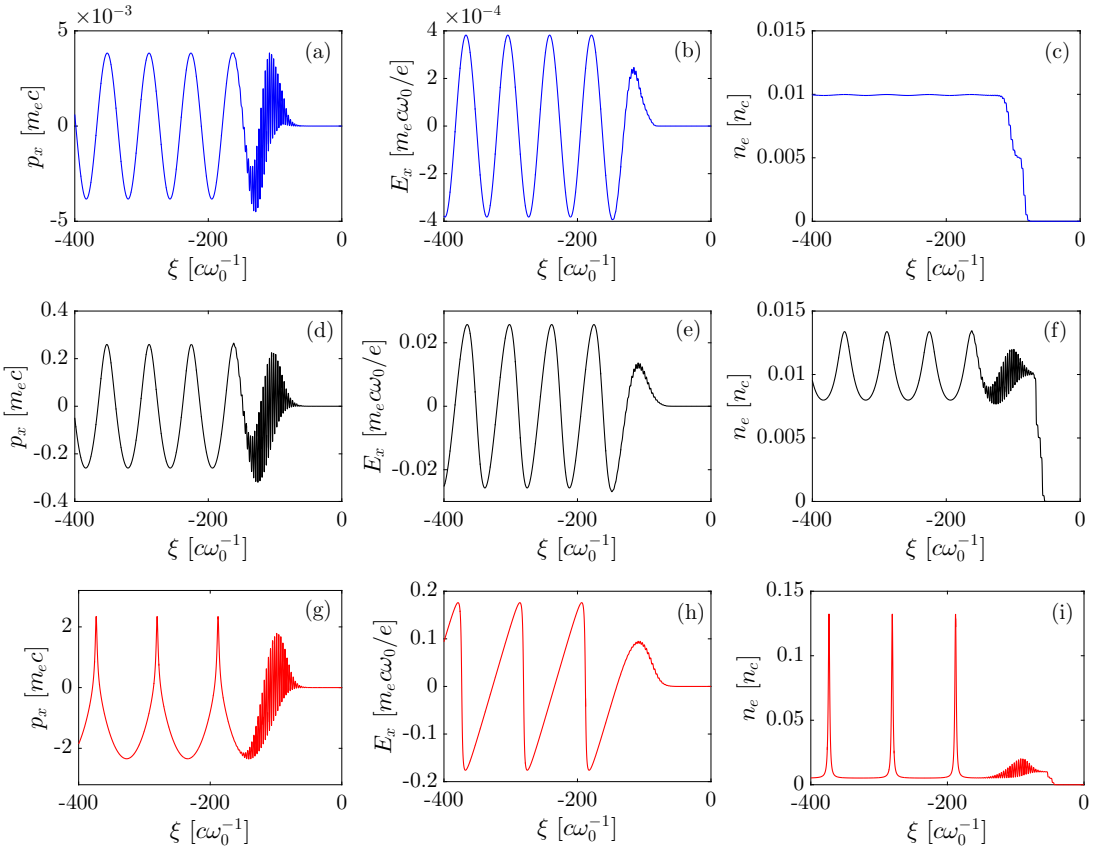

Figure 3.1: Solution of the plasma wave system [Eqs. (3.11), (3.14), (3.17)] for a Gaussian laser profile with central wavelength $\lambda_0 = 1$ μm and FWHM duration of $\tau_0 = 20$ fs in a gas cell of helium with atomic density $n_a^0 = 5 \times 10^{-3} n_c \approx 5.5 \times 10^{18}$ cm^{-3}. Displayed quantities are the longitudinal momentum p_x, the longitudinal plasma wave E_x and the electron density n_e for laser intensities of (a, b, c) 1.4×10^{16} W/cm^2 ($a_0 = 0.1$), (d, e, f) 1.4×10^{18} W/cm^2 ($a_0 = 1$) and (g, h, i) 2.2×10^{19} W/cm^2 ($a_0 = 4$).

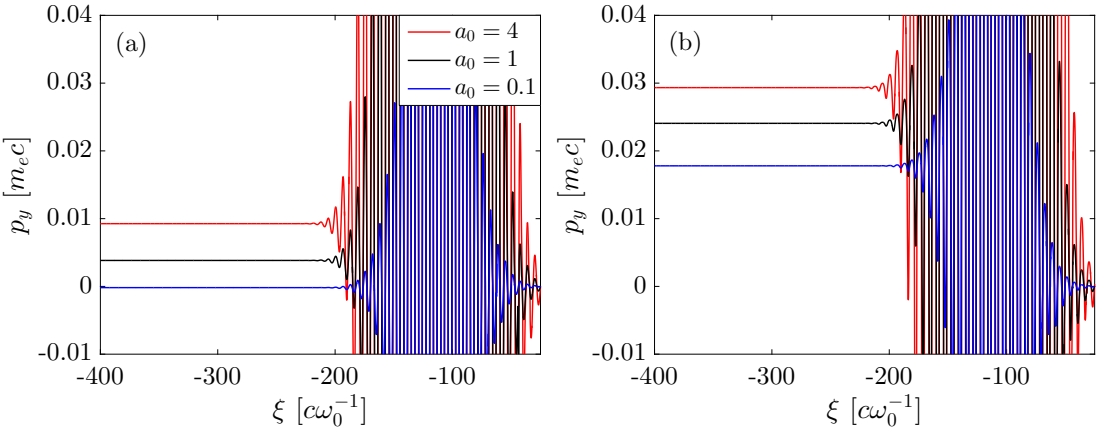

Figure 3.2: Residual transverse momentum p_y for the three normalized laser amplitudes $a_0 = 0.1$ (blue line), $a_0 = 1$ (black line), $a_0 = 4$ (red line) for (a) single-color and (b) two-color laser pulse.

as the wakefield is strengthened, the density fluctuations represented by the denominator of Eq. (3.14) are no longer negligible. Also ionization occurs earlier in the pulse profile such that freed electrons oscillate at $2\omega_0$ in the laser field due to the fast component of the ponderomotive force.

Next, when exceeding significantly the relativistic threshold with $I_0 = 2.2 \times 10^{19}$ W/cm^2 ($a_0 = 4$), relativistic effects fully develop [Figs. 3.1(g,h,i)]. The longitudinal phase space exhibits non-sinusoidal oscillations with peaked values in the forward direction ($p_x > 0$) and relativistic motions since $p_x > 1\, m_e c$ [see Fig. 3.1(g)]. Similarly the plasma wave adopts a sawtooth-like shape featuring a nonlinear plasma wave with a longer period $\lambda_{pe}\sqrt{\gamma}$ for which $\gamma \simeq 4$ [see Fig. 3.1(h)]. This effect can be interpreted as a relativistic mass increase of electrons lowering the plasma frequency $\omega_{pe}/\sqrt{\gamma}$. Such plasma wave creates high electron density regions and is able to accelerate electrons once the injection process occurs. With such strong intensity, the laser field is three orders of magnitude higher than the ionization field threshold such that atoms are stripped from their electrons in the early front part of the laser pulse. Density spikes reach ten times the ambient density at the relativistic plasma period [see Fig. 3.1(i)].

Figure 3.2 displays the transverse momentum p_y for the three laser intensities (see legend) in the case of single-color and two-color laser pulse. Due to ionization electrons gradually acquire finite momentum offsets which are conserved after the laser passage. These residual momenta logically increase when the peak laser intensity is augmented [Fig. 3.2(a)]. When a two-color laser pulse is employed, the low-frequency part of the current is clearly enhanced trough the product $n_e v_y$, as demonstrated in Section 2.1.3. Consequently the residual momentum is drastically augmented, particularly for $a_0 = 0.1$ underlying the weak dependency on the overall laser intensity [Fig. 3.2(b)]. This saturation effect in intensity is mainly due to the limited number of ionization sequences. When increasing $a_0 \to 4$, helium atoms are rapidly stripped from their electrons, full ionization is completed and the photocurrent source is no longer fed by additional ionization-induced transverse momentum.

Knowing the characteristics of the plasma wave for a given laser pulse, we can extract by perturbation a solution for the transverse radiated field.

3.1.2 Solution for the transverse radiated field

The propagation equation of the vector potential in a plasma subject to complete ionization can be derived, as in Section 2.2.2, by using Eqs. (2.3), (2.4) expressed in terms of the vector

potential. We obtain, similarly to Eq. (2.201),

$$(\partial_x^2 - c^{-2}\partial_t^2)A_y = -\mu_0 J_y \tag{3.18}$$

with $J_y = -en_e v_y = -en_e p_y/\gamma$. As done in the classical regime (Sec. 2.1.5), we split the transverse field A_y into the laser and radiated fields and assume that the former is unperturbed during its propagation such that

$$(\partial_x^2 - c^{-2}\partial_t^2)A_y^L = 0. \tag{3.19}$$

The transverse momentum can also be split into a zero order term accounting for the transverse momentum induced by the laser vector potential and the discrete ionization events, supplemented by a perturbation which is assumed to be equal to the radiated vector potential

$$p_y = p_y^0 + \delta p_y = p_y^0 + e\delta A_y^L. \tag{3.20}$$

Equation (3.18) thus reads as

$$(c^2\partial_x^2 - \partial_t^2)\delta A_y = \frac{e}{\epsilon_0 m_e}\frac{n_e}{\gamma}(p_y^0 + e\delta A_y). \tag{3.21}$$

Our objective is to solve Eq. (3.21) in order to find a solution for $\delta A_y(x,t)$.

In the (ξ,τ) coordinate system, Eq. (3.21) becomes

$$-\partial_\tau^2\delta A_y + 2c\partial_{\xi,\tau}^2\delta A_y = \frac{e}{\epsilon_0 m_e}\frac{n_e}{\gamma}(p_y^0 + e\delta A_y)\,, \tag{3.22}$$

with $\gamma = \sqrt{1 + (p_x^2 + p_y^2)/m_e^2c^2}$. For a laser pulse sited in the half-plane $x < ct$ (i.e., $\xi < 0$) and entering the plasma at time $t = 0$, the initial conditions are $\delta A_y(\tau, \xi = 0) = \delta A_y(\tau = 0, \xi) = 0$. We make use of the Laplace transform in time (τ) defined as

$$\mathcal{LT}[f] = \widetilde{f}(u,\xi) = \int_0^\infty f(\tau,\xi)\mathrm{e}^{-u\tau}d\tau \tag{3.23}$$

which allows, with our initial conditions, to express derivatives with respect to τ as

$$\mathcal{LT}\left[\partial_\tau\delta A_y\right] = u\widetilde{\delta A}_y - \delta A_y(\tau = 0,\xi) = u\widetilde{\delta A}_y \tag{3.24}$$

$$\mathcal{LT}\left[\partial_\tau^2\delta A_y\right] = u^2\widetilde{\delta A}_y - u\delta A_y(\tau = 0,\xi) - \partial_\tau\delta A_y(\tau = 0,\xi) = u^2\widetilde{\delta A}_y\,. \tag{3.25}$$

Applying to Eq. (3.22) and recalling that $\mathcal{LT}\left[\text{const.}\right] = \text{const.}/u$, we find:

$$\partial_\xi\widetilde{\delta A}_y - \frac{1}{2cu}\left(u^2 + \frac{e^2 n_e}{\epsilon_0 m_e\gamma}\right)\widetilde{\delta A}_y = \frac{1}{2cu^2}\frac{e}{\epsilon_0 m_e}\frac{n_e p_y^0}{\gamma}. \tag{3.26}$$

Equation (3.26) is a differential equation in ξ, the solution of which is

$$\widetilde{\delta A}_y = \int_0^\xi \left\{\frac{1}{2cu^2}\frac{e}{\epsilon_0 m_e}\frac{n_e p_y^0}{\gamma} \times \exp\left[-\int_\xi^{\xi'}\frac{1}{2cu}\left(u^2 + \frac{e^2 n_e}{\epsilon_0 m_e\gamma}\right)d\xi''\right]\right\}d\xi'. \tag{3.27}$$

Let us now introduce the function $G(\xi',\xi) = \frac{e^2}{\epsilon_0 m_e c}\int_\xi^{\xi'} d\xi''\, n_e/\gamma$. There, $\widetilde{\delta A}_y$ can be re-expresed

as

$$\widetilde{\delta A}_y = \frac{e}{2\epsilon_0 m_e c}\frac{e^{\frac{u\xi}{2c}}}{u^2}\int_0^\xi \frac{n_e p_y^0}{\gamma}\times\exp\left(-\frac{G(\xi',\xi)}{2u}-\frac{u\xi'}{2c}\right)d\xi'. \tag{3.28}$$

Returning to the original (ξ,τ) variables by performing a Bromwich inversion (or inverse Laplace transform) using the following properties [Abramovitz & Stegun 1972]:

$$\mathcal{LT}^{-1}\left[\frac{e^{au-b/u}}{u^2}\right] = \mathcal{LT}^{-1}\left[e^{au}\right] * \mathcal{LT}^{-1}\left[\frac{e^{-b/u}}{u^2}\right] \tag{3.29}$$

$$= [\delta(a+\tau)] * \left[\sqrt{\frac{\tau}{b}}J_1(2\sqrt{b\tau})\right] \tag{3.30}$$

$$= \sqrt{\frac{a+\tau}{b}}J_1(2\sqrt{b(a+\tau)}) \tag{3.31}$$

with $a=(\xi-\xi')/2c$ and $b=G(\xi',\xi)/2$ yields the transverse radiated field:

$$\delta A_y(\xi,\tau) = \frac{1}{2\sqrt{m_e\epsilon_0 c^2}}\int_0^\xi d\xi' \frac{n_e p_y^0}{\gamma}\sqrt{\frac{2c\tau+\xi-\xi'}{\int_\xi^{\xi'} d\xi'' n_e/\gamma}}J_1\left[\sqrt{\int_\xi^{\xi'} d\xi''\frac{e^2 n_e}{m_e\epsilon_0 c^2\gamma}(2c\tau+\xi-\xi')}\right]. \tag{3.32}$$

Solution (3.32) is the relativistic analog of the analytical WE and UPPE solutions [Eqs. (2.22) and (2.32)] presented in Section 2.1.5. It models the radiated field in a semi-infinite plasma subject to ionization and developing nonlinear plasma waves. The source term $n_e p_y^0/\gamma$ is the solution of the plasma wave system Eqs. (3.11), (3.12), (3.14) and (3.17). The term p_y^0 encompasses the laser contribution together with the additional finite transverse momenta acquired during ionization. Note that the only approximation made is that $\delta p_y = e\delta A_y$, meaning that we neglect the influence of the ionization steps on the perturbative solution.

After performing a numerical integration and applying a low-pass filter for extracting THz components, we obtain the THz radiated field produced by the plasma. Figure 3.3 shows an example of the low-frequency radiated field emitted by the interaction between a marginally relativistic laser pulse ($a_0=1$, $\lambda_0=1$ μm, $\tau_0=35$ fs) and a helium gas cell ($n_a^0 = 2.2\times 10^{-4}$ n_c). A good agreement is found between our solution and the field computed by 1D CALDER simulation results. The first burst reaching ~ 5 GV/m is due to the product between the steplike increase in the electron density n_e and the transverse velocity $v_y \propto p_y^0/\gamma$ occurring in the laser pulse. Later the transverse momentum has a non zero value as presented in Fig 3.2 displaying periodic oscillations shaped by the Bessel function. The latter beats at the relativistic plasma frequency $\omega_{pe}/\sqrt{\gamma}$. For stronger intensity, the density modulation is enhanced, impacting directly the solution. Note that the phase mismatch between the numerical and analytical solutions is attributed to propagation effects including plasma linear dispersion present in the PIC simulation and which are not accounted for in the analytical solution.

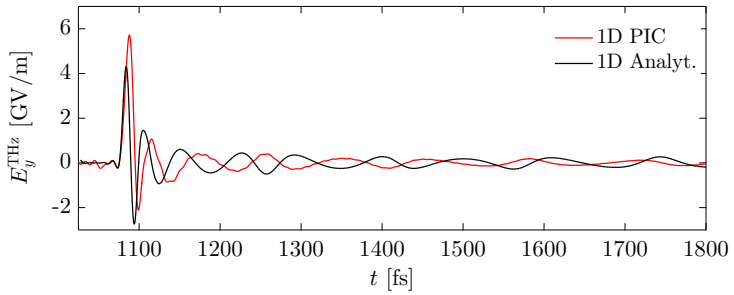

Figure 3.3: Radiated field in the laser polarization direction, filtered in the low-frequency domain ($\nu < 90$ THz), after 300 μm of propagation in an initially neutral helium gas cell ($n_a^0 = 2.2 \times 10^{-4}\ n_c$) and computed from 1D PIC simulation (red line) and from Eq. (3.32) (black line). The simulated two-color laser pulse has a central fundamental wavelength $\lambda_0 = 1$ μm and $\tau_0 = 35$ fs duration (FWHM) for an overall intensity of $I_0 = 1.4 \times 10^{18}$ W/cm^2 ($a_0 = 1$). The intensity ratio between the fundamental and the second harmonic equals to $r = 0.1$ and the initial phase shift is set to $\phi = \pi/2$.

3.2 THz emission from 3D relativistic underdense plasmas

This section comments on numerical simulations in the relativisitic regime performed with the CALDER-CIRC code. The purpose of this study is manyfold. First, we test our relativistic PIR model derived above in Section 3.1.2 and describe for the first time the generation of THz radiation by the interaction of a two-color relativistic laser pulse with an underdense plasma. Second, we demonstrate that, at the same time, transition radiation by wakefield-accelerated electrons can be relevant for THz generation with lasers available today. Section 3.2.1 presents the context and the parameters used in our baseline simulation and defines how our PIC simulation is prepared. The PIR model is compared to CALDER-CIRC results in Section 3.2.2 while Section 3.2.3 is devoted to the coherent transition radiation (CTR) arising at the plasma-vacuum interface. Finally, Section 3.2.4 presents a theoretical approach, based on the generalized Biot-Savart law, which we derive to better discriminate low-frequency radiated fields from electrostatic fields attached to the charges traveling with a relativistic velocity.

3.2.1 Context and baseline simulation

So far, plasma-based THz sources have been studied in classical regime with particular attention to the laser-to-THz conversion efficiency with respect to the laser-gas parameters. In the two-color setup, it appears that the THz energy scales linearly, before saturating, with the pump laser intensity [Wang *et al.* 2010; Oh *et al.* 2013] and the square root of the second harmonic for a laser energy comprised between 1 and 20 mJ [Koehler *et al.* 2011; Debayle *et al.* 2015]. It is also dependent on the phase shift ϕ between the two laser harmonics through the $\sin\phi$ factor [see Eq. (2.79)] [Kim *et al.* 2008; Wang *et al.* 2013]. Yet, an universal scaling seems difficult to extract since the laser and medium parameters can strongly vary along propagation, among which this phase shift [Nguyen *et al.* 2019]. At near-relativistic intensities, photocurrents go on providing a strong THz emitter [González de Alaiza Martínez *et al.* 2016], but THz waves may also originate from longitudinal and transverse plasma waves as well [D'Amico *et al.* 2007, 2008]. Also, resonant radiation excited by the ponderomotive force in increasing density ramps have been reported as supplying strong THz fields, the spectrum of which may change along both forward and backward directions by letting (or not) the plasma frequency exit the plasma channel [Miao *et al.* 2016]. An obliquely incident laser pulse can also generate THz emission

through linear mode conversion in the increasing plasma density ramp [Sheng *et al.* 2005b]. From there we notice that, in addition to the photocurrent mechanism, fields excited in the plasma channel by the ponderomotive force come into play. They should be carefully studied when they are strong, hence in the relativistic regime.

To examine the transition between the classical and relativistic regime, we simulate a two-color laser pulse focused into an initially neutral gas profile and triggering photocurrent-induced radiation (PIR). Meanwhile, the relativistic laser pulse excites a strong nonlinear plasma wave which might be responsible in turn for THz emissions. Our 3D PIC simulations are performed with the CALDER-CIRC code, which solves the coupled Vlasov-Maxwell equations. The electromagnetic fields are discretized on a (x, r) grid and decomposed over a reduced set of Fourier angular modes $\propto e^{im\theta}$ around the x axis. Only the first two modes are retained here, which is sufficient to describe LWFA [Lifschitz *et al.* 2009]. The fundamental $m = 0$ mode corresponds to axisymmetric fields such as the radially polarized ones. The $m = 1$ mode contains non-axisymmetric fields and includes the y-polarized laser field.

The simulation scenario consists in focusing into a gas target a two-color laser pulse with carrier wavelength $\lambda_0 \equiv 2\pi c/\omega_0 = 1\ \mu m$ and its second harmonic, shifted by a relative phase of $\pi/2$ to optimize the PIR [Kim *et al.* 2007; Babushkin *et al.* 2011]. The $2\omega_0/\omega_0$ intensity is 10% for a total laser intensity $I_0 = 2.2 \times 10^{19}$ W/cm^2, corresponding to a normalized field strength $a_0 = 4$ and to a 100 TW laser with 3.7 J energy. The laser components have Gaussian profiles in both space and time with equal initial widths $w_0 = 20\ \mu$m and FWHM durations $\tau_0 = 35$ fs. The target is an underdense gas of helium with neutral density $n_a^0 = 2.2 \times 10^{-4} n_c = 2.4 \times 10^{17}$ cm^{-3}. Once completely ionized it leads to the classical plasma wavelength $\lambda_{pe} = 47\ \mu$m such that the plasma frequency belongs to the THz domain $\nu_{pe} = 6.3$ THz. These laser-gas parameters ensure a bubble formation according to the scaling laws (2.223) and (2.228) ($k_{pe} w_0 \approx 1.86$ versus $2\sqrt{a_0} = 2$ and $c\tau_0 \approx 66\ c\omega_0^{-1}$ versus $2w_0/3 \approx 84\ c\omega_0^{-1}$) favoring electron acceleration [Lu *et al.* 2007]. We opt for a density profile shorter than that usually considered for standard LWFA setups, as a large simulation domain is needed in the transverse direction for not truncating the radiated fields along propagation in vacuum. The gas density has here a trapezoidal shape with a 400 μm-long plateau (L_p) and 100 μm-long ramps (L_g) on both sides to mimic the conditions met in gas-jet experiments. This plateau ensures the development of the plasma wave ($L_p/\lambda_{pe} \sim 10$) while the gradient length guarantees a smooth transition for the laser ($L_g/c\tau_0 \sim 10$). Figure 3.4 presents a scheme of the numerical setup.

The THz fields are extracted by filtering the total electromagnetic field after selecting the spectral region below a cut-off frequency $\omega_{co} = 0.3\,\omega_0$ ($\nu_{co} \equiv \omega_{co}/2\pi = 90$ THz). Attention is paid to the transmitted THz fields only, as they usually prevail over the backscattered components in gases [Koehler *et al.* 2011; Debayle *et al.* 2014]. Also, THz generation mechanisms, i.e. PIR and CTR, produce transverse field strength ($E_\perp$) exceeding the longitudinal one (E_x) by one order of magnitude [Durand 1975]. This invites us to restrict our analysis to $E_\perp$, whose PIR and CTR components can be discriminated through direct angular expansion: the PIR field is polarized along the laser field, and so is described by the $m = 1$ mode. By contrast, the wakefield-driven electron bunch is essentially axisymmetric, hence the resulting CTR (radially polarized) is mainly contained in the $m = 0$ mode.

From the numerical point of view, extracting THz emission from PIC simulations is a challenging task. The numerical noise can indeed rapidly alter the THz field since it consists of a small perturbation compared to the laser field. For example, in our simulation, we expect THz field strengths of about a few GV/m whereas the peak laser electric field amplitude reaches 13,000 GV/m. In this condition a fine spatial and time steps are needed to reduce the numer-

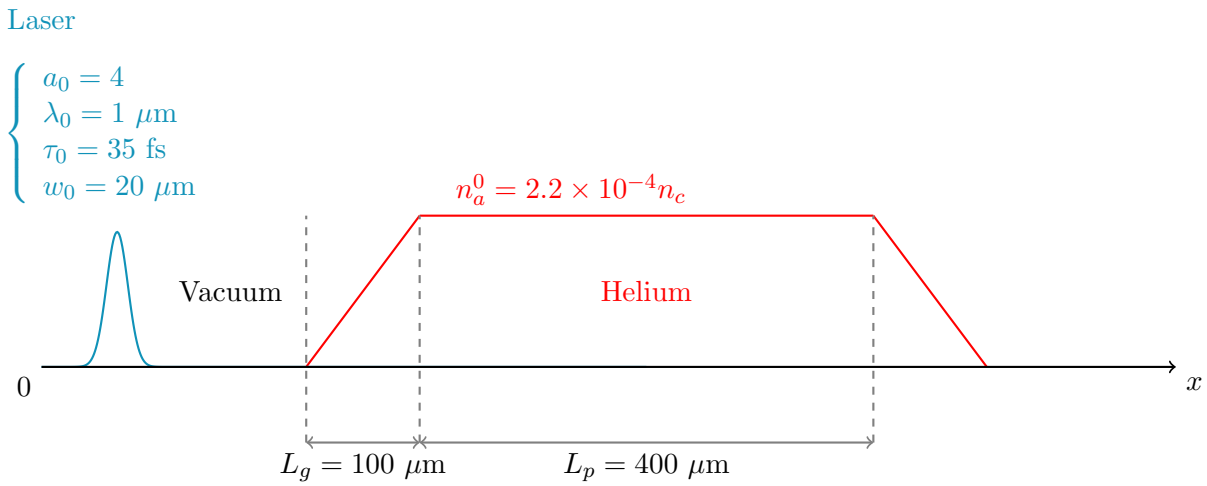

Figure 3.4: Geometry and laser-plasma parameters for our baseline simulation.

ical noise and resolve the second laser harmonic over $\lambda_0/2$. Therefore, the longitudinal spatial step is $\Delta x = \lambda_0/160 \approx 6$ nm while the transverse spatial step has to resolve the laser waist $\Delta r = w_0/30 \approx 660$ nm. Accordingly, the time step follows the CFL conditions leading to $\Delta t = 20$ as. The simulation domain is a sliding window traveling at the speed of light c, being 200 μm long and 380 μm wide and accounting almost 6 millions of cells. The simulation stops when the final number of iterations is reached. In the present case, in order to retain the genuine propagating fields against the electrostatic plasma fields (see Section 3.2.4), we cover a propagation range as long as 0.5 mm after the plasma-vacuum interface. As a result the total distance propagated by the laser is about 1300 μm (100 μm of vacuum before the gas profile, 600 μm in the gas and almost 600 μm of propagation in vacuum) corresponding to a time window of 4.3 ps[1]. Thus the number of iterations is $N_t = 4.3\ \text{ps}/\Delta t = 215,000$. The last numerical parameter of importance is the number of macro-particles per cell. If this number is too weak, some noise appears during interpolation steps in the PIC loop. On the other hand, too many macro-particles lead to an over-consumption of the computing resources. Here the plasma is composed of $(600/0.06) \times (380/0.66) = 5.75 \times 10^6$ cells and we choose to use 8 macro-particles by cell leading to a total of 46 millions of helium atoms. By using 1000 CPUs one numerical run lasts about 24 hours.

Below we examine the results of our baseline simulation. We first reveal two mechanisms responsible for THz generation, namely, the PIR in relativistic regime (Sec. 3.2.2) and the coherent transition radiation (CTR) by wakefield-accelerated electrons (Sec. 3.2.3). Then, laser-plasma parameters of the baseline simulation are modified to gauge the sensitivity of the PIR and CTR to the interaction setup. Next, we clear up, by developing an analytical model based on the generalized Biot-Savart law, the contribution of the particle self-field coming from the electron bunch in the total measured energy (Sec. 3.2.4).

3.2.2 PIR in the relativistic regime

The laser pulse reaches the focal plane at $x = 0$ and propagates over 100 μm in vacuum before interacting with the gas jet. Figure 3.5 displays three snapshots of the filtered low-frequency field in the laser polarization direction ($m = 1$), i.e., the PIR (top part) and the electron density

[1]We consider that the laser pulse group velocity $v_g = c\sqrt{1 - (\omega_{pe}^0/\omega)^2}$ is almost equal to the speed of light in an underdense plasmas, $\omega_{pe}^0 \ll \omega_0$, such that 1300 μm$/c \approx 4.3$ ps

(bottom part) during the propagation of the laser in the created plasma channel. We observe the development of the PIR field along the laser pulse propagation and also the establishment of successive ion cavities (bubbles) responsible for electron acceleration, which will lead, later, to CTR at the plasma-vacuum interface.

Photocurrents emit radiation in the laser foot (black line) where the ionization of the second electronic shell takes place (red cross) [see top of Fig. 3.5(a)]. A single cycle pulse (33 fs duration) extending over 10 μm long is emitted along the laser polarization direction and with amplitude greater than 1 GV/m. This signal can clearly be attributed to the product $n_e v_y$ in the laser region as evidenced by our analysis of Eq. (3.32) in the previous section (see Fig. 3.3). Meanwhile, the laser ponderomotive force acts on newly born electrons and expels them from the propagation axis. An ion cavity, i.e., depleted of electrons, begins to form [see bottom of Fig. 3.5(a)]. Later on, at $t = 1060$ fs, the laser fully propagates in the gas cell and, as expected, a plasma bubble has been set up. Electrons expelled from the laser path travel transversally along the ion cavity (bubble orbits) and go across the propagation axis at $x \sim 210$ μm forming a peak density of about 0.01 n_c [see bottom of Fig. 3.5(b)]. At the same location we observe a burst in the field map due to the off-axis crossing of electrons [see black rectangle in top of Fig. 3.5(b)]. This field contribution is all the more reinforced that photoionization increases the acquired transverse momentum and so amplifies the transverse electron motion. This behaviour is partially recovered in our analytical solution Eq. (3.32) by the coupling between the high density peak and the residual transverse momentum, being overall modulated by the Bessel function. Finally before the density down-ramp ($t = 2020$ fs) the PIR field reaches its maximum amplitude of about 5 GV/m with similar duration to the one reported above [see top of Fig. 3.5(c)] showing saturation in the produced THz field. The plasma is then formed by a succession of ion cavities and high electron density regions constituting the nonlinear plasma wave [see bottom of Fig. 3.5(c)]. However the absence of electron beam in the cavities demonstrates that injection did not happen yet. It will be triggered by the density down-ramp as evidenced by Fig. 3.9.

To gain insight into the PIR generation process, we plot in Fig. 3.6 the time history of the on-axis filtered E_y^{THz} field at a depth of 300 μm inside the plasma (green curve). It first displays the characteristic PIR signature due to the $n_e v_y$ product in the ionization front (laser foot) with an amplitude of about 4 GV/m (see inset). One plasma period $2\pi\sqrt{\gamma}\omega_{pe}^{-1}$ later, an important peak at 40 GV/m occurs, repeated again with smaller amplitude ($\sim$ 15 GV/m). These periodic bursts coincide with the high density regions imposed by the plasma wave. In order to assess the origin of these high amplitude peaks we compare 3D PIC to 1D PIC simulation results (red curve) using the same parameters. Relatively good agreement (within a factor ~ 2) is found between the 1D and 3D PIC data in the laser region [see also inset of Fig. 3.6]. The secondary emission, occurring one plasma wavelength later, is still present despite its lower amplitude and delayed due to differences in the dynamics and shape of the 1D and 3D plasma waves, as demonstrated below. The plasma wave system coupled to the gas ionization is solved to compute Eq. (3.32) in Fig. 3.6 (black curve). This formula correctly reproduces the 1D PIC result during the laser pulse [see top part of Fig. 3.6]. Also, due to the interplay between the residual transverse momentum and the density modulations associated to the nonlinear laser wakefield, terahertz bursts occur at each density peak with a $\sim$ 250 fs period, i.e., the relativistic plasma period. Hence, in relativistic regime, photocurrents are also responsible for additional THz emission out of the laser region by coupling with the nonlinear electron density. This effect is captured by our 1D analytical formula. Nonetheless it should be strengthened in 3D due to the (transverse) electron acceleration around the bubble. Indeed, the transverse ponderomotive force plays an important role in the bubble formation, which is not accounted for by our 1D description that

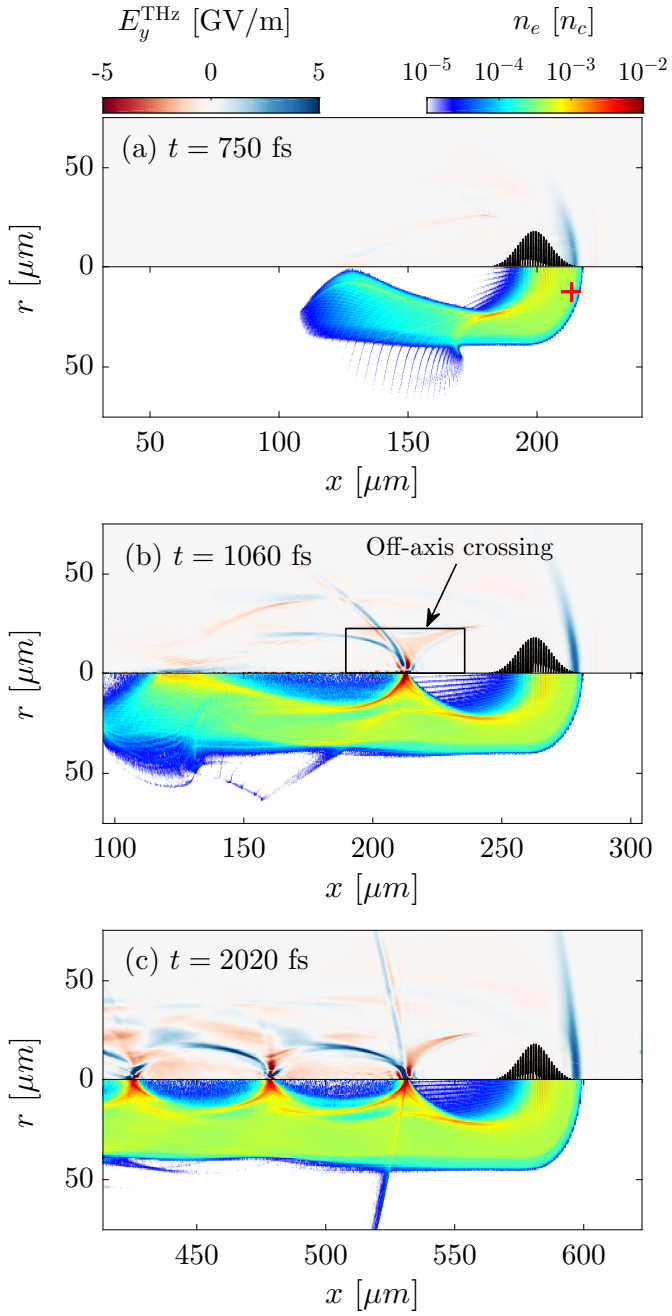

Figure 3.5: Top part shows the filtered low-frequency ($\nu < 90$ THz) PIR field E_y^{THz} [GV/m] in the laser direction while the bottom part displays the electron density n_e [n_c] in log scale for (a) $t = 750$ fs, (b) $t = 1060$ fs and (c) $t = 2020$ fs. Black areas illustrate the laser electric field. Red cross marks the second ionization step where photocurrents emit radiation.

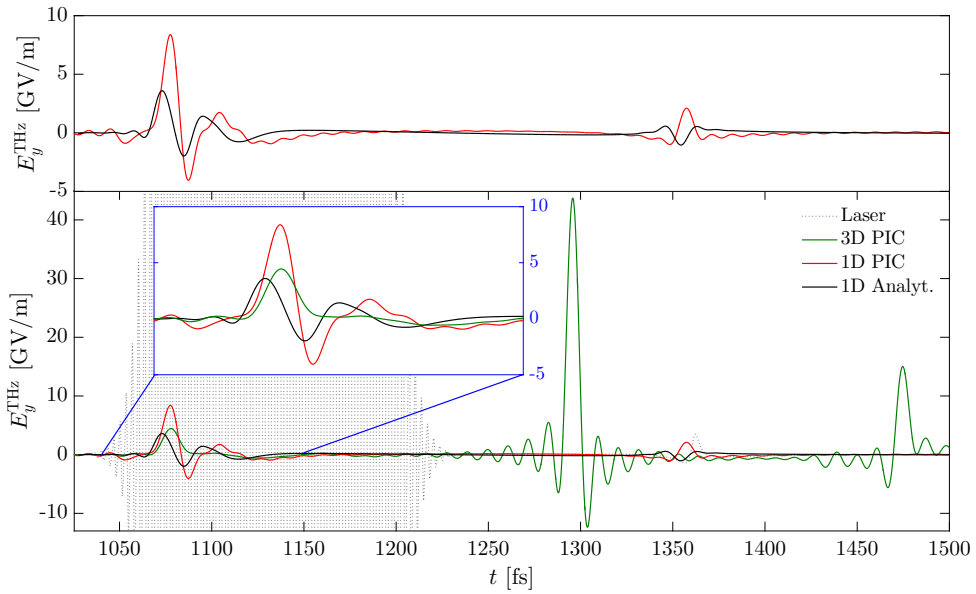

Figure 3.6: Time history of the on-axis E_y^{THz} field at 300 μm inside the plasma, as given by the 3D (green curve) and 1D (red curve) PIC simulations, and the solution of Eq. (3.32) (black curve). The grey dashed curve represents the laser electric field. The top part displays a zooms in on the 1D results while the inset in the bottom figure zooms in on the front pulse region.

underestimates the on-axis electron density (see below).

To prove that the high amplitude THz burst ~ 40 GV/m indeed originates from photoionization we reran our baseline simulation for a pre-ionized plasma ($\partial_\xi n_e^0 = 0$) and compare the time trace of the THz waveform in Fig. 3.7(a). In the absence of ionization no field emission is reported in the laser region, as expected. One clearly observes the extinction of the THz burst when photoionization is switched off, up to second-order ripples which we attribute to small asymmetry in the transverse ponderomotive force leading to a slight off-axis crossing of electrons. In this case, the transverse electron velocity, which is comparable in 1D or 3D geometries, vanishes and so does the transverse current associated with the generation of non-axisymmetric ($m = 1$) modes. Thus these data highlight the importance of the photoionization process. More important, the one order of magnitude difference between the 3D (~ 40 GV/m) and 1D (~ 5 GV/m) burst is attributed to 3D effects. In Fig. 3.7(b) we have plotted the peak electron density for the 3D simulation close to axis - accounting for ionization or not - and its counterpart for the 1D PIC simulation (including ionization only). The plasma wavelength is shorter in 3D due to transverse ponderomotive forces. We clearly observe a ten times higher density spike in 3D, which follows from the dynamics of the electrons accelerated around the bubble and subject to trajectory crossing close to the propagation axis. The curve for a preformed plasma, exhibiting similar density peaks, confirms that only 3D effects come into play here. This order of magnitude difference in the electron density (factor 10) corroborates the difference in the transverse field amplitudes.

After its passage in the gas cell, the laser pulse is accompanied by another source of low-frequency radiation, as displayed by Fig. 3.8(a,b). The latter is identified as coherent transition radiation (CTR) emitted by a wakefield-accelerated electron bunch crossing the plasma-vacuum interface. Hence, this set of isosurfaces represents the PIR (blue color map) and CTR (red color map) electric fields at a distance of 500 μm from the plasma-vacuum interface [Fig. 3.8(a)]. The propagating laser pulse is visualized by the yellow isosurface. Three low-frequency field

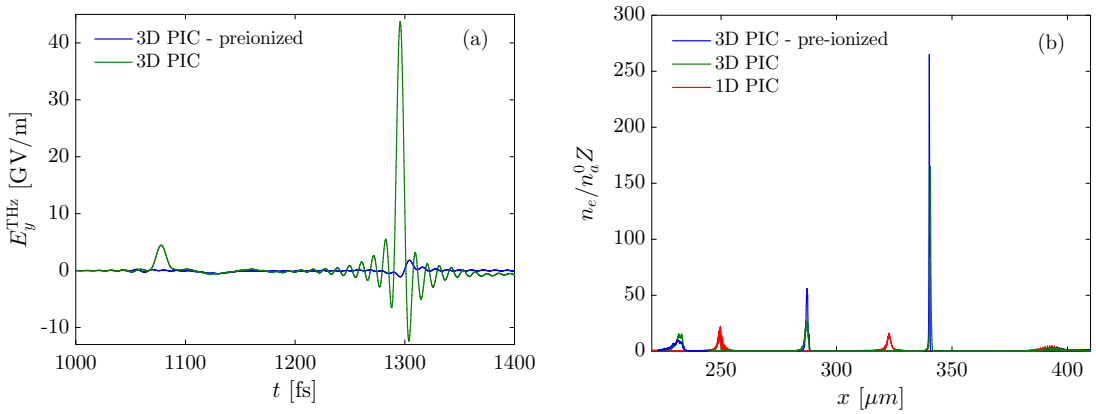

Figure 3.7: (a) Transverse laser-polarized electric field filtered in the THz window (ν_{co} = 90 THz) from the 3D baseline simulation (green line) and from the pre-ionized simulation (blue line). Partial oscillation near t = 1300 fs in the pre-ionized case is attributed to electron motions due to transverse ponderomotive forces that result in small distortions of the bubble. (b) Electron density ratio $n_e/n_a^0 Z$ (Z = 2 in helium) of the 1D PIC simulation (red line) and of the 3D PIC simulations accounting for ionization (green line) and pre-ionized gas (blue line) close to the propagation axis.

structures can be distinguished. First, due to diffraction, the primary PIR burst, located $\sim$ 20 μm in the front of the laser pulse peak, has an on-axis maximum amplitude reduced to $\sim$ 1 GV/m and carries a total energy of 1.3 μJ[2]. The secondary non-axisymmetric signal behind the laser pulse originates from the coupling of the transverse photocurrents and the strong density oscillations accompanying the wakefield. Due to strong diffraction its amplitude passes from 40 GV/m in the plasma (see above) to $\sim$ 3 GV/m, corresponding to an energy of $\sim$ 2.6 μJ. This emission is less collimated but more intense than that occurring in the laser front pulse. This THz emission is inherently linked to the relativistic nature of the interaction and one can use it as a source of intense THz radiation. For instance the delay between the PIR in the laser pulse and the secondary peak could be used as a possible diagnostic of the wakefield dynamic to access to the relativistic plasma wavelength.

Finally, about one plasma wavelength behind the laser pulse, mixed with the secondary PIR, a radially-polarized burst (red color map) produces the maximum THz field $\sim$ 15 GV/m, corresponding to a $\sim$ 160 μJ energy. The location and the hollow conical shape of this emission are consistent with CTR by electrons accelerated in the laser wakefield. We now study in details the low-frequency emission ascribed to the transition radiation phenomenon.

3.2.3 CTR as an efficient THz emission process

In Fig. 3.8(b), radiated fields are dominated by the CTR emission process [compare green and orange areas in the (x, y) cut plane]. The intense burst plotted as green lobes is emitted when the electron bunch that has been trapped into the first cavity exits vacuum. This scenario is supported by Figs. 3.9(a,b), which show (a) the $m = 0$ component of the longitudinal electron current density (J_x) and (b) the electron (x, p_x) phase space at time t = 2.55 ps. The strong peak in J_x seen at the foot of the density down-ramp ($x \simeq 690\,\mu$m) corresponds to a high-energy ($p_x \approx 25\, m_e c$) electron bunch about to exit the plasma. Subsequent cavities also accelerate a few electron packets, yet at lower energies and densities. Note that the density down-ramp allows

[2]The energy of a given field component is computed by integrating the squared modulus of the field amplitude in cylindrical coordinates.

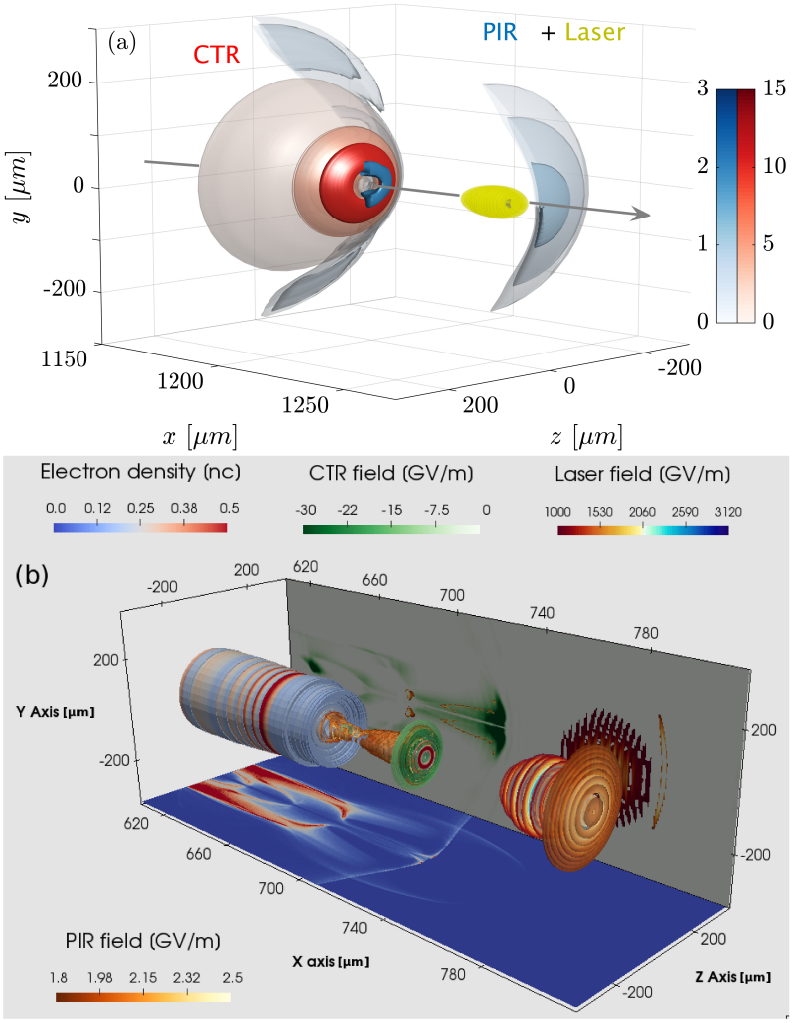

Figure 3.8: (a) THz field emission from a He gas target of $2.4 \times 10^{17}\,\mathrm{cm}^{-3}$ atomic density driven by a $2.2 \times 10^{19}\,\mathrm{W/cm}^2$, 35 fs two-color laser pulse. 3D isosurfaces of the filtered ($\nu < 90\,\mathrm{THz}$) transverse field ($E_\perp^{\mathrm{THz}}$) in vacuum at $500\,\mu$m from the plasma boundary at time $t = 4.17$ ps. Radially-polarized ($m = 0$) modes are fully displayed (red colormap); laser polarized ($m = 1$) ones are shown as half-caps for better readability (blue colormap). The yellow isosurface delineates the laser pulse envelope propagating along the grey arrow for a normalized field strength $a = 2/3$ ($E_\perp = 2140\,\mathrm{GV/m}$). (b) Same quantities shown at time $t = 2.6$ ps just after the plasma-vacuum interface plotted with the 3D visualisation tool (PARAVIEW). The projection planes detail the electron dynamics through the bubble shape (x, z) and the emitted field amplitude (y, z).

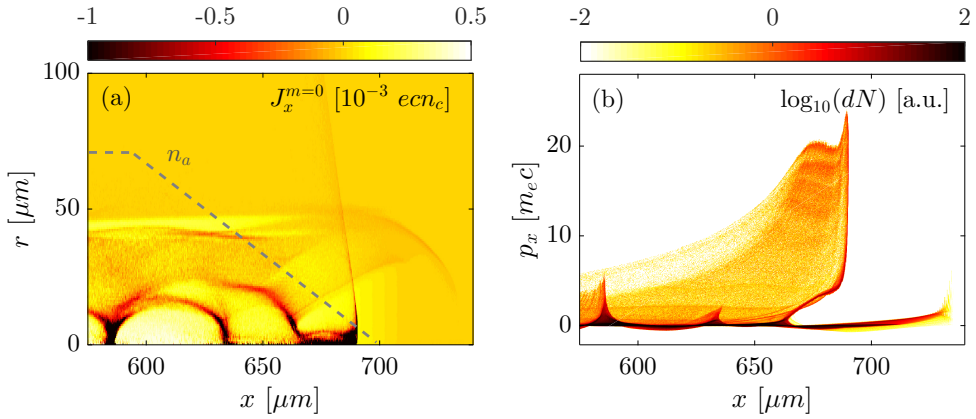

Figure 3.9: (a) Snapshot of the $m = 0$ component of the longitudinal current (J_x) at time $t = 2.55$ ps when the laser pulse exits the plasma-vacuum interface (atomic density is visualized by a gray dashed line). (b) Electron number (dN in $\log_{10}$ scale) in the (x, p_x) phase space at the same instant.

electron injection since the main electron beam is formed only at the end of the descending gradient which is illustrated by Fig. 3.9(a) [to be compared to bottom Fig. 3.5(c) where the descending gradient is not reached yet].

Thus this accelerated charge passes gradually from the plasma medium [$\epsilon(\omega) = 1 - \omega_{pe}^2/\omega^2$] to vacuum [$\epsilon(\omega) = 1$] and emits a transition radiation at ω whenever a sufficient formation length [Eq. (2.253)] is traversed (see Section 2.3.1). We first give an evaluation of the latter. Its maximum value is defined by $L_f^{\max} = \gamma c/\omega_{pe}$ for a radiation with angular frequency $\gamma\omega_{pe}$ [Eq. (2.255)]. We can extract from the PIC simulation the mean γ factor of the accelerated electron bunch by integrating the longitudinal phase space (x, p_x) shown in Fig. 3.9(b). By selecting the electron bunch ($680 \leq x \leq 695$) and discarding low energetic electrons ($p_x \geq 5m_e c$), we obtain a mean value of the Lorentz factor of about $\langle\gamma\rangle = 15$. Hence the value taken for the photon formation length is $L_f^{\max} \sim 115$ μm, where we used $\omega_{pe} = 40 \times 10^{12}$ Hz for $n_e = 4.8 \times 10^{17}$ cm^{-3}. This value is lower than the plasma length, such that transition radiation can effectively be emitted.

To confirm that the radiated field surrounding the electron bunch is really due to the CTR induced by wakefield-driven electrons, we confront its 2D energy spectrum to that predicted by the CTR theory. To do so we employ the equation derived in Section 2.3.3 for a plasma-vacuum interface [Eq. (2.286)]. The latter is considered as sharp since the electron crossing at velocity v is made in a short amount of time, i.e., the wave period is small in comparison to the formation time $2\pi/\omega \ll L_f/v$. Also we discard diffraction effect induced by the finite transverse size of the plasma. Due to the longitudinal length of the bunch L_b and the finite permittivity of the first medium, coherence effects arise in the emission as explained in Section 2.3.4. For simplicity we neglect the coherence information conveyed by the bunch spatial distributions and assume a point-like electron bunch. This assumption holds, provided that the radiation wavelengths are larger than the bunch size, in which case the emission is coherent [Schroeder *et al.* 2004]. Thus a point-like mono-energetic electron bunch exiting perpendicularly to the plasma surface emits a radiated spectrum given by Eq. (2.286) multiplied by the coherence factor $N_e(N_e - 1)$:

$$\frac{d^2\mathcal{E}}{d\Omega d\omega} = N_e(N_e-1)\times\frac{e^2}{\pi^2 c}\frac{\beta^2\sin^2\theta\cos^2\theta}{(1-\beta^2\cos^2\theta)^2}\times\left|\frac{(\epsilon-1)(1-\beta^2-\beta\sqrt{\epsilon-\sin^2\theta})}{(\epsilon\cos\theta+\sqrt{\epsilon-\sin^2\theta})(1-\beta\sqrt{\epsilon-\sin^2\theta})}\right|^2, \quad (3.33)$$

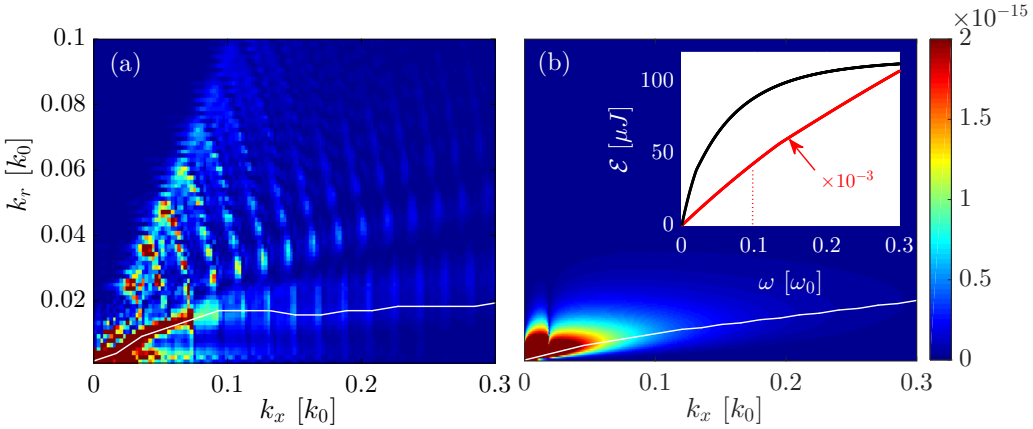

Figure 3.10: 2D (k_x, k_r) spectrum of the axisymmetric field $E_\perp^{\rm THz}$ in vacuum at 500 μm from the plasma: (a) 3D PIC simulation results; (b) CTR theory [Eq. (3.33)] for $\langle\gamma\rangle = 15$ and $N_e = 8.9 \times 10^8$. The white dashed lines indicate the direction of maximum emission, $\theta_{\rm max} = \langle\gamma\rangle^{-1}$. The inset in (b) shows the emitted field energy [μJ] versus frequency according to Eq. (3.33) for $n_a = 2.4 \times 10^{17}\,{\rm cm}^{-3}$ (black curve) and $n_a = 9.7 \times 10^{17}\,{\rm cm}^{-3}$ (red curve). In the latter case discussed in Fig. 3.11(d), the electron bunch parameters are $\langle\gamma\rangle = 150$ and the electron number is $N_e = 1.06 \times 10^{10}$.

where N_e is the number of electron inside the bunch. In order to compare the computed 2D energy spectrum from the PIC simulation, Eq. (3.33) needs to be recast in terms of the longitudinal (k_x) and transverse (k_r) wave numbers using the transformation $\theta = \arctan(k_r/k_x)$ and $\omega = c\sqrt{k_x^2 + k_r^2}$.

Figures 3.10(a,b) show the THz spectra computed from (a) the 3D PIC simulation and (b) Eq. (3.33) using the mean values $\langle\gamma\rangle = 1\sqrt{1-\beta^2} = 15$ and $N_e = 8.9 \times 10^8$ that best fit the electron bunch issued from the first wakefield bucket. Despite the crude simplifications of Eq. (3.33) (e.g., neglecting the electron beam's energy and angle spread), the two spectra fairly agree in intensity and shape: both present a maximum emission along $\theta_{\rm max} \simeq \langle\gamma\rangle^{-1}$ (white dashed line) with a cutoff frequency $\omega_{\rm max} \simeq \gamma_e \omega_{pe} \approx 0.3\,\omega_0$, as expected from CTR by relativistic electrons [Jackson 1999] (see Section 2.3.3). The PIC spectrum, however, differs from the theoretical one by additional weaker emissions at larger angles and spectral modulations separated by $\Delta k_r \simeq \omega_{pe}/c$, which are ascribed to radiation by lower-energy electron bunches produced in the second and third wakefield buckets. The inset of Fig. 3.10(b) plots the theoretical radiated energy in μJ computed from Eq. (2.286). To evaluate this quantity, we first integrate Eq. (3.33) over the solid angle $d\Omega = 2\pi \sin\theta d\theta$ in a collection angle $\theta_0 \approx \pi/5$ corresponding to the angular opening of the simulation 500 μm after the interface. Then a cumulative integral over the frequency domain ω is performed to obtain the radiated energy as a function of the frequency (black curve). In the THz frequency range $\omega < 0.3\,\omega_0$, we obtain a total energy of $\sim 100\,\mu$J, comparable with the $\sim 160\,\mu$J yield measured in the simulation in which 75% of the radiated energy (~ 120 μJ) is emitted below 30 THz (0.1 ω_0).

The CTR yield depends on the efficiency of the wakefield acceleration, and is therefore sensitive to the gas parameters. As shown in Fig. 3.11(a), when decreasing the gas density to $n_a = 6 \times 10^{16}\,{\rm cm}^{-3}$ (4-fold decrease), the energy and number of the escaping electrons significantly drop ($\langle\gamma\rangle \simeq 4$, $N_e \simeq 10^7$), which in turn reduces the CTR ($\sim 0.1\,$GV/m) much below the PIR level ($\sim 1\,$GV/m). The reason is that the electron density of the ionized gas is too low to trigger an efficient wakefield acceleration, which thus strongly weakens CTR at the plasma boundary. Similar pattern is found when decreasing the maximum laser field strength

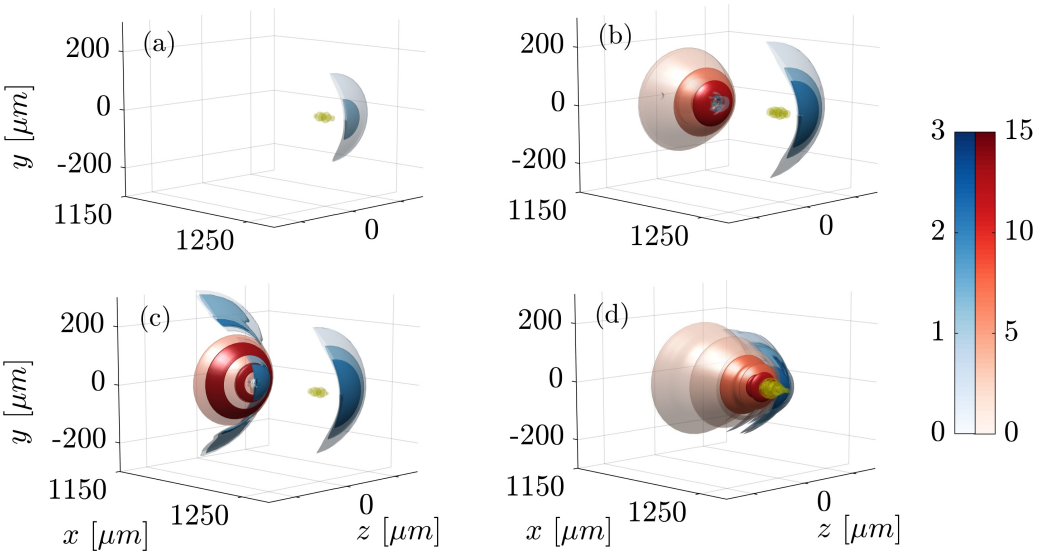

Figure 3.11: 3D isosurfaces of the THz transverse field (E_y^{THz} [GV/m]) at 500 μm from the plasma-vacuum interface for different laser-gas parameters: (a) $a_0 = 4$ with a 4-fold decrease in the atomic density ($n_a = 6 \times 10^{16}\,\mathrm{cm}^{-3}$) compared with the baseline simulation; (b) $a_0 = 2.5$ with the baseline density $n_a = 2.4 \times 10^{17}\,\mathrm{cm}^{-3}$; (c) $a_0 = 4$, $n_a = 2.4 \times 10^{17}\,\mathrm{cm}^{-3}$ with a step-like rear plasma boundary and (d) $a_0 = 4$, $n_a = 97 \times 10^{17}\,\mathrm{cm}^{-3}$ corresponding to a 40 times denser plasma. Red (blue) colormaps correspond to axisymmetric (resp. non-axisymmetric) fields.

to $a_0 = 1$ because of the quasilinear plasma wave suppressing particle injection, so that only PIR (~ 1 GV/m) occurs. At the baseline density $n_a = 2.4 \times 10^{17}$ cm^{-3}, CTR is found to take over PIR from $a_0 = 2.5$. A small number of electrons ($N_e = 4 \times 10^8$) start to be accelerated and escape from the plasma, giving rise to comparable CTR and PIR signals [see Fig. 3.11(b)].

Returning to the reference configuration but changing the density ramp at the rear side of the gas to a sharp gradient [Fig. 3.11(c)], the PIR signal is essentially unmodified [compare with Fig. 3.8], while the CTR signal is significantly weakened ($\sim 2\,$GV/m) due to one order of magnitude reduced N_e. This pinpoints the beneficial role of the 100-μm density down-ramp in our reference setup, which promotes gradient injection [Bulanov *et al.* 1998].

Finally, Fig. 3.11(d) illustrates the case of a 40 times denser gas ($n_a = 97 \times 10^{17}$ cm^{-3} with a 100 μm-long ramp). This setup leads to stronger wakefields, still in the blowout regime. As the plasma length $L_p = 400$ μm remains much shorter than the dephasing length $L_{\mathrm{deph.}} \simeq 800$ μm [Eq. (2.227)], there result electron bunches of larger charge and energy (electron number $N_e \simeq 1.06 \times 10^{10}$ and $\langle\gamma\rangle \simeq 150$), thus generating via CTR an unprecedented THz signal with ~ 100 GV/m field strength and ~ 29 mJ energy yield. These values are consistent with the theoretical CTR spectrum carrying ~ 43 mJ displayed in the inset of Fig. 3.10(b). In this situation, the emission is coherent mainly in the frequency range $\omega < 0.1\,\omega_0$, as the longitudinal bunch length is larger than 10 μm. Hence, most of the THz energy (22 mJ) is confined below 10 THz ($0.033\,\omega_0$). Compared to the input laser energy, this simulation supplies an energy yield of $\sim 5 \times 10^{-3}$ of low frequency radiation.

In addition to CTR able to propagate in the far-field, the radially-polarized THz spectrum measured outside the plasma in the PIC simulation also includes the proper field of the electron bunch, which is not described by Eq. (3.33). This field is of electrostatic character in the rest frame of the bunch, and should thus be discarded when evaluating the source efficiency in emitting purely electromagnetic THz radiations supposed to be detected far away from the electron bunch. To model the space-time field distribution resulting from both the plasma-

boundary crossing (CTR) and subsequent propagation of the electron bunch (particles self-field), we establish an analytical model based on the generalized Biot-Savart law in the next section.

3.2.4 Biot-Savart model

Particle's field or Transition Radiation ?

The transition radiation theory presented so far in Section 2.3 relies on the far field approximation. Here, we consider that the fields collected at the observer position result from the plasma-vacuum interface crossed by the charged particle. The radiated field amplitude decays as $1/R$, where R is the distance between the source and the observer, whereas electrostatic fields behaves as $1/R^2$ and thus vanish far from the emitting point [Jackson 1999]. However, in our case of interest, the source is the electron bunch moving at velocity v, close to the speed of light. As a result the radiated field is mixed up with fields attached to the charges particles, the "self-field", and it takes some time t_s (or a distance ct_s) before both field components split.

Figure 3.12 displays the two distinct situations before and after the splitting time t_s which we henceforth define as the "immersion" and the "separation" phase, respectively. The red circle represents an electron bunch with a longitudinal extent L_b emerging from medium 1 (blue area) into medium 2 (white area) and propagating ballistically. The spherical grey wave front depicts the coherent transition radiation emitted at the interface with a length equal to the beam length due to coherence effect. Both overlap during the immersion phase ($t < t_s$) and behave as $1/r$ (or $1/R$ for fixed θ) [Fig. 3.12(a)]. Indeed, the Lorentz transformed Coulomb field decays as $1/r$ for $r < \gamma L_b$ and $1/r^2$ for $r > \gamma L_b$ such that it appears radiative as long as its transverse extent is limited by causality (i.e. the time needed to reach its asymptotic distribution) and by relativity since the radial extent equals to γL_b [Carron 2000]. Then, during the separation phase ($t > t_s$), the particle self-field develops until reaching its asymptotic expression given by Eqs. (2.246), (2.247) while the CTR field continues to propagate in the second medium [Fig. 3.12(b)]. The peak emission angle θ is given by the intersection between the Coulomb and the radiation fields. Simple geometric considerations allow us to recover the expected $\sin\theta \sim 1/\gamma$ radiation angle.

The splitting time t_s (or distance ct_s) can be easily evaluated. The electron bunch is characterized by its velocity $v = \beta c$, its length L_b and its duration $\tau_b = L_b/v$. The CTR field that travels at velocity c, completely overtakes the bunch self-field whenever:

$$ct_s - vt_s > c\tau_b \tag{3.34}$$

$$c(1-\beta)t_s > \frac{L_b}{\beta} \tag{3.35}$$

$$ct_s > \frac{1}{\beta(1-\beta)} L_b \tag{3.36}$$

$$ct_s > \frac{1+\beta}{\beta}\gamma^2 L_b \approx 2\gamma^2 L_b. \tag{3.37}$$

Figure 3.12(c) plots Eq. (3.37) as a function of the mean γ factor of the electron bunch for a bunch length $L_b = 10$ μm being typical of laser wakefield accelerator. Even for small value of $\langle\gamma\rangle$ the splitting time is of several tens of picoseconds, which is too long to be covered by current PIC simulations. As a result, the fields collected in PIC simulations are most of the time a mix of CTR and bunch self-field. Besides being spatially overlapped, the two types of fields belong to the same low frequency domain making impossible to distinguish them from one another.

One way to discriminate between the radiated and the self generated fields is to resort to the generalized Biot-Savart law. A simpler ansatz for the electron current is plugged, from which we

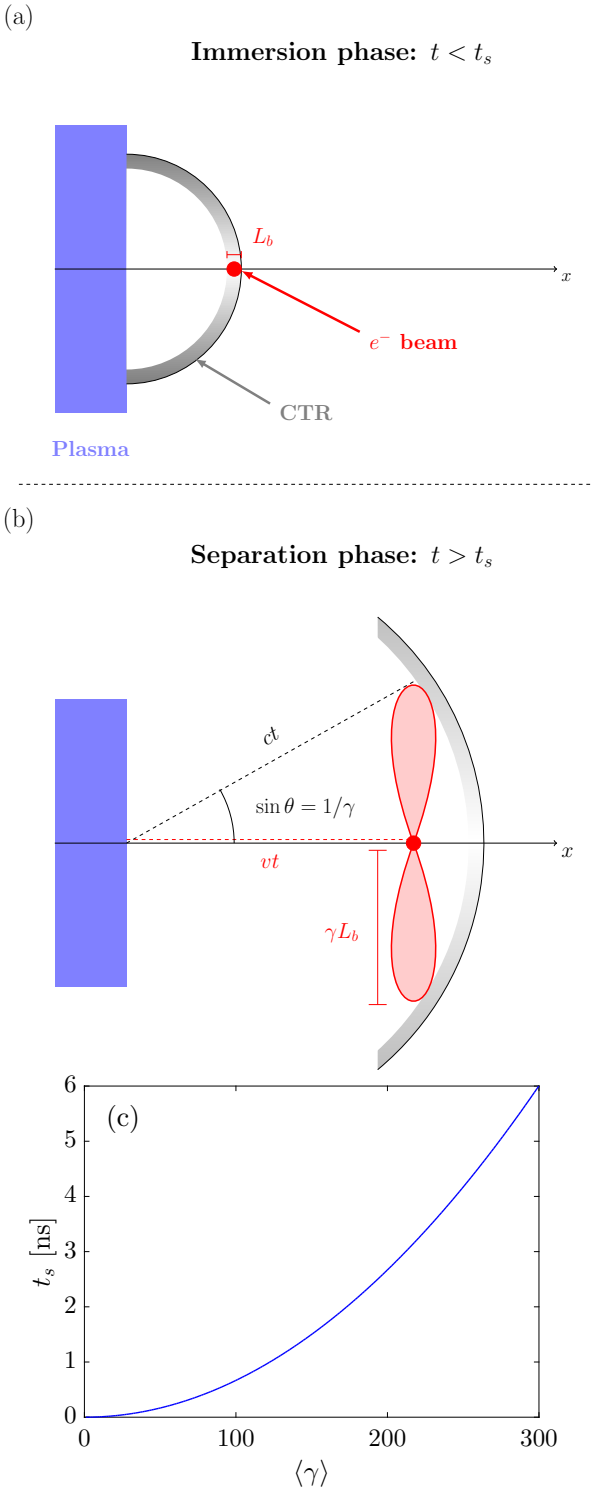

Figure 3.12: Scheme of the radiated field induced by the plasma-vacuum interface crossing mixed with the particles self-field in (a) the immersion phase and (b) the separation phase. (c) Splitting time t_s between the particles (non-radiating) self-field and the (radiating) CTR field for a bunch length $L_b = 10$ μm as a function of the mean Lorentz factor $\langle\gamma\rangle$ of the bunch.

can readily discriminate both contributions over long enough integration times. For technical convenience we go back to the simpler situation when an electron beam goes across a perfect conductor/vacuum interface.

Generalized Biot-Savart law

In this section, we evaluate the radiation by a finite-length electron bunch coming out of the perfect conductor and propagating ballistically in vacuum. The goal of the present analysis is to describe both the transition radiation at the interface and the proper field of the relativistically moving electron bunch. Our starting point is the generalized Biot-Savart law [Bellotti & Bornatici 1996]:

$$\mathbf{B}(\mathbf{r},t) = \int d\mathbf{r'} \left\{ \frac{[\mathbf{J}]}{R^2 c} + \frac{1}{Rc^2} \left[\frac{\partial \mathbf{J}}{\partial t} \right] \right\} \frac{\mathbf{R}}{R}, \tag{3.38}$$

where $R \equiv |\mathbf{r} - \mathbf{r'}|$ is the distance between the observation point $\mathbf{r}$ and the emission point $\mathbf{r'}$, brackets denote evaluation at the retarded time $t' = t - R/c$, and $\mathbf{J}$ is the current density. Basically the total magnetic field can be split into a radiated field decaying as $1/R$ and the proper field of the charge mainly behaving as $1/R^2$. We model the electron bunch as a uniformly charged filament of length L_b and zero radius, moving at constant velocity $v_b = \beta c$ along the x-axis. This corresponds to the current density

$$\mathbf{J}(\xi, y, z, t, L_b) = J_0 F(\xi, L_b) H(x) \delta(y) \delta(z) \mathbf{e}_x, \tag{3.39}$$

$$F(\xi, L_b) = \frac{H(\xi + L_b/2) - H(\xi - L_b/2)}{L_b}, \tag{3.40}$$

where $\xi = x - v_b t$, $H(u)$ [resp. $\delta(u)$] is the Heaviside [resp. Dirac] function, and $J_0 = -eN_e v_b$ where N_e is the number of electrons inside the bunch. Equation (3.39) describes the progressive emergence of the electron bunch from the plasma into vacuum occupying the half-space $x \geq 0$. This implies complete screening of the bunch inside the plasma, and hence treating the latter as a perfect conductor. Boundary conditions at the interface are solved by computing the image charge generated by a counterpropagating positron bunch, as it is classically done in transition radiation theory. This is equivalent to taking into account the contribution of the induced plasma currents.

The complete derivation is available in Appendix C, so that we give here some of the main steps. By injecting the current expression (3.39) into Eq. (3.38) we obtain the azimuthal radiated magnetic field:

$$B_\theta(x, \rho, t) = J_0 \rho \int_{-\infty}^{\infty} \left(\frac{[F]}{cR^3} + \frac{1}{c^2 R^2} \left[\frac{\partial F}{\partial t} \right] \right) H(x') dx', \tag{3.41}$$

where we have changed to polar coordinates (ρ, θ) in the transverse (y, z) plane. According to Fig. 3.13, one has

$$R^2 = \rho^2 + (x - x')^2 = \rho^2 + (\xi - \xi' + \beta R)^2, \tag{3.42}$$

admitting the solution $R = \gamma^2 \left[\beta(\xi - \xi') + S \right]$ where $S = \sqrt{\rho^2/\gamma^2 + (\xi - \xi')^2}$. Making use of $dx' = (R/S) d\xi'$, one obtains

$$B_\theta(\xi, \rho, t) = \frac{J_0 \rho}{c} \int_{-\infty}^{\infty} d\xi' \frac{1}{S} \left(\frac{[F]}{R^2} - \frac{\beta}{R} \left[\frac{\partial F}{\partial \xi'} \right] \right) H(x'). \tag{3.43}$$

The two terms of Eq. (3.43) are generated by different mechanisms. The first term corresponds

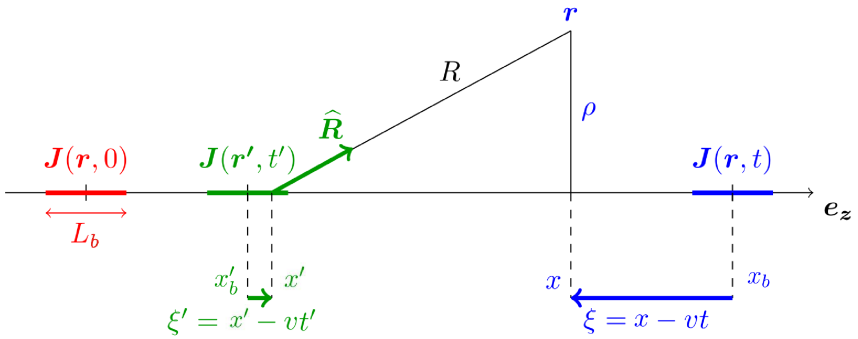

Figure 3.13: Geometry of the field emission for an extended charge distribution. At $t = 0$ the field is centered at $x = 0$ and is non-zero between the coordinates $x = -L_b/2$ and $x = L_b/2$ (red trace). The magnetic field is measured at position $\mathbf{r}$ [coordinates (ρ, x)] and time t (blue lines). At this instant, the current is centered at $x_b = vt$. The field measured at (ρ, x) has been emitted by the current $\mathbf{J}$ at the retarded time t' (green lines) and longitudinal position x'. The distance between the points $(\rho' = 0, x')$ and (ρ, x) is defined by R.

to the proper field of the ballistic bunch (self-field), i.e., the electrostatic field asymptotically generated by the bunch in its rest frame and Lorentz-transformed in the laboratory frame with velocity $-v$. Due to perfect screening in the conductor ($x < 0$) and the finite speed of light, this self-generated field builds up in the course of propagation ($x > 0$). Over long enough distances, this component corresponds to the field of the charged particles reached asymptotically, i.e., the field computed in the absence of the step function $H(x)$ in Eq. (3.39). The second component is the CTR field which is emitted at the interface and propagates at the speed of light. This component is computed by subtracting the asymptotic self-field, denoted B_θ^∞, to the total field:

$$B_\theta^{\mathrm{CTR}} = B_\theta - B_\theta^\infty. \tag{3.44}$$

In order to validate this model we performed a numerical simulation on a test case with the CALDER-CIRC code. A ballistic electron bunch of 20 $c\omega_0^{-1}$ length with a transverse size of one radial cell is initialized in a perfect conductor. The interface is set at $x = 250\ c\omega_0^{-1}$. The beginning of the separation phase, corresponding to the far field where transition radiation theories applied, is given by Eq. (3.37). For our parameters one finds $ct_s = 1000\ c\omega_0^{-1}$ predicting thus a splitting between the particle's self-field and the CTR field at time $t > 1000\ \omega_0^{-1}$, where the origin of time corresponds to the instant when the electron bunch crosses the interface.

Figure 3.14 shows the result of the comparison between the Biot-Savart model [Fig. 3.14(a)] and the CALDER-CIRC test case [Fig. 3.14(b)] at $t_0 = 3000\ \omega_0^{-1}$. At a first glance a remarkable agreement can be noticed on the two structures corresponding to the particle's field and the CTR field. The space shift between the two wave fronts corresponds to the velocity difference times the traveling time $\Delta x = (c - v_g)t_0$. Hence, the CTR is effectively located at $x_{\mathrm{CTR}} = 3250\ c\omega_0^{-1}$. A cut in the x-axis in the middle of the electron bunch over a wide range of r values is performed [Fig. 3.14(c)]. A very good agreement is recovered for the self-field (between $r = 0$ and $r = 600$) and the CTR (narrow peak after $r = 600$). The radial decay of the particle's field first follows an $1/r$ law characteristic of the electrostatic field of a line charge. After a distance of a few $\gamma L_b = 100\ c\omega_0^{-1}$ the bunch is viewed as a single particle and its related field decays as $1/r^2$. Discrepancies for small r ($r = 0$) and around the TR field are due to the interpolation method and the numerical shape function, respectively. Also unphysical field oscillations occur in front of the TR field. This is because of the electron rectangular shape favoring strong gradients that cause small numerical artifacts. Since differences between the Biot-Savart model and CALDER-

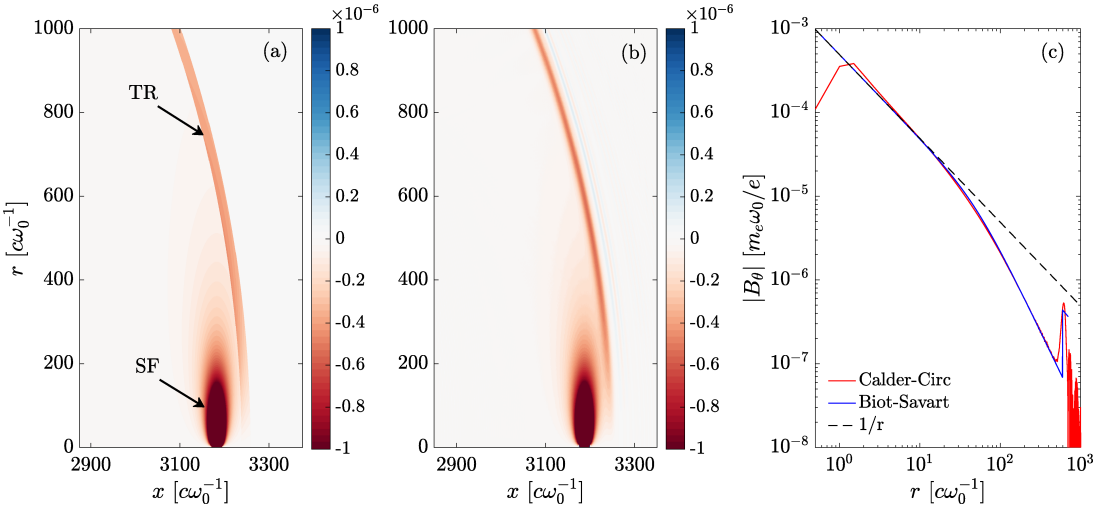

Figure 3.14: Comparison between results of (a) the Biot-Savart model and (b) the PIC code CALDER-CIRC simulating a rectangular electron bunch with length $L_b = 3$ μm and $\gamma = 5$ emerging from a perfect conductor into vacuum. (c) Radial cut profile at $x = 3250\ c\omega_0^{-1}$ from CALDER-CIRC results (red line) and Biot-Savart model (blue line), compared to $1/r$ decay (black dashed line).

CIRC are well identified and rather limited we can conclude on the relevance of the former to mimic the transition radiation phenomenon in the case of an interface separating a perfect conductor from vacuum.

Emitted fields by an electron bunch emerging from a perfect conductor

The Biot-Savart model used in the previous section enabled us to roughly evaluate the contribution of the particles self-field, which should be removed from the overall radiated energy yield computed in the simulations in order to retain only the CTR field. Here we want to give a more precise evaluation by still using the Biot-Savart model. We simulate an electron bunch of 3 μm-long and no transverse extent emerging from a perfect conductor at $t = 0$. The total azimuthal magnetic field B_θ is computed at a time larger than the splitting time such that both fields have reached their asymptotic behavior. The model is then run for different γ values.

Figure 3.15(a) shows the energy yield for the particle self-field (blue line) and the CTR field (red line) as a function of the γ factor of the electron beam. The energy repartition is clearly in favor of the self-field ($\eta \sim 0.8$) but the contribution of the latter tends to decrease with γ. As a result the CTR yield increases following a logarithmic fit (black dashed line). Note that we recover the dependancy in $\ln\gamma$ given by Ginzburg and Frank formula (2.263) for a perfect conductor-vacuum interface. The sum of the self-field and the CTR contributions (black line) is almost equal to 1; second-order discrepancies are due to the limited spatial resolution for large simulation domains. Then, higher values of γ are computationally too demanding due to the squared scaling of the splitting time, $t_s \propto \gamma^2$ [Eq. (3.37)]. Instead we extend the fitting curve up to $\gamma = 300$, in inset of Fig. 3.15(a), leading to a maximum CTR yield of ~ 0.4. Figure 3.15(b) is obtained by measuring the energy yield at each time step between 0 and 1650 fs, corresponding to 500 μm of propagation after the plasma-vacuum interface, for different values of γ. At this final instant the CTR yield is about 0.1 and 0.25 for $\gamma = 5$ and $\gamma = 150$, respectively. Also the CTR contribution is weakly dependent of γ such that only slight difference is observed between $\gamma = 150$ and $\gamma = 300$. Since we consider an ideal case for transition radiation (perfect conductor,

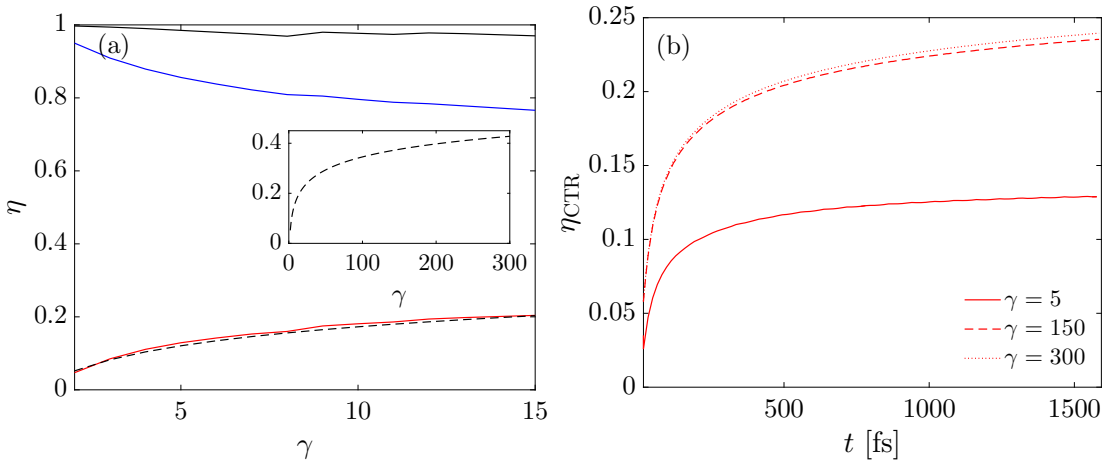

Figure 3.15: Results of the Biot-Savart model for a mono-energetic electron beam with zero radius and longitudinal length $L_b = 3$ μm. (a) Energy of the particles self-field (blue line), CTR (red line) and their sum (black line) normalized to the total emitted energy and computed at long time after the field separation [Eq. (3.37)] as a function of the electron γ factor. The black dashed line fits logarithmically the CTR yield and inset extends the fitting curve for large γ values. (b) Energy of the CTR field normalized to the total field energy as a function of the propagation time after the interface for $\gamma = 5$ (red solid line), $\gamma = 150$ (red dashed line) and $\gamma = 300$ (red dotted line).

sharp interface, infinite transverse extent, no transverse beam size, maximized coherence), the value of 25% coming from CTR can be considered as an upper limit. In other words one should only retain the CTR fraction in the measured energy yield and not include the particle self-field in these evaluations. Indeed, the latter, that contribute for at least 75% in the radiated energy, is expected to be unable to reach detectors positioned in the far field.

Going back to our main simulation we can now make use of Eq. (3.38) computed for a mono-energetic electron bunch of zero transverse radius and finite length L_b, moving at constant velocity along the x-axis. Transition radiation, given by Eqs. (3.43), (3.44), assumes that the beam emerges into vacuum through the plasma surface, assimilated to a perfect conductor (see Section 2.3).

Figure 3.16(a,b) compares the axisymmetric B_θ field measured in the 3D simulation [Fig. 3.16(a)] with the result of Eq. (3.38) [Fig. 3.16(b)] when the main electron bunch has propagated 500 μm beyond the interface. In Fig. 3.16(b), we use the parameter values $\gamma = 15$, $N_e = 8.9 \times 10^8$, and $L_b = 1.5$ μm. Good agreement is found outside the bunch ($r \geq 30\,\mu$m) between the two maps of B_θ filtered in the THz band $\nu < 90$ THz, both in amplitude and spatial shape. The main discrepancy is found inside the bunch, for which Eq. (3.38) overestimates the simulated field due to the assumed zero radius of the bunch, whereas the latter diverges to some extent in the simulation [inset of Fig. 3.16(a)]. To isolate the CTR in our calculation, we subtract the asymptotic proper field of the bunch from the total field to only retain the field contribution coming from the plasma surface. The resulting field is plotted in the inset of Fig. 3.16(b). From comparing this graph with the total field distributions of Figs. 3.16(a,b), it appears that most of the off-axis (axisymmetric) THz emission ($r \geq 30\,\mu$m) indeed originates from the plasma-vacuum interface. Nevertheless, one should be aware of the strong approximation made in the Biot-Savart model (perfect conductor-vacuum interface, balistic electron motion, zero transverse size) such that the present model can only give a rough estimate of the CTR contribution. In term of numbers, the measured energy in the baseline simulation domain is about ~ 160 μJ with 25% of which

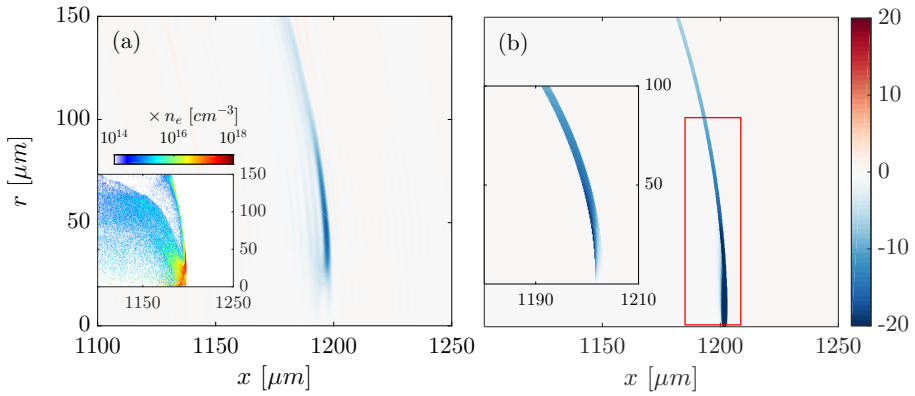

Figure 3.16: (a) 2D (x, r) map of the azimuthal magnetic field, cB_θ [GV/m], extracted at time $t = 4\,\text{ps}$ from the 3D PIC simulation of Fig. 3.8. The electron bunch and the plasma-vacuum interface are located at $x \approx 1200\,\mu\text{m}$ and $x = 700\,\mu\text{m}$, respectively. Inset shows the electron density n_e $[n_c]$. (b) Same quantity as in (a) but given by the Biot-Savart law [Eq. (3.38)]. The electron bunch parameters are detailed in the text. The inset displays the field emitted at the plasma-vacuum surface, obtained by subtracting the asymptotic proper field of the electron bunch to the total Biot-Savart field [Eq. (3.44)]. All fields in (a) and (b) are filtered in the frequency range $\nu < 90\,\text{THz}$.

should be considered as energy due to CTR (~ 40 μJ). On the other hand, Garibian formula for a point-like electron [Eq. (3.33)] predicts about 110 μJ of CTR energy in the far-field, so that the simulation domain of the PIC simulation may appear too small to capture the complete radiated field. Nevertheless, in regards of the assumptions made and the intrinsic differences with the PIC wakefield-accelerated electron bunch, a relative fair agreement is reached between the Garibian formula and the Biot-Savart evaluation.

Conclusion

In summary, by means of full-scale 3D PIC simulations, we have evidenced the sequential production of intense terahertz bursts using two-color UHI ultrashort laser pulses interacting with He gases of submillimeter lengths and $> 10^{17}\,\text{cm}^{-3}$ atomic densities. Following a primary terahertz burst induced by photocurrents, CTR by wakefield-driven relativistic electrons traversing the plasma boundary can generate terahertz pulses of $\sim 100\,\text{GV/m}$ field strengths and tens of millijoule energies using relatively modest laser parameters (3.7 J in energy, $2.2 \times 10^{19}\,\text{W/cm}^2$ in intensity). We here report a conversion efficiency of the overall emitted fields over the laser pump energy of about $\sim 5 \times 10^{-3}$. This value applies to both electron self-field and CTR; the latter is expected to represent at most 25% of the measured radiated field.

In addition, we obtained an analytical formula that captures the on-axis patterns of the GV/m-level PIR in the laser region and behind, as predicted by 1D and 3D simulations. Moreover, analytical CTR models satisfactorily match the simulated radiation in terms of spectral and field distributions. For this purpose, we have gauged the sensitivity of the CTR and PIR to the interaction setup by varying several laser and gas parameters. We finally performed a semi-analytical work on the generalized Biot-Savart law in order to extract the propagation component associated to the genuine CTR field. Our next study focuses on a parametric analysis of the electron acceleration stage performed to design even more powerful terahertz sources through CTR.

Simulations #	n_e [10^{18}cm^{-3}]	n_e [n_c]	L_p [μm]	λ_{pe} [μm]	P_c [TW]	$L_{\text{acc.}}$ [μm]
1	0.48	0.00044	16 000	47	39	30 000
2	2.4	0.0022	3 200	21	8	6 000
3	4.8	0.0044	1 600	15	4	3 000
4	9.7	0.0088	800	10	2	1 500
5	19	0.0176	400	7.5	1	750
6	48	0.044	160	4.7	0.4	300
7	121	0.11	64	3.0	0.15	120
8	242	0.22	32	2.1	0.07	60
9	484	0.44	16	1.5	0.04	30
10	1100	1	7	1	0.02	13

Table 3.1: Plasma parameters (n_e, L_p) as well as relevant plasma quantities for ten different simulations.

3.3 CTR from underdense to near-critical plasmas

The previous section proved the relevance of CTR for THz pulse generation in the relativistic regime for various input laser fields a_0 and helium neutral densities n_a. However, an optimum emission in terms of THz energy was not reached. We tackle this open issue by varying the plasma density from underdense to near-critical densities in order to scan different electron acceleration process capable of altering or improving the CTR-induced THz performances. Since we consider only transition radiation and discard PIR, the plasma is here assumed pre-ionized and a single-color laser will here be used, releasing greatly several numerical constraints (no photoionization calculation and use of larger spatial steps). We first present the interaction geometry and the simulation parameters in Section 3.3.1. Section 3.3.2 presents 10 CALDER-CIRC simulations for different plasma densities increased from underdense to near-critical values. In addition to the search for an optimum in the CTR energy yield, we report a remarkable robustness of this conversion mechanism over three decades of plasma density.

3.3.1 Framework of the parametric study

Our set of 10 simulations use the same laser input parameters as in the previous study ($a_0 = 4$, $\lambda_0 = 1$ μm, $\tau_0 = 35$ fs, $w_0 = 20$ μm) albeit with modified focusing conditions to avoid laser filamentation whenever $w_0 < \lambda_{pe}$ [see Fig. 3.20]. We again consider 3.7 J laser energy with 100 TW power and a Rayleigh length of 0.9 mm. The plasma profile is tuned such that the areal density $n_e L_p$ is kept constant. Also gradient up- and down-ramps follow the same law, $n_e L_g = cte$ where L_g is the gradient length. By doing so the pulse interacts with a similar number of electrons from one simulation to the other. The product $n_e L_p$ is fixed by the highest density used in the preceding study ($\times 40$), i.e., $n_e = 1.95 \times 10^{19}$ cm^{-3} and $L_p = 400$ μm ($L_g = 100$ μm). Thus long plasmas with low densities as well as short near-critical plasmas are studied. Scaling laws for the blow-out regime depends of the electron density such that they will vary between these simulations and affect the underlying physics. Table 3.1 details the key parameter values for each simulation labelled from 1 to 10. As the electron density increases, the plasma wavelength and the electron bubble size decrease together with the threshold for laser self-focusing P_c [Eq. (2.221)]. As a result, diffraction starts to be counterbalanced from simulation 2 ($P/P_c \sim 10$) such that the laser pulse propagates over a distance greater than the Rayleigh length by means of the self-focusing process. Also the acceleration length L_{acc} is

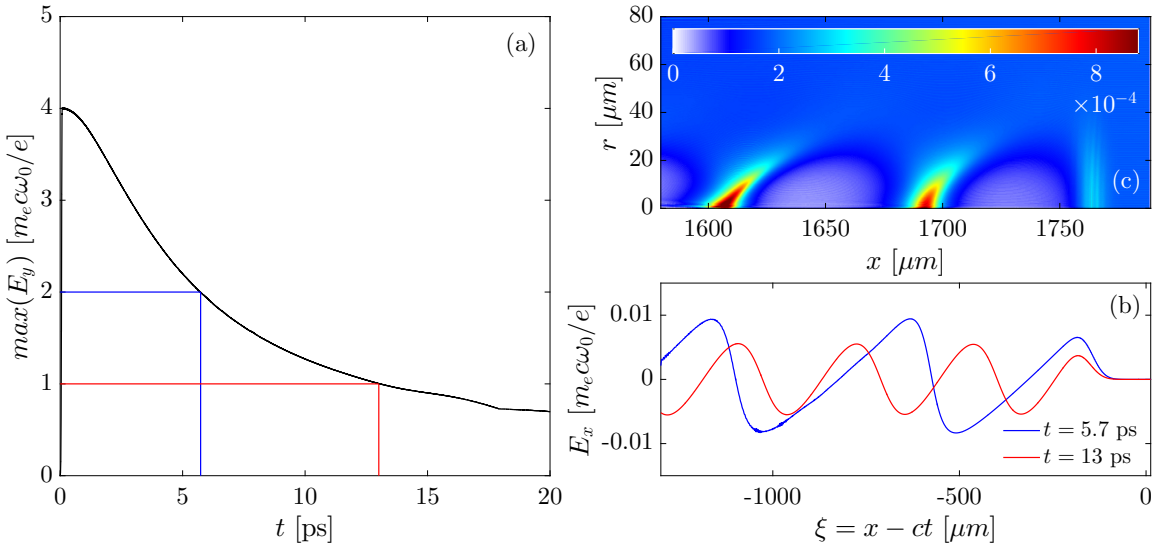

Figure 3.17: (a) Maximum transverse field E_y $[m_e c\omega_0/e]$ in the laser-polarization direction y for simulation 1. (b) Electron density $[n_c]$ in the (x, r) plane at $t = 5.7$ ps. (c) On-axis longitudinal electric field E_x $[m_e c\omega_0/e]$ at $t = 5.7$ ps (blue line) and $t = 13$ ps (red line).

always larger than the plasma length which guarantees to avoid electron dephasing (see Section 2.2.2). Varying the plasma density should then allow us to find the best electron acceleration scheme yielding maximum THz emission by CTR.

3.3.2 Simulation results

The goal of these 10 PIC simulations is to extract a map of CTR energy yield as a function of the plasma density. We seek an optimum in the radiated energy corresponding to a specific electron acceleration regime. Similar simulations are presented in the same package such as simulations 2, 3, 4 and 5 as well as 7, 8 and 9.

The smallest electron density in simulation 1 ($n_e = 2.4 \times 10^{17}$ cm^{-3} $= 4.4 \times 10^{-4} n_c$) is associated to the longest plasma length ($L_p = 16$ mm). Due to the long linear density up-ramp ($L_g = 4$ mm), the laser pulse does not self-focus ($P/P_c \leq 2.5$) and just diffracts as illustrated by Fig. 3.17(a). In addition the plasma wavelength is not matched to the longitudinal and transverse dimension of the laser beam, $\lambda_{pe}/c\tau_0 = 4.5$ and $\lambda_{pe}/w_0 = 2.35$. Therefore, the plasma wave is not resonantly excited by the laser pulse. When the amplitude of the laser pulse reaches a normalized amplitude of $E_y = 2$, a quasilinear plasma wave is nevertheless excited and induces regions of higher electron density [see Fig. 3.17(b,c)]. The laser amplitude continues to drop along propagation until reaching sub-relativistic intensity ($E_y < 1$). There, the longitudinal plasma wave recovers linear, harmonic oscillations [see Fig. 3.17(c)] and is thus unable to promote particle injection such that no CTR can be reported.

Simulations 2 to 5 exhibit similar features during the laser propagation in the plasma channel. We plot in Fig. 3.18 the electron density (top) and energy distribution along the x axis (bottom), just before the plasma exit for these four simulations. They all develop a bubble shape with an injected electron beam. Indeed, the blow-out regime is satisfied from simulation 2 ($\lambda_{pe}/w_0 \sim 1$ and $P/P_c \sim 10$) in which self-injection occurs prior to the density down-ramp. Successive ion cavities are formed and the electron energy distribution adopts a V-shape around 800 MeV and 400 MeV for the first and second injected bunch, respectively [see Fig. 3.18(a)]. This particular form comes from the interplay between the longitudinal accelerating field and the own electron

beam field (beamloading), which modulates the maximum energy acquired by the accelerated electrons, before the exiting density gradient. By contrast, the dense line for $4840 \leq x \leq 4860$ μm corresponds to electrons injected continuously in the density down-ramp. The same apply for the second bunch ($4820 \leq x \leq 4830$ μm). This dynamics results in an elongated bubble whose longitudinal dimension (~ 100 μm) is due to the linear decrease along the density down-ramp ($\lambda_{pe} \propto 1/\sqrt{n_e}$). Figure 3.18(a) shows a snapshot of the electron density just before the plasma exit where the self-injected electron populations, created all along the plasma channel, merge with the lower energetic population injected in the linear density transition [Bulanov *et al.* 1998]. The two electron population tend to form a unique long bunch of about ~ 50 μm containing a nC-level charge ($Q \sim 2.5$ nC). Due to longitudinal coherence effect (see Section 2.3.4) we can expect radiated wavelength $\lambda > 50$ μm corresponding to frequencies lower than 6 THz.

A similar energy pattern is found in simulation 3 for which the plasma density is twice higher [see Fig. 3.18(b)]. However, due to the shorter plasma length, only one bunch is accelerated up to ~ 500 MeV. Hence the electron bunch exiting vacuum is shorter (~ 30 μm).

Increasing again the density by a factor two yields the plasma wavelength $\lambda_{pe} = 10$ μm that matches the laser length $c\tau_0$ such that a high charged bunch ($Q \sim 5$ nC) can be formed [Fig. 3.18(c)]. Despite this optimum configuration for LWFA, the gradient length is shorter ($L_g n_e = cte$) and the bubble is less elongated than in previous simulation resulting in a shorter bunch too. The V-shape of self-injected electrons is modified since the front of the beam is decelerated by the continuous decrease of the plasma wave amplitude in the density down-ramp. Also the field of the electron bunch alters the longitudinal accelerating field (beam loading, see Section 2.2.2) contributing to the characteristic shape of the energy distribution. This dynamics limits the bunch maximum energy to 300 MeV.

The last simulation of this series corresponds to the final case of the previous study [Fig. 3.18(d)]. Beamloading happens before the density gradient within a rather small electronic bubble ($\lambda_{pe} = 7.5$ μm). Nevertheless due to strong self-focusing [$P/P_c \sim 100$ and $max(E_y) = 22$] particle acceleration is still efficient and a large amount of charge escapes from the plasma, still yielding (rather) energetic electrons (200 MeV).

Figure 3.19 presents the axisymmetric ($m = 0$) azimuthal field B_θ filtered by a low pass filter ($\omega < 0.3\,\omega_0$) at a distance of ~ 500 μm after the plasma-vacuum interface for simulations 2, 3, 4 and 5. The emitted fields show common features such as an important amplitude higher than 50 GV/m as well as a spherical propagating wave front. The blue field region above the CTR fields are due to the expanding wall of the bubble. As anticipated when looking at the bunch lengths, the radiated frequency ω builds up coherently up to $2\pi c/L_b$ (see Section 2.3.4) such that a long bunch leads to long pulse duration (short frequencies). Hence, simulation 5 exhibits the shortest pulse length [see Fig. 3.19(d)] associated in the frequency domain to a broader spectrum going up to $2\pi c/L_b = 2\pi \times 30$ THz for $L_b = 10$ μm. Higher frequencies are also present but they are of negligible amplitude and they correspond to an incoherent emission for $\nu > 2\pi c/L_b$.

From simulation 6 illustrated in Fig. 3.20(a) the plasma wavelength becomes smaller than the laser focal spot ($\lambda_{pe} = 4.7$ μm versus $w_0 = 20$ μm) and transverse multiple filamentation occurs. The dispersion relation inferred from a plane wave analysis of the propagation equation for the transverse electric field leads to [Drake *et al.* 1974]:

$$k^2 = \frac{1}{4\omega_0^2}\left(k_\perp^4 c^2 - 2\omega_{pe}^2 a_0^2 k_\perp^2\right), \tag{3.45}$$

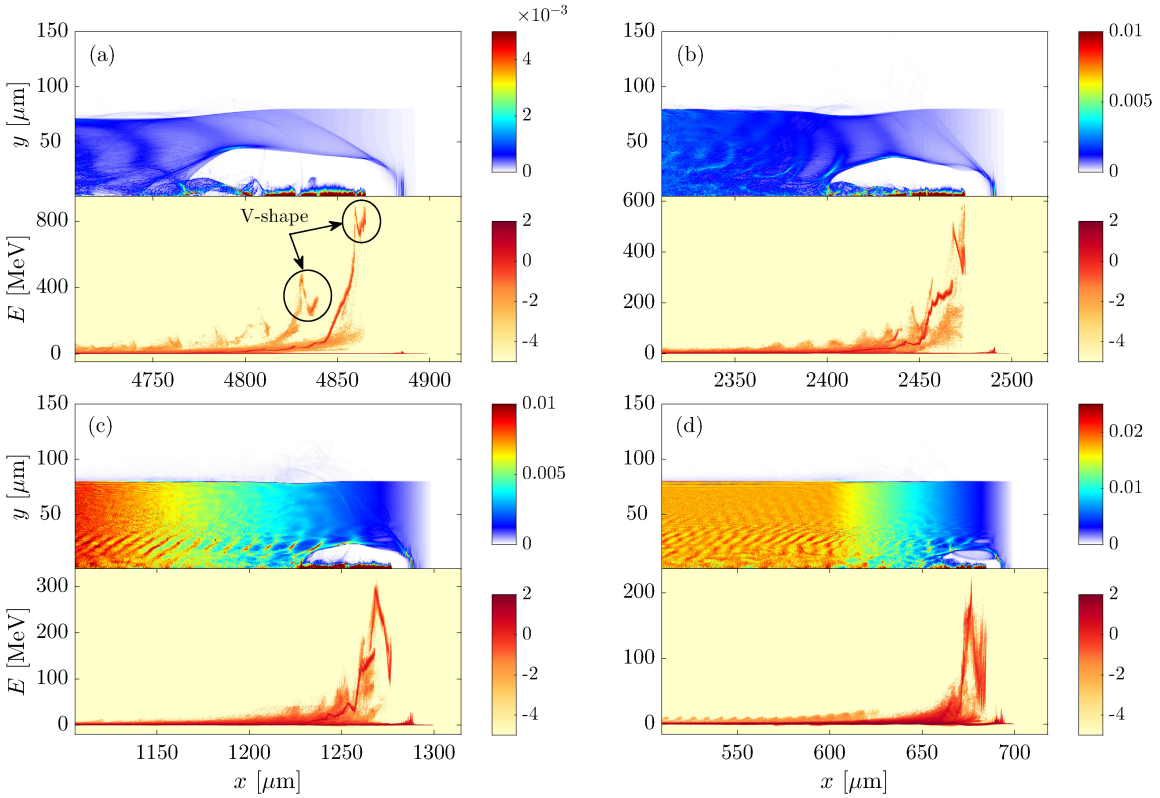

Figure 3.18: Electron density map n_e $[n_c]$ (top part) and energy distribution E [MeV] along the x-axis in $\log_{10}$ scale (bottom part) before the plasma exit for (a) simulation 2, (b) simulation 3, (c) simulation 4 and (d) simulation 5.

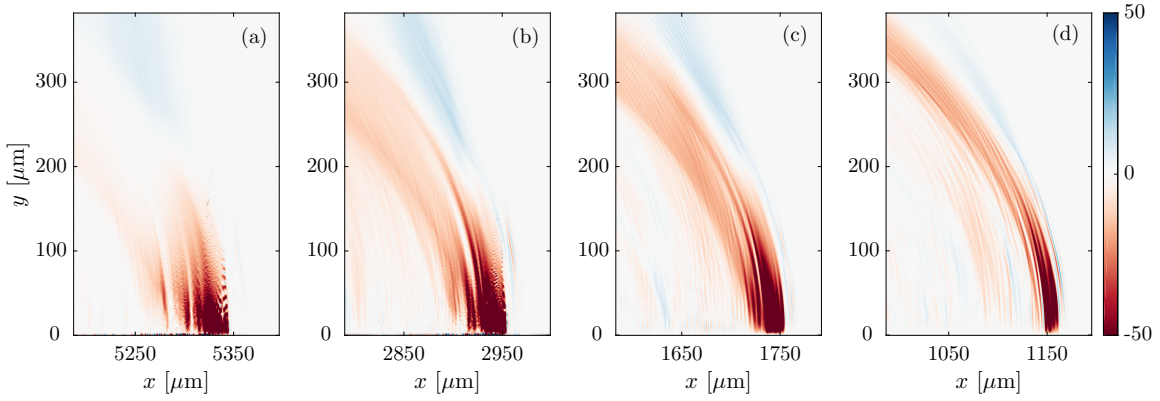

Figure 3.19: Radiated axisymmetric cB_θ [GV/m] field $\sim$ 500 μm after the plasma-vacuum interface for (a) simulation 2, (b) simulation 3, (c) simulation 4 and (d) simulation 5.

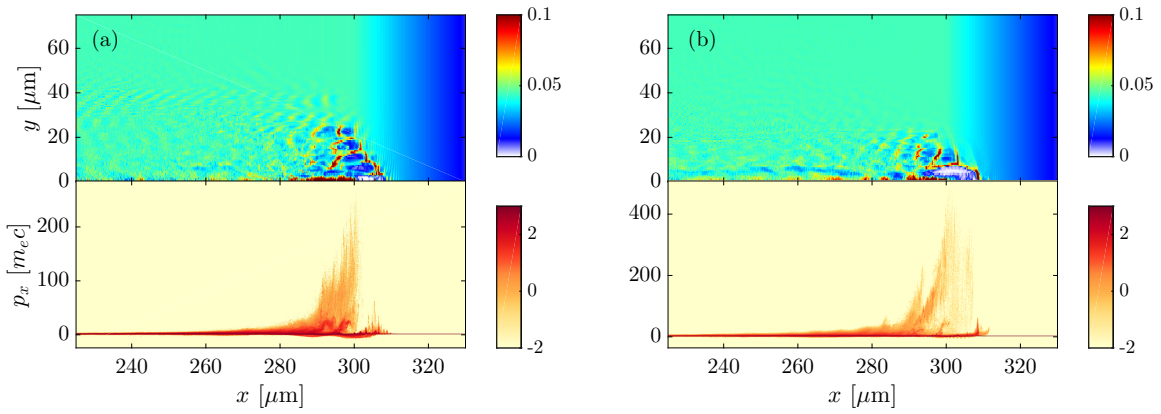

Figure 3.20: Electron density map n_e [n_c] (top part) and longitudinal phase space (x, p_x) in $\log_{10}$ scale (bottom part) before the plasma exit for simulation 6 for a laser waist (a) $w_0 = 20$ μm and (b) $w_0 = 5$ μm.

with $k_\perp = 2\pi/w_0$ denoting the transverse wave vector. The instability is triggered for perturbations with complex wave numbers, $k^2 < 0$, corresponding to $k_\perp < k_{\rm lim} = \sqrt{2}\omega_{pe}a_0/c$. In our case the limit transverse vector is $k_{\rm lim} = 1.18\ k_0$ while a waist of $w_0 = 20$ μm implies that $k_\perp = 0.05\ k_0$, such that filamentation can no longer be avoided, as observed in this figure. This physical phenomenon is not well described by CALDER-CIRC since we take into account a limited number of azimuthal modes only. As a result electron acceleration is less efficient. We thus decided to decrease the laser waist ($w_0 = 5$ μm) and to increase the maximum amplitude at the focal point ($a_0 = 16$) such that the overall laser energy injected in the simulation domain is conserved. The out-going bubble is naturally elongated with an important energy dispersion [see bottom of Fig. 3.20(b)]. Nevertheless, the laser energy is better confined, which favors the production of more energetic and a better homogeneity of the transverse profile.

From there the interaction regime changes and the plasma becomes too dense to be resonantly excited. Due to the fixed pulse length ($c\tau_0 = 10$ μm), the blowout matching conditions [Eqs. (2.223), (2.228)] are not fulfilled anymore ($\lambda_{pe} < 3$ μm), even if the laser waist has been decreased. Laser parameters for simulation 7, 8 and 9 are $(a_0, w_0) = (27, 3); (32, 2.5); (32, 2.5)$, respectively. The electron density map of Fig. 3.21(a) still shows a bubble shape with radius $\sim \lambda_{pe} = 3$ μm and a similar phase space of the previous simulation [Fig. 3.20(b)]. The front of the laser pulse begins to be depleted and develops an optical shock (see transverse field E_y) pushing electrons forward [Debayle *et al.* 2017]. In simulation 8 [Fig. 3.21(b)], electron acceleration occurs all along the laser profile with a period $2\omega_0$ as observed on the electron density and the longitudinal phase space. We enter in a regime of extreme beam loading in which the hot electron self-field inhibits the longitudinal accelerating field. Also the background neutralizing cold electron current (weaker values of $p_x < 0$) seems weaker than reported in Debayle *et al.* [2017], partially due to the small transverse size of our laser beam. Simulation 9 [Fig. 3.21(c)] shows similar features in a twice denser plasma ($n_e = 0.44 n_c$). The emitted low frequency field (not shown) recovers the one presented in Fig. 3.19(d) with lower amplitude and reduced spatial extent. The last simulation at $n_e = n_c$ with 7 μm thick plasma exhibits similar behaviour with an optical shock pushing electrons over the laser pulse length (not shown).

Summarizing the above simulation results, Fig. 3.22 displays the low frequency ($\omega < 0.3\omega_0 \equiv$ 90 THz) energy computed at $x = 500$ μm after the plasma-vacuum interface with respect to the initial plasma density (blue line). An optimum is reached for simulation 4, corresponding to Fig. 3.18(c) and Fig. 3.19(c), with a total energy of about ~ 40 mJ. Since the CTR energy

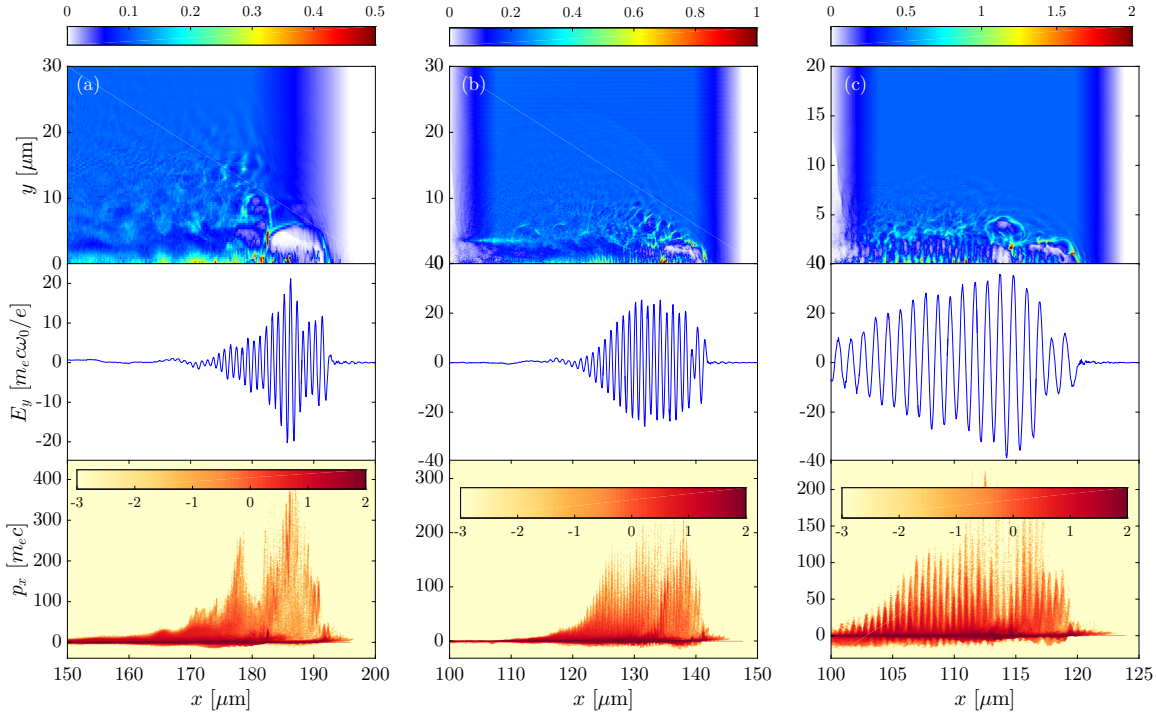

Figure 3.21: Electron density n_e $[n_c]$ map (top part), on-axis laser electric field E_y $[m_e c\omega_0/e]$ (middle part) and longitudinal phase space (x, p_x) in $\log_{10}$ scale (bottom part) for (a) simulation 7, (b) simulation 8 and (c) simulation 9.

depends linearly on the bunch energy E and quadratically on the bunch charge Q, we also plot the result of $\langle E\rangle n_e^{2/3}$ (black dashed line) and Q (red dashed line). According to the blow-out scaling law Eq. (2.230), the injected electron energy scales as $n_e^{-2/3}$ at fixed laser wavelength and power. Hence the flat portion of the $\langle E\rangle n_e^{2/3}$ curve means that the mean bunch energy follows the blow-out scaling law and corroborates the dynamical scenarios of Fig. 3.18. Maximum radiated energy yield (simulation 4) is reached when the ejected charge Q is also maximized, which is consistent with the classical Q-scaling of the CTR (see Sec. 2.3). For denser plasmas ($n_e > 4.4 \times 10^{-2} n_c$) the mean THz energy increases while the charge, after a fall of 40%, does not vary so much. The main result is the remarkable robustness of the total energy yield that only varies by a factor ~ 5 over three plasma density decades. Indeed, albeit simulation 1, our extracted values reach the same order of magnitude despite very different acceleration processes. We should moreover keep in mind that, as demonstrated in Section 3.2.4, the energy measured 500 μm after the plasma-vacuum interface also contains the contribution of particles self-field. The absolute value measured in simulation 4 is 40 mJ, yielding more realistically a radiated CTR energy of a few mJ only.

Conclusion

This chapter investigated for the first time the generation of THz waves by two-color laser pulses in the relativistic regime. We solved semi-analytically the photocurrent-induced radiated field coupled to photoionization and the nonlinear plasma wave. Our analytical expression, compared to 1D and 3D PIC simulations, correctly reproduced the two different THz emissions. The first one happens in the laser head and results from the coupling between rapidly-varying density steplike increase and the laser electric field rendered asymmetric by the two colors. This is a direct extension of the photocurrent emission in the classical regime. Due to coupling with

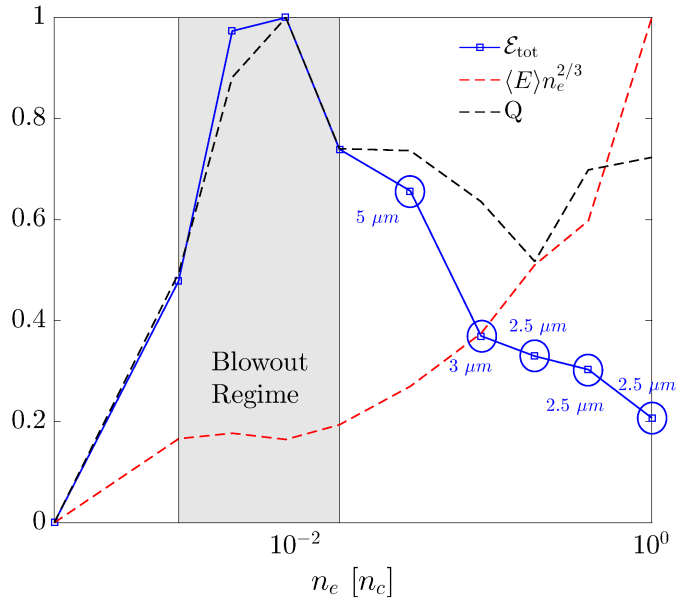

Figure 3.22: Total radiated energy (blue line), $\langle E \rangle n_e^{2/3}$ product (red dashed line) and electron bunch charge Q (black dashed line) extracted from simulations and normalized to their respective maximum value, as function of the plasma electron density (simulation 2-10). Blue circles give the value of the laser waist. Gray area delineates electron density values matching the blowout regime (see text).

the remnant transverse momentum after the laser passage, secondary emissions occur at the high density peaks which form the nonlinear plasma wave. Meanwhile, electrons are eventually injected into ion cavities forming a wakefield-accelerated electron bunch. When crossing the plasma-vacuum interface they emit CTR. We uncovered an unexpected strong THz signal from CTR, being at least one order of magnitude higher than the PIR. A second study focusing on optimization of this mechanism demonstrated the robustness of CTR for a wide range of plasma parameters. An optimum for low-frequency emission has been found in the highly-charged blow-out regime with a measured energy of about 40 mJ. Despite the difficulty to split the CTR contribution from the particle self-field, the Biot-Savart model applied to a uniform 1D electron density suggests to limit the effective CTR component contribution to 25% of the total measured energy. As a result transition radiation induced by a wakefield-accelerated electron bunch at the plasma-vacuum interface can reach high field amplitude associated to few mJ energy, which makes UHI lasers quite attractive for producing energetic THz fields.

Chapter 4

THz emission with long laser wavelength

Contents

The current chapter is devoted to laser-plasma interactions using long pump wavelengths. Recently new light sources operating in the mid-infrared spectral range (1.6, 2, and 3.9 μm) have shown their ability and advantages in overcoming the relativistic threshold. Generally speaking, such drivers provide a more efficient coupling between the laser energy and the plasma, compared to near-infrared pulses. Their inherent dynamics is explained in Section 4.1 by means of an analytical 1D model. With 2D PIC simulations (Sec. 4.2), we then study the nontrivial impact of the photoionization on the transverse and longitudinal momenta when considering mid- to far-infrared laser pulses interacting with an underdense helium gas (Sec. 4.2.2). The plasma wave is enhanced and its feedback on the propagating laser pulse results in an important frequency downshift. The latter is found to be responsible for an efficient low-frequency field emission in the THz spectral band (Sec. 4.2.3). Also, the nonlinear plasma wave favors pulse self-focusing, and thus better electron acceleration leading to coherent transition radiation (CTR) at the plasma-vacuum interface (Sec. 4.2.4) which promotes higher conversion efficiency than Chapter in 3.

4.1 Influence of the laser wavelength on laser-plasma interaction

4.1.1 Relativistic mid-infrared lasers

In the perspective of optimizing a THz source, it is important to gauge the influence of the accessible experimental parameters on the different generation mechanisms, either in classical or relativistic regime. In Chapter 3 we modified the initial gas density as well as the laser focusing condition (decrease of the waist) to seek an optimum for CTR in the THz range. Here we want to address the influence of the laser wavelength on the relativistic plasma dynamics.

This purpose is motivated by recent original works exploring the strong influence of the carrier wavelength, which demonstrated the advantages of using long laser wavelengths to increase the THz yield in classical laser-gas interactions. Experimentally Clerici *et al.* [2013] showed with a two-color laser that 1.8 μm pump wavelength leads to 30 times stronger THz signal compared to a 800 nm fundamental wavelength, thus an effective wavelength scaling for the THz energy of $\lambda_0^{4.6}$ was inferred. This strong scaling was claimed to follow from the combined effect of the λ_0 dependance with respect to (i) the induced plasma current [Eq. (2.72)] (λ_0^2 in energy) and (ii) the plasma volume, determined by the focusing conditions. Even stronger scaling might be expected with TOPAS systems (λ_0^α, with $5.6 \leq \alpha \leq 14.3$) as reported by Nguyen *et al.* [2019]. Those experiments have been completed by 3D numerical simulations of the UPPE to clear up the scaling on theoretical grounds. The numerical data recovered quantitatively the experimental results of Clerici *et al.* [2013] whereas the role of the plasma volume seems minor, the accurate knowledge of the relative phase between the two laser harmonics at the exit of the doubling crystal was proven to be the key parameter. Nevertheless the overall THz energy is of a few μJ, limiting *de facto* applications requiring high energy fields.

Passing from near- to mid-infrared wavelength with a relativistic field amplitude is complex, mainly due to the nonlinear nature of the interaction. Recently, tunable, relativistic single-cycle pulses in the range 10-40 THz with 1.7% conversion efficiency were numerically reported [Nie *et al.* 2018], based on photon frequency downshift monitored by a tailored plasma density profile. On the other hand, mid- and far-infrared light sources supplying TW peak powers are nowadays available. Femtosecond laser facilities with 3.9 μm central wavelength opened the way to multi-octave supercontinuum generation [Kartashov *et al.* 2012] and were shown to accelerate electrons by means of relativistic self-focusing up to 12 MeV energy in gas jets [Woodbury *et al.* 2018]. CO_2 lasers ($\lambda_0 = 10.6\,\mu$m) are today operational in the ps range [Tochitsky *et al.* 2012, 2018]. Their technology, rapidly evolving to the 100 TW level, will soon provide revolutionary sources for studying new regimes in particle acceleration [Palmer *et al.* 2011; Tresca *et al.* 2015] and future colliders [Pogorelsky *et al.* 2016a,b,c]. Therefore, it is worth anticipating the gain that such optical sources may offer in THz science, since their carrier wavelength is already close to the spectroscopy range of interest. Exploring relativistic interactions for this scope remains to be addressed.

4.1.2 Laser propagation and photoionization at long wavelength

The interaction of a laser pulse with a plasma is dependent on its intensity I_0 and wavelength λ_0. Together they allow to define the ponderomotive force $F_p \simeq -m_e c^2 \nabla a^2/2$ (with a the vector potential envelope) acting on the particles composing the plasma. For strong enough normalized vector potential, the ponderomotive force accelerates particles close to the speed of light. The onset of this nonlinear relativistic regime is given by the maximum value of the normalized vector potential $a_0 = 0.85\sqrt{I_{18}}\lambda_{\mu m} \geq 1$ [Eq. (2.179)]. Historically, the CPA method

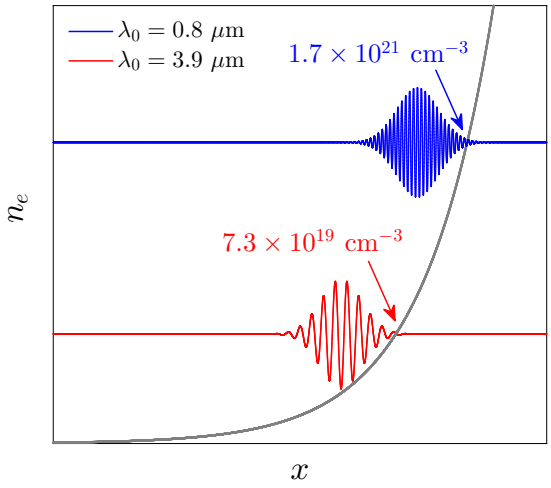

Figure 4.1: Schematic of the critical density threshold before plasma opacity for two different laser wavelengths.

allowed Ti:sapphire lasers ($\lambda_{\mu m} = 0.8$) to deliver optical pulses with ultrashort duration (~ 100 fs), opening the route to ultra-high intensities ($I_{18} \geq 2.1$ for $\lambda_{\mu m} = 0.8$). Thus, the field of relativistic laser-plasma interaction made an impressive jump in the 2000's and seems to initiate new promising perspectives with mid-infrared lasers. Indeed, shorter and shorter lasers pulses with long wavelength become available, providing few-to-single optical cycles and rendering the relativistic threshold easily exceeded at much smaller intensity because of the strong λ-scaling: $a_0^2 \propto I_0 \lambda_0^2$.

Also, the onset for plasma opacity is defined by the critical density, which is a λ_0-dependent quantity: $n_c \propto 1/\lambda_0^2$ as given by Eq. (2.81). Figure 4.1 illustrates an exponential density ramp $n_e(x)$ with two laser pulses having different carrier wavelength, 0.8 μm (blue line) and 3.9 μm (red line). Due to the plasma dispersion, $\epsilon = 1 - n_e(x)/n_c$, the reflection point of the mid-infrared laser appears at much smaller plasma density than that of the 0.8 μm pulse. Indeed, underdense plasmas created by a standard gas jet for laser wakefield acceleration serves as near-critical targets for mid-infrared laser pulses. As a result, well characterized and reproducible near-critical target can be easier to produce at long wavelength whereas one has to consider cryogenic helium modified gas-jets with near-infrared pumps, which is technologically more difficult. Hence, for a fixed physical plasma density n_e, the relative density n_e/n_c is increased when increasing the laser wavelength. Mid-infrared laser pulses are suitable to unveil the underlying physical mechanisms in the parameters region $a_0 \geq 1$ and $n_e/n_c \sim 1$ for which there is a lack of clear experimental and theoretical studies. The relativistic near-critical regime is specially rich of phenomena because the relative plasma density n_e/n_c appears in numerous nonlinear effects, e.g. self-focusing and plasma instabilities, such as the Raman instability. The critical power for self-focusing decreases when increasing the relative plasma density $P_c \propto (n_e/n_c)^{-1}$ and results in a easier self-focusing favorable to electron acceleration as demonstrated by Woodbury *et al.* [2018]. Also the Raman growth rate in relativistic regime derived by Guérin *et al.* [1995] scales as $\Gamma \propto (n_e/n_c)/\omega_0 \propto \lambda_0$ favoring SRS for mid-infrared pulses.

The last process of interest is the photoionization. In the context of laser-wakefield acceleration, near-infrared lasers ($\lambda_{\mu m} = 0.8$) are usually employed to drive the plasma wake created in an helium gas jet. Electron acceleration occurs by self-injection for $a_0 \geq 3 - 4$ such that ultra-high intensities of about $\sim 10^{19}$ W/cm^2 are needed (see Section 2.2.2). Helium atoms are quasi-instantaneously ionized in the foot of the laser pulse since the ionization potential for

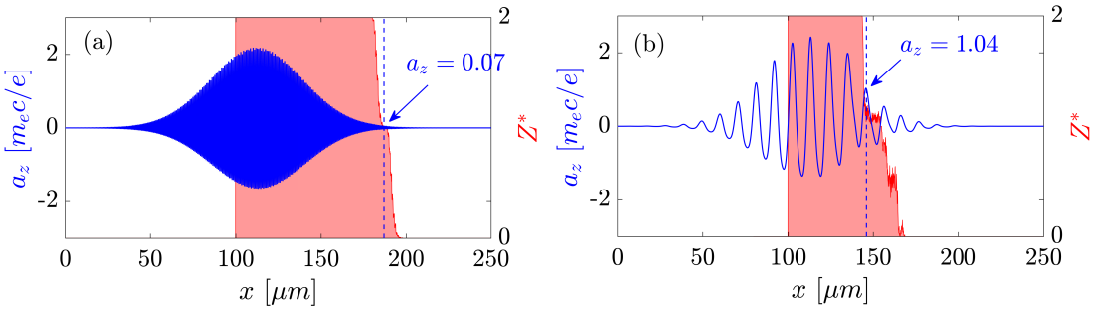

Figure 4.2: Normalized vector potential a_z $[m_e c/e]$ (blue line) and ionization degree Z^* reached in a helium gas jet for (a) $\lambda_0 = 0.8$ μm and (b) $\lambda_0 = 10.6$ μm. The normalized maximum vector potential of the two lasers is $a_0 = 2.2$ with a duration of 150 fs. Blue arrows indicate the value of a_z for the ionization of the second electronic shell. The vertical dotted lines point out to the second ionization position $x_{ioni.}$.

the second electronic shell, $U(\mathrm{He}^{2+}) = 54.5$ eV, corresponds to an intensity of $\sim 10^{16}$ W/cm^2 only. This is the reason why numerical PIC simulations often consider a pre-ionized plasma in order to reduce the computational cost. By doing so, we assume that the influence of the ionization on the electron dynamics is weak. We will see in the present chapter that this is no longer the case when using mid-to-far-infrared laser wavelength, e.g. $\lambda_{\mu m} = 10.6$. Indeed, due to the longer wavelength, the latter can drive a similar plasma wake, with identical a_0, at much smaller intensity $\sim 10^{16-17}$ W/cm^2. As a result, ionization occurs in the laser field where the residual transverse momentum, which is equal to the vector potential at the ionization instant, is not necessary negligible. Figure 4.2 illustrates this situation for a near-infrared ($\lambda_0 = 0.8$ μm) and a CO_2 laser ($\lambda_0 = 10.6$ μm) both propagating in a helium gas jet with initial density $n_a^0 = 5.5 \times 10^{17}$ cm^{-3} (see Section 4.2 for details). Due to the strong field amplitude, helium atoms are rapidly ionized in the very beginning of the pulse [see Fig. 4.2(a)]. This is the usual situation in which the residual momentum evidenced in Section 3.1.2 is small [$a_z(x_{ioni.}) = 0.07$, where $x_{ioni.}$ is the position of the second ionization]. By contrast, a mid-infrared laser pulse extracts electrons with a much higher transverse momentum [$a_z(x_{ioni.}) = 1.04$], close to the peak maximum, leading to a stronger transverse current. Also, ionization happens within a few steep density steps following the optical cycles. This simple particle description needs of course to be completed with comprehensive PIC simulations (see Section 4.2) but it already underlines the peculiar ionization dynamics at long pump wavelengths. Before dwelling with these simulations we first propose a 1D fluid model to foresee the possible consequences of the above properties on the plasma wave.

4.1.3 1D model for ionization pressure

We again resort to our fluid model derived in Section 3.1.1 which now takes into account the complete influence of the ionization by solving the system Eqs. (2.61), (2.63) with the ADK rate. As demonstrated, the canonical transverse momentum is not conserved since electrons acquire a residual momentum. Here we improve this model in two steps under the previous approximations (1D cold quasi-static wave). First, we consider that the laser pulse propagates in a plasma at the group velocity $v_g = c\beta_g = c\sqrt{1 - Z^* n_a^0/n_c}$ instead of vacuum. This is important at long wavelengths, i.e., when the relative density is close to 1, to model the plasma

wave. The variable of the co-moving laser frame are

$$\xi = x - c\beta_g t \tag{4.1}$$

$$\tau = t. \tag{4.2}$$

Second, because of the physical reasons described above, the source term S_{ext} modeling the electron generation by photoionization is now included in the longitudinal momentum equation [see Eq. (3.11)] leading to

$$\left(\frac{p_x}{\gamma} - \beta_g\right)\partial_\xi p_x = \partial_\xi \phi - \frac{p_\perp}{\gamma}\partial_\xi a_\perp - \frac{p_x S_{\text{ext}}}{c n_e}, \tag{4.3}$$

where p_x and $p_\perp \equiv (p_y^2 + p_z^2)^{1/2}$ are expressed in $m_e c$ units, $a_\perp \equiv eA_\perp/m_e c$ is the normalized transverse vector potential and $\phi \equiv e\Phi/m_e c$ is the normalized potential of the plasma wave. The transverse momentum, the scalar potential and the electron density recover the expression given by Eqs. (3.12), (3.17), (3.14), respectively, accounting in addition the influence of the laser group velocity ($v_g = c\beta_g$):

$$\partial_\xi(p_\perp - a_\perp) = -\frac{p_\perp S_{\text{ext}}}{c n_e(p_x/\gamma - \beta_g)}, \tag{4.4}$$

$$\partial_\xi^2 \phi = \frac{\omega_{pe}^2}{c^2}\frac{p_x}{\gamma\beta_g - p_x}, \tag{4.5}$$

$$n_e = \frac{\sum_{j=1}^{Z} j n_i^{(j)}}{1 - p_x/(\gamma\beta_g)} = \frac{n_e^0}{1 - p_x/(\gamma\beta_g)}, \tag{4.6}$$

with $n_e^0 = \sum_j j n_i^{(j)}$ just stands for the ion density steps driven by the ionization [Eqs. (2.61), (2.63] system without the influence of the plasma wave oscillations $1 - p_x/(\gamma\beta_g)$.

The photoionization source term of the longitudinal and transverse momenta can be re-expressed as the gradient of the ionization front since $S_{\text{ext}} = -c\beta_g \partial_\xi n_e^0$. Hence, by using Eq. (4.6), the photoionization source term becomes

$$-\frac{p_i S_{\text{ext}}}{c n_e} = \frac{\beta_g p_i}{n_e}\partial_\xi n_e^0 = -\left(\frac{p_x}{\gamma} - \beta_g\right) \times p_i \frac{\partial_\xi n_e^0}{n_e^0} \tag{4.7}$$

with $i = \{x, \perp\}$ in p_i. After simplification, the coupled momenta equations are:

$$\partial_\xi p_x = \left(\partial_\xi \phi - \frac{p_\perp}{\gamma}\partial_\xi a_\perp\right)\left(\frac{p_x}{\gamma} - \beta_g\right)^{-1} - p_x \frac{\partial_\xi n_e^0}{n_e^0}, \tag{4.8}$$

$$\partial_\xi(p_\perp - a_\perp) = -p_\perp \frac{\partial_\xi n_e^0}{n_e^0}. \tag{4.9}$$

The additional photoionization source term breaks the conservation law of the transverse momentum as already underlined and, more importantly, it now appears in the longitudinal momentum equation with the same sign than the ponderomotive force.

The factor $\partial_\xi n_e^0/n_e^0$ measures the steepness of the ionization front. When $|\partial_\xi n_e^0/n_e^0| > 1$, ionization happens in a few laser cycles with steep density steps leading to a strong photoionization term [Gordon *et al.* 2001]. This ionization-induced ponderomotive force, or ionization

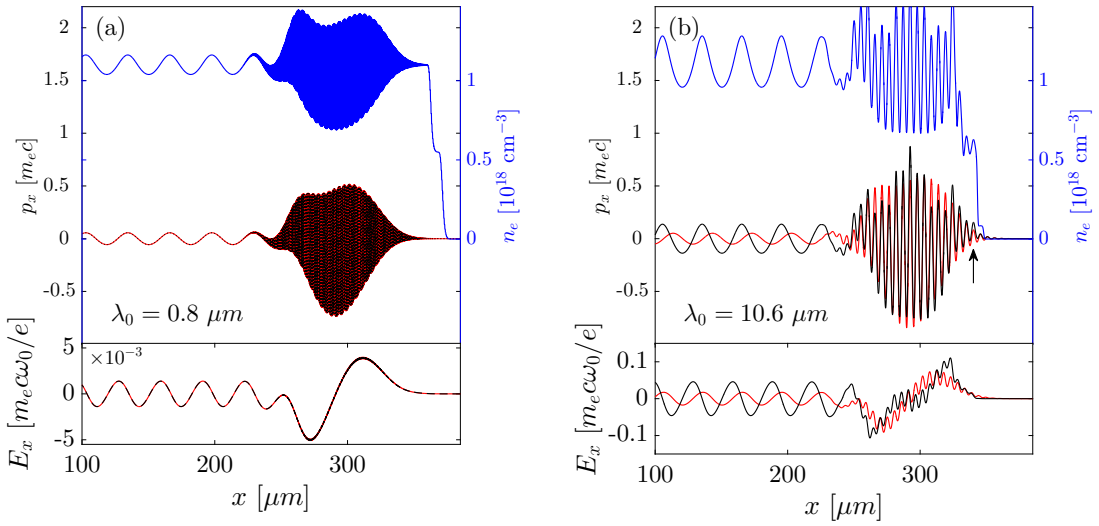

Figure 4.3: (a,b) On-axis longitudinal momenta computed from the 1D quasi-static fluid model Eqs. (4.3)-(4.6). Red curves refer to a pre-ionized plasma; black curves to ionized helium [both superimposed in (a)]. The blue curve details the increase in the electron density (right-hand side axis). Bottom plots show the longitudinal electric field E_x $[m_e c\omega_0/e]$ with the same colorstyle.

pressure, is responsible for the enhancement of the plasma wave since the longitudinal momentum is constantly added to the electron fluid in the ionization front region [Mori & Katsouleas 1992]. Hence one needs first to create the plasma wave from a primary ionization sequence, before inducing additional pressure from next ionization events. This requires a multi-ion gas species as demonstrated below with PIC simulations. Interestingly ionization is able to develop its own wake behind the laser just as the ponderomotive force [Andreev *et al.* 2000] and can seed forward Raman instability as reported by Gordon *et al.* [2001].

Equations (4.3)-(4.6) forming the plasma wave system are solved numerically, using a normalized transverse vector potential $a_\perp \equiv eA_\perp/m_e c$ with a single-color Gaussian pulse and near- to far-infrared wavelengths. For both configurations the FWHM pulse duration is $\tau_0 = 150$ fs and the normalized potential vector is $a_0 = 2$. The ionized gas is helium with an initial atomic density $n_a^0 = 5.5 \times 10^{17}$ cm^{-3}.

The electron density, longitudinal momentum and plasma wave of this model are plotted in Figs. 4.3(a,b) for $\lambda_0 = 0.8$ and 10.6 μm. For near-infrared laser pump [Fig. 4.3(a)] the ionization front is rather smooth ($360 \leq x_{\mathrm{ioni}} \leq 375$ μm) since many laser cycles are involved in the ionization (see below for details). Next freed electrons oscillate in the laser electric field ($x \sim 300$ μm) before forming a sinusoidal plasma wave at the plasma period $\lambda_{pe} = 32$ μm. Activating ($\partial_\xi n_e^0 \neq 0$) or not gas ionization does not affect the longitudinal momentum in this case since both superimpose perfectly. The plasma wave developing in the laser pulse does not show any differences either (see bottom plot). Note that sinusoidal oscillations featuring a quasi-linear wave are observed despite the strong laser amplitude ($a_0 = 2$) because the pulse duration ($\tau_0 = 150$ fs) is not matched to the half-plasma period $\pi\omega_{pe}^{-1} = 50$ fs such that no resonant excitation occurs.

By contrast, with the CO_2 laser pump, ionization is more important [Fig. 4.3(b)]. The first electronic shell is extracted over one laser cycle ($x_{\mathrm{ioni}} \sim 340$ μm) creating a strong ionization front $\partial_\xi n_e^0/n_e^0$ which in turn, increases the longitudinal momentum (see position indicated by the black arrow) through the third term in the right-hand side of Eq. (4.8). When ionization of the second electronic shell occurs, the density step value is augmented due to the electron

density modulation imposed by the early plasma wave. A density peak is formed resulting in a longitudinal momentum stronger than in the pre-ionized case. The final consequence is an increase in the resulting plasma wave amplitude that starts to modulate the laser envelope. Later on, the transverse momentum offset is conserved during plasma oscillations. The wake amplitude due to the ponderomotive force only ($\partial_\xi n_e^0 = 0$) is about 0.017 $m_e c\omega_0/e \approx 5$ GV/m whereas the effect of the ionization pressure term leads to a reinforcement of the ponderomotive motion with an amplitude of 0.046 $m_e c\omega_0/e \approx 14$ GV/m. This drastic change (factor ~ 3) have strong consequences in the underlying physics as demonstrated by means of 2D PIC simulations in the next section.

An additional effect due to the ionization front is the ionization-induced steepening of the laser pulse during its propagation [Gordon *et al.* 2001]. Due to the abrupt change of optical properties, the group velocity decreases, the pulse width broadens and the laser field amplitude decreases corresponding to a photon deceleration or redshift. Physically, photons give their energy to form the plasma wake excited either by the ponderomotive force ($-p_\perp \partial_\xi a_\perp \gamma$) or by the ionization pressure ($-p_x \partial_\xi n_e^0/n_e^0$). In order to link the laser envelope to the ionization front, one can use the propagation equation for the normalized potential vector given by Eq. (2.202), which can be simplified into

$$(2c\partial_\xi - \partial_\tau)\partial_\tau a_\perp = \omega_{pe}^2 \frac{p_\perp}{\gamma} \tag{4.10}$$

when considering that $\beta_g \to 1$. In a first approximation as applied in Gordon *et al.* [2001], i.e., assuming $p_\perp \approx a_\perp$ slowly varying in τ such as $a_\perp = a\exp(ik_0\xi) + c.c.$ (*c.c.* denotes complex conjugate), the amplitude of the pulse envelope is found to evolve as

$$\partial_\tau |a| \approx \frac{1}{2i\omega_0}\left(1 + \frac{ic}{\omega_0}\frac{\partial}{\partial_\xi}\right)\left(\frac{n_e|a|}{\gamma}\right), \tag{4.11}$$

and steepens like the ionization fronts since $\partial_\tau |a| \propto \lambda_0^2 |a|(\gamma - p_x)^{-1}\partial_\xi n_e^0$. Hence pulse steepening is stronger for long pump wavelengths and is directly linked to the ionization front. The steep laser intensity gradient promotes an enhanced ponderomotive force. Over sufficient long propagation time, the laser amplitude depletion can lead to a notch in the laser envelope [Gordon *et al.* 2001]. Our 1D model assumes an unperturbed laser preventing to observe this effect. Nevertheless typical self-steepening signatures are observed on PIC simulations analyzed in the next section.

Finally, since the ionization pressure depends strongly on the ionization front profile, we want to illustrate the influence of the laser envelope at long wavelength ($\lambda_0 = 10.6$ μm). We compare a Gaussian envelope to a $\sin^2$ pulse (compact support). To isolate the effect of the ionization pressure we initialize the two pulses with the same intensity profile possessing almost identical gradients of their respective envelopes. By doing so the standard ponderomotive force will be identical. The Gaussian envelope is given by:

$$\mathcal{E}(t) = \exp\left[-\left(\frac{t}{t_0}\right)^2\right] \tag{4.12}$$

with t_0 being the $1/e$ duration linked to the FWHM duration according to $t_0 = \tau_0/\sqrt{2\ln 2} = 0.8493\tau_0$. The $\sin^2$ profile is defined, for $-\pi t_0/2c_0 \leq t \leq \pi t_0/c_0$, by:

$$\mathcal{E}(t) = \sin^2\left(\frac{c_0 t}{t_0}\right) \tag{4.13}$$

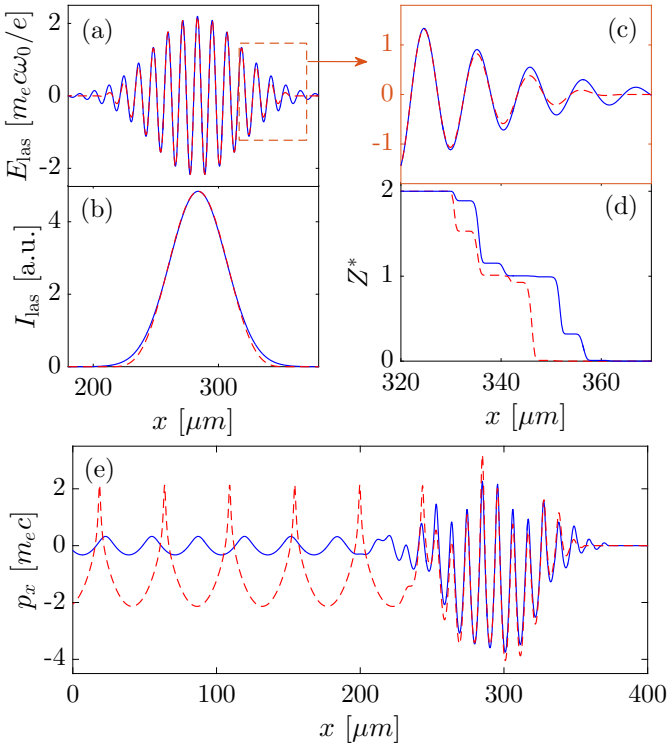

Figure 4.4: Laser (a) electric field and (b) intensity profile for a Gaussian (blue line) and a $\sin^2$ (red dashed line) envelope with $\tau_0 = 150$ fs, $\lambda_0 = 10.6$ μm and $a_0 = 2$. (c) Zoom in of plot (a). (d) Ionization degree in helium for the two considered laser pulse. (e) Solution of Eq. (4.8).

and 0 otherwise. The c_0 coefficient is $c_0 = \arccos(e^{-1/2}) \approx 0.9191$ and $t_0 = c_0\tau_0/2 \arccos(\sqrt[4]{2}) \approx 0.8036\tau_0$. The duration is set to $\tau_0 = 150$ fs and the intensity profiles are very close, except the laser pulse front and rear parts [Figs. 4.4(a,b)]. Indeed, a closer look at the front pulse [Fig. 4.4(c)] shows that the $\sin^2$ profile has a greater difference between the successive maxima in the amplitudes resulting in a stronger ionization slope over the same time interval [see Fig. 4.4(d)]. The solution of the longitudinal plasma wave [Eq. (4.8)] plotted in Fig. 4.4(e) evidences that, despite identical intensity gradients associated to the standard ponderomotive force, the longitudinal field and related wakefield inherently depend on the shape of the laser envelopes. In particular the ionization-induced ponderomotive pressure is higher for the $\sin^2$ waveform due to faster ionization response, which enhances the wakefield oscillations.

The present analysis justifies the important role of the ionization events and how the latter influence both the longitudinal and transverse fields along the laser pulse history and beyond. Our 1D model (omitting transverse effects) describes the main phenomena met in the literature but, by construction, can not deal with the feedback of the enhanced plasma wave on the laser pulse profile. To do so we propose a comprehensive numerical study based on the code CALDER.

4.2 PIC simulations

4.2.1 Physical context

Our study on laser-plasma interaction at long wavelength is motivated by the lack of results in the relativistic regime, specially for THz generation. Our purpose is to adopt a natural approach where three different fundamental laser wavelengths are considered. The physical plasma density is kept constant in order to investigate the effect of the increase in n_e/n_c when increasing λ_0.

Laser pulse #	λ_0 [μm]	I_0 [W/cm^2]	a_0 [$m_e c/e$]	τ_0 [fs]	w_0 [μm]	E [J]	P [TW]
1	0.8	1.1×10^{19}	2.2	150	20	7.6	47
2	3.9	4.4×10^{17}	2.2	150	50	0.3	2
3	10.6	6.0×10^{16}	2.2	150	50	0.04	0.3

Table 4.1: Laser pulse parameters for the three configurations.

Also the normalized vector potential is unchanged such that the laser intensity varies between the three laser pulse configurations. This allows us to stay in the relativistic regime and to explore the photoionization dynamics described above. Table 4.1 sums up the chosen laser parameters.

Simulations are performed with the PIC, kinetic code CALDER (see Section 2.2.1) in 2D Cartesian coordinates (x, y) employing again a two-color laser pulse composed of its fundamental and second harmonic. The Maxwell-Vlasov equations system is solved with strong-field ionization [Ammosov *et al.* 1986]. The longitudinal (transverse) axis is set along x (resp. y), while the laser pulse is linearly polarized in the z direction. In that way, the photocurrent induced radiation (PIR) is polarized out of the simulation plane avoiding coupling with the field of the plasma wake contained in the (x, y) plane. The three fundamental wavelengths considered are $\lambda_0 \equiv 2\pi c/\omega_0 = 0.8$, 3.9 and 10.6 μm for the same normalized field $a_0 = 2.2$, associated to the input laser intensities $I_0 \simeq 10.5$, 0.44 and 0.06×10^{18} W/cm^2, respectively (see Table 4.1). The laser pulse is Gaussian in time and space with its two harmonics (ω_0, $2\omega_0$) having the same FWHM duration $\tau_0 = 150$ fs and a transverse width w_0 varying between 20 and 50 μm. The intensity ratio between second and first harmonics is 10 % and their initial phase shift is $\pi/2$. The two-color laser field is focused into a gas cell of helium with atomic density $n_a^0 = 5.5 \times 10^{17}$ cm^{-3}, along a trapezoidal density profile with 200 μm-long plateau and 25 μm of in- and out-ramp. The frequency window chosen to extract the THz waveforms is $\nu \equiv \omega/2\pi < \nu_0/3$. The plasma wavelength after ionization of the two electronic shells is $\lambda_p = \lambda_0\sqrt{n_c/n_e} = 32$ μm.

Analysis of simulation results will begin with the study of the transverse and longitudinal phase spaces in order to confirm the impact of the ionization-induced ponderomotive force on the plasma wave. Then we shall look at the feedback of this dynamics on the laser pulse shape (self-steepening) and spectral distribution (photon deceleration/redshift). Finally we disclose, at the exit of the plasma channel, an high amplitude, high energy low-frequency field in the laser polarization direction. Meanwhile, electron acceleration yields an intense CTR field in the simulation plane.

4.2.2 Transverse and longitudinal momenta

Figures 4.5(a,b) display the (x, p_z) electron phase space for the transverse momentum when the laser is fully inside the plasma for $\lambda_0 = 0.8$ and 10.6 μm, respectively. The blue curves plot the growth in the ion charge Z^* along the on-axis optical path. At each ionization instant, freed electrons acquire a kick in their transverse momentum, p_z, proportional to the laser vector potential, A_z [Mori & Katsouleas 1992] (see Section 3.1.1). For $\lambda_0 = 0.8\,\mu$m, the transverse drift momentum initiated by ionization and exiting the rear pulse is small. This is due to the high intensity triggering ionization in the foot of the laser pulse where A_z is small. In contrast, for the 10.6 μm pulse, Fig. 4.5(b) displays higher values of p_z close to the ionization zone with lesser intensity. For both laser pulse configurations we expect photocurrent-induced radiation (PIR) to built along propagation in the plasma channel.

Now, as done in the 1D model above, we compare the longitudinal phase space (x, p_x) at

the same instant in pre-ionized or initially-neutral helium for $\lambda_0 = 0.8$ [Figs. 4.5(c,d)] and 10.6 μm [Figs. 4.5(e,f)]. For the near-infrared wavelength the longitudinal momentum develops two characteristic oscillations as already evidenced in Fig. 4.3: The $2\omega_0$ fast component of the laser ponderomotive force and the plasma frequency ω_{pe}. No noticeable change occurs, whether or not ionization is acting, due to the transfer of weak transverse momentum and smooth ionization slope. This confirms the results inferred from our 1D model.

By contrast, when employing a CO_2 laser ($\lambda_0 = 10.6$ μm), the phase space distribution is drastically modified. In pre-ionized helium we observe the $2\omega_0$ oscillations in the laser pulse with similar p_x values to those attained at 0.8 μm [Fig. 4.5(c)]. The longitudinal electric field E_x (gray curve, right axis) is also affected by these $2\omega_0$ oscillations and modulates the laser pulse with sinusoidal oscillations at the plasma frequency. Here, the plasma wave is quasi-linear with relatively low amplitude $\sim$ 30 GV/m due to the unmatched laser duration with respect to ω_{pe}^{-1}. In contrast, activating ionization triggers the ionization pressure contribution [Fig. 4.5(d)]. Globally, the longitudinal phase space exhibits strong values with a completely different plasma wave shape. The first strong p_x peak corresponds to the highest charge state of helium ($x \sim 220$ μm) reached at the end of the ionization zone [see Fig. 4.5(b)]. This acts as a seed enhancing the longitudinal electric field which develops a sawtooth-like profile featuring a nonlinear plasma wave. Sharp gradients occurring at each plasma wavelength promotes electron acceleration ($p_x > 0$ and $p_x \sim 5\ m_e c$) inside the accelerating-focusing zone with length $\lambda_{pe}/4$. Photoionization hence directly impacts the plasma wakefield dynamics through the ionization pressure. The difference with the pre-ionized plasma is more spectacular than reported in the 1D model due to the modification of the laser pulse profile which in turn affects the excitation of the plasma wave. Finally insets in Figs. 4.5(e,f) show no change for a hydrogen gas. They thus evidence that the amplification of the plasma wave requires at least one ionization event after the formation of the wakefield.

Consequently, ionization-induced steepening comes into play and alters the laser pulse envelope. To study this phenomenon we focus the laser on the same plasma profile made of hydrogen or helium with atomic density tuned such that the laser pulses propagate in the same final electron density. By doing so we discard other propagation effect induced by the plasma and depending on the plasma density, e.g., self-focusing that will be addressed later. Figures 4.6(a,b) show the PIC on-axis transverse vector potential for H and He. In the pre-ionized case [Fig. 4.6(a)] all fields are superimposed as expected. In contrast, in Fig. 4.6(b) sharper gradients appear in the front pulse due to ionization-induced steepening in He only. Also due to the long duration of the laser pulse compared to the plasma wavelength, $c\tau_0 = 45$ μm $> \lambda_{pe}$ ($\tau_0\omega_{pe} = 8.8$), the laser envelope begins to be modulated at the relativistic plasma period $c\tilde{\nu}_{pe} \equiv c\nu_{pe}/\sqrt{\gamma} \approx 75$ μm with $\gamma = \sqrt{1 + a_0^2} \approx 2.4$ (see black arrow). This so-called self-modulated-LWFA (SM-LWFA) has been used previously to femtosecond pulses to accelerate electrons. The increase in the field amplitude by self-steepening is also accompanied by the self-focusing of the laser pulse as described below. Both phenomena combine to increase the ponderomotive force establishing the nonlinear plasma wave. Note that experiments and simulations have been carried out by Malka *et al.* [2002] in an intermediate regime between the standard and self-modulated LWFA, where the laser pulse is a little bit longer than the plasma wavelength. Same results of pulse undergoing significant self-steepening and leading to enhanced plasma wave generation were reported. Nevertheless the influence of photoionization was not taken into account in this reference.

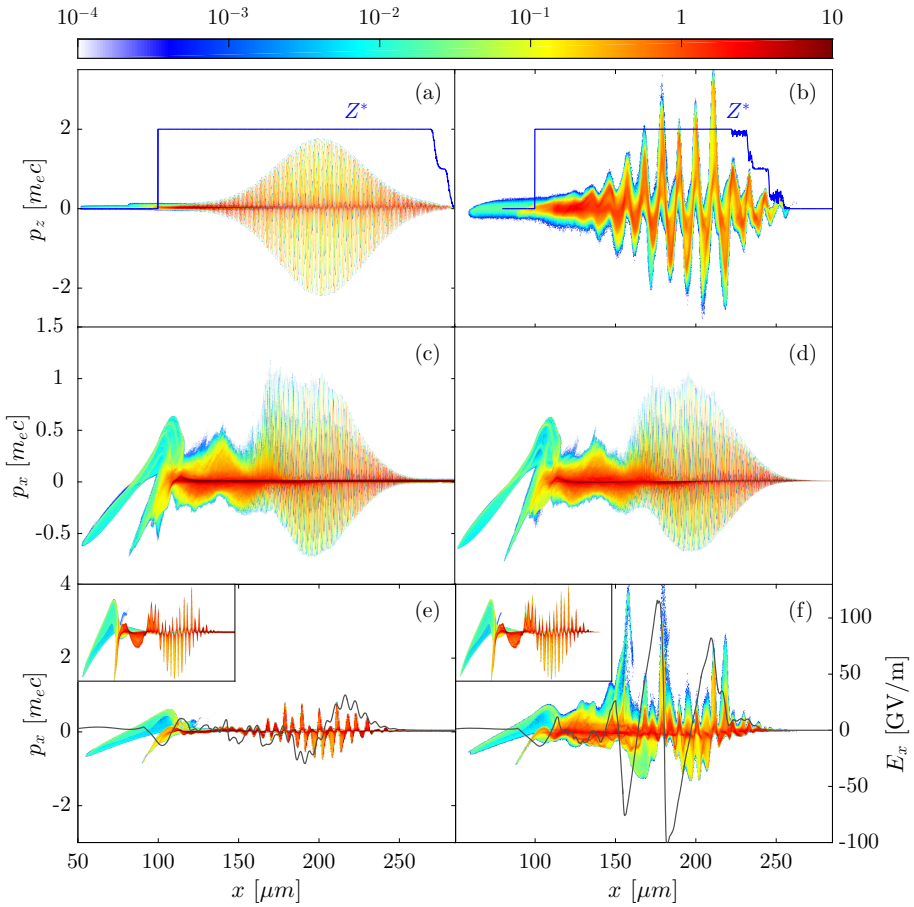

Figure 4.5: (a,b) Transverse momentum for (a) $\lambda_0 = 0.8$ and (b) $\lambda_0 = 10.6$ μm. The blue curves show the ionization degree of He. (c,d) Longitudinal momentum for $\lambda_0 = 0.8$ μm in (c) pre-ionized helium and (d) helium undergoing ionization. (e,f) same information for $\lambda_0 = 10.6$ μm. Gray curves display the longitudinal electric field $E_x = -\partial_x \Phi$ (right axis). Insets show the same phase space (x, p_x) for hydrogen.

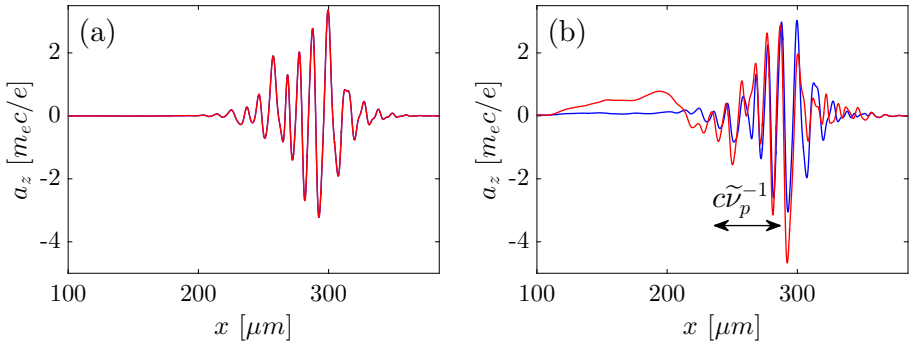

Figure 4.6: On-axis PIC transverse vector potential at same time for H (blue line), He (red line) (a) in a pre-ionized plasma (curves are superimposed) and (b) for gases undergoing ionization. Note that the laser pulses experience the same final electron density for these plots only.

4.2.3 Redshift of the optical spectrum

The feedback of the sharp plasma wave fluctuations on the laser pulse nonlinearly modifies the optical refractive index, $\eta = \sqrt{1 - n_e/n_c\gamma}$, which promotes the creation of new wavelengths through the space-time variation of the electron density [Mori 1997]. The dispersion relation for the local frequency ω is

$$\omega = \sqrt{k^2c^2 + \frac{\omega_{pe}^2(x,t)}{\gamma}}. \tag{4.14}$$

Moreover, in a local volume the number of photons is conserved (we omit ionization) such that the action of the frequency ω is conserved. As a result, when the laser looses energy, the wavenumber has to decrease to fulfill the requirement of action conservation. One can apply the Hamilton's equation to the wavenumber of the wave packet, varying along propagation as [Zhu *et al.* 2012], namely:

$$\frac{dk}{dt} = \frac{dk/dt}{dx/dt} = -\frac{\partial\omega/\partial x}{\partial\omega/\partial k}. \tag{4.15}$$

By using Eq. (4.14), we obtain the local shift in wavenumber:

$$\frac{dk}{dx} = \frac{1}{2c\sqrt{\omega^2 - \omega_{pe}^2/\gamma}} \frac{\partial}{\partial\xi}\left(\frac{\omega_{pe}^2}{\gamma}\right) \sim \frac{\partial}{\partial\xi}\left(\frac{n_e}{\gamma}\right). \tag{4.16}$$

Hence the shift of the laser spectrum in k depends on the plasma gradient. Figure 4.7 illustrates the case of a short pulse propagating in an underdense plasma as usually met in the LWFA context. Here, for the sake of simplicity, we assume a pre-ionized plasma. First, the ponderomotive force acting in the front pulse accumulates electrons like a snowplow and forms a positive density gradient $\partial_\xi n_e$. Hence, according to Eq. (4.16), blue shift occurs since $\partial_\xi n_e > 0$ is equivalent to $dk/dx > 0$. Next electrons are still subject to the intensity gradient and are expelled from high intensity region resulting in the formation of an ion cavity. The group velocity $v_g = \eta c$ follows the electron density variation and decreases. This is the so-called "photon deceleration", or redshift process by which photons loose energy to create the plasma wave [Mori & Katsouleas 1992]. Finally, depending of the laser length compared to the plasma period, the first plasma oscillation sits at the back of the laser pulse such that a region of blueshift can be set up. When considering the overall dynamics, the front of the pulse travels essentially slower than the rear pulse due to the group velocity dispersion (GVD) of the plasma inducing thereby pulse compression. Self-compression has been observed, among others by Faure *et al.* [2005] who reported a pulse shortening from 38±2 fs to 10-14 fs with 20% energy efficiency. In the case of long pulse duration ($c\tau_0 \gg \lambda_{pe}$), as it was usually the case before the invention of the CPA technique, the plasma wave develops completely into the laser pulse and modulates its envelope. At the end of the process, the single long laser pulse is broken up into a train of short pulses with $\sim \lambda_{pe}$ length. The plasma wave is resonantly excited by the succession of short pulses and can promote electron acceleration as well [Malka *et al.* 2001]. Note that this 1D picture is of course limited since diffraction and self-focusing should be considered to explain properly the establishment of this regime [Max *et al.* 1974; Esarey *et al.* 2009]. In the case of ionization, the first blueshift region in the pulse front presents a steeper positive electron density gradient. The frequency up-shift is thus enhanced. This process has been suggested by Wilks *et al.* [1988] to convert electromagnetic radiation to higher frequencies and demonstrated for the first time for microwaves by Savage *et al.* [1992].

In order to examine the spectral influence of the plasma wave on the laser pulse we use the

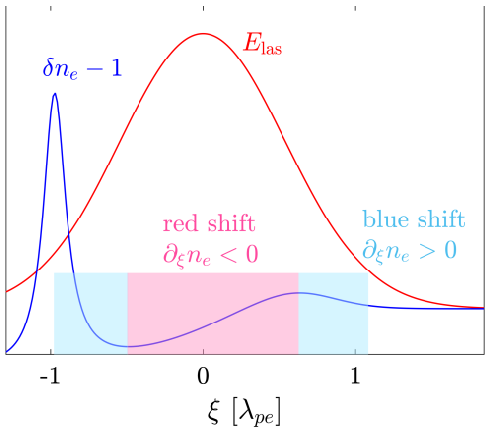

Figure 4.7: Scheme of an ultra-intense laser propagating in an underdense plasma and triggering an electron density modulation δn_e. Areas of blueshift and redshift given by Eq. (4.16) are delineated by blue and red rectangles, respectively.

Wigner transform [Wigner 1932] for the electric field defined by

$$\mathcal{W}_E(x,k) = \int_{-\infty}^{+\infty} E(x+x'/2)E^*(x-x'/2)e^{-ikx'}\,dx'. \tag{4.17}$$

Basically this transformation is equivalent to a space averaged Fourier transform such that we can access to the local spatial-wavenumber distribution of the laser pulse. Figure 4.8(a) shows the Wigner transform of the on-axis laser electric field near the exit of the pre-ionized plasma channel. We clearly observe a frequency downshift ($\partial_x k < 0$) induced by the propagation in the plasma. When photoionization is included, the ionization-induced ponderomotive force creates higher modulations of the plasma wave which leads to an even stronger redshift [Fig. 4.8(b)]. Th amount of photon deceleration can be correlated to the refractive index, impacted by the density modulations according to

$$\eta\partial_\xi\eta = -\frac{1}{2}\partial_\xi n_e/n_c\gamma. \tag{4.18}$$

This is illustrated by Figs. 4.8(a,b), detailing the gradients in the refractive index (dotted black curve). Comparing Figs. 4.8(a) and 4.8(b) displays evidence of (i) a photon downshift in the pulse head at the top of the plasma out-ramp and (ii) the amplification of this downshift by photoionization.

In the frequency domain, Fig. 4.8(c) shows the log-log amplitude spectrum of the transverse field transmitted to vacuum for the longest fundamental wavelengths investigated ($\lambda_0 = 3.9$ and 10.6 μm). Unlike the 3.9 μm pump (red curve), the 10.6 μm laser spectrum (black curves) widely broadens between 1 and 100 THz around the pump wave and develops a net enlargement around the relativistic plasma frequency $\nu_{pe}/\sqrt{\gamma} \simeq 7$ THz. For both wavelengths, satellites at harmonics of the plasma frequency (shifted by ω_0) are clearly observed and they are attributed to the Raman instability. Electromagnetic waves are indeed scattered according to the matching conditions $\omega_0 = \omega_s \pm m\tilde{\omega}_{pe}$ (m is an integer). As a result the pulse envelope is modulated by the plasma wave, which completes our picture of the SM-LWFA regime given above. Interestingly the 10.6 μm pre-ionized spectrum (black dotted curve) presents weaker Raman satellites suggesting that ionization acts as a seed for this instability, as already proposed by Gordon *et al.* [2001]. Therefore, the spectral amplitude is significantly smaller below 10 THz (vertical dashed line)

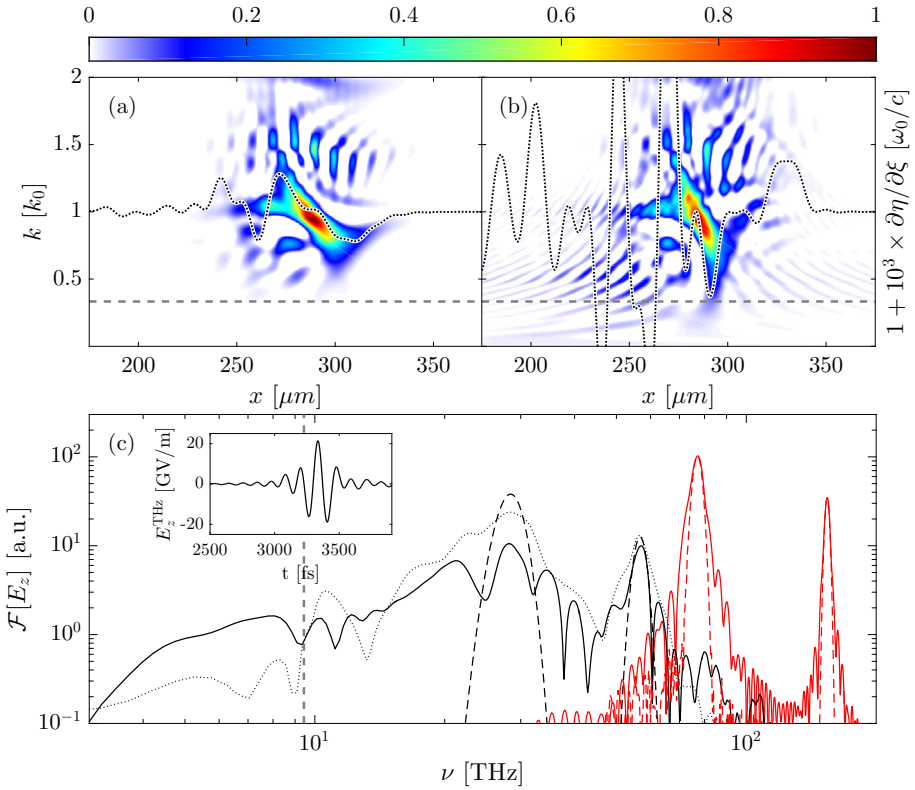

Figure 4.8: Wigner Transform of the on-axis two-color laser electric field at $t = 1400$ fs in (a) preionized plasma and (b) ionized helium for $\lambda_0 = 10.6\,\mu$m along with the gradient of the refractive index computed from the ratio $n_e/n_c\gamma$ using PIC simulation data (dotted black curves). The dashed line indicates the cut-off frequency (9.33 THz) and wavenumber. (c) On-axis log-log scaled spectrum of E_z at the entrance of the simulation domain (dashed black curves) and at $x = 840\,\mu$m (solid curves) for ionized He. Inset: THz field. Red curves: $3.9\,\mu$m, black curves: $10.6\,\mu$m. The dotted black curve shows the on-axis spectrum for 10.6 μm in preionized helium.

suggesting a less efficient photon frequency conversion process. For the ionized plasma, we evaluated the efficiency generated by this photon deceleration process to 1.2% for the frequency window $\nu < 9.5$ THz (i.e., 2.6 mJ for 222 mJ input pulse energy estimated for a focal spot radius equal to $w_0 = 50$ μm). The inset shows the inverse Fourier transform of the 10.6 μm ionized gas spectrum below 9.5 THz and yields the resulting THz waveform. A quasi-single cycle THz pulse formed by the huge broadening of the laser spectrum is thus emitted out of the plasma channel. The field amplitude reaches 20 GV/m rendering it attractive for applications needing strong, broadband ($\gtrsim 10$ THz) and high energy THz field.

Let us now test and confirm the origin of this emission by changing the laser pulse configurations (see Table 4.1) and some key simulation parameters.

Figure 4.9(a) shows a snapshot of the transverse, z-polarized THz field for $\lambda_0 = 0.8\,\mu$m at 500 μm after the plasma-vacuum interface. The two-color laser configurations allow the formation of a low-frequency component in the photocurrent. The corresponding radiation (PIR) is made of two peaks with about 0.5 GV/m maximum amplitude, one for each electronic shell of helium. Note that this peculiar structure is directly due to the distinct ionization of the two electronic shells [see inset of Fig. 4.9(a)].

When increasing the laser wavelength to $\lambda_0 = 3.9$ μm, the PIR becomes more efficient since the electron transverse momentum, p_z, and related current density linearly scale with λ_0 [Debayle *et al.* 2014], which is confirmed by the field strength (3 GV/m) of Fig. 4.9(b).

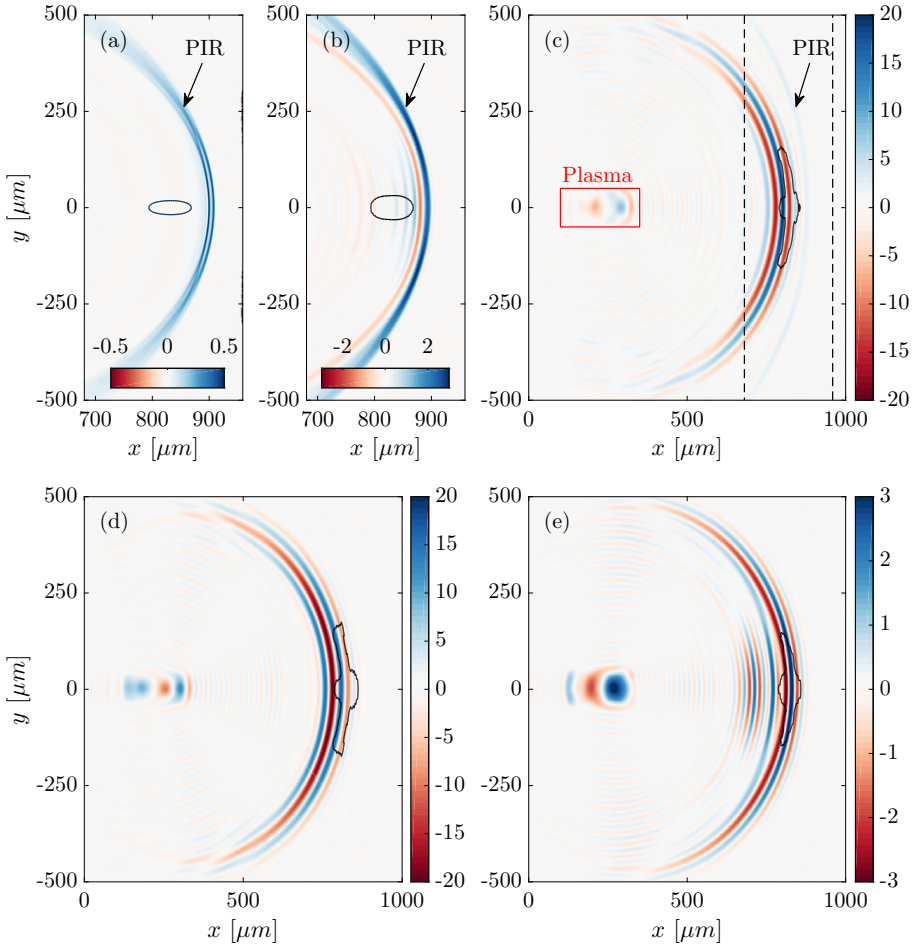

Figure 4.9: (a-c) Electric field E_z (color bars in GV/m) produced by a two-color Gaussian pulse with $a_0 = 2.2$ ionizing a He gas, filtered in the THz range ($\nu < \nu_0/3$) and transmitted to vacuum at $t = 3200$ fs (500 μm after the plasma channel) for $\lambda_0 =$ (a) 0.8, (b) 3.9 and (c) 10.6 μm. The arrow points out to the PIR field. In (c) the black dashed rectangle indicates the simulation domain of (a,b) encompassing the laser region; the red rectangle delineates the plasma zone. (d,e) show the same field pattern for (d) a single-color pulse and (e) a pre-ionized plasma at 10.6 μm.

With $\lambda_0 = 10.6$ μm, however, photocurrents only deliver the first wavefront on the right-hand side of Fig. 4.9(c), being much weaker than expected ($\sim$ 2 GV/m, see arrow). We attribute this sudden drop of PIR to the fall in the photocurrent efficiency, decreased as the ionization sequences develop together with the wakefield. Behind we observe the THz emission evidenced in the inset of Fig. 4.8(c) which cannot be attributed to the PIR process as its emission angle and field amplitude are different. To tackle this THz waveform, other simulations have been performed with one color only ($\lambda_0 = 10.6$ μm), yielding a similar pattern without the PIR field [Fig. 4.9(d)] and thereby confirming its disconnection with two-color induced photocurrents. Furthermore, when simulating a pre-ionized plasma, we observe a net decrease in the THz field strength by a factor ~ 6 [compare color bars of Figs. 4.9(c) and 4.9(e)]. Hence, when long-wavelength pumps are employed, photoionization keeps a non-trivial impact on the transverse THz emission, but its action differs from the standard photocurrent conversion mechanism. As demonstrated above, additional emission is mediated by the impact of the plasma wave on the laser pulse spectrum.

4.2.4 CTR at the plasma-vacuum interface

To end with, let us go back to the CTR process. So far we focused our analysis on the radiated field polarized out of the simulation plane and thus coming from the laser driven current. The emitted field components (E_x, E_y) from the plasma wave lie in the simulation plane and can contain secondary THz radiation, e.g., through the CTR mechanism. These can be simultaneously evaluated by looking at the emitted out-of-plane magnetic field since $B_z = \partial_x E_y - \partial_y E_x$. Also, by looking at the steep gradients in the longitudinal field [see Fig. 4.5(f)], particle injection might occur. This property is clearly evidenced in the inset of Fig. 4.10(a) where a well-shaped plasma bubble hosts an electron beam about to exit from the plasma ($x \sim 350$ μm). Here, particle injection is also promoted by the transverse beam dynamics, namely self-focusing, which is reinforced at long wavelength due to the scaling of the critical power $P_c \propto n_c/n_e$.

Figure 4.10(a) shows the maximum normalized laser electric field along the propagation axis for the three studied wavelengths. The 0.8 and 3.9-μm pumps do not self-focus due to the weak ratio n_e/n_c. In contrast, a clear sequence of collapse and plasma blow-out occurs at $\lambda_0 = 10.6$ μm, where the intensity is amplified by a factor ~ 4 and reinforced by pulse steepening through multi-ionization of He. Photoionization also appears as an important player here and accelerates the bubble formation. As a result, the laser spot enters the blowout wakefield regime (see Section 2.2.2), leading to electron injection [Lu *et al.* 2007].

Later, the electron bunch will pass the plasma-vacuum boundary, generating a CTR field radiating in the THz range [Leemans *et al.* 2003; Déchard *et al.* 2018]. A normally incident electron beam leads, in full 3D geometry, to a radially polarized emission (see Section 2.3). In our 2D geometry, the CTR field is contained in the simulation plane and is completely described by B_z. To visualize the correlation between the accelerated particles and the CTR field, Fig. 4.10(b) shows the spatially resolved energy electron density map revealing three distinct populations. The first one constituting the plasma channel has rather low energy and is located near axis at $y \approx 0$, $x \leq 400\,\mu$m. The second electron population forms the expanded bubble outside the plasma at $y \approx \pm 400\,\mu$m. At $x \simeq 700\,\mu$m, the third, wakefield-accelerated electron population reaches an energy as high as 12 MeV. The CTR field generated by the escaping electrons is represented by the z-polarized magnetic field B_z (green-red colormap). This single-cycle field has a maximum amplitude of about 20 GV/m and corresponds to 1.4% conversion efficiency ($\nu < 9.5$ THz). We thus obtain similar THz energy as the optimum case of the previous study (see Section 3.3), but with a much lower laser pulse energy (~ 0.22 J instead of 4 J). Moreover CO_2 lasers seem to be suitable to accelerate low energy, high charge electron beams which is ideal for CTR-based THz emission. Note that, again, these numbers may be subject to further correction knowing that the part of genuine CTR field can be decreased by a factor 4 as discussed in Chapter 3.

Conclusion

In summary, we demonstrated that photoionization matters when long laser wavelengths are employed to create intense THz fields in relativistic plasmas. First, the ionization-induced pressure is non zero from the second electron extraction, which increases the plasma wakefield amplitude. Meanwhile, optical shocks cause photon deceleration at the laser front where the electron density starts to fluctuate. This dynamics generates high THz fields through frequency downshifts in the optical spectrum. Second, CTR by the wakefield-accelerated electrons is enhanced by a more efficient self-focusing. On the whole, a laser-to-THz conversion efficiency of a few percent can be reached, demonstrating another relevance of CO_2 lasers in relativistic

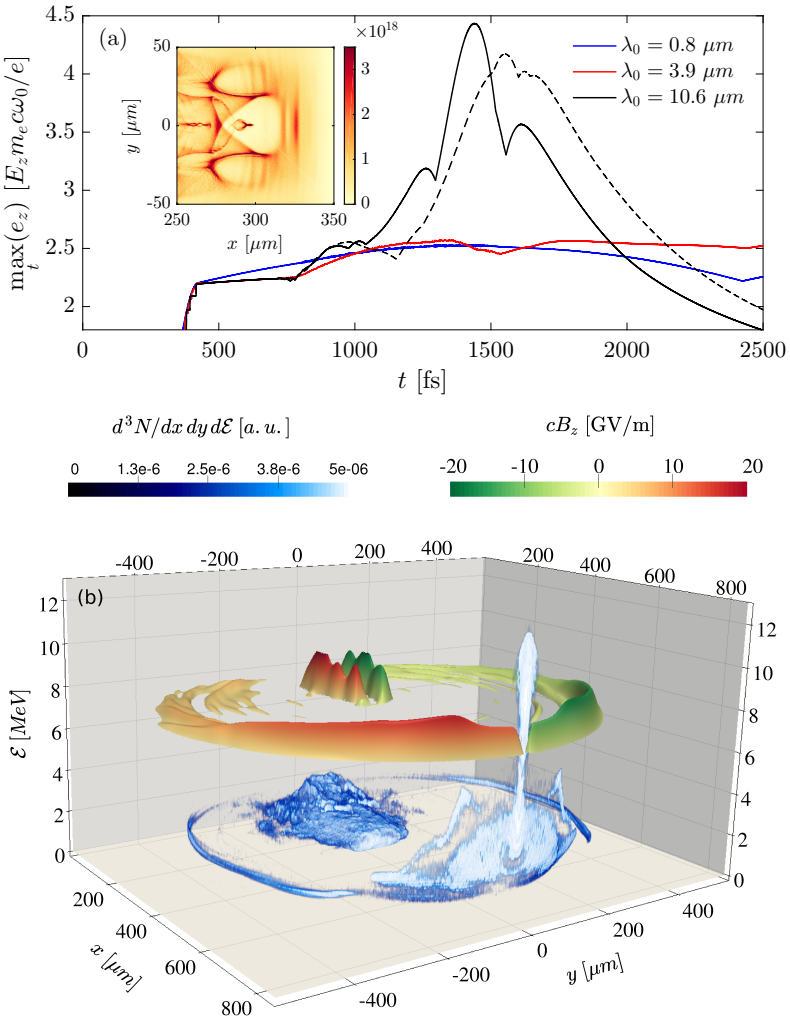

Figure 4.10: (a) Maximum normalized two-color laser field amplitude for the three wavelengths λ_0. The dashed curve shows the normalized laser electric field, e_z, for pre-ionized helium when $\lambda_0 = 10.6\,\mu$m. Inset displays a plasma bubble where electron injection takes place at the plasma exit ($t = 1400$ fs). (b) Density map (blue colormap) in the phase space $(x, y, \mathcal{E})$ at $t = 2500$ fs, where $\mathcal{E}$ [MeV] denotes the electron energy. On top of it the radiated CTR magnetic field cB_z [GV/m] is plotted (green-red colormap).

laser-plasma interaction.

Chapter 5

THz emission by ultra-thin solid targets irradiated by UHI laser pulses

Contents

Since the pioneering work by Hamster *et al.* [1993], THz emission by irradiated solid targets has led to numerous works to understand still unclear underlying physical mechanisms such that the role of surface currents and accelerated ions. In this Chapter we propose to tackle this issue with state-of-the-art PIC simulations. Section 5.1 presents the basis of the laser-solid interaction physics with a rapid review of THz generation by solid targets. We next analyze the dynamics of the interaction by means of self-consistent 2D CALDER simulations and give some clues of the main THz emission processes in Section 5.2.

5.1 Physics of the laser-solid interaction

Up to now, we have focused our work on laser-gas interactions up to near critical plasma densities ($n_e/n_c \sim 1$).

Since laser-plasma interactions at overcritical densities involve distinct physical processes, we first present a summary here (Sec. 5.1.2 and 5.1.3), which will be used to analyse PIC simulations. While THz emission in gases has been extensively investigated, little attention has been paid so far to THz emission from laser-driven solid targets. Previous works on this topic will be briefly reviewed in Section 5.1.4.

5.1.1 From laser-gas to laser-solid interaction

As demonstrated in the previous chapters, laser-gas interaction is suitable for particle acceleration (LWFA) and radiation (THz, X-rays, γ-rays) sources. In the same vein, laser-solid interaction has been intensively studied first in the picosecond regime in the context of the fast ignition approach to inertial confinement fusion [Tabak *et al.* 1994]. With the advance of laser technology in the 2000's, laser-solid interactions demonstrated breakthrough features, specially for the generation of high-energy ion [Macchi *et al.* 2013] and radiation [Kmetec *et al.* 1992] sources, the production of warm dense matter [Hoarty *et al.* 2013] or astrophysical applications [Chen *et al.* 2015].

Laser-solid interaction experiments typically require powerful laser pulses ($P \sim 0.1 - 1$ PW) focused on a few micrometer spot. Targets can consist of either metallic (carbon, aluminum, copper, gold) or plastic (CH_2) foils, with micrometric thickness. Recently, the use of sub-micrometic targets allowed ion acceleration to be optimized in terms of maximum (cut-off) energy [Henig *et al.* 2009; Kar *et al.* 2012; Kim *et al.* 2013], provided that the target integrity is conserved before the arrival of the laser pulse maximum. From now on, we will consider overdense targets with atomic density $\geq 100\ n_c$. The plasma skin depth is thus very small, $c/\omega_{pe} \ll \lambda_0$, and the electromagnetic laser fields exponentially decay in the target. As a result the laser pulse is mainly reflected while the plasma is significantly heated depending on the laser intensity and polarization state. A seminal PIC simulation study, performed by Wilks *et al.* [1992], demonstrated a Boltzmann-like energy distribution for electrons, characterized by its mean energy (usually referred to as "temperature") $T_h \sim m_e c^2 \sqrt{1 + a_0^2/2} \propto \sqrt{I_0}$, known as the ponderomotive scaling. Since then, various mechanisms have been suggested to explain this behavior. In the following we focus on electron vacuum heating [Bauer & Mulser 2007] fed by different potential processes such as the Lorentz force $\mathbf{J} \times \mathbf{B}$ (skin layer) heating [Kruer & Estabrook 1985].

Moreover, in real experimental conditions, the laser pulse temporal profil is not a perfect Gaussian and presents a pre-pulse called pedestal. For a laser intensity of 10^{22} W/cm^2, a contrast of 10^{-8} leads to a pre-pulse of 10^{14} W/cm^2 with multi-ps duration which is well enough to pre-ionize the target. Thus the main pulse commonly hits an expanded underdense plasma altering the interaction with the overdense target. For the sake of simplicity, we will only describe the direct interaction between the laser pulse, assumed with perfect contrast, and a solid target having sharp interfaces. Accordingly, our PIC simulations will be performed for an ideal Gaussian pulse interacting with the medium through a sharp vacuum-target boundary.

5.1.2 Generation of hot electrons

An ultraintense, ultrashort laser pulse is mainly reflected over the plasma skin depth. This leads to a steep gradient in the electromagnetic wave profile between vacuum and the newly formed plasma. The laser energy is deposited in the target in the form of a hot electron population, which thus plays a crucial role in the interaction.

From a general perspective, the motion of a test electron in a finite duration, electromagnetic propagating wave $\mathbf{A}(x,t) = A_0(x,t)\cos(k_0 x - \omega_0 t)\mathbf{e_y}$ is given by Eqs. (2.173), (2.175). After being overtaken by the pulse, the electron recovers its initial momentum, so that no energy gain occurs. In overcritical plasmas, however the electromagnetic profile departs from a propagating wave, so that finite energy transfers are allowed. Let us recall that adiabatic motions have to be broken so that electrons gain energy from the laser pulse. This can be done by an abrupt density step (vacuum heating) or a fast spatial variation of the laser electromagnetic fields ($\mathbf{J}\times\mathbf{B}$ heating) such that the cycle averaged work $-e\langle \mathbf{E}\cdot\mathbf{v}\rangle$ exerted on the particle does not cancel out.

Vacuum heating is a collisionless mechanism accounting for the generation of high-energy electrons in overdense plasmas with steep gradient. The incoming linearly polarized $(\mathbf{E},\mathbf{B})$ fields of the laser pulse reflect on the overdense surface and form a standing wave given, in terms of vector potential, by [Marburger & Tooper 1975]:

$$a(x) = \begin{cases} 2a_0\cos\left(x - x_d + \theta\right) & \text{if } x < x_d \\ \frac{2a_0}{\sqrt{n_e}}\exp\left[-\sqrt{n_e - 1}(x - x_d)\right] & \text{if } x > x_d \end{cases} \tag{5.1}$$

where $\tan\theta = \sqrt{n_0 - 1}$ and x_d is the electron depletion layer. The latter is obtained by counterbalancing the ponderomotive $(2I_0/c)$ and the electrostatic $(\epsilon_0 E_x x_d^2/2)$ pressures. Equating these two quantities gives the layer thickness x_d (in normalized units):

$$x_d = \frac{a_0\sqrt{2}}{n_0}. \tag{5.2}$$

The resulting $(\mathbf{E},\mathbf{B})$ fields are plotted on Fig. 5.1(a,c,e).

Now let us consider a test electron. In vacuum, it will be subject to the standing wave (5.1), and so, to the ponderomotive force of the laser. Its dynamics is ruled by the equations of motion (2.173) and (2.175) which can be recast as:

$$p_y = a_0\cos\left(\omega_0 t\right)\sin(k_0 x), \tag{5.3}$$

$$\frac{dp_x}{dt} = m_e c\omega_0\frac{a_0^2}{\gamma}\sin(2k_0 x)[1 - \cos(2\omega_0 t)], \tag{5.4}$$

whereas $dp_\perp/dt = 0$ in the plasma (absence of fields). Thus the particle might gain significant energy if interacting with the vacuum laser field. Bauer & Mulser [2007] injected a bunch of test particle in the plasma with an initial longitudinal momentum $\mathbf{p_0} = (-|p_{x,0}|, 0, 0)$ (see Figs. 5.1), and phase $0 \leq t \leq 2\pi$, in order to interact with the standing wave (5.1) according to Eq. (5.4).

Generally speaking, the overall spread of the final momentum $\Delta p_{x,f}$ increases up to $1.5\, m_e c$ when increasing $p_{x,0}$ for plasma densities between 10 and 250 n_e/n_c at a laser intensity of 3.51×10^{18} W/cm^2 ($\lambda_0 = 0.8$ μm). Interestingly, above a threshold value corresponding to $p_{x,0}\approx a_0$ the distribution becomes chaotic with $p_{x,f} \leq 4\ m_e c$. Let us focus on three well chosen $p_{x,0}$ values illustrating three different situations.

For $p_{x,0} \ll a_0$ ($p_{x,0} = 0.1$) electrons do not escape into vacuum and are reflected in the

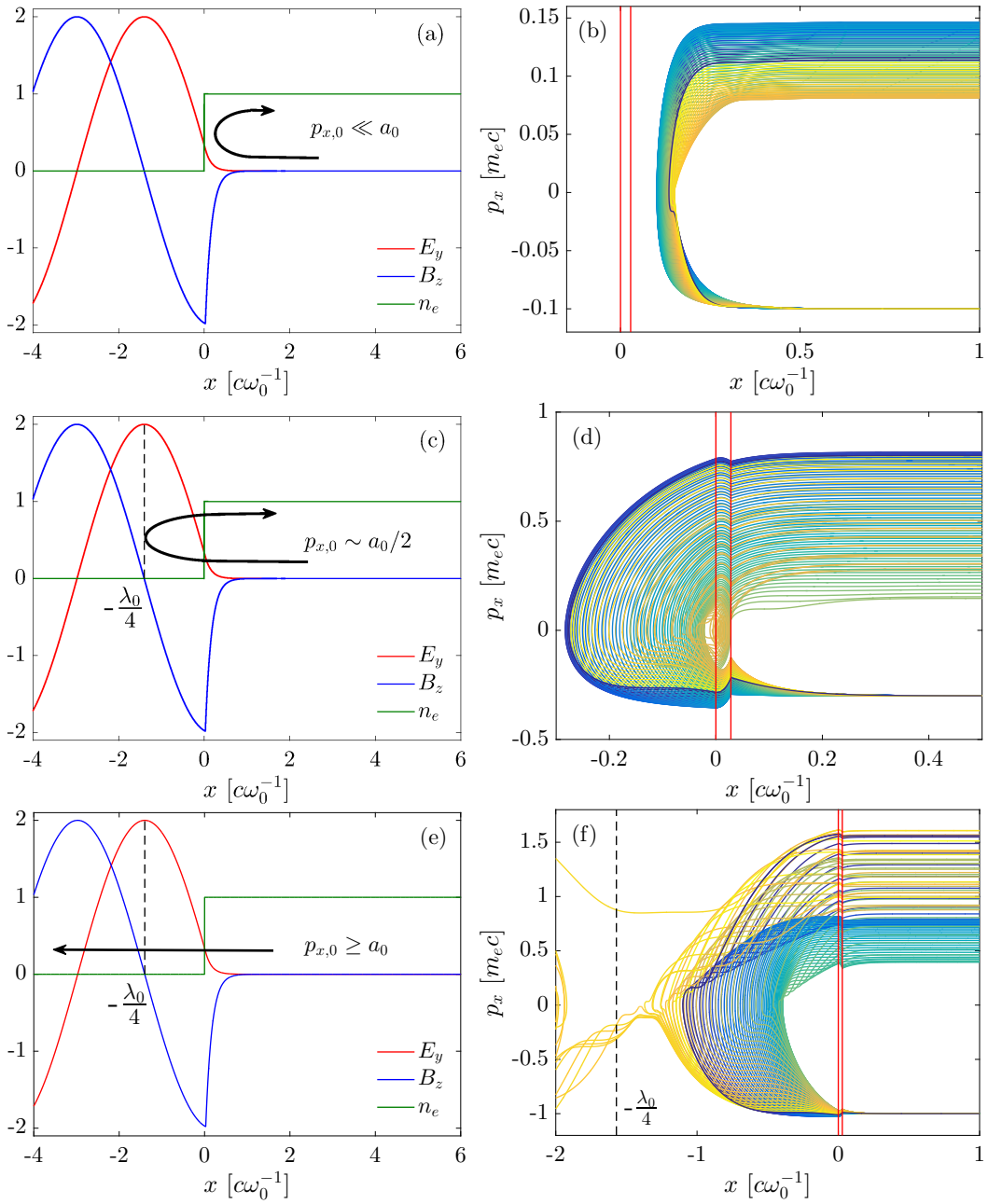

Figure 5.1: Illustration of vacuum heating for three different values of the initial longitudinal momentum $p_{x,0}$. (a, c, e) Standing wave formed by the incoming and the reflected laser field over the overdense plasma ($n_e = 50\, n_c$) with a steep gradient for the three cases: (a) $p_{x,0} \ll a_0$, (b) $p_{x,0} \sim a_0/2$ and (c) $p_{x,0} \geq a_0$. (b ,d, f) Related phase space (x, p_x) of 100 electron trajectories given by Eq. (5.4) for a normalized laser amplitude $a_0 = 1$, a plasma density $n_0 = 50\, n_c$ and an initial momentum equals to (b) $p_{x,0} = 0.1\, m_e c$, (d) $p_{x,0} = 0.3\, m_e c$ and (f) $p_{x,0} = 1\, m_e c$. Colors follow the initial phase $0 \leq t_0 \leq 2\pi$, vertical red lines delineate the initial target interface ($x = 0$) and the depleted layer ($x = x_d$) while vertical black dashed lines locate the electric field maximum.

plasma [see Fig. 5.1(b)]. The energy gain occurs in the skin layer with a phase dependence due to interaction with the $2\omega_0$-oscillating ponderomotive force [Bauer & Mulser 2007].

Then, for $p_{x,0} \sim a_0/2$ ($p_{x,0} = 0.3$), electrons are able to go through the depleted electronic layer and escape in vacuum when the B_z field starts to decline [see Fig. 5.1(c)]. Here they gain energy when approaching the maximum electric field location $x = -\lambda_0/4$ (antinode) before being pushed back in the plasma by the ponderomotive force. The role of the surface B_z field has been studied in detail by May *et al.* [2011] and, notably, the influence of the initial transverse momentum (here neglected) to maximize the energy transfer up to $p_{x,f} \sim 2m_e c a_0$. The transit motion of the electrons through the standing wave lasts about half laser cycle. Thus a $2\omega_0$ signature in the collected spectrum is expected as it is the case for the $\mathbf{J} \times \mathbf{B}$ ponderomotive heating ($2\omega_0$-oscillating component). However the former occurs in vacuum from a collisionless process while the latter happens in the plasma skin depth where a collective fluid description can be applied.

Above the threshold value $p_{x,0} \geq a_0$ ($p_{x,0} = 1$), the electron motion becomes stochastic. As before, electrons exit the plasma and gain energy in the E_y field but some of them go straight ahead due to their high momentum [see Fig. 5.1(e,f)]. They stochastically interact with the standing wave and continue to gain energy as long as they are not ejected from it back into the plasma [Kemp *et al.* 2014].

In this test particle picture, electrons are injected in the standing wave according to *ad hoc* initial conditions. In practice one needs some preheating due, for instance, to the $2\omega_0$ oscillating plasma boundary [Sanz *et al.* 2012] or the skin layer heating mechanism. This results in a fraction of the electrons having supra-thermal energies, thus particularly prone to vacuum heating. The longitudinal electric field can also accelerate and inject electron from the skin layer to vacuum. Moreover, the interpenetration of the $2\omega_0$-periodic fast electron jets and the bulk electrons can trigger streaming instabilities, responsible for additional plasma heating [Robinson *et al.* 2014].

To end with, the generation of hot electrons may be strongly impacted by transverse effects. In the case of a finite laser spot size, the plasma surface is curved by the ponderomotive pressure such that a normal electric field component appears. The latter is able to pull surface electrons in vacuum via the Brunel effect [Brunel 1987]. Also, the plasma surface may develop modulations as a result of various processes, ranging from surface waves [Macchi *et al.* 2002], Weibel [Sentoku *et al.* 2003], modulational [Wan *et al.* 2016] or Rayleigh-Taylor [Pegoraro & Bulanov 2007] instabilities. Because of this, identifying a leading mechanism from simple models becomes cumbersome and we need to rely on PIC simulations.

5.1.3 Ion acceleration

Since they have a large mass, the target ions are not accelerated directly by the laser oscillating field, but, rather, by the electrostatic (charge separation) fields set up at the target boundaries, caused by the laser-driven motion of hot electrons. Due to the complex underlying physics, ion acceleration is a multi-parameter problem depending on the laser pulse (intensity, duration, contrast, polarization) as well as on the target parameters (density, geometry). Usually two main regimes (TNSA, RPA/LSA) can be distinguished, corresponding roughly to two classes of high power lasers.

Target Normal Sheath Acceleration (TNSA)

Historically, the use of relatively long duration pulses ($\sim$ 1 ps) with high intensity ($> 10^{18}$ W/cm^2) has demonstrated the possibility to accelerate ion beams at energies of a few tens of MeV

[Clark *et al.* 2000; Maksimchuk *et al.* 2000; Snavely *et al.* 2000]. Experiments and simulations have shown that the acceleration mechanism occurs mainly at the back of the target, following the expanding cloud of hot electrons [Mackinnon *et al.* 2001]. The measured ion spectrum has a Boltzmann-like distribution, suggesting that the acceleration results from a thermal expansion, referred to Target Normal Sheath Acceleration (TNSA) by Wilks *et al.* [2001].

A first estimate of the TNSA field amplitude can be obtained with hand-waving arguments. The typical strength of the electrostatic field driving the expansion of a quasi-neutral plasma into vacuum is

$$E_x \approx \frac{T_h}{eL_n}, \tag{5.5}$$

where $T_h \approx m_e c^2 a_0$ is the hot electron temperature given by the ponderomotive scaling and L_n is the local plasma density scale length. At the illuminated target side, L_n is given by the plasma expansion after the laser irradiation. By contrast, at the rear surface, the gradient is steeper and L_n is of the order of the Debye length of hot electrons $\lambda_D = \sqrt{\epsilon_0 T_h / e^2 n_h}$ with n_h their density, which is much shorter than the front gradient length. As a result, ion acceleration is enhanced at the target backside. Typical values of $T_h \equiv 1$ MeV and $\lambda_D = 1$ μm lead to an accelerating field of about one MV/μm. Hence atoms at the back surface are quasi-instantaneously ionized and resulting ions are accelerated to MeV energies over only a few micrometers. The acceleration process depends on the Z/A ratio, such that light ions react more quickly to the TNSA field. In practice, contaminant layers of light atoms (mainly hydrogen) are naturally present at the target boundaries prior to the interaction (e.g. H_2O) and are, thus, preferentially accelerated.

In order to foresee the dynamics of the accelerating field and the maximum ion energy, different analytical models and scaling laws have been proposed. Here, we give the fundamental one based on plasma expansion in vacuum [Gurevich *et al.* 1966] and the widely used laws proposed later by Mora [2003].

Ion acceleration by the electrostatic field induced by the hot electron cloud is similar to a long standing problem of plasma physics, which is the expansion of a hot plasma in vacuum. Let us consider a collisionless plasma in the half-space $x < 0$. The ions are cold and initially at rest with a step-like density profile: $n_i = n_i^0$ for $x < 0$ and $n_i = 0$ for $x > 0$. Electrons have a temperature T_h and expand in vacuum at $t > 0$. The electron distribution, the Poisson equation as well as the fluid equations describing the ion expansion are given by [Gurevich *et al.* 1966]:

$$n_h = n_h^0 \exp(e\Phi/T_h), \tag{5.6}$$

$$\epsilon_0 \frac{\partial^2 \Phi}{\partial x^2} = e(n_e - Z n_i), \tag{5.7}$$

$$\left(\frac{\partial}{\partial t} + v_i \frac{\partial}{\partial x}\right) n_i = -n_i \frac{\partial v_i}{\partial x}, \tag{5.8}$$

$$\left(\frac{\partial}{\partial t} + v_i \frac{\partial}{\partial x}\right) v_i = -\frac{Ze}{m_i} \frac{\partial \Phi}{\partial x}, \tag{5.9}$$

where we assume a Boltzmann distribution for the single fast electron population n_h. In actual conditions, one has to take into account, at least, an additional low energy electron population since only a portion of it is laser accelerated and drags ions [Diaw & Mora 2012; Lécz *et al.* 2013]. A self-similar solution for electron density, ion velocity and sheath field can be found

under the quasineutrality assumption $n_h \approx Z n_i$:

$$n_h \approx Z n_i = n_h^0 \exp(-x/c_s t - 1), \tag{5.10}$$

$$v_i = c_s + x/t, \tag{5.11}$$

$$E_x^{ss} = -\partial\Phi/\partial x = T_h/e c_s t, \tag{5.12}$$

with $c_s = \sqrt{ZT_h/m_i}$ the ion sound velocity. We recover here the field amplitude given by Eq. (5.5) with a scale length $L_n = c_s t$. The maximal ion velocity is localized at the ion front. There the scale length equates to the local Debye length $\lambda_D = \lambda_D^0 \sqrt{n_h^0/n_h}$, hence

$$v_i^f = c_s[2\ln(\omega_{pi} t) + 1], \tag{5.13}$$

$$E_x^f \approx 2E_x^{ss} = \frac{2}{\omega_{pi} t}\sqrt{\frac{n_h^0 T_h}{\epsilon_0}}, \tag{5.14}$$

with $\omega_{pi} = \sqrt{e^2 Z n_h^0/\epsilon_0 m_i}$ being the ion plasma frequency. Besides breaking down once $\lambda_D^0 > c_s t$ (hence for $t < \omega_{pi}^{-1}$), the self-similar solution predicts a diverging velocity when $x \to +\infty$ for $t \gg \omega_{pi}^{-1}$. Hence new models have been studied to overcome this difficulty.

Mora [2003] examined the self-similar solution by numerically solving the ion motion and the Poisson equation with the Boltzmann electron distribution, Eqs. (5.6-5.9). A fitting formula then gives the new value of the charge separation field at the ion front:

$$E_x^f \simeq \frac{2}{\sqrt{2e^1 + (\omega_{pi} t)^2}}\sqrt{\frac{n_h^0 T_h}{\epsilon_0}}, \tag{5.15}$$

related to the ion front velocity

$$v_i^f \simeq 2c_s \ln(\tau + \sqrt{\tau^2 + 1}), \tag{5.16}$$

with $\tau = \omega_{pi} t/\sqrt{2e^1}$. These two equations have been compared to the numerical solutions, demonstrating remarkable good agreement [Mora 2003]. Also, the scaling law of the maximum ion energy inferred from this analysis ($\mathcal{E}_i^f \propto (v_i^f)^2 \propto T_h \propto \sqrt{I_0}$) is consistent with experimental measurements [Robson *et al.* 2007]. Nevertheless, some intrinsic assumptions cannot avoid certain unphysical behaviors. For instance the ion velocity, despite being valid over long times, diverges logarithmically due to the 1D geometry and the constant electron temperature.

As an illustrative example, Fig. 5.2 presents the result of a 1D PIC simulation for an ultraintense ($a_0 = 10$), ultrashort ($\tau_0 = 30$ fs) laser irradiating a 5 μm thick overdense plasma ($n_i = n_e = 100\, n_c$). Ions are set into motion at the rear side of the target [see Fig. 5.2(a)]. At $t = 800\ \omega_0^{-1}$, Fig. 5.2(b) shows the ion density profile preceded by the electron cloud (top plot). At the ion front, the longitudinal charge space field is peaked at $\sim 0.12 \times m_e c\omega_0/e = 385$ GV/m in agreement with the evaluation of Eq. (5.15) ($\omega_0 t = 530$).

Radiation Pressure Acceleration (RPA)

Recently, progress in laser technology has made it possible to achieve laser pulses with < 100 fs and $> 10^{20}$ W/cm^2 intensity. At such intensity the slow component of the ponderomotive force is high enough to push inward the front-side electrons. An electron-depleted layer is created with a strong electrostatic field which balances the ponderomotive pressure [see Fig. 5.3(a)]. Hence

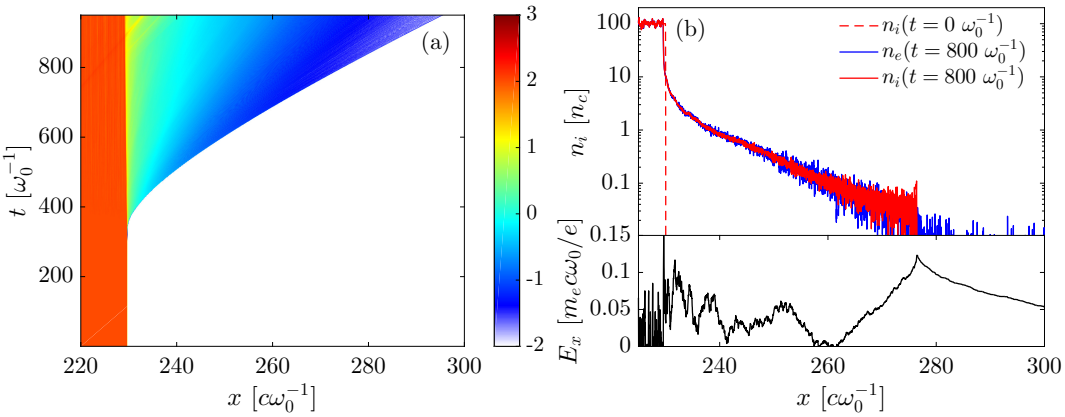

Figure 5.2: Results of 1D PIC simulation illustrating ion TNSA induced by a laser pulses with amplitude $a_0 = 10$ and FWHM duration $\tau_0 = 30$ fs interacting with a 5 μm thick overdense plasma ($n_i = n_e = 100\, n_c$). (a) (x, t) map of the ion density at the target backside. (b) Top plot shows the ion front (red curve) and electron (blue curve) density at $t = 800\ \omega_0^{-1}$. For reference, the initial target is also plotted (red dashed curve). Bottom plot displays the longitudinal TNSA field E_x with peak value $\sim 0.12 \times m_e c\omega_0/e = 385$ GV/m.

ions experiencing a decreasing field in the compressed electron layer are accelerated towards the inner neutral region where they propagate ballistically, resulting in a peaked ion spectrum [Macchi *et al.* 2005]. This Radiation Pressure Acceleration (RPA) process is particularly well suited for circularly polarized laser pulses thanks to the absence of the oscillating component in the ponderomotive force, thus minimizing surface instabilities and electron heating.

The thin layered structure created by the laser pressure acts as a piston upon the front-side ions, and moves at normalized velocity $\beta_p = v_p/c$. Let us derive the momentum flux balance between laser radiation and plasma species in order to find the piston velocity, and so the ion velocity. We assume that the reflection of the laser is almost total, $R \approx 1$, such that a radiation pressure, $P_{rad} = 2I_0'/c$, is imposed on the target. Prime quantities are evaluated in the piston co-moving frame with the Lorentz factor γ_p. The ion momentum flux in the piston frame is given by $2c\beta_p n_i' p_i'$ where we neglect the energy deposited into electrons. We should now equate these two terms in the piston frame in which we have $I_0' = I_0(1-\beta_p)/(1+\beta_p)$ (relativistic Doppler-shifted radiation pressure) and $n_i' p_i' = \gamma_p^2 n_i p_i$. This gives [Robinson *et al.* 2009]:

$$\frac{I_0}{\rho c^3}\frac{1-\beta_p}{1+\beta_p} = \gamma_p^2 \beta_p^2, \tag{5.17}$$

with $\rho = m_i n_i$. After defining the quantity $B = \sqrt{I_0/\rho c^3} = a_0\sqrt{\alpha (n_c/n_i)(m_e/m_i)}$ with $\alpha = 1/2$ or 1 for a linear or circularly polarized laser, respectively, we obtain the piston velocity

$$\beta_p = \frac{B}{1+B}. \tag{5.18}$$

The electrostatic reflection of ions on the piston results in a maximum velocity $\beta_i = 2\beta_p/(1+\beta_p^2)$ corresponding to the kinetic energy:

$$\epsilon_i = m_i c^2 \frac{2B^2}{1+2B}. \tag{5.19}$$

In the non-relativistic limit, $\epsilon_i \propto I_0/n_i$ suggesting a more performant scaling with respect to

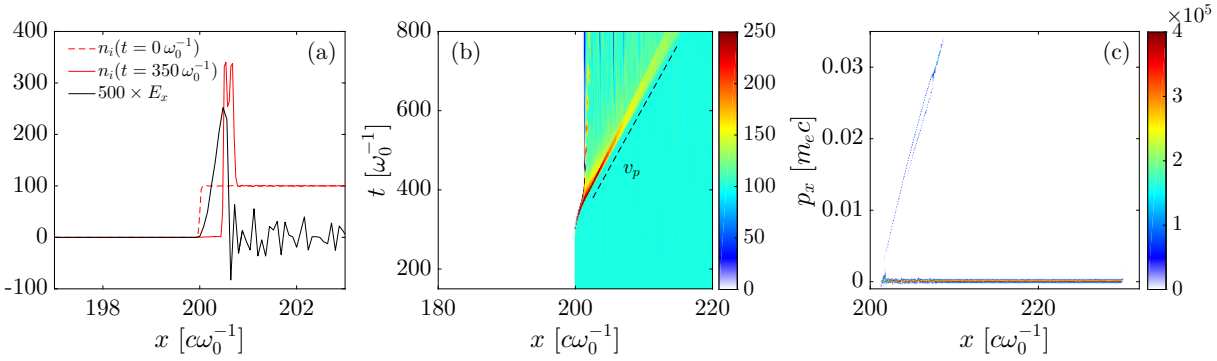

Figure 5.3: Illustration of RPA in an overdense hydrogen plasma at $100\,n_c$ density with an incoming laser amplitude $a_0 = 10$ and duration $\tau_0 = 30$ fs. (a) Initial and pushed density profile (red curves) with the accelerating electrostatic field E_x (black curve). (b) (x,t) map of the hydrogen density showing the plasma compression and the ion velocity. (c) Longitudinal ion phase space at $t = 600\ \omega_0^{-1}$.

the laser intensity compared to TNSA ($\propto \sqrt{I_0}$). Hence the RPA mechanism is capable, in principle, of producing high density and peaked energy ions with circularly polarized pulses. Those properties are somewhat mitigated with a linear polarization due to the interplay with TNSA arising at the target backside (and, also, to a lesser degree at the front side). Also the ponderomotive pressure is compensated for by a stronger electron heating which weakens the electrostatic pressure. Note that in a multi-dimensional description with a finite laser spot size, the laser penetrates inside the target via hole boring (HB) of the surface ions. Both terms, RPA and HB, can be met in the literature and are used interchangeably.

As an example we simulate, in 1D, a laser pulse with a normalized amplitude of $a_0 = 10$ and $\tau_0 = 30$ fs duration interacting with an overdense pre-ionized plasma of hydrogen ($n_i = n_e = 100\ n_c$) beginning at $x = 200\ c\omega_0^{-1}$. As described above the ponderomotive pressure piles up an electron layer and a longitudinal electrostatic field is set up [black curve in Fig. 5.3(a)]. Thus ions are accelerated and form a density spike which compresses the plasma [compare plain and dashed red curves in Fig. 5.3(a)]. The ion motion in the laser piston is particularly visible after $t \equiv 400\ \omega_0^{-1}$ on the (x,t) map of the ion density [Fig. 5.3(b)] where the trajectory of the peak density gives the ion velocity $\beta_i \approx \Delta x/\Delta t = 0.033$. The longitudinal ion phase space taken at $t = 600\ \omega_0^{-1}$ exhibits the energetic ion population propagating ballistically in the target [see Fig. 5.3(c)]. The ion velocity theoretically predicted by the RPA model gives $\beta_i = 0.033$ in agreement with the velocity measured in the simulation. As a result, an ion beam centered at $\epsilon_i = m_i c^2[(1-\beta_i^{-1/2})-1] \approx 500$ keV energy is produced.

Light Sail Acceleration (LSA)

The Light Sail Acceleration regime is an extreme case of RPA in which the laser piston travels a distance larger than the target thickness, $v_p\tau_0 > d_0$. As a result, the target is accelerated as a whole [Esirkepov *et al.* 2004]. Once again linearly polarized pulses are subject to TNSA such that RPA ions have to catch up backside TNSA ions to form a single bunch undergoing a hybrid light-sail-target normal sheath acceleration [$v_p > v_i^f(d_0/v_p)$ with v_i^f given by Eq. (5.16)] [Qiao *et al.* 2012].

We quickly recall the evolution of the ion Lorentz factor as a function of time. The equations

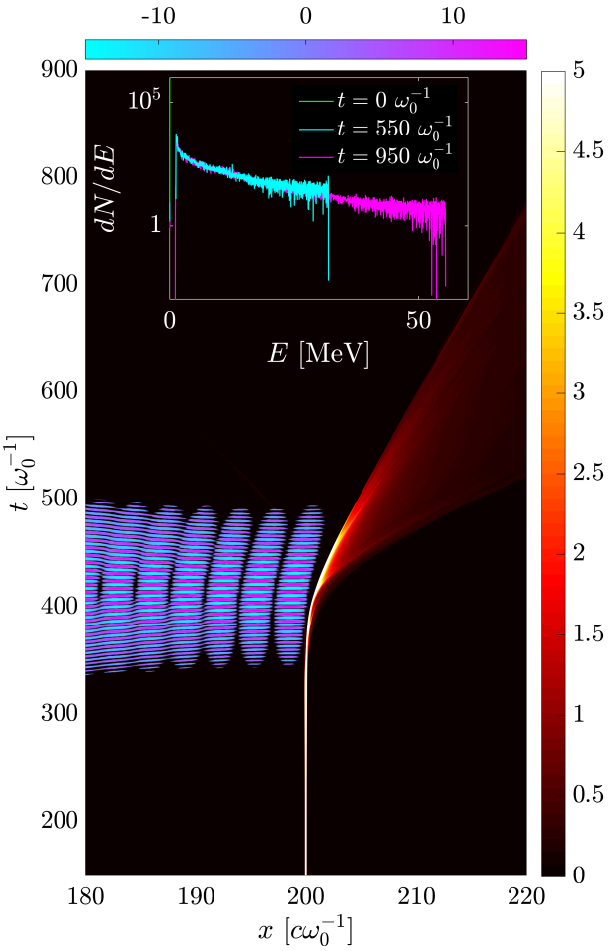

Figure 5.4: (x, t) map of the hydrogen density (hot colormap in log scale) and laser electric field (oscillating structure and related cyan-magenta colormap) with amplitude $a_0 = 10$, duration $\tau_0 = 30$ fs and linearly polarized, interacting with a plastic foil (CH_2) of 15 nm thickness. Inset shows proton spectra at three different instants (see legend) underlying the continuous acceleration of the LSA regime.

of motion of the whole (supposed rigid) target are given by [Marx 1966]:

$$\frac{d}{dt}(\gamma_i \beta_i) = \frac{2}{\sigma c^2} I(t - x_i/c) \frac{1 - \beta_i}{1 + \beta_i}, \tag{5.20}$$

$$\frac{d}{dt} x_i = \beta_i c, \tag{5.21}$$

with $\sigma = m_i n_i d_0$ is the areal mass density. As previously we recover the radiation pressure term function of the laser intensity seen by the ions. For a constant intensity profile I_0, an analytical solution with the following limits can be derived [Simmons & McInnes 1993]:

$$\gamma_i(t) \approx \begin{cases} 1 + 4(\Omega t)^2 & \text{if } \Omega t \ll 1 \\ (3\Omega t/4)^{1/3} & \text{if } \Omega t \gg 1 \end{cases} \tag{5.22}$$

where $\Omega = 2I_0/\sigma c^2$. Interestingly the target motion is not at constant velocity as in RPA, but continually accelerated. A major challenge concerns the laser temporal contrast, which has to be high enough to maintain the target integrity before the arrival of the main peak intensity.

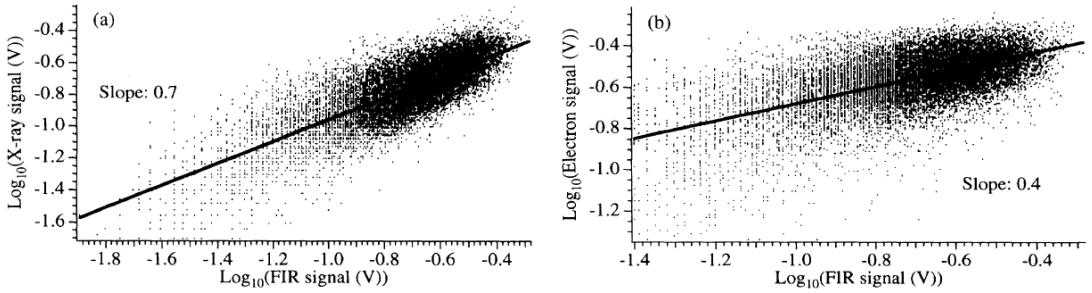

Figure 5.5: Far infrared signal versus (a) X-ray and (b) electron scintillator signal from an aluminum irradiated target. *Extracted from* Hamster *et al.* [1993].

As an illustration of this process, Fig 5.4 shows a (x, t) map of a linearly polarized laser electric field ($a_0 = 10$) coming from the left and reflecting on an ultra-thin (15 nm) plastic target of CH_2. The proton density (hot colormap in log scale) demonstrates that the whole target is accelerated by the laser. A weak part of it is transmitted (not shown). The inset illustrates the continuous acceleration feature in the LSA regime: the proton spectrum becomes more energetic as time passes by. At $t = 50\ \omega_0^{-1}$, Eq. (5.22) gives an estimate $\gamma_i \approx 1.0016$ ($\Omega t \sim 0.02$) corresponging to $\mathcal{E}_i \approx 1.5$ MeV which is a fair approximation of the proton energy inferred from the ion trajectory.

5.1.4 Origin of the THz emission by irradiated solid targets

The emission of low-frequency fields by solid targets has evolved from a subject of curiosity to a strong candidate for high energy THz pulse generation and plasma diagnostic. To better understand the involved physics as well as the trajectory of the research on this subject, we propose, below, a rapid (and certainly non-exhaustive) review of the literature.

The pioneering work of Hamster *et al.* [1993] paved the way for numerous studies clearing up the origin of THz generation in both overdense and underdense plasmas (given the limited intensity contrast then available). As demonstrated in this reference, the transient space charge field driven by the ponderomotive force of the laser pulse first explained successfully the low-frequency emission in underdense plasma. This description has been extended by D'Amico *et al.* [2008] to propose an explanation of THz emission in long atmospheric plasma filaments (see Section 2.1.4). However the fair agreement between the model and experimental results next breaks down for overdense plasmas in which more complex dynamics occurs. Indeed, the poor quality of the laser contrast suggests the formation of a pre-plasma in which low-frequency emission occurs. An interesting point is the observed correlation between the low-frequency signal and hot electron generation and X-rays emission (see Fig. 5.5).

Since then, many studies have been dedicated to unveil the physical processes responsible for THz emission. This task is complex since the laser energy is transferred by various absorption mechanisms, each of them leading directly or indirectly to low-frequency emission. In order to give a clear overview we propose to classify the different contributions according to key parameters (intensity and plasma scale length) instead of the chronological order only. Figure 5.6 sketches this approach. THz pulse generation in solids is first divided into two branches according to the involved laser intensity.

Moderately relativistic intensities ($a_0 < 1$) have been widely used to study THz emission from the front surface. To preserve the laser system integrity and to optimize the interaction, the laser pulse is usually p-polarized and focused with a moderate incidence angle ($> 20°$).

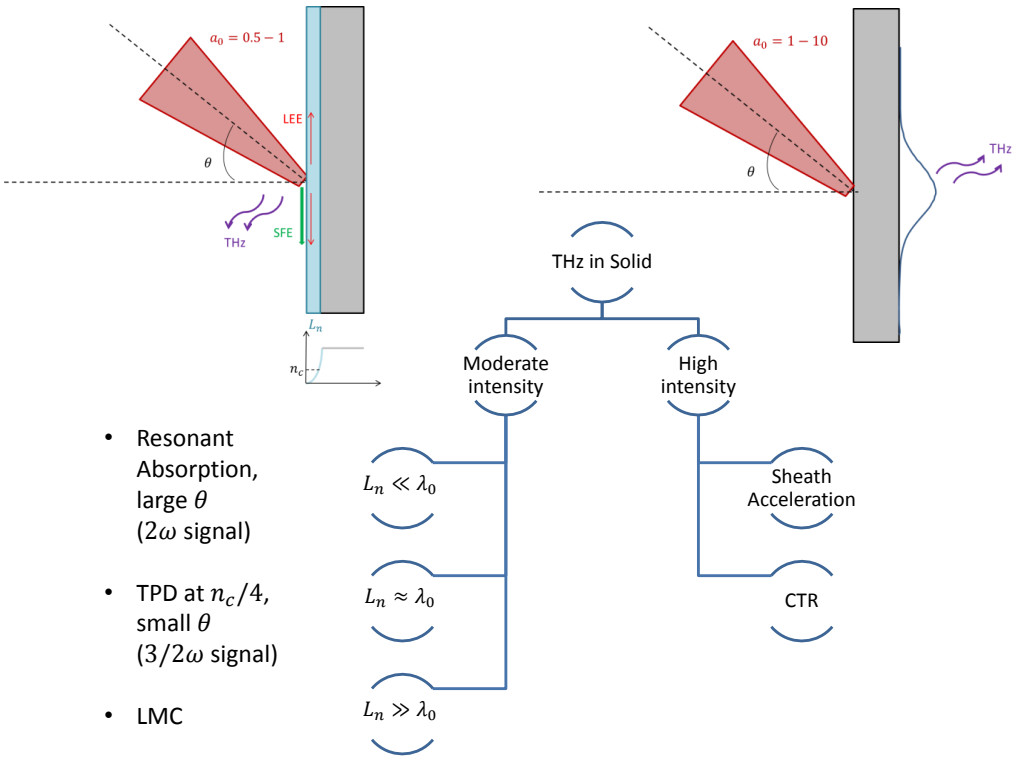

Figure 5.6: Sketches of the different mechanisms responsible for THz emission in solids. for moderately relativistic intensity ($a_0 = 0.5 - 1$) reported THz emission comes from the front surface of the irradiated target (see upper right). Depending on the density scale length L_n compared to the laser wavelength λ_0 and the incident laser pulse angle, different mechanisms can be invoked [resonant absorption, two plasmon decay (TPD) or linear mode conversion (LMC)] [Kruer 1988]. For high intensity laser pulses, low-frequency emission is mainly observed from the rear target surface and is strongly correlated to the hot electron cloud (CTR) and ion acceleration (sheath acceleration).

By doing so the laser electric field has a component along the target normal and is able to excite an electron plasma wave. The amplitude of the latter grows at each laser cycle similarly to a driven harmonic oscillator. This so-called resonant absorption [Ginzburg 1964; Freidberg *et al.* 1972] has a dependence with the density scale length and the incidence angle: It is characterized by the conversion efficiency $\eta = (k_0 L)^{2/3} \sin^2\theta$, reaching a maximum around ~ 0.5. For strong laser electric field ($I_0 > 10^{16}$ W/cm^2), electrons are directly dragged into vacuum by the normal component E_x and reinjected back into the plasma at each laser cycle resulting in higher absorption (up to $\eta \sim 0.8$) and emission at ω_0 and higher harmonics [von der Linde *et al.* 1992; Gizzi *et al.* 1996]. This signature of the Brunel effect is now used in experiment as a tracer for electron heating by resonant absorption.

Meanwhile, this hot electron population leads to transient surface currents able to radiate low-frequency electromagnetic waves. This antenna-like emission (see Fig. 5.7) was proposed by [Sagisaka *et al.* 2008] who also observed, for the first time, a correlation between THz emission and proton acceleration ($\sim$ 450 keV) when limiting the laser pre-pulse. The measured THz energy was of about 50 nJ/sr corresponding to a total of 5 μJ in agreement with the analytical evaluation $\sim$ 7 μJ. The latter considers that the THz energy is given by the magnetic field generated by the surface current inside the volume defined by the electron excursion length $r \sim L_\perp/2$, with $L_\perp$ being the target width:

$$E_{\mathrm{THz}} = \epsilon_0 B^2 \frac{4\pi r^3}{3} \tag{5.23}$$

and where the magnetic field amplitude is evaluated with the Maxwell-Ampere equation [Eq. (2.4)]. The THz pulse should be centered around the frequency $\sim 2c/L_\perp$($\sim$ 0.12 THz for $L_\perp = 5$ mm) whereas the measured spectrum peaks at 0.2 THz ($\sim$ 2 ps duration with 25 kW estimated power). A similar experiment was conducted by [Gao *et al.* 2008] on a copper wire with the first direct measurements of THz pulse amplitude and phase. According to this antenna model, the peak frequency should be lowered since $L_\perp$ is very large. However the central frequency was measured at 0.15 THz and was correlated to the emission of X-rays, suggesting a similar driving mechanism. From there no clear picture was achieved since neither the ponderomotive approach of Hamster *et al.* [1993] nor surface currents could explain the experimental data. Nevertheless, the key point is the importance of the hot electron generation mechanism since those studies underlined the correlation between various high frequency emissions (X-rays, $3\omega_0/2$) and particle acceleration, both being intrinsically linked to the electron dynamics.

A few years later, Li *et al.* [2011] studied THz emission from the front target surface (copper foil) with a 100 fs laser duration at intensity $\sim 10^{18}$ W/cm^2 ($a_0 = 0.7 - 1$) with three different intensity contrast ratios from 10^{-8} to 10^{-6}. By definition, the contrast is high when the contrast ratio is actually small, i.e., the pedestal has much lower intensity than the main pulse. In this case the target is gently pre-heated by the pre-pulse and one can fairly assume that the plasma scale length is small. Alternatively, for bad contrast, i.e. high contrast ratio, the pre-pulse is able to significantly heat the target and the plasma expands in vacuum prior to the arrival of the main pulse. As a result, varying the contrast ratio is similar to changing the laser absorption condition so that different hot electron populations are generated. Due to the high incidence angle ($\theta = 67.5°$), a high contrast (10^{-8}) is favorable to resonant absorption and $2\omega_0$ line emission is clearly observed, correlated to a THz signal with ~ 0.2 μJ/sr [see Figs. 5.8(a,b,c,d)]. For an intermediate contrast ratio, both the THz signal and $2\omega_0$ emission decreases while a $3\omega_0/2$ line arises [see Fig. 5.8(a,b,e,f)]. This spectral signature is due to the two plasmon decay (TPD) instability occurring at the quarter critical density $n_c/4$ in a sufficiently smooth plasma

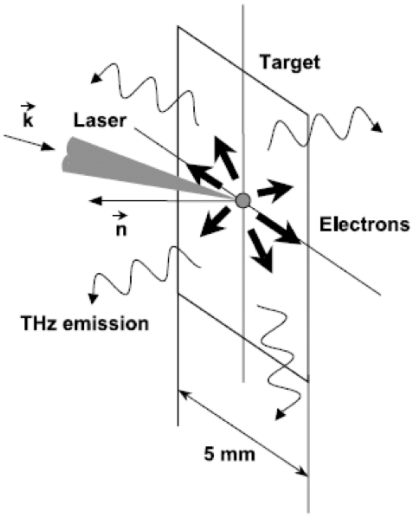

Figure 5.7: The incident laser pulse generates a surface electron current emitting the THz radiation. **k** and **n** are the light wave vector and the unit vector normal to the target surface, respectively. *Extracted from* Sagisaka *et al.* [2008].

density profile [Kruer 1988]. For the smallest contrast (10^{-6}), the $3\omega_0/2$ signal vanishes and THz emission reaches its minimum. Complementary 2D PIC simulations show similar trends and suggest that stimulated Raman scattering (SRS) is responsible for low-frequency emission in long scale length plasmas. Finally, s-polarized light was tested experimentally in the high-contrast configuration (10^{-8}), leading to 4 times less THz radiation yield. Accordingly, no second harmonic was observed in the reflected light spectra. These results are consistent with an efficient resonant absorption mechanism which is absent using s-polarization.

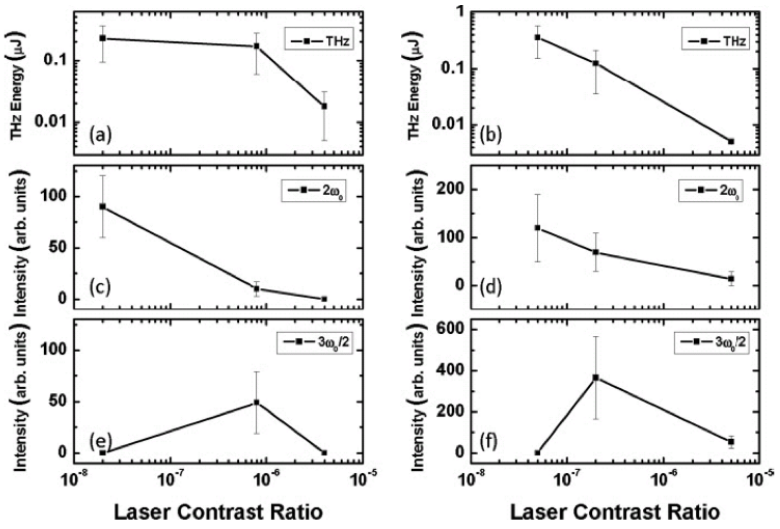

Figure 5.8: Terahertz (a,b), $2\omega_0$ (c,d) and $3\omega_0/2$ (e,f) signal (averaged over 100 shots) dependence with respect to the laser contrast ratio for $a_0 = 0.7$ (a,c,e) and $a_0 = 1$ (b,d,f). *Extracted from* Li *et al.* [2011].

Appart from this picture in which resonant absorption is the main heating mechanism, the THz emission due to the surface fast electron (SFE) current was evidenced by [Nakamura *et al.* 2004; Sentoku *et al.* 2004; Li *et al.* 2006; Chen *et al.* 2006; Yuan *et al.* 2008]. The latter, due to surface quasi-static electromagnetic fields, arises only for small plasma scale lengths and

is naturally optimized for large incidence angles since the turning point $n_c \cos^2\theta$ decreases the effective pre-plasma length. Experiments dedicated to test THz waves driven by the SFE current were conducted by [Li *et al.* 2012b] who used marginally relativistic ($I_0 \sim 2.7 \times 10^{18}$ W/cm^2) p-polarized laser pulses focused on copper targets at large incidence angle ($\theta = 67.5°$). The measured THz waveform duration was of about 1.5 ps with a peak frequency at 0.5 THz and a collected energy corresponding to 50 μJ/sr. Changing to a s-polarized laser decreased the THz emission by a factor 5 and increasing the laser energy led to a linear increase in the THz yield with no saturation effect, contrary to laser-gas driven THz sources. The role of the SFE current was supported by 2D PIC simulation showing a net transient transverse current at the plasma-vacuum interface.

Let us now reconsider the two first proposed THz generation mechanisms. The contribution of the ponderomotive force suggested by Hamster *et al.* [1993] may effectively push a fraction of electrons along the target surface at very large incidence angles. However, this usually creates a longitudinal current in high density regions from which THz waves can not escape, withdrawing thus the ponderomotive force from the main THz emitters. The antenna model proposed by Sagisaka *et al.* [2008] has been tested by varying the position of the focal spot on the target to influence the peak frequency, which gave no convincing effect. Also, examining the role of the target dimension, Li *et al.* [2012b] reported that the peak frequency should be equal to 0.006 THz which is not the case. Nevertheless no direct observation of THz radiation induced by surface currents and resonant absorption has been reported in this experiment.

Simultaneous measurement of THz and second harmonic signals at different laser incidence angles (67.5°, 45° and 22.5°) have been performed by Li *et al.* [2014]. Contrary to Li *et al.* [2011]'s experiment where the density scale length varied shot-to-shot, a net correlation between THz and $2\omega_0$ signals for similar pre-plasma conditions but different incident angles was demonstrated here, hence proving a real dependence of the THz yield with respect to the resonant absorption rate [see Fig. 5.9(a)]. Note also the net linear increase in the THz signal with the laser intensity without any clamping [see Fig. 5.9(b)]. As an intermediate conclusion, THz emission from the front target surface at large incidence angles and short plasma scale lengths was mainly attributed to resonant absorption (see Fig. 5.6).

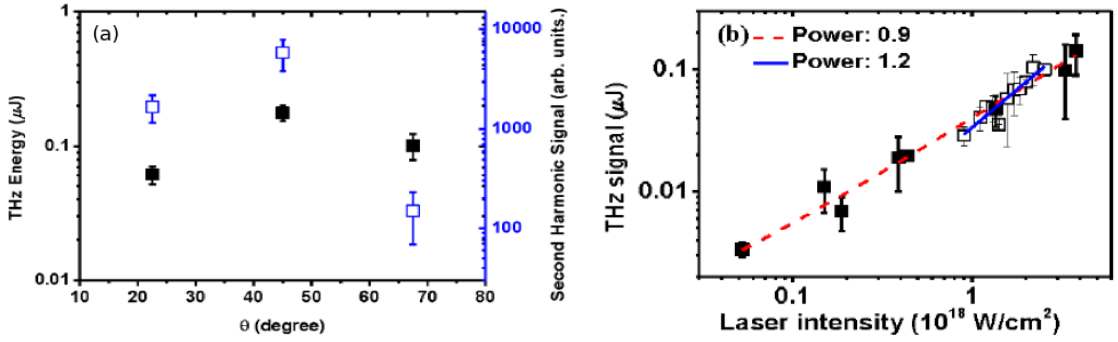

Figure 5.9: (a) Averaged (∼ 20 shots) THz energy (black solid squares) and second harmonic signal (open blue squares) measured along three different incident angles θ of a p-polarized laser pulse. *Extracted from* Li *et al.* [2014].

An attempt to unify the antenna model and the SFE current mechanism by investigating independently different laser incidence angles and plasma scale lengths was made by Li *et al.* [2016]. In addition to SFE, a low energy electron (LEE) current can be observed in the under-dense pre-plasma [Stephens *et al.* 2004] and might be responsible for the THz emission reported

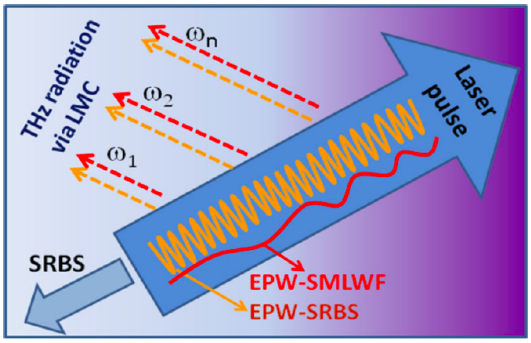

Figure 5.10: Scheme of THz emission by linear mode conversion (LMC) et local plasma frequencies. The plasma wave is excited by plasma instabilities such that Raman backward scattering (EPW-SRBS) and relativistic self-modulation instability (EPW-SMLWF). *Extracted from* Liao *et al.* [2015].

by Sagisaka *et al.* [2008]. Indeed, two THz peaks were observed in front of the target surface: one normal to the interface due to LEE with high frequency components (> 10 THz) and a minor one along the target surface due to SFE with low frequencies (< 3 THz). When changing the contrast ratio from 10^{-8} to 10^{-6} the $2\omega_0$ signal decreases while the $3\omega_0/2$ one rises as already reported but, here, the higher frequency radiation (> 10 THz) is moreover enhanced by a factor 1.7 while the drop in the low frequency (< 3 THz) signal suggests a transition in the heating mechanisms from resonant absorption to two plasmon decay (TPD). The latter induces LEE currents emitting THz radiation at the plasma boundary. A complementary study carried out by [Liao *et al.* 2016a] demonstrated the relevance of the TPD mechanism at small incidence angle ($\sim 10°$) and intermediate plasma scale length where similar THz and $3\omega_0/2$ signals are recorded. Note that unlike previous observations, degrading the contrast enhances the THz yield before saturation happens whatever the contrast value may be. Hence, when the plasma scale length increases, TPD becomes the dominant heating mechanism with higher THz frequency emission (see Fig. 5.6).

The last case of interest is that of a large pre-plasma scale length in front of the solid target. Experiments realized by [Liao *et al.* 2015] demonstrated that 100 μJ/sr of THz radiation mainly in the range > 10 THz can be collected in the laser specular direction (62.5°) for a pre-plasma length of 40-50 μm with no saturation effect with respect to the laser energy involved. The invoked mechanism is the linear mode conversion (LMC) of electron plasma waves into THz radiation, first proposed by Sheng *et al.* [2005a,b]. Due to the long pulse duration (0.5 ps), laser wakefield with frequency higher than 2 THz can not be excited by the laser ponderomotive force. Instead, a collection of plasma instabilities (SRS, self-modulation instability) excite plasma waves which in turn emit electromagnetic waves at local plasma frequencies belonging to the THz range (see Fig. 5.10). This explanation completes the left branch of Fig. 5.6.

The use of powerful laser facilities (JETI, VULCAN) led to efficient THz emission from the rear target surface. Gopal *et al.* [2012] were the first to observe it by irradiating a 5 μm thick titanium foil with the JETI laser beam (1 J, 800 nm, 30 fs, $1 - 6 \times 10^{19}$ W/cm^2). A pulse of 2 μJ energy in the band 0.15-2 THz has been recorded in noncollinear direction (large angles with respect to the target normal direction). Such THz emission was attributed to the plasma expansion at the target backside (TNSA) induced by the escaping hot electron cloud. 2D PIC simulations confirmed this radiation process. Good agreement on the spatial distribution of the emission between simulation data and a dipole-like radiation model was reported. Also, the

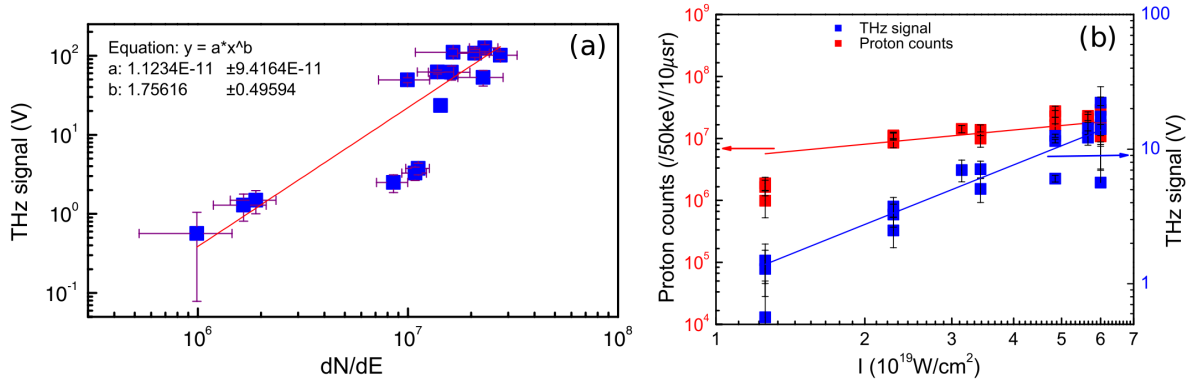

Figure 5.11: (a) Terahertz signal as a function of proton number. The fitting line has a power law exponent of 1.76 ± 0.49, *extracted from* Gopal *et al.* [2013a]. (b) Proton number and noncollinear THz signal as a function of the laser intensity. The former scales quadratically as previsously reported while the latter scales linearly without signs of saturation, *extracted from* Gopal *et al.* [2013b].

assumption of a TNSA field driven emission is in agreement with experimental data showing a radially polarized emission. Nevertheless no clear correlation between the emitted THz pulse and the number of accelerated protons has been measured. Later the same experiment has been conducted with better laser contrast and more favorable target configuration [Gopal *et al.* 2013a]. Simultaneous recording of the THz pulse and ion spectrum confirmed a common driving mechanism [see Fig. 5.11(a)]. As a result, as high as 460 μJ energy pulses were collected in the spectral band 0.1-30 THz. 2D PIC simulations revealed a transient current at the rear target surface with a radial polarization confirming the proposed generation mechanism. Similar measurements were realized in a broader spectral range (0.1-133 THz) leading to 700 μJ THz pulse energy [Gopal *et al.* 2013b]. In addition to the square law dependence of the number of protons, the THz signal was found to scale linearly with the laser intensity without any saturation effect [see Fig. 5.11(b)].

A similar laser system (30 fs, 800 nm, $0.88 - 3.5 \times 10^{19}$ W/cm^2) with higher contrast (10^{-10}) recently overcame the millijoule level with 10.5 mJ THz energy corresponding to 1.7% conversion efficiency [Jin *et al.* 2016]. Terahertz radiation was measured to increase dramatically when reducing the target thickness from 30 μm to 2 μm. There results a higher hot electron density, and therefore, a stronger TNSA sheath field. The adverse effect of the pre-plasma was also demonstrated, a lower energy being collected (30 μJ) with a contrast of 10^{-5}. These impressive results further demonstrate once again the relevance of laser-plasma driven THz sources. However alternative driving mechanisms can be invoked to explain the observations.

Among those, coherent transition radiation (CTR) should occur when the hot electron cloud escapes in vacuum. This scenario was investigated by Liao *et al.* [2016b] using 1.5×10^{19} W/cm^2 laser pulses (2 J, 30 fs, 800 nm, contrast of 10^{-5}) impinging on various targets (metal, metal-polyethylene, polyethylene). Good agreement on the spatial distribution between experimental data and numerical/theoretical curves was demonstrated. Unlike previous works, the emitted THz field, with 460 μJ energy, was elliptically polarized as predicted by CTR theory from non-normal crossing particles [Ter-Mikaelian 1972]. The nature of the emission seemed to be coherent even if the accelerated electron charge was not measured. Interestingly, the THz features (energy, polarization) differed significantly from the work of Jin *et al.* [2016] whereas laser systems and targets are similar, in spite of similar laser systems (with the exception of the temporal contrast). Hence, a high contrast seems to favour ion acceleration which in turn

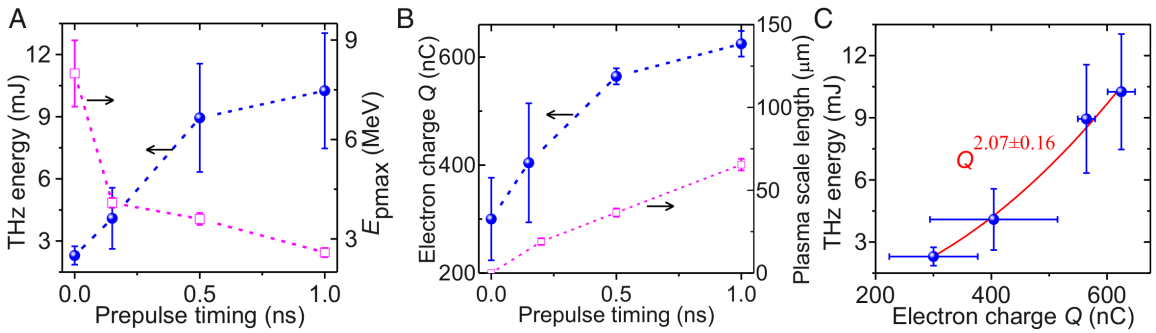

Figure 5.12: (a) THz energy (blue circles) and maximum proton energy (magenta sqaures) as function of the timing between the pre-pulse at the target rear. (b) Measured electron charge (blue circles) and simulated (MULTI-fs code) density scale length (magenta squares). (c) THz energy versus electron charge (blue circles) with a power-law fitting curve (red). *Extracted from* Liao *et al.* [2019].

gives rise to intense THz pulse, while a low contrast contributes to the creation of a pre-plasma lowering the sheath radiation and promoting CTR.

Lately, Herzer *et al.* [2018] highlighted the distinct emission directions of the two processes when irradiating a 5 μm thick titanium foil with the JETI laser beam ($\geq 5\times10^{19}$ W/cm^2, 30 fs, 0.8 μm). These authors ascribed the THz emissions in the non-collinear and collinear directions to, respectively, the TNSA-induced radiation (712 μJ) and CTR (40 μJ). In principle, each emission scales quadratically with the proton (sheath radiation) and electron (CTR) number allowing to identify them easily. However, particle energy measurements were not performed in this work. Recently, Liao *et al.* [2019] explored a new regime of longer pulse irradiation with the VULCAN laser (60 J, $\sim$ 1.5 ps, $\sim 5\times10^{19}$ W/cm^2, 1 μm). A low intensity ($3-6\times10^{13}$ W/cm^2) additional beam was used to create a pre-plasma at the rear surface of a 100 μm thick copper target, allowing direct manipulation of the sheath field amplitude: The pre-plasma scale length varied with the relative timing between the pre-pulse and the main pulse. The experiment showed an expected decrease in the maximum proton energy, correlated to a decrease in the sheath field, when increasing the pre-plasma scale length [see Fig. 5.12(a)]. At the same time, the measured electron charge followed the growth of the THz energy with a quadratic power law [see Figs. 5.12(b,c)]. Also, the THz angular distributions and spectra match well the CTR model. These trends indicate that the sheath radiation is not the driving mechanism in this configuration. The increase in the THz energy with the pre-plasma scale length was explained as follows: When the sheath field is strong (small scale length), the hot electrons re-entering the target emit backward CTR which interferes destructively with the forward CTR. These re-circulating electrons are less numerous for a weak sheath field (long scale length) resulting in a more efficient CTR emission ($\sim$ 4 enhancement factor). The maximum THz energy then reached is of about 50 mJ below $<$ 3 THz (due to the long pulse duration) offering an alternative to fs-pulse laser-solid interactions that produce broader spectra ($\sim$ 30 THz).

To conclude this summary, recent experimental measurements have demonstrated the potential of relativistic laser-solid interactions to produce table-top THz sources. Mechanisms of emission from the front surface with marginally relativistic lasers have been cleared up, revealing the complex interplay of surface currents. At higher intensities, the proton-accelerating sheath field acts as a moving dipole emitting THz radiation. Also, the expanding hot electron cloud drives CTR in the THz band at the target rear-vacuum interface. Both processes can lead to mJ-level THz pulses. Nevertheless, further investigations remain to be conducted to assess the

interplay of TNSA, CTR and surface currents for THz emission.

5.2 Laser-solid interaction for THz emission

Our purpose is to investigate the generation of THz radiation in laser-solid interaction for a given laser-target configuration favouring ion acceleration. In the following, we first present the numerical parameters of our baseline simulation. Then we describe the electron and ion dynamics resulting from the laser-plasma interaction. Finally, we adress the different THz radiation mechanisms as they occur during the interaction.

5.2.1 Numerical setup

We again use the PIC code CALDER in 2D Cartesian geometry. The notable change compared to the laser-gas simulations studied so far is the high numerical constraint imposed by the laser-solid interaction, which requires a sufficient discretization of the characteristic lengths and timescales. In overcritical targets, the smallest dimension to be resolved is indeed the plasma skin depth c/ω_{pe} which is much smaller than the 1 μm laser wavelength.

In our study, we consider ultra-thin CH_2 plastic targets with density of $\rho = 1.1$ g/cm^3 corresponding to a total electron density of $n_e = 400\ n_c$. The plasma skin depth is $c/\omega_{pe} = 0.05\ c\omega_0^{-1} \approx 8$ nm. The spatial resolution is set to $\Delta x = \Delta y = 0.03\ c\omega_0^{-1} \approx 5$ nm, which corresponds to state-of-the-art, high resolution PIC simulations in 2D geometry. The simultion domain has dimensions of $600\times600(c/\omega_0)^2 = 95\times95\ \mu$m^2, hence totalizing $(600/0.03)^2 = 4\times10^8$ cells. The time step is $\Delta t = 10$ as. The simulation lasts about 1 picosecond to capture low-frequency oscillations which corresponds to $10^5\ \Delta t$.

For the baseline simulation we opt for a target thickness of $d_0 = 500$ nm and a transverse size of $300\ c\omega_0^{-1} \approx 45\ \mu$m (see Fig. 5.13). To begin with, the target is assumed completely pre-ionized. Each of the three particle species (C^{6+}, H^+ and electrons) is represented by 400 macro-particles per cell. The total number of target cells is $(\pi/0.03)\times(300/0.03) \approx 10^6$ leading to a total of 1.2×10^9 particles. The simulation is run in parallel over 1000 CPUs during a week.

Figure 5.13 shows a snapshot of the simulation domain before the interaction. The 1 μm wavelength laser pulse is relatively modest with 1.2 J energy and 40 TW power. It is polarized in the y direction and is normally incident onto the target. The FWHM pulse duration is set to 30 fs and the focal spot waist to 5 μm. As a result, the initial intensity is 1.4×10^{20} W/cm^2, corresponding to a normalized vector potential of $a_0 = 10$. The plastic foil is placed in the middle of the simulation domain in order to allow us to analyze the electromagnetic emission from both sides of the target.

5.2.2 Global behaviours

Before dwelling upon the THz emission, we present the main processes occurring in the baseline simulation. We first look at the generation of the hot electron population in light of the mechanisms described in Section 5.1.2. Then we focus on the ion acceleration, which the ultrathin target design is expected to enhance.

Hot electron generation

Owing to their small mass, electrons react the fastest to the laser electromagnetic field and are energized through a combination of vacuum and skin layer heating. Figure 5.14 shows four

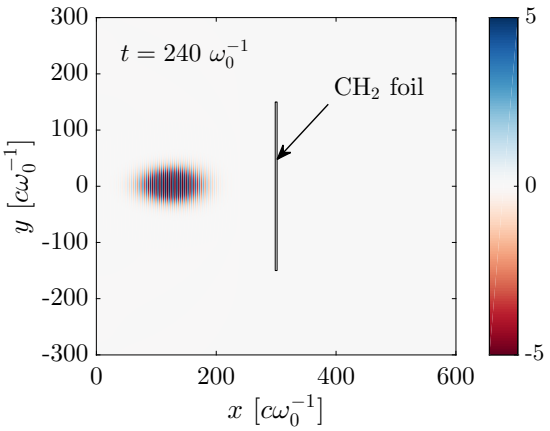

Figure 5.13: Snapshot of the incoming laser electric field E_y $[m_e c\omega_0/e]$ before its interaction with the ultra-thin solid target ($d_0 = 500$ nm) of plastic.

snapshots of the electron phase space (x, p_x) along with the on-axis laser electromagnetic fields (E_y, B_z). Before the interaction, at $t = 300\ \omega_0^{-1}$, both fields are overlapped [see Fig. 5.14(a)].

A moment later, the laser pulse starts to interact with the front surface of the target and strong electron heating occurs [see Fig. 5.14(b)]. A fraction of electrons are pushed forward by the laser and escape in vacuum ($p_x > 0$) while others are pulled back by ions ($p_x < 0$). The forward propagating electrons are bunched with a $\lambda_0/2$ period corresponding to the fast component of the ponderomotive force. As underlined in Section 5.1.2, the electric field (red curve) prevents most of the electrons from escaping into vacuum and from interacting with the standing wave. A few laser periods later, we observe in Fig. 5.14(c) a $\lambda_0/2$ bunched population of hot electrons traveling backward in front of the target ($p_x < 0$ and $x < 300$). This picture is consistent with the situation sketched in Fig. 5.1(b) where electrons having enough negative longitudinal momentum escape in vacuum and are heated by the standing wave. The low-energy fraction is injected back into the target and eventually cross it again while higher energy electrons are stochastically heated and can even experience direct laser acceleration.

Figure 5.14(d) shows the reflected laser pulse with now a π phase shift between E_y and B_z due to the reflection on the foil. A small part of light is transmitted through the target and accompany the forward-moving electron bunch. The estimated temperature of this hot electron population is given by the slope of the energy spectrum and is of ~ 6.5 MeV comparable with the ponderomotive scaling $T_h \equiv 4.6$ MeV. Note that a similar effect based on high-energy electrons being injected and re-accelerated in the reflected pulse has been pointed out by Yu *et al.* [2000] in the case of an underdense pre-plasma in front of the solid target.

Ion acceleration

Once the hot electron cloud starts to expand in vacuum, a space charge field is created. Figure 5.15 shows the successive steps of proton acceleration, developing over much longer timescales than electron acceleration ($t = 700 - 1500\ \omega_0^{-1}$). The forked shape of the phase space for $p_x > 0$ is due to a mixed acceleration regime involving both TNSA and RPA. The rear-side ion front is pulled by the TNSA field (black curve) whose amplitude reaches 0.1 $[m_e c\omega_0/e] \approx 1$ TV/m. The second peak in the proton phase space is due to the laser ponderomotive force on the target front surface. In this configuration, protons accelerated by TNSA and RPA do not merge to form a unique ion front such as in LSA regime for instance. Note that some hydrogen ions are also accelerated in the backward direction ($p_x < 0$) as a result of an additional TNSA-like

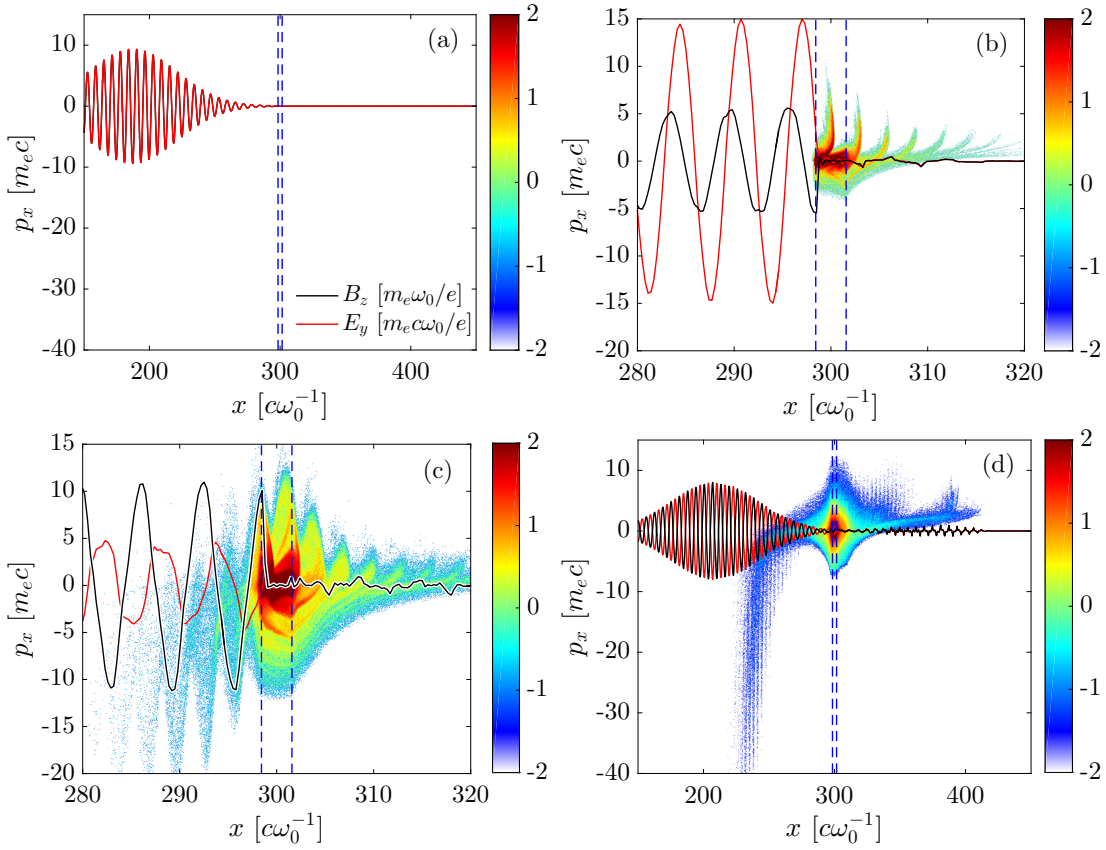

Figure 5.14: Overlap of the longitudinal electron phase space map (x, p_x) and of the on-axis (E_y, B_z) laser fields at (a) $t = 300\ \omega_0^{-1}$, (b) $t = 400\ \omega_0^{-1}$, (c) $t = 440\ \omega_0^{-1}$ and (d) $t = 500\ \omega_0^{-1}$ for the 500 nm thick plastic target. The vertical blue dashed lines represent the initial target limits. Note the change of scale in (a,d) compared to (b,c).

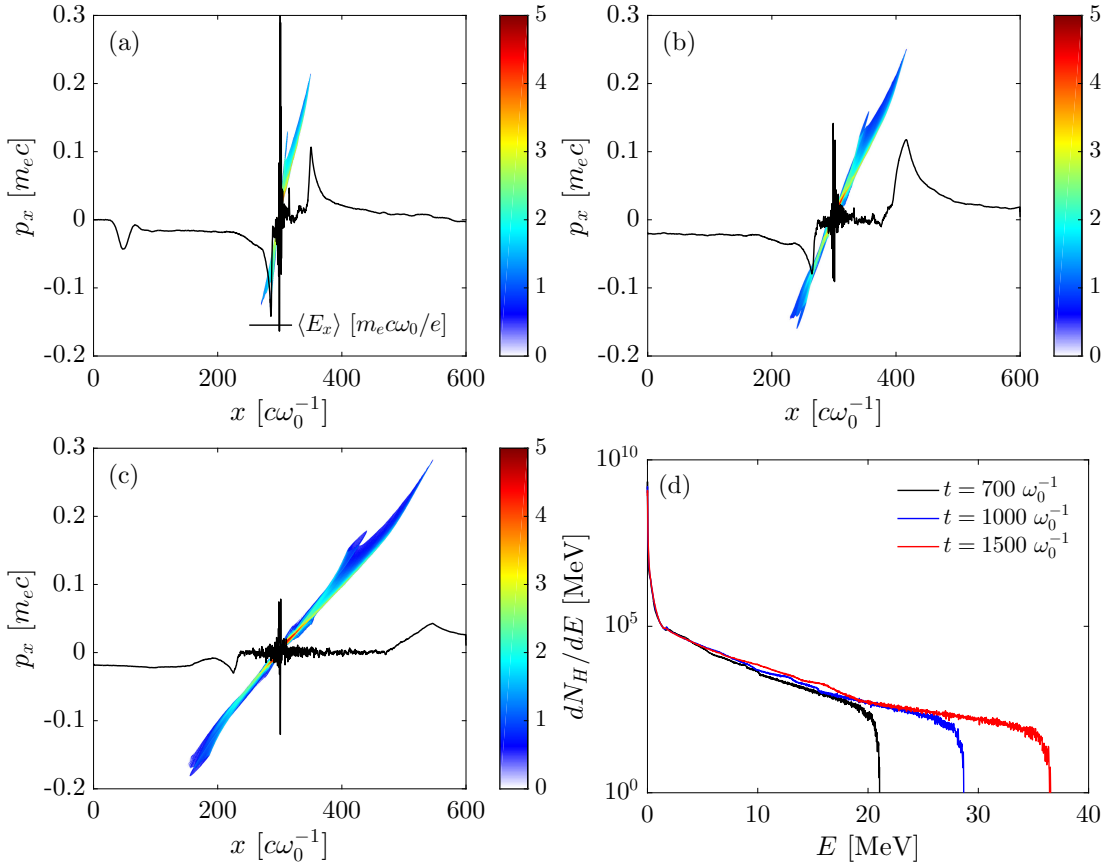

Figure 5.15: Proton longitudinal phase space (x, p_x) overlapped with the on-axis longitudinal electric field averaged over one laser period at (a) $t = 700\ \omega_0^{-1}$, (b) $t = 1000\ \omega_0^{-1}$ and (c) $t = 1500\ \omega_0^{-1}$. (d) Proton spectra at the three snapshots.

process. As time increases the maximum proton energy grows from ~ 20 MeV up to 36 MeV [see Fig. 5.15(d)].

Since the pioneering studies on ion acceleration by relativistic laser pulses [Snavely *et al.* 2000], many theoretical, numerical and experimental studies have been conducted to reach higher and higher ion energies. It has been shown that thin targets enhance ion acceleration by giving rise to higher electron density at the rear surface [Mackinnon *et al.* 2002]. In the case of subpicoseond laser pulses, optimum ion acceleration has been found in ultrathin (typically nanometer-sized) foils at the threshold of relativistic transparency [Esirkepov *et al.* 2006; Brantov *et al.* 2015]. This correponds to an optimum thickness [Brantov *et al.* 2015]

$$d_0 = \frac{a_0 \lambda_0 n_c}{2 n_e}. \tag{5.24}$$

For our parameters ($a_0 = 10$, $\lambda_0 = 1\ \mu$m and $n_e/n_c = 400$) we have $d_0 = 12.5$ nm. Due to numerical constraints we have run two additional simulations with $d_0 = 50$ nm and $d_0 = 15$ nm. Figure 5.16 shows the maximum proton energy as a function of time. After a rapid increase at early times, the ion energy increases more slowly by $t \sim 500\ \omega_0^{-1}$, yet without showing a clear saturation trend. This continual increase is probably a consequence of the reduced 2D geometry: In 3D, the sheath field should drop more rapidly once the ion front has travelled a distance comparable with the transverse size of the sheath, thus arresting the ion acceleration at lower energy levels. The proton energy is effectively increased when using a target thickness

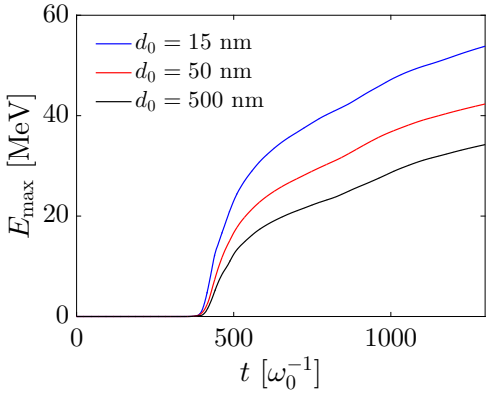

Figure 5.16: Maximum proton energy in MeV as a function of time for the three target thicknesses (see legend).

close to the requirement Eq. (5.24). Thus, for the same laser system, it evolves from 28 MeV at $d_0 = 500$ nm to 45 MeV at $d_0 = 15$ nm.

5.2.3 Processes responsible for THz emissions

We now adress the emission of low-frequency fields as a result of the plasma currents generated by the laser pulse. To extract them properly an hypergaussian filter with cut-off frequency $k_c = 0.3k_0$ is applied to the Fourier transformed fields. An inverse transformation gives the low-frequency field map in the real domain.

Figures 5.17(a-i) show the filtered fields (E_x, E_y, B_z) just after the laser interaction with the 500 nm thick target. They give a global overview of the emitted field dynamics. Several structures can be distinguished despite their rather complex patterns. For instance, one easily observes the TNSA field [see ① in Fig. 5.17(b)] driven by electrons expanding into vacuum [Figs. 5.17(a,b,c)] . By contrast, the quadrupolar field [see ② in Fig. 5.17(d)] propagating backward is less expected even if we may suspect a link with the suprathermal electron population following the reflected laser pulse. Note also the field pattern emitted from the target top/bottom edges [see ③ in Fig. 5.17(e)] as revealed by the E_y field maps [Figs. 5.17(d,e,f)]. Our main purpose in the following is to identify the generation mechanism attached to each field structure. To do so we mainly focus on the B_z field maps to discard electrostatic contributions [Figs. 5.17(g,h,i)].

To shed light on the THz emission mechanisms, we wish to distinguish between the contributions of the longitudinal (J_x) and transverse (J_y) plasma currents. For instance, by looking at the longitudinal electron phase space (see Fig. 5.14) we expect a strong current J_x in both the forward and backward directions across the target/vacuum interface, potentially yielding coherent transition radiation (CTR). Indeed, several authors [Zheng *et al.* 2002, 2003; Baton *et al.* 2003; Bellei *et al.* 2012] showed that CTR could account for optical emissions from laser-irradiated solid foils at relativistic intensities, and thus be used as a diagnostic tool for the hot electron distributions. The transverse current dynamics seems more complex to model since one has to take into account the neutralization current as well as the target deformation resulting from ion acceleration. To correctly analyze our field patterns, we thus propose to use uncouple fields generated either by the longitudinal (J_x) or the transverse current (J_y) component. The calculation of electromagnetic fields inside the PIC loop for the current time step is done by integrating the Maxwell-Ampere [Eq. (2.4)] and the Maxwell-Faraday [Eq. (2.3)] equations to obtain E_x, E_y and B_z (in 2D planar geometry). In order to isolate the roles of J_x and J_y currents

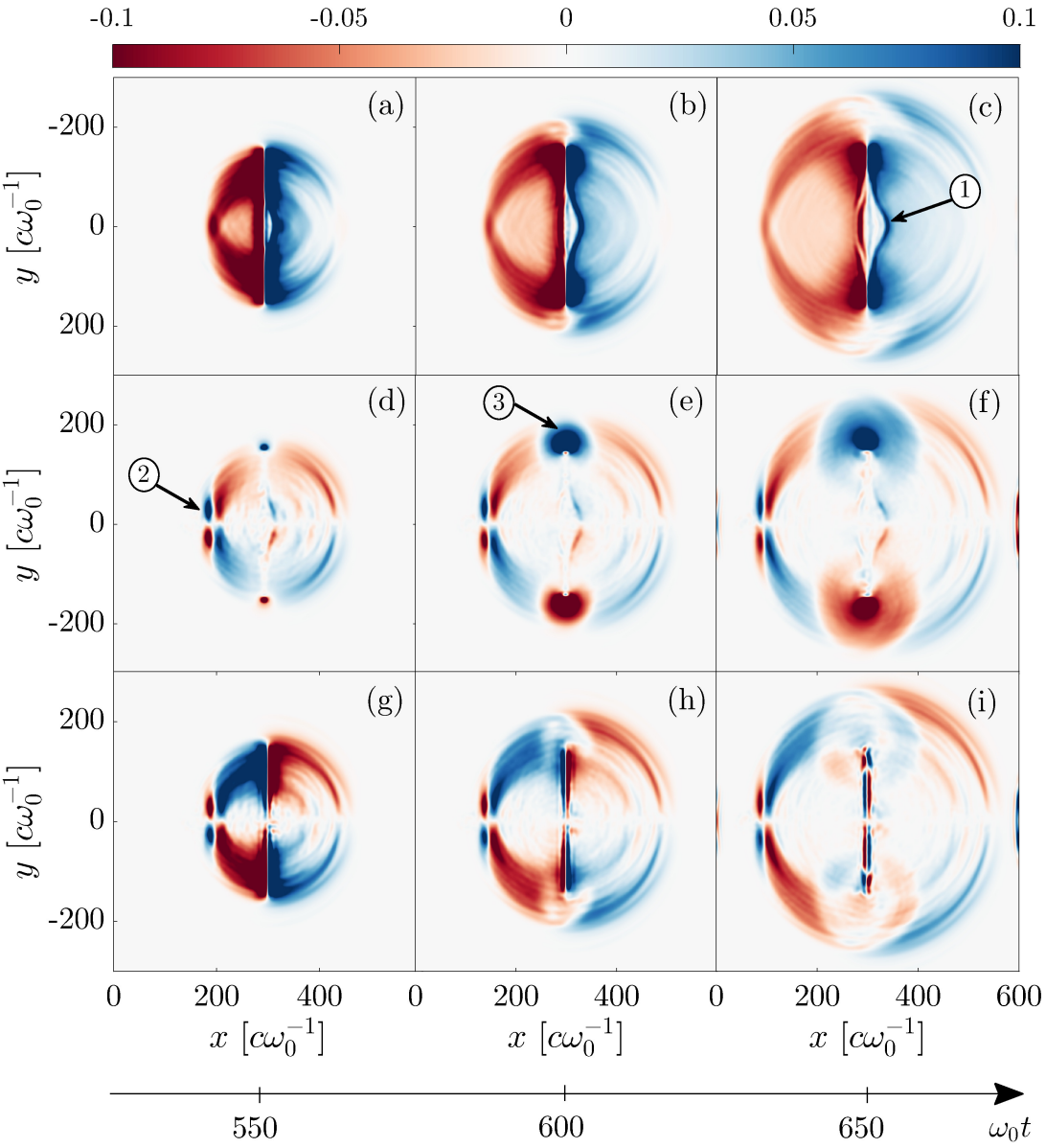

Figure 5.17: (a,b,c) E_x $[m_e c\omega_0/e]$, (d,e,f) E_y $[m_e c\omega_0/e]$ and (g,h,i) B_z $[m_e\omega_0/e]$ field maps filtered in the THz range ($\omega < 0.3\omega_0$) at $t = 550\ \omega_0^{-1}$, $t = 600\ \omega_0^{-1}$ and $t = 650\ \omega_0^{-1}$ (see time arrow) for the 500 nm thick target. ①, ② and ③ point out the TNSA field, the quadrupolar reflected pulse and the emission from the target edge, respectively.

in the THz field emission, the idea is to duplicate two times this system and alternatively turn off J_y and J_x in the right-hand side of Maxwell-Ampere equations to obtain:

$$\frac{dE_x^{\parallel}}{dt} = \frac{dB_z^{\parallel}}{dy} - J_x, \tag{5.25}$$

$$\frac{dE_y^{\parallel}}{dt} = -\frac{dB_z^{\parallel}}{dy} - 0, \tag{5.26}$$

$$\frac{dB_z^{\parallel}}{dt} = \frac{dE_x^{\parallel}}{dy} - \frac{dE_y^{\parallel}}{dx}, \tag{5.27}$$

and

$$\frac{dE_x^{\perp}}{dt} = \frac{dB_z^{\perp}}{dy} - 0, \tag{5.28}$$

$$\frac{dE_y^{\perp}}{dt} = -\frac{dB_z^{\perp}}{dy} - J_y, \tag{5.29}$$

$$\frac{dB_z^{\perp}}{dt} = \frac{dE_x^{\perp}}{dy} - \frac{dE_y^{\perp}}{dx}. \tag{5.30}$$

This allows us to compute the fields, $B_z^{\parallel}$ and $B_z^{\perp}$, induced by the longitudinal and the transverse currents,respectively.

Figures 5.18(a-i) present the results of this approach at three different times t =500, 600 and 650 ω_0^{-1}. At (t = 500 ω_0^{-1}), in the forward direction, the spherical half-cycle emission is mainly driven by J_x [see Figs. 5.18(a,g)] due to the hot electrons escaping in vacuum and thus generating CTR [e.g. see Ⓐ in Fig. 5.18(h)]. The strong sheath field at the interface forces other electrons to recirculate inside the target and eventually cross the front surface to interact with the laser field. This also gives rise to transition radiation from the other side of the target.

At t = 600 ω_0^{-1}, the field patterns corresponding to CTR have propagated as spherical waves. The slight delay between the forward and the backward emission is due to the hot electron refluxing dynamics. No other J_x induced emission is observed subsequently. By contrast, J_y gives rise to secondary emission, which we attribute to transient surface currents [e.g. see Ⓑ in Fig. 5.18(h)]. In the backward direction, a single-cycle $B_z^{\perp}$ structure emerges [see Fig. 5.18(e)] and mixes with the half-cycle of $B_z^{\parallel}$ structure [see Fig. 5.18(b)]. The $B_z^{\perp}$ sign changes due to the oscillating J_y current on the front surface that is, first, negative (for $y > 0$, electrons move aways from the focal spot), and then positive due to the cold return current. The sum of the longitudinal and transverse contributions leads to an overall strong quadrupolar signal [see Figs 5.18(g,h,i)].

At t = 650 ω_0^{-1}, the $B_z^{\perp}$ map [see Fig. 5.18(f)] evidences an antenna-like emission from the target edges following the arrival/reflection of the hot electrons [e.g. see Ⓒ in Fig. 5.18(i)]. Note also that the oscillating surface current leads to the formation of magnetic field nodes on the target. At even longer times ($\sim$ 1000 ω_0^{-1}), the recirculating current is deflected by the deformed target, causing further emission (see below).

The other simulations with thickness d_0 = 15 nm and d_0 = 50 nm exhibit similar features up to slight modifications. For thorough quantitative comparisons, we use a probe at the coordinate x = 600 $c\omega_0^{-1}$ and y = 100 $c\omega_0^{-1}$ to record the E_y field as a function of time (see Fig. 5.19). The CTR field emitted when hot electrons cross the target-vacuum interface at $t \sim$ 400 ω_0^{-1} is detected at $t \sim$ 700 ω_0^{-1} (see Ⓐ in Fig. 5.19) in agreement with the radiation time of flight (the

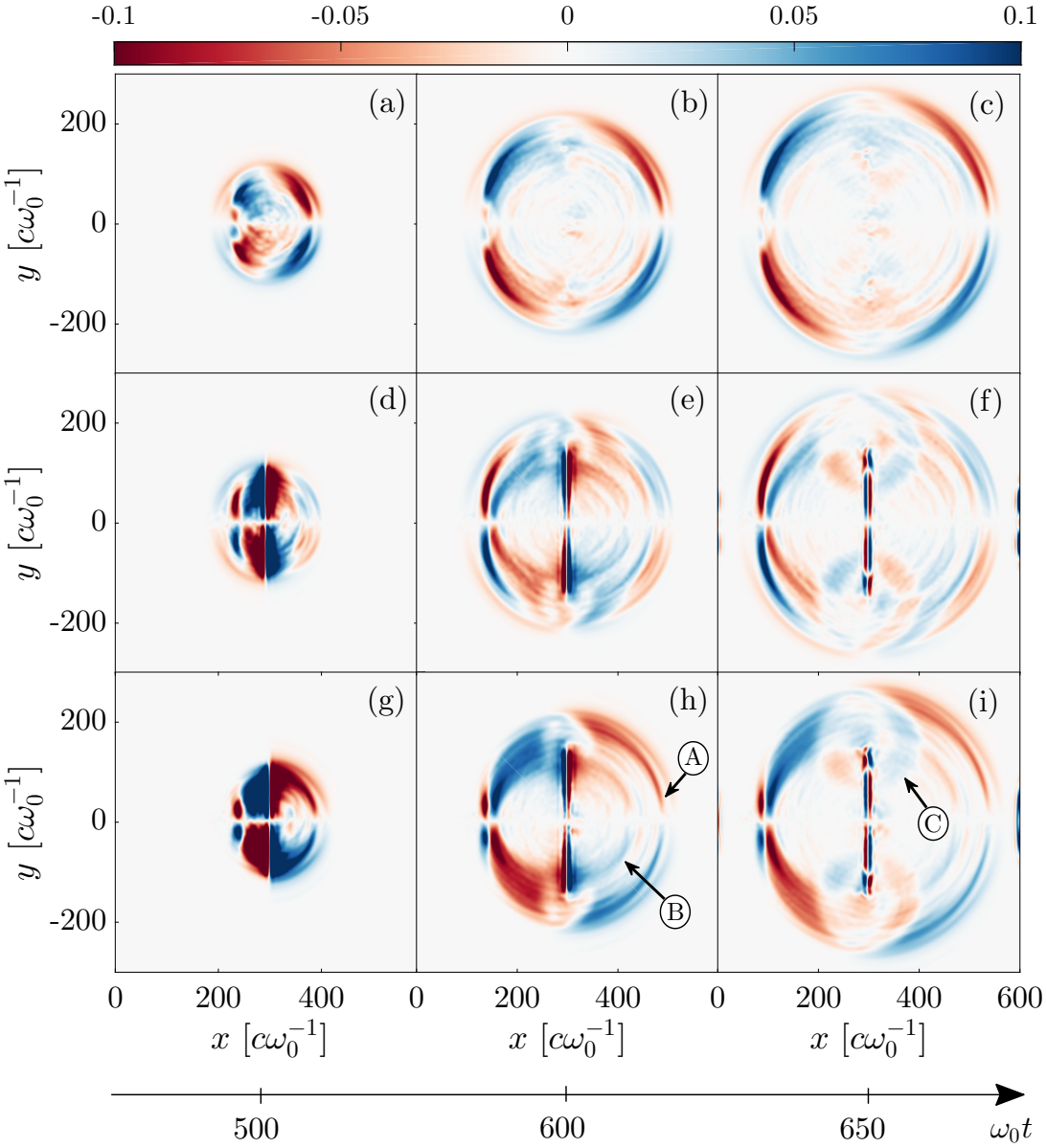

Figure 5.18: (a,b,c) $B_z^{\parallel}$, (d,e,f) $B_z^{\perp}$ and (g,h,i) B_z $[m_e\omega_0/e]$ field maps filtered in the THz range ($\omega < 0.3\omega_0$) at $t = 500\ \omega_0^{-1}$, $t = 600\ \omega_0^{-1}$ and $t = 650\ \omega_0^{-1}$ (see time arrow) for the 500 nm thick target. For a given column, the sum of the first and the second line gives the third line: $B_z^{\parallel} + B_z^{\perp} = B_z$. Ⓐ, Ⓑ and Ⓒ indicates the forward CTR, the transverse surface current induced radiation and the emission from the target edge, respectively.

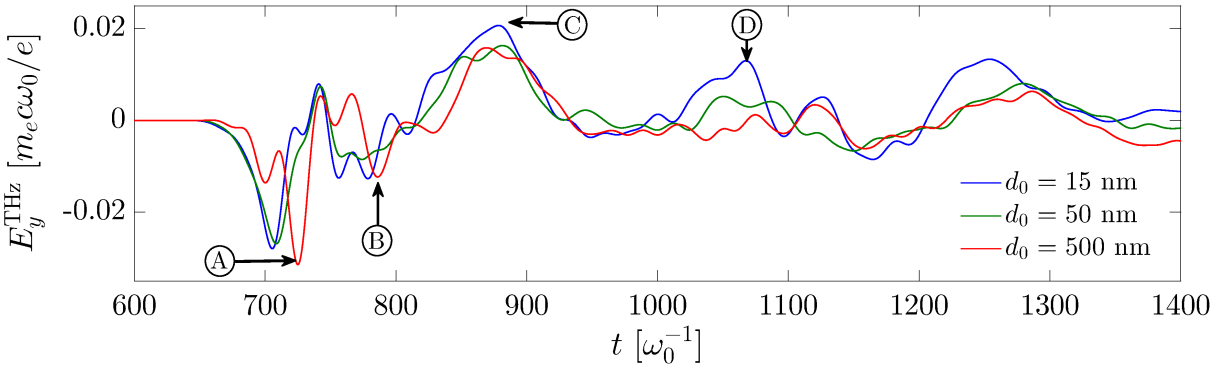

Figure 5.19: Low-frequency waveform of the E_y $[m_e c\omega_0/e]$ field recorded at coordinate (x, y)=$(600, 100)$ $c\omega_0^{-1}$ for the three target thicknesses (see legend). Ⓐ, Ⓑ, Ⓒ and Ⓓ shows the signal attached to the forward CTR, the transverse surface current induced radiation, the emission from the target edge and one caused by the deformed target, respectively.

target is located at $x = 300$ $c\omega_0^{-1}$). For the two thinnest targets the early half-cycle signal are almost identical with an amplitude of 0.028 $m_e c\omega_0/e \approx 90$ GV/m and pulse duration of ~ 50 fs: A small difference arises for the 500 nm thick target, which we ascribe to the early interaction of the laser with the front target surface. Later on, around $t \sim 750 - 850$ ω_0^{-1}, one can distinguish a second half-cycle signal (see Ⓑ in Fig. 5.19) due to transverse current on the target surface acting like an antenna line [Smith & Hertel 2001].

Let us now analyze the two next observed field structures at $t = 880$ ω_0^{-1} and 1050 ω_0^{-1} (see Ⓒ and Ⓓ, respectively, in Fig. 5.19). The first one is the emission from the target edges already mentioned in Fig. 5.18. When the normally incident laser pulse interacts with the target, the generated hot electrons expand radially towards the target edges. If we consider only the upper part, the negative moving charge can be seen as a traveling wave current, responsible for the low-frequency emission detected at $t \sim 800$ ω_0^{-1} (see Ⓑ in Fig. 5.19). Later on at $t \sim 880$ ω_0^{-1}, the traveling current reaches the target edge and recirculate. From a particle point of view, this is equivalent to stopping abruptly the conducting line, which leads to field emission (see Ⓒ in Fig. 5.19). This dynamics is illustrated by Fig. 5.20 where the transverse current is plotted at three different early times. At $t = 550$ ω_0^{-1}, electrons propagating along the positive y axis form a negative current (red). Note the presence of a thin blue current sheet at the target surface corresponding to the cold return current flowing through the plasma skin layer. The hot electrons attain the edge at $t = 600$ ω_0^{-1} and the current starts to reverse while a field burst is emitted [see ③ in E_y at the same instant in Fig. 5.17(e)]. At $t = 650$ ω_0^{-1}, the recirculating hot electron flow meets the incident traveling surface current. At later instance, a low-frequency burst from the target edge is recorded by the field probe at $t \sim 880$ ω_0^{-1} (see Ⓒ in Fig. 5.19). This signal has a typical amplitude of 0.02 $m_e c\omega_0/e$ corresponding to 65 GV/m. Note also the relative weak dependency on the target thickness.

This antenna-like emission can be understood in light of the model proposed by Smith & Hertel [2001], previously used to interpret the results of Zhuo *et al.* [2017], who reported an ~ 0.15 mJ THz energy with 0.75% laser-to-THz conversion efficiency. The analytical model considers a transient surface current induced by the short laser pulse and propagating at the light speed $J(y, t) = J_L(t - y/c)$, where $J_L(t) = J_0 e^{-t^2/\tau_0^2}$ is the initial profile with J_0 the peak amplitude of the wire-shaped current. The expression of the radiated field far from the target

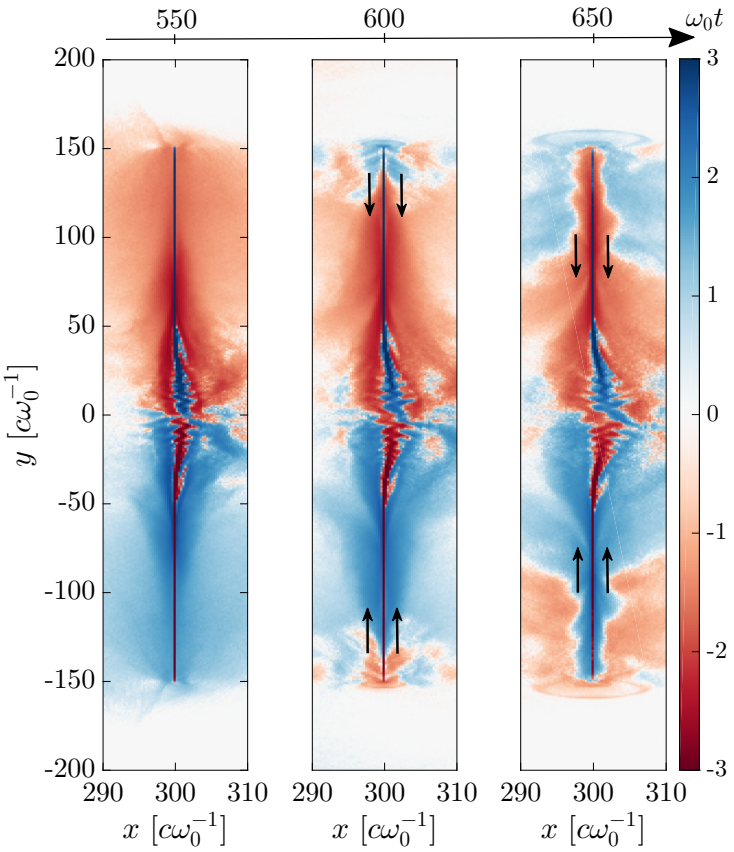

Figure 5.20: Snapshots (see time arrow) of the transverse current J_y $[ecn_c]$ reaching the targets edges for $d_0 = 50$ nm. Black arrows show the direction of the refluxing hot electron currents.

$(R/L_\perp \gg 1)$ is given by [Smith & Hertel 2001]:

$$\mathbf{E}(\mathbf{r},t) = \frac{\mu_0 c \sin\theta}{4\pi r(1-\cos\theta)} \left[I_L(t - R/c) - I_L(t - R/c - t_d) \right] \mathbf{e}_\theta \tag{5.31}$$

with R being the distance from the observer, θ the observation angle and $t_d = L(1-\cos\theta)/2c$ the retarded time with respect to the target edge. From there the radiated spectral intensity can be computed by means of the Poynting flux $\mathbf{\Pi}(\mathbf{r},t) = \mu_0^{-1}\mathbf{E}(\mathbf{r},t) \times \mathbf{B}(\mathbf{r},t)$. The first term of Eq. (5.31) corresponds to the initial transverse acceleration of electrons from the target axis $(y = 0)$, while the second term accounts for their reflection at the wire edges. This gives rise to an overall field pattern in the form of a single-cycle oscillation, first negative then positive, and with no emission in the target direction $(\theta = 0°)$. By contrast, our simulation data show two separated half-cycles, also negative then positive: First, the emission induced by the transverse surface current (see Ⓑ in Fig. 5.19) and then the emission from the target edges (see Ⓒ in Fig. 5.19), both displaying an opposite polarity at the probe location. This spatial separation might be due to the surface current speed which is here significantly lower than c, and produces a delay between the first and the second emission described by Eq. (5.31). Also the simulation domain size and other field structures make it difficult to observe the field distribution. An additional simulation performed with a twice wider target (not shown) exhibits clearly the two successive half-cycle emissions, as reported by Zhuo *et al.* [2017].

The subsequent field structure Ⓓ observed at $t \sim 1050\ \omega_0^{-1}$ in Fig. 5.19 is also linked to the recirculating current. The refluxing hot electrons, evidenced in Fig. 5.20, encounter a bended target surface due to ion expansion. Their trajectories are deflected towards vacuum,

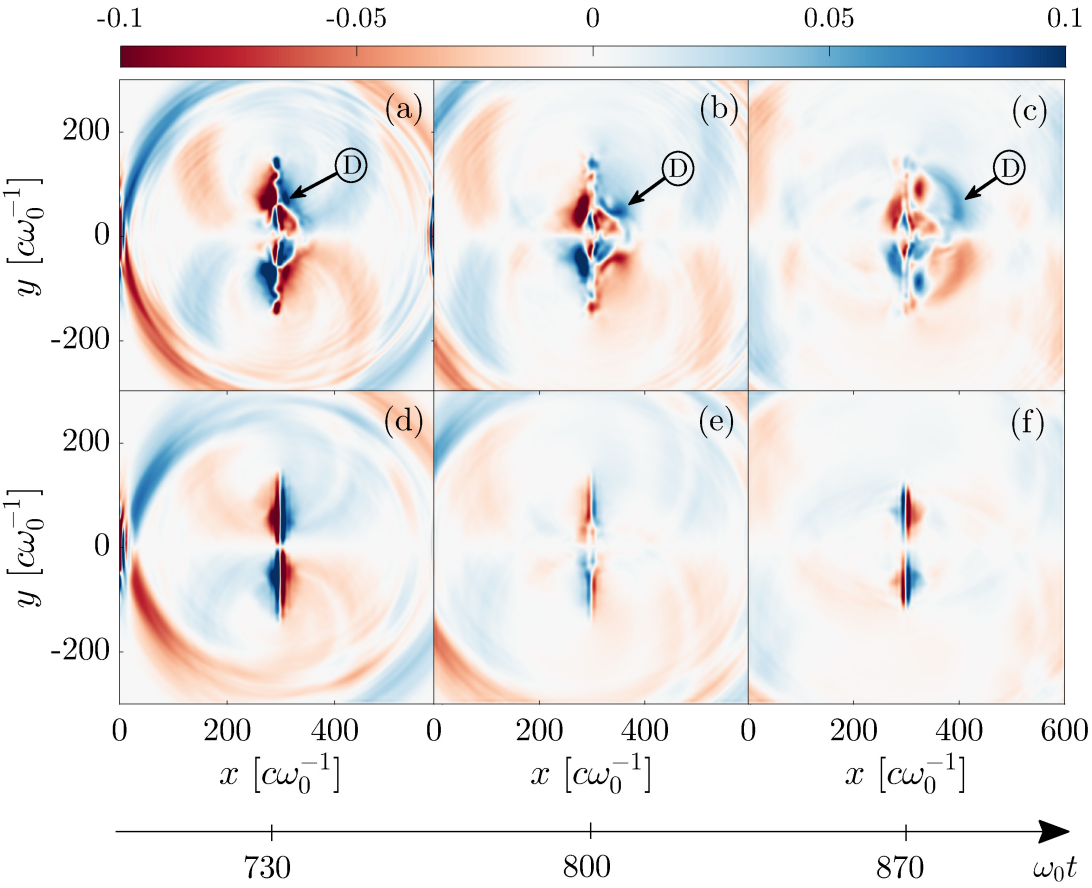

Figure 5.21: Snapshots (see time arrow) of the low-frequency magnetic field B_z $[m_e\omega_0/e]$ with (a,b,c) mobile and (d,e,f) fixed ions for the 15 nm thick target. Ⓓ shows the formation of THz emission associated to a the refluxing hot electron currents.

which results in additional THz emission. To prove this scenario, we have run a simulation with fixed ions for the smallest target thickness ($d_0 = 15$ nm), where the deformation is maximized. The idea is that immobile ions will prevent target deformations and, therefore, the associated emission. Figure 5.21 clearly demonstrates this mechanism with three B_z field maps for mobile (first line) and fixed (second line) ions. The first instant ($t = 730\ \omega_0^{-1}$) shows, for both mobile and fixed ions, the CTR and the traveling surface current induced emission reaching the simulation boundaries while the edge emission is still contained in the domain. The quasi-static magnetic field structures localized on the foil surfaces reveal their deformation due to ion expansion [Figs. 5.21(a,b,c)]. At $t = 800\ \omega_0^{-1}$ the refluxing hot electron flow reaches the deformed central part of the target where they are deflected. By contrast, with fixed ions, the upward and downward hot electron currents gently overlap at the target center [Figs. 5.21(d,e,f)]. Finally, the resulting emission is clearly seen at $t = 870\ \omega_0^{-1}$ [see Ⓓ in Fig. 5.21(c)], so that $200\ \omega_0^{-1}$ later it will be recorded by the probe ($x = 600\ c\omega_0^{-1}, y = 100\ c\omega_0^{-1}$). Note that the same signal is negligible using thick target ($d_0 = 500$ nm) being less optimized for ion acceleration. Also, as expected, no such emission is observed with immobile ions.

Finally, a comment is in order regarding the late-time ($t > 1200\ \omega_0^{-1}$) signal discernible in Fig. 5.22 at $d_0 = 50$ and 500 nm. This signal is clearly enhanced in the case of mobile ions, and so it would be tempting to ascribe it to the sheath-induced radiation investigated by Gopal *et al.* [Gopal *et al.* 2012, 2013a,b]. However, we were not able to provide unambiguous evidence for this mechanism, owing to the difficulty of discriminating its resulting radiation field from

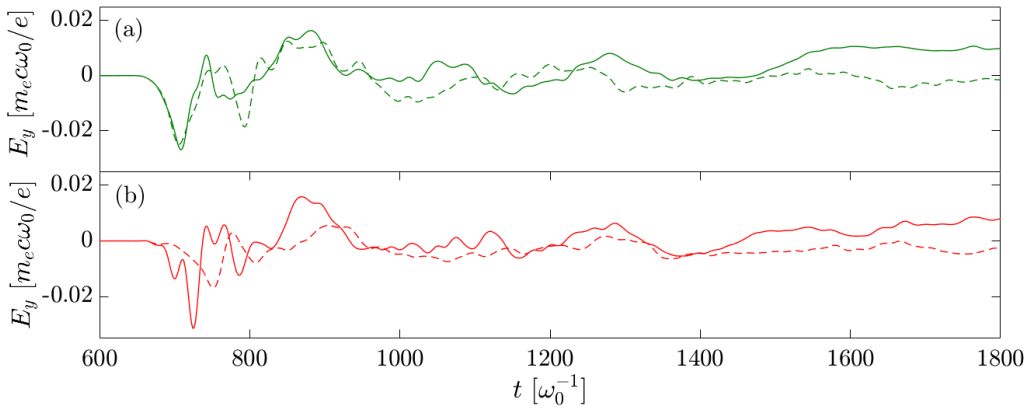

Figure 5.22: Low-frequency waveform of the E_y $[m_e c\omega_0/e]$ field recorded at coordinate (x, y)=$(600, 100)$ $c\omega_0^{-1}$ for (a) $d_0 = 50$ and (b) 500 nm with mobile (plain line) and immobile (dashed line) ions.

the quasi-static fields associated with the particle (electrons and ions) distributions which have then reached the detector.

Conclusion

This study devoted to THz generation by laser-solid interaction has revealed a wealth of emission mechanisms due to the nontrivial and coupled electron and ion dynamics. We have considered the case of nanometric solid foils irradiated by relativistic intense femtosecond pulses, near the threshold of relativistic transparency which enhances ion acceleration. We have shown that THz emission comprises several successive bursts: first, an intense signal due to CTR by a forward moving hot electron current, second, weaker signals associated with the transverse current dynamics, i.e., their generation in the irradiated region, their reflection at the target edges and their deflections by refluxing electrons into the deformed target center. The latter effect is maximized in thin targets optimizing ion acceleration.

Chapter 6

Conclusions and Perspectives

Conclusions

Laser-plasma interaction is rich in the number of physical processes involved, as well as in potential applications in societal and industrial areas. During this PhD work, we focused on THz waves produced by laser-driven classical and relativistic plasmas. This topic is attracting more and more interest because of the many applications of the THz frequencies, in particular for spectroscopy purposes. This spectral domain indeed opens the route to a frequency range unveiling new signatures of macro-molecules accessible by coherent spectroscopy techniques which can be applied to medical imaging, remote identification or material science. Compared to current THz generation technologies based on solid emitters (quantum cascade lasers, optical rectification in crystals), laser-plasmas THz sources are not subject to damage thresholds since they are formed from ionized medium such as gases. In addition, narrow emitted bandwidths and small field amplitudes can be avoided by using femtosecond two-color laser pulses in air. Using two harmonics in the laser field increases the THz energy yield through photocurrents. By combining the fast steplike profile of the electron density and the asymmetry in the laser field induced by the two colors, photocurrents produced in a plasma spot contain low-frequencies (< 100 THz) and are capable of delivering high amplitude THz fields ($0.1 - 1$ GV/m). Such setup has been extensively studied with moderate laser intensities $\sim 10^{14-16}$ W/cm^2 demonstrating an energy conversion efficiency from laser to THz of about a few 10^{-4}. However, it appears that, in gases, the THz energy yield saturates up to some tens of μJ for 800 nm-pump lasers [Oh *et al.* 2013]. In contrast, laser-solid interaction showed a monotonic increase in the THz energy with the laser intensity, but the involved physics remained unclear.

The objectives of this thesis was then two fold. First we explored the two-color laser setup in the relativistic regime. By doing so, a strong plasma wave is triggered in the laser wake with high field gradients. The latter are able to accelerate electron bunches close to the speed of light. Later on, when crossing the plasma-vacuum interface, these electrons emit a low-frequency field through the coherent transition radiation process. Hence, our first purpose was to clear up the transition between the photocurrent mechanism and the coherent transition radiation as well as to extract the most favoring regime in gases in terms of delivered THz energy.

The second objective was to explore laser-solid interactions at ultra-high intensity $\sim 10^{20}$ W/cm^2 where ion acceleration occurs. Several recent studies proposed different generation mechanisms and demonstrated the production of high THz energy without saturation effect [Gopal *et al.* 2013b; Li *et al.* 2014]. We proposed to conduct state-of-the-art 2D PIC simulations to shed light on the possible generation processes in a configuration favoring the acceleration of ions for nanometric targets.

In order to present our results spanning on a large parametric space, from underdense (gases) to overdense (solid) targets with laser intensities below ($a_0 < 1$) and above ($a_0 > 1$) the relativistic threshold, Chapter 2 described the physics of laser gas-interaction from classical to relativistic regime. First, we reviewed the THz emission mechanisms in classical regime, mainly photocurrent-induced radiation (PIR), as well as the underlying physical processes (Kerr effect, photoionization, plasma waves). The propagation of such THz waves was analyzed analytically and numerically by integrating the complete wave equation [Eq. (2.12)] and its unidirectional approximation, the UPPE [Eq. (2.32)]. We thus performed the first comparison of these two approaches for THz generation. We demonstrated that a sufficient propagation distance, corresponding to few plasma skin depths, is needed to obtain similar low-frequency spectra with an efficient plasma response increasing step-like over the pulse history, which allowed us to validate the UPPE approach over long propagation distances. After introducing the basis of laser-driven THz generation, we addressed the relativistic laser-plasma interaction by first presenting elements of plasma physics theory (Vlasov equation) and the numerical tools used in this PhD thesis, namely, the PIC codes CALDER and CALDER-CIRC. Discussing light-matter interaction in relativistic regime, the concept of laser-plasma wakefield accelerator was recalled. We established, thanks to the plasma fluid equations and a Hamiltonian approach, the possibility to accelerate electrons to hundreds of MeV energy in the wake of an UHI laser pulse. Finally, this population of accelerated charged particles can produce THz waves via the transition radiation process when they escape from the plasma. The coherent transition radiation (CTR) was explained and described in the last section, first in the ideal case of a perfect conductor-vacuum interface, and then for a plasma-vacuum interface (arbitrary dielectric function).

Next, Chapter 3 compiled two different studies of laser-gas interaction in the relativistic regime. The standard photocurrent mechanism was investigated in the context of laser-wakefield acceleration. For this purpose, an analytical formula of the radiated THz field coupled to the non-linear plasma wave and the ionization process was derived. A good agreement with 1D PIC and 3D on-axis PIC simulations was reached. This emission polarized along the laser direction and located in the front of the laser pulse was first examined. The gas ionization results in a residual transverse momentum which couples to the electron density modulations leading to residual THz bursts at each relativistic plasma wavelength $\lambda_{pe}/\sqrt{\gamma}$ behind the laser beam. This new emission in the laser polarization direction is inherently linked to the relativistic nature of the interaction and was reported for the first time to our knowledge here. We also underlined the importance of 3D effects to correctly describe the electron density modulations. Second, the ponderomotive force of the laser pulse triggers a longitudinal wake field through which electron bunches are accelerated. When crossing the interface, the charged beam emits coherent transition radiation along the direction $\theta \approx 1/\gamma$ with a spectral content depending on both the plasma density ($\Delta\omega = \gamma\omega_{pe}$) and the spatial distribution of the electron beam (coherent versus incoherent emissions). After a given photon formation length, a constructive field emerges from each electron of the beam crossing the interface such that the radiated wavelength is about the bunch longitudinal size. Usually, this size is a few micrometers long (3-30 μm) [Faure *et al.* 2006; Lundh *et al.* 2011], hence between 10-100 THz. This process is effectively observed in our 3D PIC simulations with field amplitude and energy far above the photocurrent-induced THz field. In addition, favoring the bunch charge by increasing the initial gas density may lead to an enhancement of the CTR up to 100 GV/m and mJ energies, which constituted (theoretical) record values in gases. Further, we explored the possibility to optimize THz emission generated by CTR by varying the plasma parameters, namely, the density and the length of the gas cell while maintaining the areal density constant ($n_e \times L_p = cte$). A series of ten 3D CALDER-

CIRC simulations exhibited an optimum in the radiated energy reached along the highly-charged blow-out regime. The THz energy yields expressed as a function of the electron density shows a remarkable robustness of the radiated field (variation of a factor 2-4) only over four decades, from underdense to critical plasma densities. This specific feature demonstrates once again the relevance of THz emission driven by CTR. Moreover, the use of a semi-analytical Biot-Savart model allowed us to estimate the electron beam self-field in order to discard its contribution (of about, at least, 75%) in the energy evaluation.

Chapter 4 addressed the influence of the laser wavelength in relativistic laser-gas interaction. The use of long laser wavelengths decreases significantly the relativistic threshold such that much more modest laser intensity (and therefore energy) is required to trigger relativistic nonlinear processes. We demonstrated the non trivial impact of the ionization on the evolution of the nonlinear plasma wave. A 1D analytical model showed that the density steps due to photoionization, coupled to momenta, act as an additional force enhancing the ponderomotive force and resulting in a stronger plasma wave compared to a pre-ionized plasma. Then the feedback of the plasma wave on the laser pulse propagation, through the modulation of the refractive index, led to a significant frequency downshift filling in the THz band. As a result, strong low-frequency (< 10 THz) field amplitudes (20 GV/m) were reported at the exit of the plasma channel. In addition, electron acceleration (~ 12 MeV) leads to radially polarized THz emission through CTR. Laser pulses with long pump wavelength and modest energy should thus be able to generate intense THz emission and particle acceleration [Woodbury *et al.* 2018].

The last study reported in Chapter 5 focused on THz generation in solids. After a rapid review of energetic electron generation and ion acceleration processes, we underlined the main results published in the literature about the generation of THz pulses in this context. Compared to laser-gas interaction, the main remarkable feature is, up to now, the absence of saturation when increasing the laser intensity such that tens of millijoule THz pulses have been experimentally measured [Gopal *et al.* 2013b; Li *et al.* 2014; Liao *et al.* 2019]. Nevertheless, the underlying generation mechanisms remain unclear due to the complex dynamics of particles and electromagnetic fields during the interaction. Among others, coherent transition radiation and TNSA-driven emission are suspected to play an important role in the THz generation process. Our purpose was to clear up this issue for a given set of laser-target parameters favoring the acceleration of ions. Our 2D PIC simulation results showed that successive low-frequency signatures can be extracted, each of them being linked to a specific process. We recover the presence of CTR when the hot electron population escapes in vacuum. Then, electron currents on the target surface generate antenna-like lobes when reaching the target edges. Both structures are similar for the three target thicknesses investigated (15-50-500 nm). Meanwhile, the ponderomotive pressure of the laser pulse and the hot electron cloud were found to participate together to accelerate ions and to deform the target. The recirculating current is then subject to deflection leading to another low-frequency emission. These processes are all stronger for thinner targets. Finally, the expected signature of ion motions, not completely observed due to numerical constraints because of the limited size of our simulation domain, should also contribute to some extent.

Perspectives

At this end of this PhD work, a few perspectives can be opened. The first one concerns a numerical issue. Indeed, in order to correctly describe radiated fields in PIC simulations, it appears crucial to implement a reliable and efficient numerical method. The use of analytical

models like the Biot-Savart generalized law is restricted to simple situation in, e.g., modeling the electron current source and, thus, such elementary models discard numerous effects for instance the electron beam and electromagnetic field evolution along propagation and time. To overcome this obstacle, it should be possible to define an imaginary surface in the simulated domain acting as a detector plane. At a given instant and for each detector's cell, the radiated field of each particle could be computed trough the Lienard-Wiechert retarded potentials [SPIE 2009; 45th EPS conference on Plasma Physics 2018; 46th EPS conference on Plasma Physics 2019]. Radiated field contributions could next be summed up in time taking into account the time of flight from the source point to the detector array.

The results on the laser-gas interaction showed that coherent transition radiation is an effective and robust source of THz generation. So far, we investigated the emission arising at the plasma-vacuum interface. Another interesting design would be to produce an electron beam and make it interact with a solid foil in order to study CTR from the vacuum-metal interface. Successive wakefield-accelerated electron bunches could then give rise to a train of intense THz pulses spaced by one plasma wavelength with a spectrum modulated at the plasma frequency. From the experimental point of view, a proof of concept can be easily considered in order to evaluate the performances of, either, solid and gaseous targets in various configurations (e.g. laser parameters and target composition). Nowadays, electron acceleration is routinely exploited in gas-jet setups such that a very simple experiment with a low energy, highly charged electron beam could be rapidly conducted.

Finally, we restricted our study of laser-solid interaction to short laser pulses with ultra-thin dielectric targets. It could be interesting to consider alternative target designs such as nanostructured foils [Mondal *et al.* 2017], or laser pulse parameters (e.g. picosecond duration [Liao *et al.* 2019], circular polarization, contrast). Also, the study of ion induced emissions should be carefully measured by dedicated long simulation ("Grand Challenge"). This subject of research is still open and comparison between simulations results and experiments will be essential to understand the underlying generation mechanisms.

Appendix A

1D codes for THz pulse generation in classical regime

A.1 Maxwell-Fluid

The *Maxwell-fluid* code, named MAXFLU1D, is based on a finite volume scheme solving the wave equation (2.22) and fluid equations (2.68) and (2.72) in time. This set of equations is re-expressed in the conventional conservative form of a nonlinear hyperbolic system, e.g., for the transverse (z-polarized) field $E \equiv E_z$ through the electric displacement D_z:

$$\partial_t D_z + \mu_0^{-1} \partial_x B_y = -(J_z + J_{z,loss}), \tag{A.1}$$

$$\epsilon_0^{-1} D_z = E_z + \chi^{(3)} E_z^3. \tag{A.2}$$

This nonlinear hyperbolic system is treated numerically by splitting the advection part (source terms set equal to zero) and the evolution part (source terms included but with zero derivative in x), which are independent, at every time step Δt along an evolution-advection-evolution algorithm. First, the evolution stage is solved by using a second-order Runge-Kutta scheme. Next, the Maxwell and Fluid advective parts are solved over Δt. For the former advection, the Lax-Wendroff scheme is chosen (second-order accurate) [Lax & Wendroff 1960], even though some Gibbs oscillations might appear. For the latter advection stage, instead, we couple a First ORder CEntered (FORCE) scheme [Toro 2012], which is first-order accurate, to the Lax-Wendroff scheme, following the Flux Corrected Transport approach [Zalesak 2012]. This is necessary for treating the fluid advection; otherwise strong Gibbs oscillations may occur in the neighborhood of electron density gradients, which can render the code unstable. The calculation domain is a sliding window that moves forward at the speed of light c and, with relatively small Kerr contributions, the CFL condition of the (t, x) grid, $\Delta x = c\Delta t$, is the standard requirement.

A.2 UPPE

The UPPE1D code solves Eq. (2.32) coupled with the fluid equations (2.68) and (2.72) propagating over the optical axis x. A second-order accurate split-step scheme allows us to separate the linear and the nonlinear parts of the UPPE equation [Agrawal 2012]. The linear part (propagation) is solved exactly in the Fourier space as follows:

$$\widehat{E}(x + \Delta x, \omega) = \widehat{E}(x, \omega) \exp\left[\mathrm{i}k(\omega)\Delta x\right], \tag{A.3}$$

where $k(\omega) = \omega/c$. Then, the nonlinear contribution, including the Kerr terms, ionization and absorption losses, are advanced over one spatial step Δx as

$$\left[\partial_x E(t) + \partial_t \left(\frac{\chi^{(3)}}{2c} E(t)^3\right)\right] = -\mathcal{F}^{-1}\left[\frac{c\mu_0}{2}\left(\tilde{J}_e(\omega) + \tilde{J}_{\text{loss}}(\omega)\right)\right], \tag{A.4}$$

where $\mathcal{F}^{-1}$ means inverse Fourier transform, J_{loss} refers to a loss current due to photoionization, usually negligible in laser-gas interactions. The left-hand side of Eq. (A.4), which accounts for Kerr polarization, is first discretized in time by finite volumes at time step j ($t = j\Delta t$) as

$$\partial_x E_j = -\frac{1}{\Delta t}\left[\Phi_{j+1/2} - \Phi_{j-1/2}\right], \tag{A.5}$$

where $\Phi_{j+1/2}$ refers to the numerical flux between two neighboring cells, j and $j+1$, of the grid. Following the well-known Godunov's method [LeVeque 2002], the numerical flux is given here by

$$\Phi_{j+1/2} = \frac{\chi^{(3)}}{2c} E_{j+1/2}^3, \tag{A.6}$$

where $E_{j+1/2}$ accounts for the solution to the Riemann problem at the intercell $j + 1/2$ [Toro 2012], which aims at solving the advected solution constrained by two constant states indexed by j and $j+1$ on both sides of the intercell. In this case, the solution to the Riemann problem is straightforward: With $\chi^{(3)} \geq 0$, at first-order of accuracy, one has to choose simply $E_{j+1/2} = E_j$. To achieve second-order accuracy, we do a linear reconstruction of $\{E_j\}$ following the Essentially Non-Oscillatory (ENO) technique [Toro 2012]:

$$E_{j+1/2} = E_j + \frac{\Delta_j}{2}, \tag{A.7}$$

where Δ_j compares the downwind difference $(E_{j+1} - E_j)$ and the upwind difference $(E_j - E_{j-1})$ and retains the lower value in modulus. Limiting the slope in this way allows us to avoid Gibbs oscillations when optical shocks induced by self-steepening occur [Anderson & Lisak 1983]. With the second-order numerical flux, we can rewrite Eq. (A.4) as:

$$\partial_x E_j = -\frac{1}{\Delta t}\left[\Phi_{j+1/2} - \Phi_{j-1/2}\right] - \mathcal{F}^{-1}\left[\frac{c\mu_0}{2}\left(\hat{J}(\omega) + \hat{J}_{\text{loss}}(\omega)\right)\right], \tag{A.8}$$

which is easily solved by the second-order Runge-Kutta method. Using this discretization, provided that $\chi^{(3)}$ is weak enough, the maximum spatial step given by the Courant-Friedrichs-Lewy (CFL) stability condition of Eq. (A.5) is $\Delta x_{max} = 2c\Delta t/(3\chi^{(3)}E_0^2)$, with E_0 denoting the input amplitude of the laser field. This step is much larger than the spatial steps needed to obtain accurate solutions of Eq. (A.4) as well as those requested to integrate the WE model. Long propagation distances can then be simulated in reasonable amount of computational time with the UPPE approach.

In the UPPE1D code, the terahertz field driven by the laser field is 0 at $x = 0$. One spatial step further, the laser pulse enters the medium and triggers nonlinearities, producing thus a non zero THz field. In the MAXFLU1D code, the terahertz field grows from a laser pulse crossing a vacuum-plasma interface and admits backward contributions. Since we are interested in THz generation, one should use simultaneously a fine spectral resolution and a fine time step in order to correctly describe the low frequency spectrum below ν_{pe} and the two-color laser pulse components including its higher harmonics generated along propagation. The time window of

our simulations is, therefore, set to 3.33 ps corresponding to a frequency step of $\Delta\nu = 0.3$ THz. The time step Δt is tuned from $\lambda_0/(128c)$ down to $\lambda_0/(512c)$ leading to a spatial step of $\Delta x = \lambda_0/128$ resp. $\Delta x = \lambda_0/512$ for the MAXFLU simulations (CFL condition) and it is fixed to $\Delta x = \lambda_0/25$ for the UPPE simulations. The highest resolutions used in the MAXFLU code have been employed when it was necessary to decrease the background noise in the lowest parts of the pulse spectrum (e.g., for a Kerr response alone).

Let us finally notice that, so far, we have neglected linear dispersion $P_L = \epsilon_0\chi^{(1)} * E$, with $\chi^{(1)}$ representing the first-order susceptibility and $*$ standing for the convolution product in time. Linear gas dispersion can be accounted for as well through the pulse wave number $k(\omega) = n(\omega)\omega/c$ becoming then a function of the frequency-dependent refractive index $n(\omega) = \sqrt{1+\chi^{(1)}(\omega)}$. In that case, the UPPE code iterates the solution by always using Eq. (A.3) for solving the linear part and by performing the substitutions $\chi^{(3)} \to \chi^{(3)}/n(\omega_0)$ and $c\mu_0 \to c\mu_0/n(\omega)$ into the left-hand side and the right-hand side of Eq. (A.4) of the nonlinear contribution, respectively. In the MAXFLU1D code the only change consists in implementing the convolution product $\chi^{(1)} * E_x$ in the right-hand side of the equation (A.2).

Appendix B

Calculation of Garibian formula

Here we follow the classic treatment of transition radiation done by Garibian [1958]. The wave equation expressed in Fourier domain is composed of the inhomogeneous and the homogeneous equation. Boundary conditions are applied to the total field. Then the radiation field (homogeneous sol.) is computed through the steepest descent method to finally obtain the radiated energy per solid angle per angular frequency. Let us consider a medium 1 and 2 with permitivitty ϵ_1 and ϵ_2, respectively. The interface between the two media is the plane $x = 0$ through which the particle moves. For nototional convenience calculations are made in CGS units. Maxwell equations in space-time are:

$$\nabla \times \mathbf{H} = \frac{1}{c}\frac{\partial \mathbf{D}}{\partial t} + \frac{4\pi}{c}\mathbf{v}e\delta(\mathbf{r} - \mathbf{v}t) \tag{B.1}$$

$$\nabla \times \mathbf{E} = -\frac{1}{c}\frac{\partial \mathbf{B}}{\partial t} \tag{B.2}$$

$$\nabla \cdot \mathbf{B} = 0 \tag{B.3}$$

$$\nabla \cdot \mathbf{D} = 4\pi e\delta(\mathbf{r} - \mathbf{v}t) \tag{B.4}$$

We define the space Fourier integral as:

$$\mathbf{E}(\mathbf{r}, t) = \int \mathbf{E}(\mathbf{k})e^{i(\mathbf{k}\cdot\mathbf{r} - \omega t)}d\mathbf{k} \tag{B.5}$$

where $\omega = \mathbf{k}\cdot\mathbf{v} = k_x v$, $\mathbf{D}_{1,2}(\mathbf{k}) = \epsilon_{1,2}(\omega)\mathbf{E}_{1,2}(\mathbf{k})$ and $\mathbf{B}_{1,2}(\mathbf{k}) = \mu_{1,2}(\omega)\mathbf{H}_{1,2}(\mathbf{k})$. We first need the Fourier components of the above equation by combining Fourier transformed Maxwell equations. To do so we express the propagation equation of the electric field $\mathbf{E}$:

$$\nabla \times \nabla \times \mathbf{E} = \nabla(\nabla \cdot \mathbf{E}) - \nabla^2\mathbf{E} \tag{B.6}$$

$$= -\frac{1}{c}\frac{\partial}{\partial t}(\nabla \times \mathbf{B}) \tag{B.7}$$

$$= -\frac{1}{c}\frac{\partial}{\partial t}\left[\mu_{1,2}\left(\frac{1}{c}\frac{\partial \mathbf{D}}{\partial t} + \frac{4\pi}{c}\mathbf{v}e\delta(\mathbf{r} - \mathbf{v}t)\right)\right] \tag{B.8}$$

$$= -\frac{\chi_{1,2}}{c^2}\frac{\partial^2 \mathbf{E}}{\partial t^2} - \frac{4\pi\mu_{1,2}}{c^2}\frac{\partial(\mathbf{v}e\delta(\mathbf{r} - \mathbf{v}t))}{\partial t} \tag{B.9}$$

with $\chi_{1,2} = \mu_{1,2}\epsilon_{1,2}$. By space-time Fourier transform we have:

$$k^2\mathbf{E} - \left(\frac{\omega}{c}\right)^2 \chi_{1,2}\mathbf{E} = i\left[\omega\frac{4\pi\mu_{1,2}}{c^2}\mathbf{v}e - \mathbf{k}(\nabla\cdot\mathbf{E})\right]\frac{1}{(2\pi)^3}. \tag{B.10}$$

The $\frac{1}{(2\pi)^3}$ is due to the triple space integral. Then, by noting that $\nabla\cdot\mathbf{E} = 4\pi e/\epsilon_{1,2}$ we have:

$$(k^2 - \left(\frac{\omega}{c}\right)^2 \chi_{1,2})\mathbf{E} = \frac{ei}{2\pi^2}\left(\frac{\mu_{1,2}\omega}{c^2} - \frac{\mathbf{k}}{\epsilon_{1,2}}\right) \tag{B.11}$$

$$= \frac{ei}{2\pi^2}\frac{1}{\epsilon_{1,2}}\left(\frac{\omega}{c^2}\chi_{1,2}\mathbf{v} - \mathbf{k}\right), \tag{B.12}$$

leading to the result

$$\mathbf{E}(\mathbf{k}) = \frac{ei}{2\pi^2}\frac{1}{\epsilon_{1,2}}\frac{(\omega/c^2)\chi_{1,2}\mathbf{v} - \mathbf{k}}{k^2 - (\omega/c)^2\chi_{1,2}}. \tag{B.13}$$

The magnetic field can be deduced using

$$\mathbf{H} = \frac{c\mathbf{k}\times\mathbf{E}}{\mu_{1,2}\omega}. \tag{B.14}$$

The field in Eq. (B.5) whith Fourier components Eq. (B.13) do not satisfy the continuity equations at the interface $x = 0$. To satisfy these requirements we must add to the solution of the inhomogeneous Maxwell equations given above the solution of the homogeneous equations with arbitrary Fourier components, and then determine these from the continuity requirements on the total field at the interface between the two media. We define $\mathbf{r} = (\boldsymbol{\rho}, z)$, $\mathbf{k} = (\boldsymbol{\kappa}, k_x)$ and the solution of the homogeneous Maxwell equations as:

$$\mathbf{E'_{1,2}}(\mathbf{r},t) = \int \mathbf{E'_{1,2}}(\mathbf{k})e^{i(\mathbf{k}\cdot\mathbf{r}-\omega t)}d\mathbf{k} \tag{B.15}$$

$$= \int \mathbf{E'_{1,2}}(\mathbf{k})e^{i(\boldsymbol{\kappa}\boldsymbol{\rho}+k_x x-\omega t)}d\mathbf{k} \tag{B.16}$$

$$= \int \mathbf{E'_{1,2}}(\mathbf{k})e^{i(\boldsymbol{\kappa}\boldsymbol{\rho}+\lambda_{1,2} x-\omega t)}d\mathbf{k} \tag{B.17}$$

with $\lambda_{1,2}^2 = (\omega/c)^2\chi_{1,2} - \kappa^2$. The radiation magnetic field is then given by

$$\mathbf{H} = \frac{c\mathbf{k}\times\mathbf{E}}{\mu_{1,2}\omega} = \frac{c}{\mu_{1,2}\omega}(\boldsymbol{\kappa} + \lambda_{1,2}\mathbf{n})\times\mathbf{E}. \tag{B.18}$$

We denote the real part of λ by λ' and the imaginary part by λ''. The medium 1 is located between $z \to -\infty$ and 0. Hence to prevent the field from diverging at infinity we impose $\lambda'_1 < 0$ (reflected wave propagation only) and $\lambda''_1 < 0$. Similarly in region 2 we set $\lambda'_2 > 0$ and $\lambda''_2 > 0$. Note that signs have been assigned considering positive ω. For negative ω, signs must be reversed. We can now apply the continuity equation at $x = 0$ that is to say the tangential continuity of $\mathbf{E}$ and the normal continuity of $\mathbf{D}$ (no surface charge density). In the following we denotes by a subscript t (resp. n) the tangential (resp. normal) component of a given field. Hence we have,

$$\begin{cases} \mathbf{E_{1t}} + \mathbf{E'_{1t}} = \mathbf{E_{2t}} + \mathbf{E'_{2t}} \\ D_{1n} + D'_{1n} = D_{2n} + D'_{2n} \end{cases} \tag{B.19}$$

and by using Eq. (B.13):

$$\begin{cases} -\frac{ei}{2\pi^2}\frac{1}{\epsilon_1}\frac{\boldsymbol{\kappa}}{k^2-(\omega/c)^2\chi_1} + \mathbf{E'_{1t}} = -\frac{ei}{2\pi^2}\frac{1}{\epsilon_2}\frac{\boldsymbol{\kappa}}{k^2-(\omega/c)^2\chi_2} + \mathbf{E'_{2t}} \\ \frac{ei}{2\pi^2}\cancel{\epsilon_1}\frac{(\omega/c^2)\chi_1 v - k_x}{k^2-(\omega/c)^2\chi_1} + \epsilon_1 E'_{1n} = \frac{ei}{2\pi^2}\cancel{\epsilon_2}\frac{(\omega/c^2)\chi_2 v - k_x}{k^2-(\omega/c)^2\chi_2} + \epsilon_2 E'_{2n} \end{cases} . \tag{B.20}$$

From this point we want to extract $\mathbf{E'_{1t}}$. However two equations are missing. We can use the homogeneous Maxwell equation $\nabla \cdot \mathbf{E'} = 0$ to have the relation in Fourier space $\mathbf{k} \cdot \mathbf{E'} = 0$ and so $\boldsymbol{\kappa}\mathbf{E'_{1,2t}} + sign(\mathcal{R}e\,[\lambda_{1,2}])\lambda_{1,2}E'_{1,2n} = 0$. By assuming that the $\boldsymbol{\kappa}$ vector is parrallel to $\mathbf{E'_{1,2t}}$, two additional equations are:

$$\begin{cases} \kappa E'_{1t} - \lambda_1 E'_{1n} = 0 \\ \kappa E'_{2t} + \lambda_2 E'_{2n} = 0 \end{cases} . \tag{B.21}$$

which can be plugged into Eq. ((B.20)) to have a sytem of E'_{1t} and E'_{2t} after eliminating E'_{1n} and $E_{2n'}$. By doing so one finds

$$\begin{cases} -\frac{ei}{2\pi^2}\frac{1}{\epsilon_1}\frac{\kappa}{k^2-(\omega/c)^2\chi_1} + E'_{1t} = -\frac{ei}{2\pi^2}\frac{1}{\epsilon_2}\frac{\kappa}{k^2-(\omega/c)^2\chi_2} + E'_{2t} \\ \frac{ei}{2\pi^2}\frac{(\omega/c^2)\chi_1 v - k_x}{k^2-(\omega/c)^2\chi_1} + \kappa\frac{\epsilon_1}{\lambda_1}E'_{1t} = \frac{ei}{2\pi^2}\frac{(\omega/c^2)\chi_2 v - k_x}{k^2-(\omega/c)^2\chi_2} - \kappa\frac{\epsilon_2}{\lambda_2}E'_{2t} \end{cases} . \tag{B.22}$$

From which we extract E'_{2t} and substitue its expression to find out E'_{1t}. This is given by the relationship

$$(\lambda_1\epsilon_2 + \lambda_2\epsilon_1)E'_{1t} = \frac{ei}{2\pi^2}\left[\frac{1}{k^2-(\omega/c)^2\chi_1}\left(\frac{\epsilon_2}{\epsilon_1}\kappa\lambda_1 - \frac{\lambda_1\lambda_2}{\kappa}(\omega/c^2\chi_1 v - k_x)\right) + \ldots\right. \tag{B.23}$$

$$\left.\ldots\frac{1}{k^2-(\omega/c)^2\chi_2}\left(-\lambda_1\kappa + \frac{\lambda_1\lambda_2}{\kappa}(\omega/c^2\chi_2 v - k_x)\right)\right] . \tag{B.24}$$

Each factor in green can be simplified in turn by noting, for the first bracket, that

$$\frac{\epsilon_2}{\epsilon_1}\kappa\lambda_1 - \frac{\lambda_1\lambda_2}{\kappa}(\omega/c^2\chi_1 v - k_x) = \kappa\lambda_1\left[\frac{\epsilon_2}{\epsilon_1} - \frac{\lambda_2}{\kappa^2}(\omega/c^2\chi_1 v - k_x)\right] \tag{B.25}$$

$$= \kappa\lambda_1\left[\frac{\epsilon_2}{\epsilon_1} - \lambda_2\frac{v}{\omega}\frac{1}{\kappa^2}\underbrace{\left(\frac{\omega^2}{c^2}\chi_1 - k_x\frac{\omega}{v}\right)}_{=1}\right] \tag{B.26}$$

$$= \kappa\lambda_1\left(\frac{\epsilon_2}{\epsilon_1} - \lambda_2\frac{v}{\omega}\right) , \tag{B.27}$$

and for the second bracket:

$$-\lambda_1\kappa + \frac{\lambda_1\lambda_2}{\kappa}(\omega/c^2\chi_2 v - k_x) = \kappa\lambda_1\left[-1 + \frac{\lambda_2}{\kappa^2}(\omega/c^2\chi_2 v - k_x)\right] \tag{B.28}$$

$$= \kappa\lambda_1\left[-1 + \lambda_2\frac{v}{\omega}\frac{1}{\kappa^2}\underbrace{\left(\frac{\omega^2}{c^2}\chi_2 - k_x\frac{\omega}{v}\right)}_{=1}\right] \tag{B.29}$$

$$= \kappa\lambda_1\left(-1 + \lambda_2\frac{v}{\omega}\right) . \tag{B.30}$$

By reinserting these reduced quantities into the field expression we have

$$(\lambda_1\epsilon_2+\lambda_2\epsilon_1)E'_{1t}=\frac{ei}{2\pi^2}\left[\frac{1}{k^2-(\omega/c)^2\chi_1}\kappa\lambda_1\left(\frac{\epsilon_2}{\epsilon_1}-\lambda_2\frac{v}{\omega}\right)+\frac{1}{k^2-(\omega/c)^2\chi_2}\kappa\lambda_1\left(-1+\lambda_2\frac{v}{\omega}\right)\right], \tag{B.31}$$

leading to the final expression:

$$E'_{1t}=\frac{ei}{2\pi^2}\frac{\kappa\lambda_1}{\lambda_1\epsilon_2+\lambda_2\epsilon_1}\left[\left(\frac{\frac{\epsilon_2}{\epsilon_1}-\lambda_2\frac{v}{\omega}}{k^2-(\omega/c)^2\chi_1}\right)+\left(\frac{-1+\lambda_2\frac{v}{\omega}}{k^2-(\omega/c)^2\chi_2}\right)\right]. \tag{B.32}$$

The transverse radiation field can be expressed as:

$$E'_{1t}=\frac{ei}{2\pi^2}\frac{\kappa\lambda_1}{\xi}\eta, \tag{B.33}$$

with

$$\xi=\lambda_1\epsilon_2+\lambda_2\epsilon_1 \tag{B.34}$$

and

$$\eta=\left(\frac{\frac{\epsilon_2}{\epsilon_1}-\lambda_2\frac{v}{\omega}}{k^2-(\omega/c)^2\chi_1}\right)+\left(\frac{-1+\lambda_2\frac{v}{\omega}}{k^2-(\omega/c)^2\chi_2}\right). \tag{B.35}$$

The normal field in medium 1 is easily found thanks to the previous relation

$$E'_{1n}=-\frac{\kappa}{\lambda_1}E'_{1t}=-\frac{ei}{2\pi^2}\frac{\kappa^2}{\xi}\eta. \tag{B.36}$$

Radiation fields in the second medium can be obtained by interchanging subscripts 1 and 2. Note that the radiation field vanishes if we set $\mu_1=\mu_2$ and $\epsilon_1=\epsilon_2$.

The particle moves from a medium $\epsilon_1=\epsilon=\epsilon'+\epsilon''$ to vacuum $\epsilon_2=\mu_2=1$. Hence we have $\lambda_1^2=(\omega/c)^2\epsilon-\kappa^2$ and $\lambda_2^2=(\omega/c)^2-\kappa^2$. We are interested by the radiation field in the vaccum E'_2 and H'_2. Let's find the expression of E'_2 for instance. To do so we inject the expression of Eq. (B.33) into Eq. (B.17) leading to

$$E'_{2t}=\int E'_{2t}(\mathbf{k})e^{i(\boldsymbol{\kappa\rho}+\lambda_2 x-\omega t)}d\mathbf{k}\cdot\mathbf{e}_\perp \tag{B.37}$$

$$=\frac{ei}{2\pi^2}\int\frac{\kappa\cos\Phi\lambda_2}{\epsilon\lambda_2+\lambda_1}\left(\frac{1-\lambda_1\frac{v}{\omega}}{k^2-(\omega/c)^2\epsilon}+\frac{-\epsilon+\lambda_1\frac{v}{\omega}}{k^2-(\omega/c)^2}\right)e^{i(\kappa\rho\cos\Phi+\lambda_2 x-\omega t)}\kappa d\kappa d\Phi dk_x \tag{B.38}$$

$$=\frac{ei}{2\pi^2}\int\frac{\kappa\cos\Phi\lambda_2}{\epsilon\lambda_2+\lambda_1}\underbrace{\left(\frac{1-\lambda_1\frac{v}{\omega}}{\kappa^2+(\omega/v)^2-(\omega/c)^2\epsilon}+\frac{-\epsilon+\lambda_1\frac{v}{\omega}}{\kappa^2+(\omega/v)^2-(\omega/c)^2}\right)}_{\eta_2}e^{i(\kappa\rho\cos\Phi+\lambda_2 x-\omega t)}\kappa d\kappa d\Phi\frac{d\omega}{v} \tag{B.39}$$

where Φ is the angle between κ and ρ, $k^2=\kappa^2+\omega^2/v^2$ and $dk_x=d\omega/v$. We obtain a triple integral over Φ from 0 to 2π, over ω from $-\infty$ to $+\infty$ and over κ from 0 to $+\infty$. The integral over Φ can be computed thanks to the Bessel function [Abramovitz & Stegun 1972]:

$$J_n(x)=\frac{i^{-n}}{\pi}\int_0^\pi e^{ix\cos\theta}\cos(n\theta)d\theta. \tag{B.40}$$

Hence we set $n = 1$ and $x = \kappa\rho$ leading to:

$$E'_{2t} = \frac{ei^2}{2\pi}\int\left(\frac{1}{i\pi}\int_0^{2\pi} e^{i\kappa\rho\cos\Phi}\cos\Phi d\Phi\right)\frac{\kappa\lambda_2}{\epsilon\lambda_2+\lambda_1}\eta_2 e^{i(\lambda_2 x-\omega t)}\kappa d\kappa\frac{d\omega}{v} \tag{B.41}$$

$$= -\frac{e}{2\pi}\int 2J_1(\kappa\rho)\frac{\kappa\lambda_2}{\epsilon\lambda_2+\lambda_1}\eta_2 e^{i(\lambda_2 x-\omega t)}\kappa d\kappa\frac{d\omega}{v}. \tag{B.42}$$

We introduce R, the distance between the source point and the observer and the angle θ defined by the expression $\rho = R\sin\theta$ and $x = -R\cos\theta$ (see Fig. 2.22). If very large value of R are used ans small θ value not considered, we can asymptotically expand the Bessel function according to [Abramovitz & Stegun 1972]:

$$J_n(z) \simeq \sqrt{\frac{2}{\pi z}}\cos(z - \frac{n\pi}{2} - \frac{\pi}{4}), \tag{B.43}$$

thus for $z = \kappa R\sin\theta$

$$J_1(\kappa R\sin\theta) \simeq \sqrt{\frac{2}{\pi\kappa R\sin\theta}}\cos(\kappa R\sin\theta - \frac{3\pi}{4}). \tag{B.44}$$

Thus we have

$$E'_{1\rho} = -\frac{e}{\pi}\sqrt{\frac{2}{\pi R\sin\theta}}\int\frac{\kappa\lambda_2}{\epsilon\lambda_2+\lambda_1}\eta_2\cos(\kappa R\sin\theta - \frac{3\pi}{4})e^{i(-\lambda_2 R\cos\theta-\omega t)}\sqrt{\kappa}d\kappa\frac{d\omega}{v} \tag{B.45}$$

$$= -\frac{e}{\pi v}\sqrt{\frac{2}{\pi R\sin\theta}}\int\frac{\kappa\lambda_2\eta_2}{\epsilon\lambda_2+\lambda_1}\frac{1}{2}\left(e^{i(\kappa R\sin\theta-\frac{3\pi}{4})} + e^{-i(\kappa R\sin\theta-\frac{3\pi}{4})}\right)e^{i(-\lambda_2 R\cos\theta-\omega t)}\sqrt{\kappa}d\kappa d\omega \tag{B.46}$$

$$= -\frac{e}{\pi v}\sqrt{\frac{1}{2\pi R\sin\theta}}\int\frac{\kappa\lambda_2}{\epsilon\lambda_2+\lambda_1}\eta_2\left(e^{i(\kappa R\sin\theta-\lambda_2 R\cos\theta-\frac{3\pi}{4})} + e^{-i(\kappa R\sin\theta+\lambda_2 R\cos\theta-\frac{3\pi}{4})}\right)e^{-i\omega t}\sqrt{\kappa}d\kappa d\omega \tag{B.47}$$

$$= -\frac{e}{\pi v}\sqrt{\frac{1}{2\pi R\sin\theta}}\int\frac{\kappa\lambda_2}{\epsilon\lambda_2+\lambda_1}\eta_2\left(e^{f(\kappa)R-3i\pi/4} + e^{\phi(\kappa)R+3i\pi/4}\right)e^{-i\omega t}\sqrt{\kappa}d\kappa d\omega \tag{B.48}$$

with $f(\kappa) = i\kappa\sin\theta - i\lambda_2\cos\theta$ and $\phi(\kappa) = -i\kappa\sin\theta - i\lambda_2\cos\theta$. From this point we have to compute this integral through the saddle point method (or steepest descent method) since we consider large value of R. Here is a little reminder of the steepest descend method (that generalize the Laplace's Method for complex function). We want to compute the following integral $I(\lambda)$:

$$I(\lambda) = \int_{\mathcal{C}} f(x)e^{\lambda g(x)}dx \tag{B.49}$$

when $\lambda \to +\infty$. Since $\lambda \to +\infty$ the largest contribution in the integral come from the exponential function wherever $g(x)$ is largest hence we can Taylor expand $g(x)$ around this maximal value x_0. The function $f(x)$ is evaluated in $x = x_0$. In the case of a complex $g(x)$ function we split into a real and imaginary part, $g(x) = \phi(x) + i\psi(x)$. We cannot apply the same treatment here because rapid oscillations in the imaginary component $\psi(x)$ can lead to cancellation of the exponent. Instead we have to prescribe a contour $\mathcal{C}$ along which $\psi(x)$ is constant. This path is also the path of steepest ascent or descent [Bender & Orszag 1999]. From this family of contours, we choose one on which $\psi(x)$ attains a maximum on the interior, which requires $g'(x) = 0$ at some point on the contour. We then linearly approximate by Taylor expansion the contour at the saddle point and apply the ideas of Laplace's Method on the remaining integral.

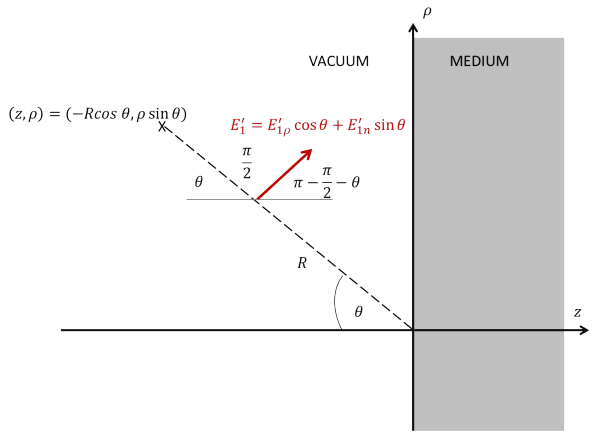

Figure B.1: Scheme of the radiated field direction in function of the orthogonal and longitudinal radiated field.

Before computing the integral we must take cuts in the κ-plane to make the integrand single valued (here it is double valued due to the presence of λ_1 and λ_2). We now turn to the first term of the integral:

$$I_1 = e^{-3i\pi/4}\int_0^{+\infty} \frac{\kappa\lambda_2}{\epsilon\lambda_2 - \lambda_1}\eta_2 e^{f(\kappa)R}\sqrt{\kappa}d\kappa. \tag{B.50}$$

The saddle point κ_0 is given by the maximum of the function $f(\kappa)$ hence

$$\left.\frac{df(\kappa)}{d\kappa}\right|_{\kappa=\kappa_0} = i\sin\theta + \frac{i\kappa_0\cos\theta}{\sqrt{(\omega/c)^2 - \kappa_0^2}} = 0 \tag{B.51}$$

$$\iff \sin\theta\sqrt{(\omega/c)^2 - \kappa_0^2} = -\kappa_0\cos\theta \tag{B.52}$$

$$\Rightarrow \kappa_0 = (\omega/c)\sin\theta. \tag{B.53}$$

Since $f(\kappa)$ in an analytic function we can Taylor it around its maximum κ_0,

$$f(\kappa) \approx f(\kappa_0) + \frac{1}{2}f''(\kappa_0)(\kappa - \kappa_0)^2 \tag{B.54}$$

and replace it into the exponential of the integral. Since the major contribution to the integral comes from the exponential term we evaluate the function $g(\kappa) = \kappa\lambda_2\eta_2\sqrt{\kappa}/(\epsilon\lambda_2 - \lambda_1)$ in $\kappa = \kappa_0$ yielding:

$$I_1 = e^{-3i\pi/4}g(\kappa_0)\int_{\kappa_0-\varepsilon}^{\kappa_0+\varepsilon} e^{(f(\kappa_0)+\frac{1}{2}f''(\kappa_0)(\kappa-\kappa_0)^2)R}d\kappa \tag{B.55}$$

$$= e^{-3i\pi/4}g(\kappa_0)e^{Rf(\kappa_0)}\int_{\kappa_0-\varepsilon}^{\kappa_0+\varepsilon} e^{\frac{1}{2}Rf''(\kappa_0)(\kappa-\kappa_0)^2}d\kappa \tag{B.56}$$

We set $\kappa - \kappa_0 = re^{i\psi}$ and $f''(\kappa_0) = |f''(\kappa_0)|e^{i\zeta}$ to find a Gaussian integrand,

$$I_1 = e^{-3i\pi/4+2\psi+\zeta} g(\kappa_0) e^{Rf(\kappa_0)} \int_{\kappa_0-\varepsilon}^{\kappa_0+\varepsilon} e^{\frac{1}{2}R|f''(\kappa_0)|r^2} e^{i\psi} dr \tag{B.57}$$

$$= g(\kappa_0) e^{Rf(\kappa_0)} \int_{\kappa_0-\varepsilon}^{\kappa_0+\varepsilon} e^{-\frac{1}{2}R|f''(\kappa_0)|r^2} e^{i\psi} dr \tag{B.58}$$

$$= g(\kappa_0) e^{Rf(\kappa_0)} \int_{0}^{\infty} e^{-\frac{1}{2}R|f''(\kappa_0)|r^2} e^{i\psi} dr \tag{B.59}$$

requesting $-3i\pi/4 + 2\psi + \zeta = \pi$. Hence we have

$$I_1 = g(\kappa_0) e^{Rf(\kappa_0)} e^{i\psi} \sqrt{\frac{2\pi}{R|f''(\kappa_0)|}}, \tag{B.60}$$

with

$$g(\kappa_0) = \frac{\kappa_0 \lambda_2(\kappa_0)}{\epsilon\lambda_2(\kappa_0) + \lambda_1(\kappa_0)} \eta_2(\kappa_0) \sqrt{\kappa_0} \tag{B.61}$$

$$= \frac{(\omega/c)\sin\theta\sqrt{(\omega/c)^2 - (\omega/c)^2\sin^2\theta}}{\epsilon\sqrt{(\omega/c)^2 - (\omega/c)^2\sin^2\theta} + \sqrt{(\omega/c)^2\epsilon - (\omega/c)^2\sin^2\theta}} \times \tag{B.62}$$

$$\left(\frac{1 - (v/\omega)\sqrt{(\omega/c)^2\epsilon - (\omega/c)^2\sin^2\theta}}{(\omega/c)^2\sin^2\theta + (\omega/v)^2 - (\omega/c)^2\epsilon} + \frac{-\epsilon + (v/\omega)\sqrt{(\omega/c)^2\epsilon - (\omega/c)^2\sin^2\theta}}{(\omega/c)^2\sin^2\theta + (\omega/v)^2 - (\omega/c)^2} \right) \sqrt{\omega/c\sin\theta} \tag{B.63}$$

$$= \frac{(\omega/c)^2\sin\theta\sqrt{1 - \sin^2\theta}}{\epsilon(\omega/c)\sqrt{1 - \sin^2\theta} + (\omega/c)\sqrt{\epsilon - \sin^2\theta}} \times \tag{B.64}$$

$$\left(\frac{1 - \beta\sqrt{\epsilon - \sin^2\theta}}{(\omega/v)^2 - (\omega/c)^2(\epsilon - \sin^2\theta)} + \frac{-\epsilon + \beta\sqrt{\epsilon - \sin^2\theta}}{(\omega/v)^2 - (\omega/c)^2(1 - \sin^2\theta)} \right) \sqrt{\omega/c\sin\theta} \tag{B.65}$$

$$= \frac{(\omega/c)\sin\theta\cos\theta}{\epsilon\cos\theta + \sqrt{\epsilon - \sin^2\theta}} \left(\frac{1 - \beta\sqrt{\epsilon - \sin^2\theta}}{(\omega/v)^2(1 - \beta^2(\epsilon - \sin^2\theta))} + \frac{-\epsilon + \beta\sqrt{\epsilon - \sin^2\theta}}{(\omega/v)^2(1 - \beta^2\cos^2\theta)} \right) \sqrt{\omega/c\sin\theta} \tag{B.66}$$

$$= \frac{(\omega/c)\sin\theta\cos\theta}{\epsilon\cos\theta + \sqrt{\epsilon - \sin^2\theta}} \times \left(\frac{1 - \beta\sqrt{\epsilon - \sin^2\theta}}{1 - \beta^2(\epsilon - \sin^2\theta)} - \frac{-\epsilon + \beta\sqrt{\epsilon - \sin^2\theta}}{1 - \beta^2\cos^2\theta} \right) \frac{v^2}{\omega^2} \sqrt{\omega/c\sin\theta} \tag{B.67}$$

$$= \frac{(\omega/c)\sin\theta\cos\theta}{\epsilon\cos\theta + \sqrt{\epsilon - \sin^2\theta}} \times \left(\frac{1}{1 - \beta\sqrt{\epsilon\sin^2\theta}} - \frac{-\epsilon + \beta\sqrt{\epsilon - \sin^2\theta}}{1 - \beta^2\cos^2\theta} \right) \frac{v^2}{\omega^2} \sqrt{\omega/c\sin\theta} \tag{B.68}$$

$$\tag{B.69}$$

and

$$\sqrt{\frac{2\pi}{R|f''(\kappa_0)|}} = \sqrt{\frac{2\pi}{R(\frac{\cos\theta}{\sqrt{(\omega/c)^2-(\omega/c)^2\sin^2\theta}} + \frac{(\omega/c)^2\sin^2\theta\cos\theta}{(\sqrt{(\omega/c)^2-(\omega/c)^2\sin^2\theta)^3}})}} \tag{B.70}$$

$$= \sqrt{\frac{2\pi}{R(\frac{c}{\omega} + \frac{c\sin^2\theta}{\omega\cos^2\theta}}} = \sqrt{\frac{2\pi}{R(\frac{c}{\omega}(1+\tan^2\theta)}} \tag{B.71}$$

$$= \sqrt{\frac{2\pi}{R\frac{c}{\omega\cos^2\theta}}} = \cos\theta\sqrt{\frac{2\pi\omega}{Rc}} \tag{B.72}$$

and also

$$e^{Rf(\kappa_0)} = e^{iR\omega/c\sin^2\theta - iR\cos\theta\sqrt{(\omega/c)^2-(\omega/c)^2\sin^2\theta}} \tag{B.73}$$

$$= e^{iR\omega/c(\sin^2\theta + cos^2\theta)} \tag{B.74}$$

$$= e^{iR\omega/c}. \tag{B.75}$$

The second term of the integration involving the function $\phi(\kappa)$ vanishes at large R since the path of integration does not pass by the saddle point. Hence if we put everything together to compute the transverse field we have:

$$E'_{2t} = \frac{e}{\pi v}\sqrt{\frac{1}{2\pi R\sin\theta}}\int \frac{\kappa\lambda_2}{\epsilon\lambda_2+\lambda_1}\eta_1\left(e^{f(\kappa)R-3i\pi/4} + e^{\phi(\kappa)R+3i\pi/4}\right)e^{-i\omega t}\sqrt{\kappa}d\kappa d\omega \tag{B.76}$$

$$= \frac{e}{\pi v}\sqrt{\frac{1}{2\pi R\sin\theta}}\frac{(\omega/c)\sin\theta\cos\theta}{\epsilon\cos\theta+\sqrt{\epsilon-\sin^2\theta}} \times \int\left(\frac{1}{1-\beta\sqrt{\epsilon\sin^2\theta}} - \frac{-\epsilon+\beta\sqrt{\epsilon-\sin^2\theta}}{1-\beta^2\cos^2\theta}\right) \tag{B.77}$$

$$\frac{v^2}{\omega^2}\sqrt{\omega/c\sin\theta}\cos\theta\sqrt{\frac{2\pi\omega}{Rc}}e^{iR\omega/c}e^{-i\omega t}d\omega \tag{B.78}$$

$$= \frac{e\beta^2}{\pi vR}\int \frac{\sin\theta\cos^2\theta}{\epsilon\cos\theta+\sqrt{\epsilon-\sin^2\theta}} \times \left(\frac{1}{1-\beta\sqrt{\epsilon\sin^2\theta}} - \frac{-\epsilon+\beta\sqrt{\epsilon-\sin^2\theta}}{1-\beta^2\cos^2\theta}\right)e^{i\omega(R/c-t)}d\omega \tag{B.79}$$

which can be recast as

$$E'_{2t} = \frac{e\beta^2}{\pi vR}\int \sin\theta\cos^2\theta\xi e^{i\omega(R/c-t)}d\omega \tag{B.80}$$

with

$$\xi = \frac{1}{\epsilon\cos\theta+\sqrt{\epsilon-\sin^2\theta}} \times \left(\frac{1}{1-\beta\sqrt{\epsilon\sin^2\theta}} - \frac{-\epsilon+\beta\sqrt{\epsilon-\sin^2\theta}}{1-\beta^2\cos^2\theta}\right) \tag{B.81}$$

There are one difference with the formula of Garibian: the minus sign in front of the expression depend on how the integration is made. A similar expression for the normal radiated field can be obtained and is given by

$$E'_{2n} = -\frac{e\beta^2}{\pi vR}\int \sin^2\theta\cos\theta\xi e^{i\omega(R/c-t)}d\omega. \tag{B.82}$$

We now are able to find the total radiated field (see Fig. B.1):

$$E'_2 = E'_{2t}\cos\theta + E'_{2n}\sin\theta = -\frac{e\beta^2}{\pi v R}\int \sin\theta\cos\theta\xi e^{i\omega(R/c-t)}d\omega. \tag{B.83}$$

The azimuthal radiated field $H'_{2\phi}$can also be calculated and is yields the radiated field from which we can determine the radiated energy per solid angle unit $d\Omega = \sin\theta d\theta d\phi$ during the time of flight of the particle:

$$\frac{dW}{d\Omega} = \frac{c}{4\pi}R^2\int_{-\infty}^{+\infty}|E'_2 H'_{2\phi}|dt \tag{B.84}$$

$$= \frac{c}{4\pi}\frac{e^2\beta^4}{\pi^2 v^2}4\int_0^{\infty}|\sin^2\theta\cos^2\theta\xi^2|^2 d\omega \tag{B.85}$$

$$= \frac{ce^2\beta^4}{\pi^3 v^2}\sin^2\theta\cos^2\theta\int_0^{\infty}\left|\frac{1}{\epsilon\cos\theta+\sqrt{\epsilon-\sin^2\theta}}\times\left(\frac{-\epsilon+\beta\sqrt{\epsilon-\sin^2\theta}}{1-\beta^2\cos^2\theta}+\frac{1}{1-\beta\sqrt{\epsilon-\sin^2\theta}}\right)\right|^2 d\omega \tag{B.86}$$

$$= \frac{ce^2\beta^4}{\pi^3 v^2}\sin^2\theta\cos^2\theta\int_0^{\infty}\left|\frac{1}{\epsilon\cos\theta+\sqrt{\epsilon-\sin^2\theta}}\times\left(\frac{(-\epsilon+\beta\sqrt{\epsilon-\sin^2\theta})(1-\beta\sqrt{\epsilon-\sin^2\theta})+1+\beta^2\cos^2}{(1-\beta^2\cos^2\theta)(1+\beta\sqrt{\epsilon-\sin^2\theta})}\right)\right. \tag{B.87}$$

$$= \frac{e^2}{\pi^3 c}\frac{\beta^2\sin^2\theta\cos^2\theta}{(1-\beta^2\cos^2\theta)^2}\int_0^{\infty}\left|\frac{(\epsilon-1)(1-\beta^2-\beta\sqrt{\epsilon-\sin^2\theta})}{(\epsilon\cos\theta+\sqrt{\epsilon-\sin^2\theta})(1-\beta\sqrt{\epsilon-\sin^2\theta})}\right|^2 d\omega \tag{B.88}$$

which is the desired result. This formula describes the transition radiation in the wave zone, far from the interface since we used the asymptotic expansion of the Bessel function instead of the Bessel function itself. We also used the steepest descent method for integration. The saddle point is $\kappa_0 = \omega/c\sin^2\theta$ hence our approach is valid for $(\omega/c)R\sin^2\theta \gg 1$ (argument for the Bessel function evaluated at the saddle point must be large). Therefore, in the spatial region close to the particle trajectory (near-field) where the radiation is in formation, our expression does not give the right evaluation.

Appendix C

Calculation of the Biot-Savart model

In this section, we evaluate the radiation by a finite-length electron bunch coming out of the plasma and propagating ballistically in vacuum. The goal is to describe both the transition radiation at the plasma-vacuum interface and the proper field of the relativistically moving electron bunch. Our starting point is the generalized Biot-Savart law [Bellotti & Bornatici 1996]:

$$\mathbf{B}(\mathbf{r},t) = \int d\mathbf{r}' \left\{ \frac{[\mathbf{J}]}{R^2 c} + \frac{1}{Rc^2}\left[\frac{\partial \mathbf{J}}{\partial t}\right] \right\} \frac{\mathbf{R}}{R}\,, \tag{C.1}$$

where $R \equiv |\mathbf{r}-\mathbf{r}'|$ is the distance between the observation point $\mathbf{r}$ and the emission point $\mathbf{r}'$, brackets denote evaluation at the retarded time $t' = t - R/c$, and $\mathbf{J}$ is the current density. In the following, we equate $\mathbf{J}$ with the current density of the electron bunch, i.e., we neglect the contribution of the induced plasma currents, in particular the surface plasma currents [Pukhov & Tueckmantel 2012]. We model the electron bunch as a uniformly charged filament of length L_e and zero radius, moving at constant velocity $v = \beta c$ along the x-axis. This corresponds to the current density

$$\mathbf{J}(\xi,x,y,t,L_b) = J_0 F(\xi,L_b) H(x)\delta(y)\delta(z)\mathbf{e}_x\,, \tag{C.2}$$

$$F(\xi,L_b) = \frac{H(\xi+L_b/2) - H(\xi-L_b/2)}{L_e}\,, \tag{C.3}$$

where $\xi = x - vt$, $H(u)$ [resp. $\delta(u)$] is the Heaviside [resp. Dirac] function, and $J_0 = -eN_e v$ (N_e is the number of electrons inside the bunch). Equation (C.2) describes the progressive emergence of the electron bunch from the plasma into vacuum (occupying the half-space $x \geq 0$). This implies complete screening of the bunch inside the plasma, and hence treating the latter as a perfect conductor.

The radiated magnetic field is given by Eq. (C.1):

$$B_\theta(x,\rho,t) = J_0 \rho \int_{-\infty}^{\infty} dx' \left(\frac{[F]}{cR^3} + \frac{1}{c^2 R^2}\left[\frac{\partial F}{\partial t}\right] \right) H(x')\,, \tag{C.4}$$

where we have changed to polar coordinates (ρ,θ) in the transverse (y,z) plane. According to Fig. C.1, one has $R^2 = \rho^2 + (x-x')^2 = \rho^2 + (\xi - \xi' + \beta R)^2$, admitting the solution $R = \gamma^2\left[\beta(\xi-\xi') + S\right]$ where $S = \sqrt{\rho^2/\gamma^2 + (\xi-\xi')^2}$. Making use of $dx' = (R/S)d\xi'$, one obtains

$$B_\theta(\xi,\rho,t) = \frac{J_0\rho}{c} \int_{-\infty}^{\infty} d\xi' \frac{1}{S}\left(\frac{[F]}{R^2} - \frac{\beta}{R}\left[\frac{\partial F}{\partial \xi'}\right] \right) H(x')\,. \tag{C.5}$$

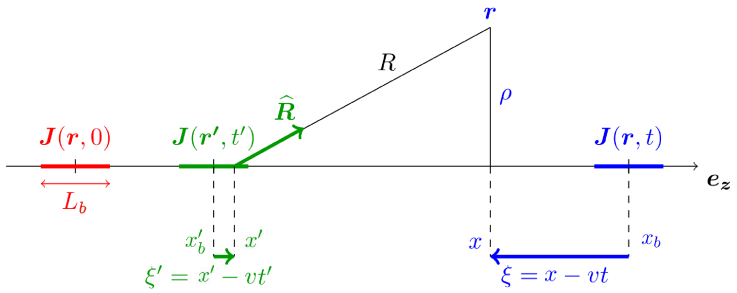

Figure C.1: Geometry of the field emission for an extended charge distribution. At $t = 0$ the field is centered at $x = 0$ and is non-zero between the coordinates $x = -L_b/2$ and $x = L_b/2$ (red trace). The magnetic field is measured at position $\mathbf{r}$ [coordinates (ρ, x)] and time t (blue lines). At this instant, the current is centered at $x_b = vt$. The field measured at (ρ, x) has been emitted by the current $\mathbf{J}$ at the retarded time t' (green lines) and longitudinal position x'. The distance between the points $(\rho' = 0, x')$ et (ρ, x) is defined by R.

To calculate B_θ, it is useful to introduce the following primitive

$$G(\rho, \xi, \xi') = \int^{\xi'} du \frac{1}{R^2(u)S(u)} = -\frac{\beta\rho^2 + S(\xi - \xi')}{\rho^2[\rho^2 + (\xi - \xi')^2]} \tag{C.6}$$

$$= -\frac{\beta\rho^2 + \sqrt{\rho^2/\gamma^2 + (\xi - \xi')^2}(\xi - \xi')}{\rho^2[\rho^2 + (\xi - \xi')^2]}\,. \tag{C.7}$$

The Heaviside function $H(x')$ in Eq. (C.5) bounds the transition zone between the perfectly conducting plasma and vacuum. As $\xi' = x' - vt' = x' + \beta\sqrt{(x - x')^2 + \rho^2} - vt$ increases monotonously with x', we only have to consider the range $\xi' > v(R_0/c - t)$ for $x' > 0$, where $R_0 \equiv R(x' = 0) = \sqrt{\rho^2 + x^2}$. At the right-hand side boundary of the electron beam, $\xi' = L_b/2$, this function implies that the emitted field is non-zero for $\tau \equiv t - R_0/c > -L_b/2v$. Similarly, for $\xi' = -L_b/2$, the field is non-zero at times $\tau > L_b/2v$. It is then straightforward to evaluate

$$B_{\theta,R}(\xi, \rho, t) \equiv -\frac{J_0\rho}{c}\int_{-\infty}^{\infty} d\xi' \frac{\beta}{RS}\left[\frac{\partial F}{\partial \xi'}\right] H[\xi' - \beta(R_0 - ct)] \tag{C.8}$$

$$= \frac{J_0\beta\rho}{cL_b}\left[\frac{H(\tau + \frac{L_b}{2v})}{R_{L_b/2}S_{L_b/2}} - \frac{H(\tau - \frac{L_b}{2v})}{R_{-L_b/2}S_{-L_b/2}}\right], \tag{C.9}$$

where $S_{\pm L_b/2} \equiv \sqrt{\rho^2/\gamma^2 + (\xi \mp L_b/2)^2}$ and $R_{\pm L_b/2} = \gamma^2(\beta(\xi \mp L_b/2) + S_{\pm L_b/2})$. Likewise,

$$B_{\theta,S}(\xi, \rho, t) \equiv \frac{J_0\rho}{c}\int_{-\infty}^{\infty} d\xi' \frac{[F]}{R^2 S} H[\xi' - \beta(R_0 - ct)] \tag{C.10}$$

$$= \frac{J_0\rho}{cL_b}\left\{H\left(\tau + \frac{L_b}{2v}\right) G\left(\rho, \xi, \frac{L_b}{2}\right) - H\left(\tau - \frac{L_b}{2v}\right) G\left(\rho, \xi, -\frac{L_b}{2}\right)\right. \tag{C.11}$$

$$\left. - \left[H\left(\tau + \frac{L_b}{2v}\right) - H\left(\tau - \frac{L_b}{2v}\right)\right] G\left(\rho, \xi, v(\frac{R_0}{c} - t)\right)\right\}. \tag{C.12}$$

The overall magnetic field is given by the sum

$$B_\theta(\xi, \rho, t) = B_{\theta,R}(\xi, \rho, t) + B_{\theta,S}(\xi, \rho, t). \tag{C.13}$$

The CTR component is emitted at the plasma-vacuum boundary and propagates at the speed of light. Denoting by B_θ^{asymp} the limit of Eq. (C.13) when $H(\tau \pm L_b/2v) \to 1$, the CTR field is

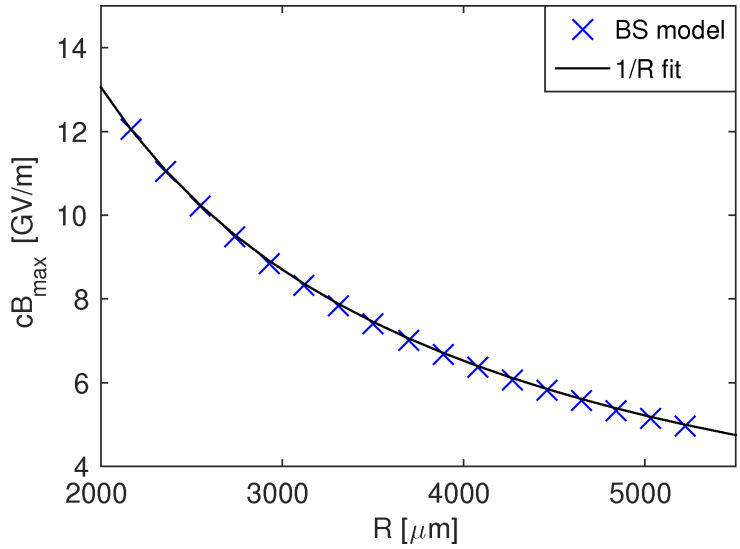

Figure C.2: Maximum CTR field [Eq. (C.14)] as a function of R (blue crosses) and $1/R$ fitting law (black line).

thus determined by

$$B_{\theta,\mathrm{CTR}}(\xi,\rho,t) = B_\theta(\xi,\rho,t) - B_\theta^{\mathrm{asymp}}(\xi,\rho,t). \tag{C.14}$$

To demonstrate the radiative nature of the CTR field Fig. C.2 details the profile of $B_{\theta,\mathrm{CTR}}(x_{\max}(t),\rho_{\max}(t),t)$ at every instant as a function of $R_{\max}(t) \equiv \sqrt{\rho_{\max}^2(t)+x_{\max}^2(t)}$, where $B_{\theta,\mathrm{CTR}}(\rho_{\max}(t),z_{\max}(t),t) \equiv \max_{\rho,x}(B_{\theta,\mathrm{CTR}}(\rho,x,t))$. The $1/R_{\max}$ decay of $B_{\theta,\mathrm{CTR}}$ demonstrates its radiative character. The corresponding angle of maximum emission in the (x,ρ) plane is moreover found to be $\theta_{\mathrm{CTR}} = \arctan(\rho_{max}/x_{max}) \approx 1/\gamma$.

Appendix D

List of communications

D.1 Publications

- J. Déchard, X. Davoine & L. Bergé (2019). *Terahertz wave generation from relativistic plasmas driven by far-infrared laser pulses*, accepted to Phys. Rev. Lett..

- J. Déchard, A. Debayle, X. Davoine, L. Gremillet & L. Bergé (2018). *Terahertz pulse generation in underdense relativistic plasmas: from photoionization-induced radiation to coherent transition radiation*, Phys. Rev. Lett. **120**, p. 144801.

- J. Déchard, A. Nguyen, P. González de Alaiza Martínez, I. Thiele, S. Skupin & L Bergé (2017). *Validity of the unidirectional propagation model: application to laser-driven terahertz emission*, Journal of Physics Communications **1**, p. 055009.

- I. Thiele, B. Zhou, A. Nguyen, E. Smetanina, R. Nuter, K. J. Kaltenecker, P. González de Alaiza Martínez, J. Déchard, L. Bergé, P. U. Jepsen & S. Skupin (2018). *Terahertz emission from laser-driven gas plasmas: a plasmonic point of view*, Optica **5**, p. 1617.

- A. Nguyen, P. González de Alaiza Martínez, J. Déchard, I. Thiele, I. Babushkin, S. Skupin & L. Bergé (2017). *Spectral dynamics of THz pulses generated by two-color laser filaments in air: the role of Kerr nonlinearities and pump wavelength*, Opt. Express **25**, p. 4720.

D.2 Oral presentations

- J. Déchard, A. Debayle, X. Davoine, L. Gremillet & L. Bergé (2019). *Terahertz pulse generation by laser plasma accelerators*, Laser Plasma Accelerator Workshop (LPAW) - Split (Croatia)

- J. Déchard, A. Debayle, X. Davoine, L. Gremillet & L. Bergé (2018). *Terahertz pulse generation by relativistic plasmas*, High Intensity Laser and High Field Phenomena (HILAS) - Strasbourg (France)

- J. Déchard, A. Debayle, X. Davoine, L. Gremillet & L. Bergé (2018). *Terahertz pulse generation by underdense relativistic plasmas*, Scientific Days EDOM - Saclay (France)

- J. Déchard, P. González de Alaiza Martínez, A. Nguyen, I. Thiele, S. Skupin & L Bergé (2017). *Suitability of the unidirectional approach for describing laser-driven terahertz emission*, Conference on Lasers and Electro-Optics (CLEO/Europe-EQEC) - Munich (Germany)

D.3 Poster presentations

- J. Déchard, A. Debayle, X. Davoine, L. Gremillet & L. Bergé (2018). *Terahertz emission by underdense relativistic plasmas*, Conference on Lasers and Electro-Optics (CLEO) - San Jose (U.S.A.)

- J. Déchard, A. Debayle, X. Davoine, L. Gremillet & L. Bergé (2018). *Terahertz emission by underdense relativistic plasmas*, Journée des Doctorants - Arpajon (France)

- J. Déchard, A. Debayle, X. Davoine, L. Gremillet & L. Bergé (2017). *Terahertz pulse generation by laser plasma accelerators*, 8-th Summer school on Atoms and Plasmas in Super-intense Laser Fields - Erice (Italy)

Bibliography

Abramovitz, M. & Stegun, I. A. (1972). *Handbook of Mathematical Functions*. Dover, New York. → 32, 78, 164, 165

Agrawal, G. (2012). *Nonlinear fiber optics*. Academic Press 5th edition. → 17, 18, 157

Akhiezer, A. I. & Polovin, R. V. (1956). *Theory of wave motion of an electron plasma*. Sov. Phys. JETP **3**, p. 696. → 49, 51

Ammosov, M. V., Delone, N. B. & Krakanov, V. P. (1986). *Tunnel ionization of complex atoms and of atomic ions in an alternating electromagnetic fields*. Sov. Phys. JETP **64**, p. 1191. → 22, 113

Anderson, D. & Lisak, M. (1983). *Nonlinear asymmetric self-phase modulation and self-steepening of pulses in long optical waveguides*. Phys. Rev. A **27**, p. 1393. → 158

Andreasen, J. & Kolesik, M. (2012). *Nonlinear propagation of light in structured media: Generalized unidirectional pulse propagation equation*. Phys. Rev. E **86**, p. 036706. → 15

Andreev, N. E., Veĭsman, M. E., Cadjan, M. G. & Chegotov, M. V. (2000). *Generation of a Wakefield during Gas Ionization*. Plasma Physics Reports **26**, p. 959. → 110

Andreeva, V. A., Kosareva, O. G., Panov, N. A., Shipilo, D. E., Solyankin, P. M., Esaulkov, M. N., González de Alaiza Martínez, P., Shkurinov, A. P., Makarov, V. A., Bergé, L. & Chin, S. L. (2016). *Ultrabroad terahertz spectrum generation from an air-based filament plasma*. Phys. Rev. Lett. **116**, p. 063902. → 19, 30

Babushkin, I., Skupin, S., Husakou, A., Köhler, C., Cabrera-Granado, E., Bergé, L. & Herrmann, J. (2011). *Tailoring terahertz radiation by controling tunnel photoionization events in gases*. New J. Phys. **13**, p. 123029. → 24, 27, 80

Bae, L. & Cho, B. (2015). *Coherent transition radiation from thin targets irradiated by high intensity laser pulses*. Current Applied Physics **15**, p. 242. → 64

Bass, F. G. & Yakovenko, V. M. (1965). *Theory of radiation from a charge passing through an electrically inhomogeneous medium*. Soviet Physics Uspekhi **8**, p. 420. → 59

Baton, S. D., Santos, J. J., Amiranoff, F., Popescu, H., Gremillet, L., Koenig, M., Martinolli, E., Guilbaud, O., Rousseaux, C., Rabec Le Gloahec, M., Hall, T., Batani, D., Perelli, E., Scianitti, F. & Cowan, T. E. (2003). *Evidence of ultrashort electron bunches in laser-plasma interactions at relativistic intensities*. Phys. Rev. Lett. **91**, p. 105001. → 145

Bauer, D. & Mulser, P. (2007). *Vacuum heating versus skin layer absorption of intense femtosecond laser pulses.* Phys. Plasmas **14**, p. 023301. → 124, 125, 127

Bellei, C., Davies, J. R., Chauhan, P. K. & Najmudin, Z. (2012). *Coherent transition radiation in relativistic laser-solid interactions.* Plasma Physics and Controlled Fusion **54**, p. 035011. → 68, 145

Bellei, C., Nagel, S. R., Kar, S., Henig, A., Kneip, S., Palmer, C., Savert, A., Willingale, L., Carroll, D., Dromey, B., Green, J. S., Markey, K., Simpson, P., Clarke, R. J., Lowe, H., Neely, D., Spindloe, C., Tolley, M., Kaluza, M. C., Mangles, S. P. D., McKenna, P., Norreys, P. A., Schreiber, J., Zepf, M., Davies, J. R., Krushelnick, K. & Najmudin, Z. (2010). *Micron-scale fast electron filaments and recirculation determined from rear-side optical emission in high-intensity laser-solid interactions.* New Journal of Physics **12**, p. 073016. → 68

Bellotti, U. & Bornatici, M. (1996). *Time-dependent, generalized coulomb and biot-savart laws: A derivation based on fourier transforms.* Am. J. Phys. **64**, p. 569. → 92, 171

Bender, C. M. & Orszag, S. A. (1999). *Advanced Mathematical Methods for Scientists and Engineers I.* ??Springer-Verlag, New York. → 67, 165

Berezhiani, V. I. & Murusidze, I. G. (1992). *Interaction of highly relativistic short laser pulses with plasmas and nonlinear wake-field generation.* Physica Scripta **45**, p. 87. → 51

Bergé, L., Kaltenecker, K., Engelbrecht, S., Nguyen, A., Skupin, S., Merlat, L., Fischer, B., Zhou, B., Thiele, I. & Jepsen, P. U. (2019). *Terahertz spectroscopy from air plasmas created by two-color femtosecond laser pulses: The altesse project.* EPL **126**, no. 2, p. 24001. → 6

Bergé, L., Skupin, S., Nuter, R., Kasparian, J. & Wolf, J.-P. (2007). *Ultrashort filaments of light in weakly ionized,optically transparent media.* Reports on Progress in Physics **70**, p. 1633. → 7, 15, 16, 17

Birdsall, C. K. & Langdon, A. B. (1985). *Plasma Physic via Computer Simulation.* McGraw-Hill Book Company. → 38, 41

Boris, J. P. (1970). *Relativistic plasma simulation-optimization of a hybrid code.* Dans *Proceedings of the 4th Conference on Numerical Simulation of Plasmas*, p. 3–67. → 43

Brabec, T. & Krausz, F. (1997). *Nonlinear optical pulse propagation in the single-cycle regime.* Phys. Rev. Lett. **78**, p. 3282. → 15

Brabec, T. & Krausz, F. (2000). *Intense few-cycle laser fields: Frontiers of nonlinear optics.* Rev. Mod. Phys. **72**, p. 545. → 4

Brantov, A. V., Govras, E. A., Bychenkov, V. Y. & Rozmus, W. (2015). *Ion energy scaling under optimum conditions of laser plasma acceleration from solid density targets.* Phys. Rev. ST Accel. Beams **18**, p. 021301. → 144

Brunel, F. (1987). *Not-so-resonant, resonant absorption.* Phys. Rev. Lett. **59**, p. 52. → 127

Buccheri, F. & Zhang, X.-C. (2015). *Terahertz emission from laser-induced microplasma in ambient air.* Optica **2**, p. 366–369. → 29

Bulanov, S., Naumova, N., Pegoraro, F. & Sakai, J. (1998). *Particle injection into the wave acceleration phase due to nonlinear wake wave breaking.* Phys. Rev. E **58**, p. R5257–R5260. → 55, 89, 99

Burford, N. M. & El-Shenawee, M. O. (2017). *Review of terahertz photoconductive antenna technology.* Optical Engineering **56**, no. 1, p. 1 – 20 – 20. → 7

Carron, N. J. (2000). *Fields of particles and beams exiting a conductor.* Progress in Electromagnetics Reasearch **28**, p. 147. → 90

Chan, W. L., Deibel, J. & Mittleman, D. M. (2007). *Imaging with terahertz radiation.* Reports on Progress in Physics **70**, p. 1325. → 5

Chen, H., Fiuza, F., Link, A., Hazi, A., Hill, M., Hoarty, D., James, S., Kerr, S., Meyerhofer, D. D., Myatt, J., Park, J., Sentoku, Y. & Williams, G. J. (2015). *Scaling the Yield of Laser-Driven Electron-Positron Jets to Laboratory Astrophysical Applications.* Phys. Rev. Lett. **114**, no. 21, p. 215001. → 124

Chen, M., Esarey, E., Schroeder, C. B., Geddes, C. G. R. & Leemans, W. P. (2012). *Theory of ionization-induced trapping in laser-plasma accelerators.* Phys. Plasmas **19**, p. 033101. → 55, 73

Chen, M., Sheng, Z.-M. & Zhang, J. (2006). *On the angular distribution of fast electrons generated in intense laser interaction with solid targets.* Physics of Plasmas **13**, p. 014504. → 136

Clark, E. L., Krushelnick, K., Davies, J. R., Zepf, M., Tatarakis, M., Beg, F. N., Machacek, A., Norreys, P. A., Santala, M. I. K., Watts, I. & Dangor, A. E. (2000). *Measurements of energetic proton transport through magnetized plasma from intense laser interactions with solids.* Phys. Rev. Lett. **84**, p. 670. → 128

Clerici, M., Peccianti, M., Schmidt, B. E., Caspani, L., Shalaby, M., Giguère, M., Lotti, A., Couairon, A., Légaré, F., Ozaki, T., Faccio, D. & Morandotti, R. (2013). *Wavelength scaling of terahertz generation by gas ionization.* Phys. Rev. Lett. **110**, p. 253901. → 106

Cook, D. J. & Hochstrasser, R. M. (2000). *Intense terahertz pulses by four-wave rectification in air.* Opt. Lett. **25**, p. 1210. → 7, 19

Corde, S., Ta Phuoc, K., Lambert, G., Fitour, R., Malka, V., Rousse, A., Beck, A. & Lefebvre, E. (2013). *Femtosecond x rays from laser-plasma accelerators.* Rev. Mod. Phys. **85**, p. 1–48. → 47

Corkum, P. B. (1993). *Plasma perspective on strong field multiphoton ionization.* Phys. Rev. Lett. **71**, p. 1994. → 4

Couairon, A. & Mysyrowicz, A. (2007). *Femtosecond filamentation in transparent media.* Phys. Rep. **441**, p. 47. → 15

D'Amico, C., Houard, A., Akturk, S., Liu, Y., Bloas, J. L., Franco, M., Prade, B., Couairon, A., Tikhonchuk, V. & Mysyrowicz, A. (2008). *Forward thz radiation emission by femtosecond filamentation in gases: theory and experiment.* New J. Phys. **10**, p. 013015. → 29, 79, 133

D'Amico, C., Houard, A. & Franco *et al.*, M. (2007). *Conical forward thz emission from femtoseond-maser-beam filamentation in air.* Phys. Rev. Lett. **98**, p. 235002. → 29, 79

Davoine, X. (2009). *Accélération électronique par sillage laser et sources de rayonnements associées.* Thèse de doctorat, Université de Versailles Saint-Quentin-en-Yvelines. → 44

Debayle, A., González de Alaiza Martínez, P., Gremillet, L. & Bergé, L. (2015). *Non-monotonic increase in laser-driven thz emissions through multiple ionization events.* Phys. Rev. A **91**, p. 041801. → 24, 79

Debayle, A., Gremillet, L., Bergé, L. & Köhler, C. (2014). *Analytical model for thz emissions induced by laser-gas interaction.* Opt. Express **22**, p. 13691. → 31, 80, 118

Debayle, A., Mollica, F., Vauzour, B., Wan, Y., Flacco, A., Malka, V., Davoine, X. & Gremillet, L. (2017). *Electron heating by intense short-pulse lasers propagating through near-critical plasmas.* New Journal of Physics **19**, p. 123013. → 101

Déchard, J., Debayle, A., Davoine, X., Gremillet, L. & Bergé, L. (2018). *Terahertz pulse generation in underdense relativistic plasmas: From photoionization-induced radiation to coherent transition radiation.* Phys. Rev. Lett. **120**, p. 144801. → 120

Déchard, J., Nguyen, A., de Alaiza Martínez, P. G., Thiele, I., Skupin, S. & Bergé, L. (2017). *Validity of the unidirectional propagation model: application to laser-driven terahertz emission.* Journal of Physics Communications **1**, no. 5, p. 055009. → 30

Decker, C. D., Mori, W. B., Tzeng, K.-C. & Katsouleas, T. (1996). *The evolution of ultra-intense, short pulse lasers in underdense plasma.* Physics of Plasmas **3**, p. 2047–2056. → 57

Diaw, A. & Mora, P. (2012). *Thin-foil expansion into a vacuum with a two-temperature electron distribution function.* Phys. Rev. E **86**, p. 026403. → 128

Dolgoshein, B. (1993). *Transition radiation detectors.* Nuclear Instruments and Methods in Physics Research A **326**, p. 434–469. → 59

Drake, J. F., Kaw, P. K., Lee, Y. C., Schmid, G., Liu, C. S. & Rosenbluth, M. N. (1974). *Parametric instabilities of electromagnetic waves in plasmas.* The Physics of Fluids **17**, p. 778–785. → 99

Durand, L. (1975). *Transition radiation from ultrarelativistic particles.* Phys. Rev. D **11**, p. 89. → 80

Esarey, E., Hubbard, R. F., Leemans, W. P., Ting, A. & Sprangle, P. (1997). *Electron injection into plasma wakefields by colliding laser pulses.* Phys. Rev. Lett. **79**, p. 2682. → 55

Esarey, E. & Pilloff, M. (1995). *Trapping and acceleration in nonlinear plasma waves.* Physics of Plasmas **2**, p. 1432–1436. → 52

Esarey, E., Ride, S. K. & Sprangle, P. (1993). *Nonlinear thomson scattering of intense laser pulses from beams and plasmas.* Phys. Rev. E **48**, p. 3003. → 4

Esarey, E., Schroeder, C. B. & Leemans, W. P. (2009). *Physics of laser-driven plasma-based electron accelerators.* Rev. Mod. Phys. **81**, p. 1229. → 49, 51, 53, 116

Esarey, E., Shadwick, B. A., Catravas, P. & Leemans, W. P. (2002). *Synchrotron radiation from electron beams in plasma-focusing channels.* Phys. Rev. E **65**, p. 056505. → 4, 47

Esarey, E., Sprangle, P., Krall, J. & Ting, A. (1996). *Overview of plasma-based accelerator concepts.* IEEE Transactions on Plasma Science **24**, p. 252. → 51, 54

Esirkepov, T. (2001). *Exact charge conservation scheme for particle-in-cell simulation with an arbitrary form-factor.* Computer Physics Communications **135**, p. 144 – 153. → 42

Esirkepov, T., Borghesi, M., Bulanov, S. V., Mourou, G. & Tajima, T. (2004). *Highly efficient relativistic-ion generation in the laser-piston regime.* Phys. Rev. Lett. **92**, p. 175003. → 131

Esirkepov, T., Yamagiwa, M. & Tajima, T. (2006). *Laser ion-acceleration scaling laws seen in multiparametric particle-in-cell simulations.* Phys. Rev. Lett. **96**, p. 105001. → 144

Faure, J. (2016). *Plasma injection schemes for laser-plasma accelerators.* CERN Yellow Reports **1**, no. 0, p. 143. → 53

Faure, J., Glinec, Y., Gallot, G. & Malka, V. (2006). *Ultrashort laser pulses and ultrashort electron bunches generated in relativistic laser-plasma interaction.* Physics of Plasmas **13**, no. 5, p. 056706. → 154

Faure, J., Glinec, Y., Pukhov, A., Kiselev, S., Gordienko, S., Lefebvre, E., Rousseau, J.-P., Burgy, F. & Malka, V. (2004). *A laser-plasma accelerator producing monoenergetic electron beams.* Nature **431**, p. 541–544. → 47

Faure, J., Glinec, Y., Santos, J. J., Ewald, F., Rousseau, J.-P., Kiselev, S., Pukhov, A., Hosokai, T. & Malka, V. (2005). *Observation of laser-pulse shortening in nonlinear plasma waves.* Phys. Rev. Lett. **95**, p. 205003. → 116

Fibich, G., Ilan, B. & Tsynkov, S. (2002). *Computation of nonlinear backscattering using a high-order numerical method.* J. Scien. Comput. **17**, p. 351. → 16

Fork, R. L., Greene, B. I. & Shank, C. V. (1981). *Generation of optical pulses shorter than 0.1 psec by colliding pulse mode locking.* Applied Physics Letters **38**, p. 671. → 2

Fork, R. L., Martinez, O. E. & Gordon, J. P. (1984). *Negative dispersion using pairs of prisms.* Opt. Lett. **9**, p. 150. → 2

Fourmaux, S., Corde, S., Phuoc, K. T., Leguay, P. M., Payeur, S., Lassonde, P., Gnedyuk, S., Lebrun, G., Fourment, C., Malka, V., Sebban, S., Rousse, A. & Kieffer, J. C. (2011). *Demonstration of the synchrotron-type spectrum of laser-produced betatron radiation.* New Journal of Physics **13**, p. 033017. → 4

Freidberg, J. P., Mitchell, R. W., Morse, R. L. & Rudsinski, L. I. (1972). *Resonant absorption of laser light by plasma targets.* Phys. Rev. Lett. **28**, p. 795. → 135

Fülöp, J. A., Ollmann, Z., Lombosi, C., Skrobol, C., Klingebiel, S., Pálfalvi, L., Krausz, F., Karsch, S. & Hebling, J. (2014). *0.4 mj thz pulses by optical rectification.* Dans *19th International Conference on Ultrafast Phenomena.* Optical Society of America. → 7

Galeev, A. A. (1964). *Transition radiation from a uniformly moving charge crossing a diffuse boundary between two media.* J. Exp. Theor. Phys. **19**, p. 904. → 59

Galy, J., Maučec, M., Hamilton, D. J., Edwards, R. & Magill, J. (2007). *Bremsstrahlung production with high-intensity laser matter interactions and applications.* New Journal of Physics **9**, p. 23. → 5

Gao, Y., Drake, T., Chen, Z. & DeCamp, M. F. (2008). *Half-cycle-pulse terahertz emission from an ultrafast laser plasma in a solid target.* Opt. Lett. **33**, no. 23, p. 2776. → 135

Garibian, G. M. (1958). *Contribution to the theory of transition radiation.* J. Exp. Theor. Phys. **6 (33)**, p. 1079. → 59, 62, 65, 68, 161

Garibian, G. M. (1971). *Contribution to the theory of formation of transition x-ray in a stack of plates.* J. Exp. Theor. Phys. **33**, p. 23. → 68

Garibian, G. M. & Chalikian, G. A. (1958). *The radiation from a charged particle passing through a plate.* J. Exp. Theor. Phys. **35**, p. 1282. → 59

Geddes, C., Tóth, C., van Tilborg, J., Esarey, E., Schroeder, C., Bruhwiler, D., Nieter, C., Cary, J. & Leemans, W. (2004). *High-quality electron beams from a laser wakefield accelerator using plasma-channel guiding.* Nature **431**, p. 538–541. → 47

Geddes, C. G. R., Nakamura, K., Plateau, G. R., Toth, C., Cormier-Michel, E., Esarey, E., Schroeder, C. B., Cary, J. R. & Leemans, W. P. (2008). *Plasma-density-gradient injection of low absolute-momentum-spread electron bunches.* Phys. Rev. Lett. **100**, p. 215004. → 55

Ginzburg, V. L. (1964). *Propagation of Electromagnetic Waves in Plasma.* New York: Pergamon. → 64, 135

Ginzburg, V. L. (1982). *Transition radiation and transition scattering.* Physica Scripta **T2A**, p. 182. → 64

Ginzburg, V. L. & Frank, I. M. (1945). *Radiation of a uniformly moving electron due to its transition from one medium into another.* J. Phys.(USSR) **9**, p. 353. [Zh. Eksp. Teor. Fiz.16,15(1946)]. → 59, 62, 64

Ginzburg, V. L. & Tsytovich, V. N. (1974). *On the theory of transition radiation in a nonstationary medium.* Soviet Journal of Experimental and Theoretical Physics **38**, p. 65. → 59

Gizzi, L. A., Giulietti, D., Giulietti, A., Audebert, P., Bastiani, S., Geindre, J. P. & Mysyrowicz, A. (1996). *Simultaneous measurements of hard x rays and second-harmonic emission in fs laser-target interactions.* Phys. Rev. Lett. **76**, p. 2278–2281. → 135

Goldsmith, P. & Jelley, J. V. (1959). *Optical transition radiation from protons entering metal surfaces.* The Philosophical Magazine: A Journal of Theoretical Experimental and Applied Physics **4**, no. 43, p. 836. → 59

Gonsalves, A. J., Nakamura, K., Daniels, J., Benedetti, C., Pieronek, C., de Raadt, T. C. H., Steinke, S., Bin, J. H., Bulanov, S. S., van Tilborg, J.,

Geddes, C. G. R., Schroeder, C. B., Tóth, C., Esarey, E., Swanson, K., Fan-Chiang, L., Bagdasarov, G., Bobrova, N., Gasilov, V., Korn, G., Sasorov, P. & Leemans, W. P. (2019). *Petawatt laser guiding and electron beam acceleration to 8 gev in a laser-heated capillary discharge waveguide.* Phys. Rev. Lett. **122**, p. 084801. → 4, 47

González de Alaiza Martínez, P., Babushkin, I., Bergé, L., Skupin, S., Cabrera-Granado, E., Köhler, C., Morgner, U., Husakou, A. & Herrmann, J. (2015). *Boosting terahertz generation in laser-field ionized gases using a sawtooth wave shape.* Phys. Rev. Lett. **114**, p. 183901. → 27

González de Alaiza Martínez, P. & Bergé, L. (2014). *Influence of multiple ionization in laser filamentation.* J. Phys. B: At. Mol. Opt. Phys. **47**, no. 20, p. 204017. → 22

González de Alaiza Martínez, P., Davoine, X., Debayle, A., Gremillet, L. & Bergé, L. (2016). *Terahertz emission by two-color laser pulses at near-relativistic intensities: competition between photoionization and wakefield effects.* Sci. Reports **6**, p. 26743. → 30, 79

Gopal, A., Herzer, S., Schmidt, A., Singh, P., Reinhard, A., Ziegler, W., Brömmel, D., Karmakar, A., Gibbon, P., Dillner, U., May, T., Meyer, H.-G. & Paulus, G. G. (2013a). *Observation of gigawatt-class thz pulses from a compact laser-driven particle accelerator.* Phys. Rev. Lett. **111**, p. 074802. → 139, 151

Gopal, A., May, T., Herzer, S., Reinhard, A., Minardi, S., Schubert, M., Dillner, U., Pradarutti, B., Polz, J., Gaumnitz, T., Kaluza, M. C., Jackel, O., Riehemann, S., Ziegler, W., Gemuend, H.-P., Meyer, H.-G. & Paulus, G. G. (2012). *Observation of energetic terahertz pulses from relativistic solid density plasmas.* New Journal of Physics **14**, p. 083012. → 138, 151

Gopal, A., Singh, P., Herzer, S., Reinhard, A., Schmidt, A., Dillner, U., May, T., Meyer, H.-G., Ziegler, W. & Paulus, G. G. (2013b). *Characterization of 700μj t rays generated during high-power laser solid interaction.* Opt. Lett. **38**, no. 22, p. 4705. → 139, 151, 153, 155

Gordienko, S. & Pukhov, A. (2005). *Scalings for ultrarelativistic laser plasmas and quasi-monoenergetic electrons.* Physics of Plasmas **12**, p. 043109. → 57

Gordon, D. F., Hafizi, B., Sprangle, P., Hubbard, R. F., Peñano, J. R. & Mori, W. B. (2001). *Seeding of the forward raman instability by ionization fronts and raman backscatter.* Phys. Rev. E **64**, p. 046404. → 109, 110, 111, 117

Goulielmakis, E., Schultze, M., Hofstetter, M., Yakovlev, V. S., Gagnon, J., Uiberacker, M., Aquila, A. L., Gullikson, E. M., Attwood, D. T., Kienberger, R., Krausz, F. & Kleineberg, U. (2008). *Single-cycle nonlinear optics.* Science **320**, p. 1614. → 4

Grismayer, T., Vranic, M., Martins, J. L., Fonseca, R. A. & Silva, L. O. (2016). *Laser absorption via quantum electrodynamics cascades in counter propagating laser pulses.* Physics of Plasmas **23**, no. 5, p. 056706. → 5

Guérin, S., Laval, G., Mora, P., Adam, J. C., Héron, A. & Bendib, A. (1995). *Modulational and raman instabilities in the relativistic regime.* Physics of Plasmas **2**, p. 2807. → 107

Gurevich, A. V., Pariĭskaya, L. V. & Pitaevskiĭ, L. P. (1966). *Self-similar Motion of Rarefied Plasma.* Sov. Phys. JETP **22**, p. 449. → 128

Hamster, H., Sullivan, A., Gordon, S., White, W. & Falcone, R. W. (1993). *Subpicosecond, electromagnetic pulses from intense laser-plasma interaction.* Phys. Rev. Lett. **71**, p. 2725–2728. → 7, 123, 133, 135, 137

Henig, A., Steinke, S., Schnürer, M., Sokollik, T., Hörlein, R., Kiefer, D., Jung, D., Schreiber, J., Hegelich, B. M., Yan, X. Q., Meyer-ter Vehn, J., Tajima, T., Nickles, P. V., Sandner, W. & Habs, D. (2009). *Radiation-pressure acceleration of ion beams driven by circularly polarized laser pulses.* Phys. Rev. Lett. **103**, p. 245003. → 124

Herzer, S., Woldegeorgis, A., Polz, J., Reinhard, A., Almassarani, M., Beleites, B., Ronneberger, F., Grosse, R., Paulus, G. G., Hubner, U., May, T. & Gopal, A. (2018). *An investigation on THz yield from laser-produced solid density plasmas at relativistic laser intensities.* New Journal of Physics **20**, p. 063019. → 140

Higginson, A., Gray, R. J., King, M., Dance, R. J., Williamson, S. D. R., Butler, N. M. H., Wilson, R., Capdessus, R., Armstrong, C., Green, J. S., Hawkes, S. J., Martin, P., Wei, W. Q., Mirfayzi, S. R., Yuan, X. H., Kar, S., Borghesi, M., Clarke, R. J., Neely, D. & McKenna, P. (2018). *Near-100 mev protons via a laser-driven transparency-enhanced hybrid acceleration scheme.* Nature Communications **9**, p. 724. → 4

Hoarty, D. J., Allan, P., James, S. F., Brown, C. R. D., Hobbs, L. M. R., Hill, M. P., Harris, J. W. O., Morton, J., Brookes, M. G., Shepherd, R., Dunn, J., Chen, H., Von Marley, E., Beiersdorfer, P., Chung, H. K., Lee, R. W., Brown, G. & Emig, J. (2013). *Observations of the effect of ionization-potential depression in hot dense plasma.* Phys. Rev. Lett. **110**, p. 265003. → 124

Huba, J. D., éditeur (2013). *NRL Plasma Formulary.* U.S. GPO, Washington, D.C. → 19

Jackson, J. D. (1999). *Classical electrodynamics (3rd ed.).* John Wiley & Sons. → 4, 12, 28, 30, 60, 63, 64, 88, 90

Jin, Z., Zhuo, H. B., Nakazawa, T., Shin, J. H., Wakamatsu, S., Yugami, N., Hosokai, T., Zou, D. B., Yu, M. Y., Sheng, Z. M. & Kodama, R. (2016). *Highly efficient terahertz radiation from a thin foil irradiated by a high-contrast laser pulse.* Phys. Rev. E **94**, p. 033206. → 139

Kalmykov, S., Yi, S. A., Khudik, V. & Shvets, G. (2009). *Electron self-injection and trapping into an evolving plasma bubble.* Phys. Rev. Lett. **103**, p. 135004. → 53, 55

Kar, S., Kakolee, K. F., Qiao, B., Macchi, A., Cerchez, M., Doria, D., Geissler, M., McKenna, P., Neely, D., Osterholz, J., Prasad, R., Quinn, K., Ramakrishna, B., Sarri, G., Willi, O., Yuan, X. Y., Zepf, M. & Borghesi, M. (2012). *Ion acceleration in multispecies targets driven by intense laser radiation pressure.* Phys. Rev. Lett. **109**, p. 185006. → 124

Kartashov, D., Ališauskas, S., Pugžlys, A., Voronin, A., Zheltikov, A., Petrarca, M., Béjot, P., Kasparian, J., Wolf, J.-P. & Baltuška, A. (2012). *White light generation over three octaves by femtosecond filament at 3.9 μm in argon.* Opt. Lett. **16**, p. 3456. → 106

Kawase, K., Ogawa, Y., Watanabe, Y. & Inoue, H. (2003). *Non-destructive terahertz imaging of illicit drugs using spectral fingerprints.* Opt. Express **11**, no. 20, p. 2549. → 6

Keldysh, L. V. (1965). *Ionization in the field of a strong electromagnetic wave.* Sov. Phys. JETP **20**, p. 1307. → 20

Kemp, A. J., Fiuza, F., Debayle, A., Johzaki, T., Mori, W. B., Patel, P. K., Sentoku, Y. & Silva, L. O. (2014). *Laser-plasma interactions for fast ignition.* Nucl. Fusion **54**, p. 054002. → 127

Kim, I. J., Pae, K. H., Kim, C. M., Kim, H. T., Sung, J. H., Lee, S. K., Yu, T. J., Choi, I. W., Lee, C.-L., Nam, K. H., Nickles, P. V., Jeong, T. M. & Lee, J. (2013). *Transition of proton energy scaling using an ultrathin target irradiated by linearly polarized femtosecond laser pulses.* Phys. Rev. Lett. **111**, p. 165003. → 124

Kim, K.-Y., Glownia, J. H., Taylor, A. J. & Rodriguez, G. (2007). *Terahertz emission from ultrafast ionizing air in symmetry-broken laser fields.* Opt. Express **15**, p. 4577. → 7, 8, 25, 80

Kim, K. Y., Taylor, A. J., Glownia, J. H. & Rodriguez, G. (2008). *Coherent control of terahertz supercontinuum generation in ultrafast laser-gas interactions.* Nature Photon. **2**, p. 605. → 8, 25, 27, 79

Kinsler, P., Radnor, S. B. P. & New, G. H. C. (2005). *Theory of directional pulse propagation.* Phys. Rev. A **72**, p. 063807. → 15

Kmetec, J. D., Gordon, C. L., Macklin, J. J., Lemoff, B. E., Brown, G. S. & Harris, S. E. (1992). *Mev x-ray generation with a femtosecond laser.* Phys. Rev. Lett. **68**, p. 1527. → 124

Koehler, C., Cabrera-Granado, E., Babushkin, I., Bergé, L., Herrmann, J. & Skupin, S. (2011). *Directionality of terahertz emission from photoinduced gas plasmas.* Opt. Lett. **36**, p. 3166. → 79, 80

Kolesik, M. & Moloney, J. V. (2004). *Nonlinear optical pulse propagation simulation: From maxwell's to unidirectionnal equations.* Phys. Rev. E **70**, p. 036604. → 15, 16

Kostyukov, I., Nerush, E., Pukhov, A. & Seredov, V. (2010). *A multidimensional theory for electron trapping by a plasma wake generated in the bubble regime.* New Journal of Physics **12**, p. 045009. → 55

Kruer, W. L. (1988). *The Physics of Laser Plasma Interactions.* Addison-Wesley, New-York. → 40, 134, 136

Kruer, W. L. & Estabrook, K. (1985). *$J \times B$ heating by very intense laser light.* Phys. Fluids **28**, no. 1, p. 430–432. → 124

Landau, L. & Lifshitz, E. (1975). *Quantum Mechanics Vol. 2 (4th ed.).* Butterworth-Heinemann. → 22

Lax, P. & Wendroff, B. (1960). *Systems of conservation laws.* Commun. Pure Appl. Math. **13**, p. 217. → 157

Lécz, Z., Boine-Frankenheim, O. & Kornilov, V. (2013). *Target normal sheath acceleration for arbitrary proton layer thickness.* Nucl. Instrum. Methods Phys. Res. A **727**, p. 51–58. → 128

Ledingham, K. W. D., Spencer, I., McCanny, T., Singhal, R. P., Santala, M. I. K., Clark, E., Watts, I., Beg, F. N., Zepf, M., Krushelnick, K., Tatarakis, M., Dangor, A. E., Norreys, P. A., Allott, R., Neely, D., Clark, R. J., Machacek, A. C., Wark, J. S., Cresswell, A. J., Sanderson, D. C. W. & Magill, J. (2000). *Photonuclear physics when a multiterawatt laser pulse interacts with solid targets.* Phys. Rev. Lett. **84**, p. 899. → 5

Leemans, W. P., Geddes, C. G., Faure, J., Tóth, C., van Tilborg, J., Schroeder, C. B., Esarey, E., Fubiani, G., Auerbach, D. & Marcelis *et al.*, B. (2003). *Observation of Terahertz Emission from a Laser-Plasma Accelerated Electron Bunch Crossing a Plasma-Vacuum Boundary.* Phys. Rev. Lett. **91**. → 7, 70, 120

Leemans, W. P., Gonsalves, A. J., Mao, H.-S., Nakamura, K., Benedetti, C., Schroeder, C. B., Tóth, C., Daniels, J., Mittelberger, D. E., Bulanov, S. S., Vay, J.-L., Geddes, C. G. R. & Esarey, E. (2014). *Multi-gev electron beams from capillary-discharge-guided subpetawatt laser pulses in the self-trapping regime.* Phys. Rev. Lett. **113**, p. 245002. → 47

Lepore, J. V. & Riddell, R. J. (1976). *Theory of transition radiation from a smoothly varying boundary.* Phys. Rev. D **13**, p. 2300. → 59

LeVeque, R. J. (2002). *Finite volume methods for hyperbolic equations.* Cambridge University Press, New York, USA. → 158

Li, C., Cui, Y.-Q., Zhou, M.-L., Du, F., Li, Y.-T., Wang, W.-M., Chen, L.-M., Sheng, Z.-M., Ma, J.-L., Lu, X. & Zhang, J. (2014). *Role of resonance absorption in terahertz radiation generation from solid targets.* Opt. Express **22**, p. 11797. → 137, 153, 155

Li, C., Liao, G.-Q., Zhou, M.-L., Du, F., Ma, J.-L., Li, Y.-T., Wang, W.-M., Sheng, Z.-M., Chen, L.-M. & Zhang, J. (2016). *Backward terahertz radiation from intense laser-solid interactions.* Opt. Express **24**, no. 4, p. 4010. → 137

Li, C., Zhou, M.-L., Ding, W.-J., Du, F., Liu, F., Li, Y.-T., Wang, W.-M., Sheng, Z.-M., Ma, J.-L., Chen, L.-M., Lu, X., Dong, Q.-L., Wang, Z.-H., Lou, Z., Shi, S.-C., Wei, Z.-Y. & Zhang, J. (2011). *Effects of laser-plasma interactions on terahertz radiation from solid targets irradiated by ultrashort intense laser pulses.* Phys. Rev. E **84**, p. 036405. → 135, 136, 137

Li, M., Li, W., Shi, Y., Lu, P., Pan, H. & Zeng, H. (2012a). *Verification of the physical mechanism of thz generation by dual-color ultrashort laser pulses.* Applied Physics Letters **101**, no. 16. → 25

Li, Y. T., Li, C., Zhou, M. L., Wang, W. M., Du, F., Ding, W. J., Lin, X. X., Liu, F., Sheng, Z. M., Peng, X. Y., Chen, L. M., Ma, J. L., Lu, X., Wang, Z. H., Wei, Z. Y. & Zhang, J. (2012b). *Strong terahertz radiation from relativistic laser interaction with solid density plasmas.* Applied Physics Letters **100**, p. 254101. → 137

Li, Y. T., Yuan, X. H., Xu, M. H., Zheng, Z. Y., Sheng, Z. M., Chen, M., Ma, Y. Y., Liang, W. X., Yu, Q. Z., Zhang, Y., Liu, F., Wang, Z. H., Wei, Z. Y., Zhao, W., Jin, Z. & Zhang, J. (2006). *Observation of a fast electron beam emitted along the surface of a target irradiated by intense femtosecond laser pulses.* Phys. Rev. Lett. **96**, p. 165003. → 136

Liao, G., Li, Y., Liu, H., Scott, G. G., Neely, D., Zhang, Y., Zhu, B., Zhang, Z., Armstrong, C., Zemaityte, E., Bradford, P., Huggard, P. G., Rusby, D. R., McKenna, P., Brenner, C. M., Woolsey, N. C., Wang, W., Sheng, Z. & Zhang, J. (2019). *Multimillijoule coherent terahertz bursts from picosecond laser-irradiated metal foils.* Proceedings of the National Academy of Sciences **116**, p. 3994. → 140, 155, 156

Liao, G.-Q., Li, Y.-T., Li, C., Mondal, S., Hafez, H. A., Fareed, M. A., Ozaki, T., Wang, W.-M., Sheng, Z.-M. & Zhang, J. (2016a). *Terahertz emission from two-plasmon-decay induced transient currents in laser-solid interactions.* Physics of Plasmas **23**, p. 013104. → 138

Liao, G. Q., Li, Y. T., Li, C., Su, L. N., Zheng, Y., Liu, M., Wang, W. M., Hu, Z. D., Yan, W. C., Dunn, J., Nilsen, J., Hunter, J., Liu, Y., Wang, X., Chen, L. M., Ma, J. L., Lu, X., Jin, Z., Kodama, R., Sheng, Z. M. & Zhang, J. (2015). *Bursts of terahertz radiation from large-scale plasmas irradiated by relativistic picosecond laser pulses.* Phys. Rev. Lett. **114**, p. 255001. → 138

Liao, G.-Q., Li, Y.-T., Zhang, Y.-H., Liu, H., Ge, X.-L., Yang, S., Wei, W.-Q., Yuan, X.-H., Deng, Y.-Q., Zhu, B.-J., Zhang, Z., Wang, W.-M., Sheng, Z.-M., Chen, L.-M., Lu, X., Ma, J.-L., Wang, X. & Zhang, J. (2016b). *Demonstration of coherent terahertz transition radiation from relativistic laser-solid interactions.* Phys. Rev. Lett. **116**, p. 205003. → 68, 139

Lifschitz, A. F., Davoine, X., Lefebvre, E., Faure, J., Rechatin, C. & Malka, V. (2009). *Particle-in-cell modelling of laser-plasma interaction using fourier decomposition.* J. Comp. Phys. **228**, p. 1803. → 44, 46, 80

Liu, J. & Zhang, X.-C. (2014). *Terahertz radiation-enhanced-emission-of-fluorescence.* Frontiers of Optoelectronics **7**, no. 2, p. 156. → 5

Lobet, M., Davoine, X., d'Humières, E. & Gremillet, L. (2017). *Generation of high-energy electron-positron pairs in the collision of a laser-accelerated electron beam with a multipetawatt laser.* Phys. Rev. Accel. Beams **20**, p. 043401. → 5

Lu, W., Huang, C., Zhou, M., Mori, W. B. & Katsouleas, T. (2006a). *Nonlinear theory for relativistic plasma wakefields in the blowout regime.* Phys. Rev. Lett. **96**, p. 165002. → 57

Lu, W., Huang, C., Zhou, M., Tzoufras, M., Tsung, F. S., Mori, W. B. & Katsouleas, T. (2006b). *A nonlinear theory for multidimensional relativistic plasma wave wakefields.* Physics of Plasmas **13**, p. 056709. → 57

Lu, W., Tzoufras, M., Joshi, C., Tsung, F. S., Mori, W. B., Vieira, J., Fonseca, R. A. & Silva, L. O. (2007). *Generating multi-gev electron bunches using single stage laser wakefield acceleration in a 3d nonlinear regime.* Phys. Rev. ST Accel. Beams **10**, p. 061301. → 57, 58, 80, 120

Lundh, O., Lim, J., Rechatin, C., Ammoura, L., Ben-Ismaïl, A., Davoine, X., Gallot, G., Goddet, J.-P., Lefebvre, E., Malka, V. & Faure, J. (2011). *Few femtosecond, few kiloampere electron bunch produced by a laser-plasma accelerator.* Nature Physics **7**, no. 3, p. 219. → 154

Macchi, A., Borghesi, M. & Passoni, M. (2013). *Ion acceleration by superintense laser-plasma interaction.* Rev. Mod. Phys. **85**, p. 751. → 4, 124

Macchi, A., Cattani, F., Liseykina, T. V. & Cornolti, F. (2005). *Laser acceleration of ion bunches at the front surface of overdense plasmas.* Phys. Rev. Lett. **94**, p. 165003. → 130

Macchi, A., Cornolti, F. & Pegoraro, F. (2002). *Two-surface wave decay.* Physics of Plasmas **9**, no. 5, p. 1704. → 127

Mackinnon, A. J., Borghesi, M., Hatchett, S., Key, M. H., Patel, P. K., Campbell, H., Schiavi, A., Snavely, R., Wilks, S. C. & Willi, O. (2001). *Effect of plasma scale length on multi-mev proton production by intense laser pulses.* Phys. Rev. Lett. **86**, p. 1769. → 128

Mackinnon, A. J., Sentoku, Y., Patel, P. K., Price, D. W., Hatchett, S., Key, M. H., Andersen, C., Snavely, R. & Freeman, R. R. (2002). *Enhancement of proton acceleration by hot-electron recirculation in thin foils irradiated by ultraintense laser pulses.* Phys. Rev. Lett. **88**, p. 215006. → 144

Maiman, T. H. (1960). *Stimulated optical radiation in ruby.* Nature **186**, p. 493. → 1

Maksimchuk, A., Gu, S., Flippo, K., Umstadter, D. & Bychenkov, V. Y. (2000). *Forward ion acceleration in thin films driven by a high-intensity laser.* Phys. Rev. Lett. **84**, p. 4108. → 128

Malka, V., Faure, J., Marquès, J. R., Amiranoff, F., Rousseau, J. P., Ranc, S., Chambaret, J. P., Najmudin, Z., Walton, B., Mora, P. & Solodov, A. (2001). *Characterization of electron beams produced by ultrashort (30 fs) laser pulses.* Physics of Plasmas **8**, no. 6, p. 2605–2608. → 116

Malka, V., Fritzler, S., Lefebvre, E., Aleonard, M.-M., Burgy, F., Chambaret, J.-P., Chemin, J.-F., Krushelnick, K., Malka, G., Mangles, S. P. D., Najmudin, Z., Pittman, M., Rousseau, J.-P., Scheurer, J.-N., Walton, B. & Dangor, A. E. (2002). *Electron acceleration by a wake field forced by an intense ultrashort laser pulse.* Science **298**, no. 5598, p. 1596. → 114

Mangles, S., Murphy, C., Najmudin, Z., Thomas, A., Collier, J., Dangor, A., Divall, E., Foster, P., Gallacher, J., Hooker, C., Jaroszynski, D., Langley, A., Mori, W., Norreys, P., Tsung, F., Viskup, R., Walton, B. & Krushelnick, K. (2004). *Monoenergetic beams of relativistic electrons from intense laser-plasma interactions.* Nature **431**, p. 535–538. → 47

Marburger, J. H. & Tooper, R. F. (1975). *Nonlinear optical standing waves in overdense plasmas.* Phys. Rev. Lett. **35**, p. 1001. → 125

Mariscal, D., Williams, G. J., Chen, H., Ayers, S., Lemos, N., Kerr, S. & Ma, T. (2018). *Calibration of proton dispersion for the nif electron positron proton spectrometer (nepps) for short-pulse laser experiments on the nif arc.* Review of Scientific Instruments **89**, p. 10I145. → 4

Marx, G. (1966). *Interstellar vehicle propelled by terrestrial laser beam.* Nature **211**, p. 22. → 132

Max, C. E., Arons, J. & Langdon, A. B. (1974). *Self-modulation and self-focusing of electromagnetic waves in plasmas.* Phys. Rev. Lett. **33**, p. 209. → 116

May, J., Tonge, J., Fiuza, F., Fonseca, R. A., Silva, L. O., Ren, C. & Mori, W. B. (2011). *Mechanism of generating fast electrons by an intense laser at a steep overdense interface.* Phys. Rev. E **84**, p. 025401. → 127

McClung, F. J. & Hellwarth, R. W. (1962). *Giant optical pulsations from ruby.* Journal of Applied Physics **33**, p. 828. → 1

McGuffey, C., Thomas, A. G. R., Schumaker, W., Matsuoka, T., Chvykov, V., Dollar, F. J., Kalintchenko, G., Yanovsky, V., Maksimchuk, A., Krushelnick, K., Bychenkov, V. Y., Glazyrin, I. V. & Karpeev, A. V. (2010). *Ionization induced trapping in a laser wakefield accelerator.* Phys. Rev. Lett. **104**, p. 025004. → 55

Miao, C., Palastro, J. P. & Antonsen, T. M. (2016). *Laser pulse driven terahertz generation via resonant transition radiation in inhomogeneous plasmas.* Phys. Plasmas **23**, p. 063103. → 79

Mondal, S., Wei, Q., Ding, W. J., Hafez, H. A., Fareed, M. A., Laramée, A., Ropagnol, X., Zhang, G., Sun, S., Sheng, Z. M., Zhang, J. & Ozaki, T. (2017). *Aligned copper nanorod arrays for highly efficient generation of intense ultra-broadband thz pulses.* Scientific Reports **7**, p. 40058. → 156

Mora, P. (2003). *Plasma expansion into a vacuum.* Phys. Rev. Lett. **90**, p. 185002. → 128, 129

Mori, W. B. (1997). *The physics of the nonlinear optics of plasmas at relativistic intensities for short-pulse lasers.* IEEE Journal of Quantum Electronics **33**, p. 1942. → 54, 116

Mori, W. B. & Katsouleas, T. (1992). *Ponderomotive force of a uniform electromagnetic wave in a time varying dielectric medium.* Phys. Rev. Lett. **69**, p. 3495. → 110, 113, 116

Mourou, G. A., Tajima, T. & Bulanov, S. V. (2006). *Optics in the relativistic regime.* Rev. Mod. Phys. **78**, p. 309. → 3

Nakamura, T., Kato, S., Nagatomo, H. & Mima, K. (2004). *Surface-magnetic-field and fast-electron current-layer formation by ultraintense laser irradiation.* Phys. Rev. Lett. **93**, p. 265002. → 136

Nguyen, A., de Alaiza Martínez, P. G., Déchard, J., Thiele, I., Babushkin, I., Skupin, S. & Bergé, L. (2017). *Spectral dynamics of thz pulses generated by two-color laser filaments in air: the role of kerr nonlinearities and pump wavelength.* Opt. Express **25**, p. 4720. → 29

Nguyen, A., Kaltenecker, K. J., Delagnes, J.-C., Zhou, B., Cormier, E., Fedorov, N., Bouillaud, R., Descamps, D., Thiele, I., Skupin, S., Jepsen, P. U. & Bergé, L. (2019). *Wavelength scaling of terahertz pulse energies delivered by two-color air plasmas.* Opt. Lett. **44**, p. 1488. → 79, 106

Nie, Z., C.-H.Pai, Hua, J., Zhang, C., Wu, Y., Y.Wan, Li, F., Zhang, J., Cheng, Z., Su, Q., Liu, S., Ma, Y., Ning, X., He, Y., Lu, W., Chu, H.-H., Wang, J., Mori, W. B. & Joshi, C. (2018). *Relativistic single-cycle tunable infrared pulses generated from a tailored plasma density structure.* Nature Photonics **12**, p. 489. → 106

Nodland, B. & McKinstrie, C. J. (1997). *Propagation of a short laser pulse in a plasma.* Phys. Rev. E **56**, p. 7174–7178. → 30

Oh, T. I., You, Y. S., Jhajj, N., Rosenthal, E. W., Milchberg, H. M. & Kim, K. Y. (2013). *Scaling and saturation of high-power terahertz radiation generation in two-color laser filamentation.* Applied Physics Letters **102**, no. 20, p. 201113. → 7, 79, 153

Pak, A., Marsh, K. A., Martins, S. F., Lu, W., Mori, W. B. & Joshi, C. (2010). *Injection and trapping of tunnel-ionized electrons into laser-produced wakes.* Phys. Rev. Lett. **104**, p. 025003. → 55

Palmer, C. A. J., Dover, N. P., Pogorelsky, I., Babzien, M., Dudnikova, G. I., Ispiriyan, M., Polyanskiy, M. N., Schreiber, J., Shkolnikov, P., Yakimenko, V. & Najmudin, Z. (2011). *Monoenergetic proton beams accelerated by a radiation pressure driven shock.* Phys. Rev. Lett. **106**, p. 014801. → 106

Pegoraro, F. & Bulanov, S. V. (2007). *Photon bubbles and ion acceleration in a plasma dominated by the radiation pressure of an electromagnetic pulse.* Phys. Rev. Lett. **99**, p. 065002. → 127

Perelomov, A. M., Popov, V. S. & Terent'ev, M. V. (1966). *Ionization of atoms in an alternating electric field: I.* Sov. Phys. JETP **23**, p. 924. → 20

Perelomov, A. M., Popov, V. S. & Terent'ev, M. V. (1967a). *Ionization of atoms in an alternating electric field: II.* Sov. Phys. JETP **24**, p. 207. → 20

Perelomov, A. M., Popov, V. S. & Terent'ev, M. V. (1967b). *Ionization of atoms in an alternating electric field: III.* Sov. Phys. JETP **25**, p. 336. → 20

45th EPS conference on Plasma Physics, éditeur (2018). *Modeling Ultra-high Frequency Radiation Emission in PIC Codes.* → 156

46th EPS conference on Plasma Physics, éditeur (2019). *RaDiO-Radiation Diagnostic for Osiris: an efficient radiation processing tool for particle-in-cell simulations.* → 156

Pogorelsky, I., Polyanskiy, M. & Kimura, W. D. (2016a). *Mid-infrared lasers for energy frontier plasma accelerators.* Phys. Rev. Acc. Beams **19**, p. 091001. → 106

Pogorelsky, I. V., Babzien, M., Ben-Zvi, I., Polyanskiy, M. N., Skaritka, J., Tresca, O., Dover, N. P., Najmudin, Z., Lu, W., Cook, N., Ting, A. & Chen, Y.-H. (2016b). *Extending laser plasma accelerators into the mid-ir spectral domain with a next-generation ultra-fast CO_2 laser.* Plasma Physics and Controlled Fusion **58**, p. 034003. → 106

Pogorelsky, I. V., Babzien, M., Ben-Zvi, I., Skaritka, J. & Polyansky, M. N. (2016c). *BESTIA - the next generation ultra-fast co_2 laser for advanced accelerator research.* Nucl. Instrum. Methods Phys. Res. A **829**, p. 432. → 106

Pukhov, A. & Tueckmantel, T. (2012). *Transverse coherent transition radiation for diagnosis of modulated proton bunches.* Phys. Rev. ST Accel. Beams **15**, p. 111301. → 171

Pukhov, A. & Meyer-ter Vehn, J. (2002). *Laser wake field acceleration: the highly nonlinear broken-wave regime.* Applied Physics B **74**, p. 355–361. → 57

Qiao, B., Kar, S., Geissler, M., Gibbon, P., Zepf, M. & Borghesi, M. (2012). *Dominance of radiation pressure in ion acceleration with linearly polarized pulses at intensities of* 10^{21} W cm^{-2}. Phys. Rev. Lett. **108**, p. 115002. → 131

Ravi, K., Huang, W. R., Carbajo, S., Nanni, E. A., Schimpf, D. N., Ippen, E. P. & Kärtner, F. X. (2015). *Theory of terahertz generation by optical rectification using tilted-pulse-fronts.* Opt. Express **23**. → 7

Robinson, A., Strozzi, D., Davies, J., Gremillet, L., Honrubia, J., Johzaki, T., Kingham, R., Sherlock, M. & Solodov, A. (2014). *Theory of fast electron transport for fast ignition.* Nuclear Fusion **54**, p. 054003. → 127

Robinson, A. P. L., Gibbon, P., Zepf, M., Kar, S., Evans, R. G. & Bellei, C. (2009). *Relativistically correct hole-boring and ion acceleration by circularly polarized laser pulses.* Plasma Phys. Control. Fus. **51**, p. 024004. → 130

Robson, L., Simpson, P. T., Clarke, R. J., Ledingham, K. W. D., Lindau, F., Lundh, O., McCanny, T., Mora, P., Neely, D., Wahlström, C.-G., Zepf, M. & McKenna, P. (2007). *Scaling of proton acceleration driven by petawatt-laser-plasma interactions.* Nature Phys. **3**, p. 58–62. → 129

Rousse, A., Phuoc, K. T., Shah, R., Pukhov, A., Lefebvre, E., Malka, V., Kiselev, S., Burgy, F., Rousseau, J.-P., Umstadter, D. & Hulin, D. (2004). *Production of a kev x-ray beam from synchrotron radiation in relativistic laser-plasma interaction.* Phys. Rev. Lett. **93**, p. 135005. → 47

Sagisaka, A., Daido, H., Nashima, S., Orimo, S., Ogura, K., Mori, M., Yogo, A., Ma, J., Daito, I., Pirozhkov, A., Bulanov, S., Esirkepov, T., Shimizu, K. & Hosoda, M. (2008). *Simultaneous generation of a proton beam and terahertz radiation in high-intensity laser and thin-foil interaction.* Applied Physics B **90**, p. 373. → 135, 136, 137, 138

Sansone, G., Benedetti, E., Calegari, F., Vozzi, C., Avaldi, L., Flammini, R., Poletto, L., Villoresi, P., Altucci, C., Velotta, R., Stagira, S., De Silvestri, S. & Nisoli, M. (2006). *Isolated single-cycle attosecond pulses.* Science **314**, p. 443. → 4

Sanz, J., Debayle, A. & Mima, K. (2012). *Model for ultraintense laser-plasma interaction at normal incidence.* Phys. Rev. E **85**, p. 046411. → 127

Savage, R. L., Joshi, C. & Mori, W. B. (1992). *Frequency upconversion of electromagnetic radiation upon transmission into an ionization front.* Phys. Rev. Lett. **68**, p. 946. → 116

Schroeder, C. B., Esarey, E., van Tilborg, J. & Leemans, W. P. (2004). *Theory of coherent transition radiation generated at a plasma-vacuum interface.* Phys. Rev. E **69**, p. 016501. → 62, 64, 69, 87

Schwoerer, H., Liesfeld, B., Schlenvoigt, H.-P., Amthor, K.-U. & Sauerbrey, R. (2006). *Thomson-backscattered x rays from laser-accelerated electrons.* Phys. Rev. Lett. **96**, p. 014802. → 4

Sentoku, Y., Mima, K., Kaw, P. & Nishikawa, K. (2003). *Anomalous resistivity resulting from mev-electron transport in overdense plasma.* Phys. Rev. Lett. **90**, p. 155001. → 127

Sentoku, Y., Mima, K., Ruhl, H., Toyama, Y., Kodama, R. & Cowan, T. E. (2004). *Laser light and hot electron micro focusing using a conical target.* Physics of Plasmas **11**, p. 3083. → 136

Seres, J., Seres, E., Verhoef, A. J., Tempea, G., Streli, C., Wobrauschek, P., Yakovlev, V., Scrinzi, A., Spielmann, C. & Krausz, F. (2005). *Source of coherent kiloelectronvolt x-rays.* Nature **433**, p. 596. → 4

Sheng, Z.-M., Mima, K. & Zhang, J. (2005a). *Powerful terahertz emission from laser wake fields excited in inhomogeneous plasmas.* Physics of Plasmas **12**, p. 123103. → 138

Sheng, Z.-M., Mima, K., Zhang, J. & Sanuki, H. (2005b). *Emission of electromagnetic pulses from laser wakefields through linear mode conversion.* Phys. Rev. Lett. **94**, p. 095003. → 80, 138

Simmons, J. F. L. & McInnes, C. R. (1993). *Was marx right? or how efficient are laser driven interstellar spacecraft?* Am. J. Phys. **61**, no. 3, p. 205–207. → 132

Smith, G. S. & Hertel, T. W. (2001). *On the transient radiation of energy from simple current distributions and linear antennas.* IEEE Antennas and Propagation Magazine **43**, p. 49. → 149, 150

Snavely, R. A., Key, M. H., Hatchett, S. P., Cowan, T. E., Roth, M., Phillips, T. W., Stoyer, M. A., Henry, E. A., Sangster, T. C., Singh, M. S., Wilks, S. C., MacKinnon, A., Offenberger, A., Pennington, D. M., Yasuike, K., Langdon, A. B., Lasinski, B. F., Johnson, J., Perry, M. D. & Campbell, E. M. (2000). *Intense high-energy proton beams from petawatt-laser irradiation of solids.* Phys. Rev. Lett. **85**, p. 2945. → 128, 144

SPIE, éditeur (2009). *Radiation post-processing in PIC codes*, tome 7359. → 156

Sprangle, P., Esarey, E. & Ting, A. (1990). *Nonlinear interaction of intense laser pulses in plasma.* Phys. Rev. A **41**, p. 4463. → 49, 51, 73

Sprangle, P., Peñano, J. R., Hafizi, B. & Kapetanakos, C. A. (2004). *Ultrashort laser pulses and electromagnetic pulse generation in air and on dielectric surfaces.* Phys. Rev. E **69**, p. 066415. → 29

Sprangle, P., Tang, C. & Esarey, E. (1987). *Relativistic self-focusing of short-pulse radiation beams in plasmas.* IEEE Transactions on Plasma Science **15**, no. 2, p. 145. → 55

Steinke, S., van Tilborg, J., Benedetti, C., Geddes, C. G., R., Schroeder, C. B., Daniels, J., Swanson, K. K., Gonsalves, A., J., Nakamura, K., Matlis, N. H., Shaw, B. H., Esarey, E. & Leemans, W. P. (2016). *Multistage coupling of independent laser-plasma accelerators.* Nature **530**, p. 190. → 4

Stephens, R. B., Snavely, R. A., Aglitskiy, Y., Amiranoff, F., Andersen, C., Batani, D., Baton, S. D., Cowan, T., Freeman, R. R., Hall, T., Hatchett, S. P., Hill, J. M., Key, M. H., King, J. A., Koch, J. A., Koenig, M., MacKinnon, A. J., Lancaster, K. L., Martinolli, E., Norreys, P., Perelli-Cippo, E., Rabec Le Gloahec, M., Rousseaux, C., Santos, J. J. & Scianitti, F. (2004). *K_α fluorescence measurement of relativistic electron transport in the context of fast ignition.* Phys. Rev. E **69**, p. 066414. → 137

Strickland, D. & Mourou, G. (1985). *Compression of amplified chirped optical pulses.* Optics Communications **56**, p. 219. → 2, 38

Sun, G.-Z., Ott, E., Lee, Y. C. & Guzdar, P. (1987). *Self-focusing of short intense pulses in plasmas.* Phys. Fluids **30**, p. 526. → 55

Tabak, M., Hammer, J., Glinsky, M. E., Kruer, W. L., Wilks, S. C., Woodworth, J., Campbell, E. M., Perry, M. D. & Mason, R. J. (1994). *Ignition and high gain with ultrapowerful lasers.* Physics of Plasmas **1**, no. 5, p. 1626. → 124

Tajima, T. & Dawson, J. M. (1979). *Laser electron accelerator.* Phys. Rev. Lett. **43**, p. 267. → 3, 46, 47

Ter-Mikaelian, M. L. (1972). *High Energy Electromagnetic Processes in Condensed Media.* John Wiley and Sons, New York. → 59, 68, 139

Thaury, C. & Quéré, F. (2010). *High-order harmonic and attosecond pulse generation on plasma mirrors: basic mechanisms.* Journal of Physics B: Atomic, Molecular and Optical Physics **43**, p. 213001. → 4

Thiele, I., Nuter, R., Bousquet, B., Tikhonchuk, V., Skupin, S., Davoine, X., Gremillet, L. & Bergé, L. (2016). *Theory of terahertz emission from femtosecond-laser-induced microplasmas.* Phys. Rev. E **94**, p. 063202. → 29, 36

Tochitsky, S., Welch, E., Polyanskiy, M., Pogorelsky, I., Panagiotopoulos, P., Kolesik, M., Wright, E. M., Koch, S. W., Moloney, J. V., Pigeon, J. & Joshi, C. (2018). *Megafilament in air formed by self-guided terawatt long-wavelength infrared laser.* Nat. Photonics **13**, p. 41. → 106

Tochitsky, S. Y., Pigeon, J. J., Haberberger, D. J., Gong, C. & Joshi, C. (2012). *Amplification of multi-gigawatt 3 ps pulses in an atmospheric co_2 laser using ac stark effect.* Opt. Express **20**, p. 13762. → 106

Tonouchi, M. (2007). *Cutting-edge terahertz technology.* Nature Photon. **1**, p. 97. → 6

Toro, E. F. (2012). *Riemann solvers and numerical methods for fluid dynamics: A practical introduction.* Springer-Verlag, Berlin & Heidelberg. → 157, 158

Tresca, O., Dover, N. P., Cook, N., Maharjan, C., Polyanskiy, M. N., Najmudin, Z., Shkolnikov, P. & Pogorelsky, I. (2015). *Spectral modification of shock accelerated ions using a hydrodynamically shaped gas target.* Phys. Rev. Lett. **115**, p. 094802. → 106

Umstadter, D., Kim, J. K. & Dodd, E. (1996). *Laser injection of ultrashort electron pulses into wakefield plasma waves.* Phys. Rev. Lett. **76**, p. 2073. → 55

von der Linde, D., Schulz, H., Engers, T. & Schuler, H. (1992). *Second harmonic generation in plasmas produced by intense femtosecond laser pulses.* IEEE Journal of Quantum Electronics **28**, p. 2388. → 135

Wan, Y., Pai, C.-H., Zhang, C. J., Li, F., Wu, Y. P., Hua, J. F., Lu, W., Gu, Y. Q., Silva, L. O., Joshi, C. & Mori, W. B. (2016). *Physical mechanism of the transverse instability in radiation pressure ion acceleration.* Phys. Rev. Lett. **117**, p. 234801. → 127

Wang, T.-J., Yuan, S., Chen, Y., Daigle, J.-F., Marceau, C., Théberge, F., Châteauneuf, M., Dubois, J. & Chin, S. L. (2010). *Toward remote high energy terahertz generation.* Applied Physics Letters **97**, p. 111108. → 79

Wang, W.-M., Li, Y.-T., Sheng, Z.-M., Lu, X. & Zhang, J. (2013). *Terahertz radiation by two-color lasers due to the field ionization of gases.* Phys. Rev. E **87**, p. 033108. → 79

Wigner, E. (1932). *On the quantum correction for the thermodynamic equilibrium.* Phys. Rev. **40**, p. 749. → 117

Wilks, S. C., Dawson, J. M. & Mori, W. B. (1988). *Frequency up-conversion of electromagnetic radiation with use of an overdense plasma.* Phys. Rev. Lett. **61**, p. 337. → 116

Wilks, S. C., Kruer, W. L., Tabak, M. & Langdon, A. B. (1992). *Absorption of ultra-intense laser pulses.* Phys. Rev. Lett. **69**, p. 1383. → 124

Wilks, S. C., Langdon, A. B., Cowan, T. E., Roth, M., Singh, M., Hatchett, S., Key, M. H., Pennington, D., MacKinnon, A. & Snavely, R. A. (2001). *Energetic proton generation in ultra-intense laser-solid interactions.* Physics of Plasmas **8**, p. 542. → 128

Williams, B. S. (2007). *Terahertz quantum-cascade lasers.* Nature Photonics **1**. → 7

Woodbury, D., Feder, L., Shumakova, V., Gollner, C., Schwartz, R., Miao, B., Salehi, F., Korolov, A., Pugžlys, A., Baltuška, A. & Milchberg, H. M. (2018). *Laser wakefield acceleration with mid-ir laser pulses.* Opt. Lett. **43**, p. 1131. → 106, 107, 155

Woodward, R. M., Wallace, V. P., Arnone, D. D., Linfield, E. H. & Pepper, M. (2003). *Terahertz pulsed imaging of skin cancer in the time and frequency domain.* Journal of biological physics **29**, no. 2, p. 257. → 5

Xie, X., Dai, J. & Zhang, X. C. (2006). *Coherent control of thz wave generation in ambient air.* Phys. Rev. Lett. **96**, p. 075005. → 19

Yee, K. (1966). *Numerical solution of initial boundary value problems involving maxwell's equations in isotropic media.* IEEE Transactions on Antennas and Propagation **14**, no. 3, p. 302–307. → 42

Yi, S. A., Khudik, V., Kalmykov, S. Y. & Shvets, G. (2010). *Hamiltonian analysis of electron self-injection and acceleration into an evolving plasma bubble.* Plasma Physics and Controlled Fusion **53**, p. 014012. → 55

Yu, W., Bychenkov, V., Sentoku, Y., Yu, M. Y., Sheng, Z. M. & Mima, K. (2000). *Electron acceleration by a short relativistic laser pulse at the front of solid targets.* Phys. Rev. Lett. **85**, p. 570. → 142

Yuan, L. C. L., Wang, C. L., Uto, H. & Prünster, S. (1970). *Formation-zone effect in transition radiation due to ultrarelativistic particles.* Phys. Rev. Lett. **25**, p. 1513. → 61

Yuan, X. H., Li, Y., Xu, M. H., Zheng, Z. Y., Yu, Q. Z., Liang, W. X., Zhang, Y., Liu, F., Bernhardt, J., Wang, S. J., Wang, Z. H., Ling, W. J., Wei, Z. Y., Zhao, W. & Zhang, J. (2008). *Effective fast electron acceleration along the target surface.* Opt. Express **16**, p. 81. → 136

Zalesak, S. (2012). *Flux corrected transport: Principles, algorithms, and applications.* Springer-Verlag, Berlin & Heidelberg. → 157

Zheng, J., Tanaka, K. A., Miyakoshi, T., Kitagawa, Y., Kodama, R., Kurahashi, T. & Yamanaka, T. (2002). *Spectrum of transition radiation from hot electrons generated in ultra-intense laser plasma interaction.* Physics of Plasmas **9**, p. 3610. → 69, 145

Zheng, J., Tanaka, K. A., Miyakoshi, T., Kitagawa, Y., Kodama, R., Kurahashi, T. & Yamanaka, T. (2003). *Theoretical study of transition radiation from hot electrons generated in the laser-solid interaction.* Physics of Plasmas **10**, p. 2994. → 69, 145

Zhu, W., Palastro, J. P. & Antonsen, T. M. (2012). *Studies of spectral modification and limitations of the modified paraxial equation in laser wakefield simulations.* Physics of Plasmas **19**, no. 3, p. 033105. → 116

Zhuo, H. B., Zhang, S. J., Li, X. H., Zhou, H. Y., Li, X. Z., Zou, D. B., Yu, M. Y., Wu, H. C., Sheng, Z. M. & Zhou, C. T. (2017). *Terahertz generation from laser-driven ultrafast current propagation along a wire target.* Phys. Rev. E **95**, p. 013201. → 149, 150

Titre: Sources térahertz produites par des impulsions laser ultra-intenses

Mots clés : Sources térahertz intenses, Interaction laser-plasma, Plasmas relativistes

Résumé : Les impulsions laser femtosecondes produisent des phénomènes non linéaires extrêmes dans la matière, conduisant à une forte émission de rayonnement secondaire qui couvre un domaine en fréquence allant du terahertz (THz) aux rayons X et gamma. De nombreuses applications utilisent la bande de fréquences terahertz (0.1-100 THz) afin de sonder la matière (spectroscopie, médecine, science des matériaux). Ce travail est dédié à l'étude théorique et numérique du rayonnement THz généré par interaction laser-plasma. Comparé aux techniques conventionnelles, ces impulsions laser permettent de créer des sources THz particulièrement énergétiques et à large bande. Notre objectif a donc d'été étudier ces régimes d'interaction relativiste, encore peu explorés, afin d'optimiser l'efficacité de conversion du laser vers les fréquences THz. L'étude de l'interaction laser-gaz en régime classique nous permet, d'abord, de valider un modèle de propagation unidirectionnelle prenant en compte la génération d'impulsion THz et de le comparer à la solution exacte des équations de Maxwell. Ensuite, en augmentant l'intensité laser au-delà du seuil relativiste, nous simulons à l'aide d'un code PIC une onde plasma non linéaire dans le sillage du laser, accélérant ainsi des électrons à plusieurs centaines de MeV. Nous montrons que le mécanisme standard des photocourrants est dominé par le rayonnement de transition cohérent induit par les électrons accélérés dans l'onde de sillage. La robustesse de ce rayonnement est ensuite observée grâce à une étude paramétrique faisant varier la densité du plasma sur plusieurs ordres de grandeur. Nous démontrons également la pertinence des grandes longueurs d'ondes laser qui sont à même de déclencher une forte pression d'ionisation augmentant la force pondéromotrice du laser. Enfin, les rayonnements THz émis à partir d'interactions laser-solide sont examinés dans le contexte de cibles ultra fine, mettant en lumière les différents processus impliqués.

Title: Terahertz sources generated by ultra-intense laser pulses

Keywords: Intense terahertz sources, Laser-plasma interaction, Relativistic plasmas

Abstract: Femtosecond laser pulses trigger extreme nonlinear events in matter, leading to intense secondary radiations spanning the frequency ranges from terahertz (THz) to X and gamma-rays. This work is dedicated to the theoretical and numerical study of THz radiation generated by laser-driven plasmas. Despite the inherent difficulty in accessing the THz spectral window (0.1-100 THz), many coming applications use the ability of THz frequencies to probe matter (spectroscopy, medicine, material science). Laser-driven THz sources appear well-suited to provide simultaneously an energetic and broadband signal compared to other conventional devices. Our goal is to investigate previously little explored interaction regimes in order to optimize the laser-to-THz conversion efficiency. Starting from classical interactions in gases, we validate a unidirectional propagation model accounting for THz pulse generation, which we compare to the exact solution of Maxwell's equations. We next increase the laser intensity above the relativistic threshold in order to trigger a nonlinear plasma wave in the laser wake, accelerating electrons to a few hundreds of MeV. We show that the standard photocurrent mechanisms is overtaken by coherent transition radiation induced by wakefield-accelerated electron bunch. Next, successive studies reveal the robustness of this latter process over a wide range of plasma parameters. We also demonstrate the relevance of long laser wavelengths in augmenting THz pulse generation through the ionization-induced pressure that increases the laser ponderomotive force. Finally, THz emission from laser-solid interaction is examined in the context of ultra-thin targets, shedding light on the different processes involved.

Université Paris-Saclay
Espace Technologique / Immeuble Discovery
Route de l'Orme aux Merisiers RD 128 / 91190 Saint-Aubin, France